Particles, prey, and purse seines: A data-driven investigation into the impacts of climate on biological processes across the global ocean

Shirley W. Leung

A dissertation

submitted in partial fulfillment of the

Requirements for the degree of

Doctor of Philosophy

University of Washington

2020

Reading Committee:

LuAnne Thompson, Chair

Allison Smith

Michael McPhaden

Program Authorized to Offer Degree:

Oceanography

University of Washington

Abstract

Particles, prey, and purse seines: A data-driven investigation into the impacts of climate on biological processes across the global ocean

Shirley W. Leung

Chair of the Supervisory Committee:
LuAnne Thompson
Oceanography

In this dissertation, I use existing large-scale public datasets to examine how climate variability and change affect ecosystem processes throughout the global oceans, with some emphasis on the Tropical Pacific because of the abundance of culturally and economically important top pelagic predator species such as tuna and billfish here. The objectives of this work are to illuminate the effects of climate on marine ecosystems, as well as to quantify and reduce uncertainties in current stock assessment and global ocean models. In Chapter 2, I use an empirically-constrained 3-D global ocean model to show that more detailed modeling of phytoplankton sizes and sinking particles can have a considerable effect on the accuracy of climate change-driven projections of particulate carbon export, which can in turn greatly affect projections of future carbon storage, mesopelagic biomass availability, and subsurface oxygen concentrations. In Chapter 3, I use *in situ* measurements of oxygen and temperature to show that El Niño-Southern Oscillation (ENSO) is the primary driver of large variations in upper-ocean oxygen content on interannual time scales in the Tropical Pacific. Oxygen therefore likely plays an important role in altering tuna habitat quality and available vertical habitat space between different phases of ENSO here. In Chapter 4, I show that of all global ocean regions, climate warming-driven deoxygenation over the next century will most greatly affect species residing in

the temperate North Pacific (including swordfish and yellowfin, bigeye, Pacific bluefin, and albacore tunas), where projected decreases in oxygen concentrations between 200-700 m depth are greatest and most certain. Conversely, the smallest and least certain projections of subsurface oxygen concentration changes and effects occur within the tuna-rich Tropical Pacific, where more attention should be focused on improving model representations of underlying ocean circulation dynamics. In Chapter 5, I analyze purse seine catch and effort data to determine where and when fishers targeting fish aggregating device (FAD)-associated skipjack tuna can most effectively reduce incidental juvenile bigeye tuna catches. Though FAD-associated skipjack and bigeye tend to strongly co-occur, there are significant variations in their lateral separability over both space and time, especially between different phases of ENSO. El Niño lowers fractional incidental bigeye catch east of ~170°E and raises it to the west, while La Niña has the opposite effect. Spatial patterns in sea surface height anomalies, which also vary greatly with ENSO, may be useful in separating different habitats preferred by skipjack and bigeye throughout the Western Tropical Pacific. In Appendix A, I show that ENSO also drives sizable variations in micronektonic prey availability and diel vertical migration depths throughout the Tropical Pacific. As was the case with subsurface oxygen concentrations, these variations in prey availability likely substantially alter tuna habitat quality between different ENSO phases and should therefore be considered in temporally-resolved habitat and stock assessment models. Collectively, this body of work has demonstrated the following three points: Firstly, climate variability and change can have profound effects on marine ecosystem processes on all scales, from the size and sinking speed of particles to the spatial distributions of top pelagic predators and their relationships with other species, including humans. Secondly, there are many ways to

improve the accuracy of models, including better accounting for small-scale processes with large effects, better constraining difficult-to-parameterize relationships with observational data, and better resolving biologically relevant environmental conditions. Finally, many important and interesting research questions can be answered using already-existing public domain data analyzed in new and creative ways.

Table of Contents

Chapter 1: Introduction

Climate change is one of the most urgent issues of our time and will have far-reaching effects on multi-scale biogeochemical processes across the global ocean (Bopp et al., 2013; Cabre et al., 2015). Marine ecosystems upon which billions rely for their food security and/or livelihoods (Badjeck et al., 2010) will be particularly hard hit, as they become threatened by ocean acidification, warming, and deoxygenation simultaneously (IPCC, 2019). Within many of these ecosystems, however, we are only beginning to understand the effects of these various changes on the constituent organisms and processes. In this dissertation, I contribute to the growing body of knowledge on how deoxygenation and warming will affect ecosystem processes throughout the global oceans, with an emphasis on the Tropical Pacific because of the abundance of culturally and economically important top pelagic predator species (namely tuna and billfish) there.

By better understanding how climate change will affect marine ecosystems, we will be able to better plan for future changes. While decreasing greenhouse gas emissions (i.e., mitigation) is undoubtedly the best strategy for reducing the impacts of climate change, widespread adaptation will also most certainly be necessary. One way in which social scientists study how we can best adapt to future climate change is by first understanding how people have successfully dealt with climate changes and variability before. Similarly, oceanographers study the potential effects of future climate change on marine ecosystems by examining how variations in climate have affected these ecosystems in the past. In this dissertation, I use this key approach, along with mechanistic biogeochemical modelling, to generate an understanding of how

important marine ecosystem processes such as particulate organic carbon export, diel vertical migrations, and pelagic predator species interactions, are affected by both climate variability and change. Through this work, I thus provide actionable information that can be used to identify effective adaptive measures that will lessen the harmful effects of both climate change and climate variability.

Aside from illuminating the effects of climate on marine ecosystems, a second goal of my work is to quantify and reduce uncertainties in models currently used to conduct stock assessments or project future conditions. In Chapter 2, I use SeaWiFS satellite measurements of particle size and net primary production to probe uncertainties in model-derived predictions of future carbon export. From this, I show that projections of particulate carbon export made by global models can be improved by including more detailed sinking particle dynamics. In Chapter 3, I analyze *in situ* measurements from the World Ocean Database to illuminate previously unknown subsurface oxygen variability patterns in the Tropical Pacific. I specifically create maps of El Niño-Southern Oscillation (ENSO)-driven variations in Tropical Pacific subsurface oxygen availability that can be used to improve tuna stock assessment models which currently lack time-varying information on oxygenated habitat quality. In Chapter 4, I combine publicly-available Earth System Model predictions with previously published physiological measurements made in the lab and field to investigate effects of climate-driven deoxygenation on tuna and billfish species around the world. Through this work, I identify where model projections of deoxygenation effects are most uncertain and need the most improvement. In Chapter 5, I analyze public domain purse seine catch and effort data collected by the Western and Central Pacfic Fisheries Commission to determine where and when fishers targeting fish

aggregating device (FAD)-associated skipjack tuna can most effectively reduce incidental bigeye tuna catches. In doing so, I help better inform the complex mental models used by both fishers during operations and fisheries managers to create policies preserving bigeye stocks in the Tropical Pacific. In Appendix A, I leverage existing public acoustic doppler current profiler (ADCP) data compiled by the Joint Archive for Shipboard ADCP to illuminate previously unknown subsurface distributions of micronekton. I thus create plots of mean and ENSO-related micronektonic prey concentrations that can be used to update stock assessment models with more accurate and better resolved prey availabilities.

As can be seen, I have sought to accomplish my two goals of informing model improvements and illuminating the effects of climate on marine ecosystems using data that is already available. Though collection of new data is crucial for measuring how the ocean is changing with anthropogenic warming over time, a single research cruise alone can cost tens of thousands of dollars per day and emit many tons of carbon dioxide. Thus, already-existing, publicly-available data should be used to answer as many research questions as possible. In each chapter of this dissertation, I pair data of this kind with careful and creative new computations to address a plethora of important research questions. As such, a key third objective of my work is to promote the use of existing, publicly-available, large-scale and/or global datasets in new ways.

In sum, this dissertation serves 3 primary purposes: 1.) To provide actionable information on the effects of climate variability and change on important marine ecosystem processes across the global ocean. 2.) To quantify stock assessment and global biogeochemical model uncertainties, as well as provide avenues for model improvements. 3.) To promote both awareness and increased use of existing publicly-available climate and ocean data.

Chapter 2: Variable phytoplankton size distributions reduce the sensitivity of global export flux to climate change

This chapter is an edited version of the submitted publication: Leung, S., Weber, T., Cram, J. A., & Deutsch, C. Variable phytoplankton size distributions reduce the sensitivity of global export flux to climate change. *Submitted to Biogeosciences and published as a preprint in Biogeociences Discussions at* https://doi.org/10.5194/bg-2020-156.

2.1 Summary

Earth System Models predict a 10-20% decrease in ocean carbon export production by the end of the 21st century due to global climate change. This decline is caused by increased stratification of the upper ocean, resulting in reduced shallow subsurface nutrient concentrations and a slower supply of nutrients to the surface euphotic zone. These predictions, however, do not account for associated changes in sinking particle size and remineralization depth. Here we combine satellite-derived export and particle size maps with a simple 3-D global biogeochemical model to investigate how shifts in sinking particle size may buffer predicted changes in surface nutrient supply and therefore export production. We show that higher export rates are correlated with larger phytoplankton and sinking particles, especially in tropical and subtropical regions. Incorporation of these empirical relationships into a global model shows that as circulation slows, a decrease in export and associated shift toward smaller phytoplankton yields particles that sink more slowly and are thus remineralized shallower; this in turn leads to greater recycling of nutrients in the upper water column and faster recirculation into the euphotic zone, boosting productivity and export to counteract the initial circulation-driven decreases. This negative

feedback mechanism (termed the particle size-remineralization feedback) slows export decline over the next century by ~14% globally and by ~20% in the tropical and subtropical oceans, where export decreases are currently predicted to be greatest. Thus, incorporating dynamic particle size-dependent remineralization depths into Earth System Models will result in more robust predictions of changes in biological pump strength in a warming climate.

2.1 Introduction

2.1.1 Carbon export in the future ocean

A key mechanism that controls the partitioning of carbon dioxide (CO_2) between the atmosphere and ocean is the biological pump, in which CO_2 is fixed into phytoplankton organic matter via photosynthesis, and then exported from the surface to the deep ocean as sinking particles (e.g., Ducklow et al., 2001). Decomposition of this particulate organic carbon (POC) in the ocean interior maintains a reservoir of respired CO_2 that is sequestered out of contact with the atmosphere, thus exerting an important control on long-term atmospheric CO_2 concentrations and global climate (e.g., Martínez-García et al., 2014; Passow & Carlson, 2012; Sarmiento & Siegenthaler, 1992). Carbon exported out of the surface euphotic zone also fuels the metabolism of organisms in the mesopelagic zone, sustaining economically and socially important fisheries, as well as ecologically important zooplankton and micronekton communities (e.g., Boyd et al., 2019; Friedland et al., 2012). POC export is also an important driver of dissolved oxygen concentrations in the water column. Where sinking POC fluxes are particularly high, enhanced bacterial breakdown of particles can deplete available oxygen and create hypoxic

or even suboxic conditions in which many organisms cannot survive (e.g., Hofmann and Schellnhuber, 2009; Oschlies et al., 2008). Given the critical role of POC export in driving ocean carbon sequestration, the global climate system, fisheries productivity, and dissolved oxygen availability, there is a growing need to better understand how export will respond to future climate warming.

State-of-the-art Earth System Models (ESMs) predict decreases in global export production (defined as the sinking POC flux at 100m) of ~10-20% by 2100 (Bopp et al., 2013; Cabré et al., 2015b) and ~30% by 2300 (Moore et al., 2018). In these models, primary production and subsequent carbon export are largely limited by the physical supply of nutrients to the surface ocean, which is predicted to slow with future warming. Mechanisms driving this nutrient supply slowdown include: (i) surface warming-induced stratification of the water column, which will shoal winter mixed layers, limit vertical exchange, and "trap" nutrients in the ocean interior (Bopp et al., 2013; Anna Cabré et al., 2015b; Capotondi et al., 2012; Moore et al., 2018), and (ii) a weakening of the trade winds, which will reduce upwelling rates and vertical nutrient supply in tropical oceans (Bopp et al., 2001; Collins et al., 2010), as well as lateral Ekman-driven nutrient supply into the subtropics (Letscher et al 2016).

Changes in the POC flux itself, however, also have the potential to modulate nutrient supply to the surface ocean and therefore impact export. Because particles release nutrients when they decompose, the depth scale of particle remineralization determines the proximity of these nutrients to the surface and their resupply rate to the euphotic zone (Kwon et al., 2009; Yamanaka & Tajika, 1996). Shallow remineralization in mesopelagic waters, especially above the permanent pycnocline, drives rapid nutrient recirculation to the surface; nutrients

remineralized in deeper waters, on the other hand, can take hundreds of years to re-emerge at the surface (Martin et al., 1987; Matsumoto, 2007). This raises the possibility of feedback loops in which changes in particle remineralization depth might either dampen or enhance circulation-driven decreases in primary production and export.

Recent work has shown that particle size plays a paramount role in determining remineralization length scales and carbon transfer efficiency to depth due to its influence on sinking speed (Cram et al., 2018; Kriest & Oschlies, 2008; Weber et al., 2016). Current ESMs, however, generally do not resolve a dynamic particle size spectrum and so cannot fully capture biological feedbacks driven by particle size (Laufkötter et al., 2016; Le Quéré et al., 2005). For example, it is common in global models to impose a power-law particle flux profile based on empirical fits to sediment trap measurements (Bopp et al., 2001; Kwon et al., 2009; Maier−Reimer, 1993; Martin et al., 1987; Najjar et al., 1992; Yamanaka & Tajika, 1996), or to explicitly simulate particles whose sinking speeds are fixed, vary over depth (Aumont & Bopp, 2006; Schmittner et al., 2005), or differ between only one large and one small size class (Aumont & Bopp, 2006; Gregg et al., 2003). More complex models that resolve aggregation-disaggregation transformations and/or continuous particle sizes have been developed (Gehlen et al., 2006; Kriest & Oschlies, 2008), but have not been used to study the effects of climate change on export production. Furthermore, parameters and processes in most previous models are not constrained by observations of particle size distributions.

Here we conduct a series of model experiments constrained by empirical relationships to isolate the effect of particle size-dependent remineralization depths on future export changes. We use satellite-derived export rates and particle size data in combination with a 3-D global

biogeochemical model to demonstrate that current ESMs, which lack particle size-dependent remineralization depths, may overestimate 21st century decreases in carbon export.

2.1.2 A hypothesized particle size-remineralization (PSR) feedback

Particle abundances in the ocean tend to follow a power-law distribution with many more small particles than large ones (Boss et al., 2001; Sheldon et al., 1972). Particle size distributions can thus be succinctly described by the negative exponent in the power-law relationship between particle diameter and number density, i.e. the negative linear slope between these two variables on log-log axes. We define the absolute value of this slope as β. A shallower slope (small β) indicates a greater proportion of large particles relative to small ones, while a steeper slope (large β) indicates a smaller proportion of large particles.

Large particles tend to exist in the ocean where larger microphytoplankton (>20 um in diameter) are dominant, while relatively small particles tend to exist where smaller picophytoplankton (<2 um in diameter) are dominant (Guidi et al., 2007; Guidi et al., 2008; Guidi et al., 2009). The presence of large phytoplankton leads to the generation of larger particles perhaps because large phytoplankton are more likely to form aggregates and be transformed into large fecal pellets by large zooplankton, whereas small phytoplankton are more likely to be degraded by bacteria and consumed by smaller zooplankton (Bopp et al., 2005; Guidi et al., 2007; Guidi et al., 2009; Michaels and Silver, 1988). The exact mechanisms governing the processes by which smaller and larger phytoplankton become smaller and larger particles are not clearly known, however, and is an active area of research.

Phytoplankton community size structure is in turn determined by the availability of nutrients. Low-nutrient conditions select for small phytoplankton with high surface area-to-volume ratios, which make them less susceptible to nutrient diffusion limitation (Litchman et al., 2007). Regions with lower nutrient concentrations thus tend to have a greater relative abundance of small picophytoplankton and particles, while regions with higher nutrient concentrations tend to be dominated by larger microphytoplankton and particles. Indeed, global patterns of annual-mean β (Kostadinov et al., 2009) and fractional picophytoplankton abundance (fpico) (Hirata et al., 2011) estimated from remote sensing correspond closely with surface nutrient concentrations (Fig. 2.1a-c).

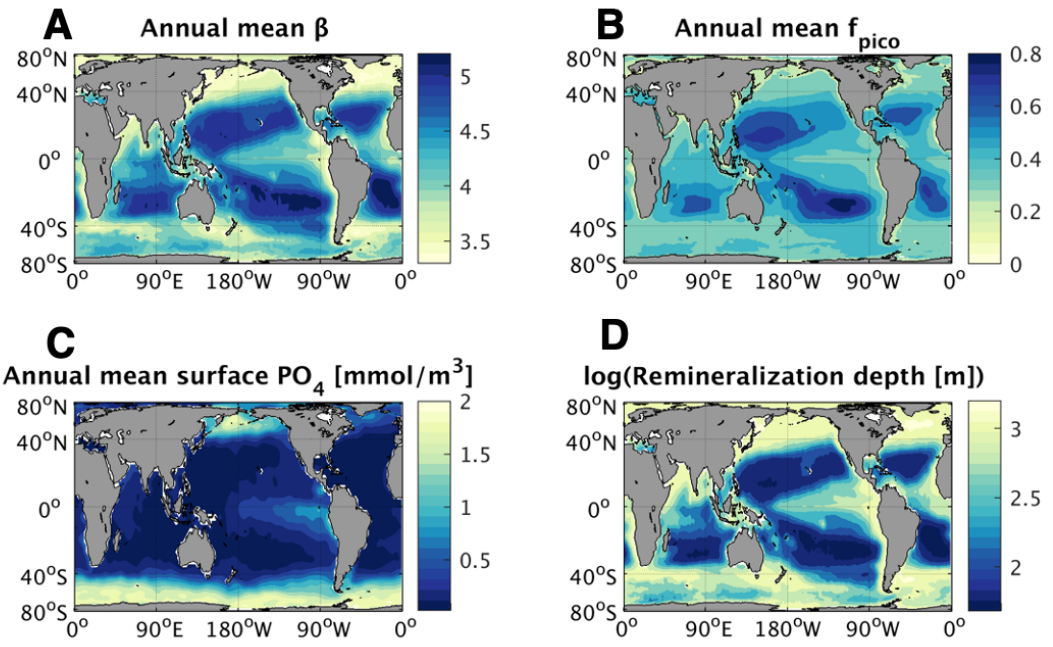

Figure 2.1 | Global maps of annual mean (A) particle size distribution slope (β) measured by remotely-sensed particulate backscatter and reproduced from Kostadinov et al. (2009), (B) fractional picophytoplankton abundance (fpico) reproduced from Hirata et al. (2011), (C) surface phosphate concentration from World Ocean Atlas, and (D) remineralization depth, defined as the depth at which particulate flux out of the euphotic zone is decreased by a factor of e assuming β in (A) at the surface, calculated using a particle remineralization and sinking model (PRiSM, described in Section 2.2.1.1).

Past work has also firmly established a strong positive relationship between particle size and sinking speed in the ocean (Alldredge and Gotschalk, 1988; Smayda, 1971) (although there are exceptions to this rule, particularly in the Southern Ocean – see McDonnell and Buesseler (2010)). The characteristic depth scale of particle remineralization is proportional to this sinking speed divided by a microbially-mediated remineralization rate (Kwon et al., 2009; McDonnell et al., 2015). Here we define remineralization depth (or remineralization depth) as the shallowest depth at which POC flux out of the euphotic zone is reduced by a factor of *e* or 63% (i.e., the *e*-folding depth of the flux) (Fig. 2.1d). The dominance of smaller phytoplankton and sinking particles in the water column results in a shallower remineralization depth, as bacteria have more time to remineralize these slow-sinking particles in the upper layers of the water column (Bach et al., 2016).

In sum, there are strong connections between nutrient availability, phytoplankton community structure, particle size, and remineralization depth, as evidenced by their closely-related global patterns (Fig. 2.1). Taken together, these connections point towards a negative feedback loop that may dampen changes in carbon export arising from physically-induced changes in surface nutrient supply. In a warming and stratifying ocean, this hypothesized feedback (hereafter known as the particle size-remineralization feedback, or PSR feedback) would proceed through the following steps, which are illustrated schematically in Fig. 2.2:

1.) Slower Circulation (SC) – First, stratification of the water column and slowing trade winds with climate warming will reduce shallow subsurface nutrient concentrations and vertical exchange/upwelling rates. This slows nutrient supply into the euphotic

zone, which in turn decreases phytoplankton productivity and resultant export production (Fig. 2.2a, b, green arrows).

2.) *Ecological Effect (EE)* – A decrease in surface nutrient supply also selects for smaller phytoplankton, which leads to a larger proportion of small particles in the export flux. The net result of this ecological effect (EE) (Fig. 2.2a, red arrow) can be captured by the relationship between export and β (Fig. 2.2c, red line), as any decrease in export driven by decreased nutrient supply would also cause a corresponding decrease in phytoplankton/particle size. The degree to which particle sizes shrink in association with decreasing export rates is represented by the negative slope of the red, theoretical export-versus-β line in Fig. 2.2c. Constrained by this relationship, the changes in export and β under slowed circulation (SC) must fall along this red line ("SC with EE" point). In the absence of the ecological effect (i.e., phytoplankton/particle sizes are not affected by changes in the nutrient supply), there is no such requirement and β would remain unchanged under a slowed circulation scenario ("SC without EE" point in Fig. 2.2c).

3.) *Sinking Speed Effect (SSE)* – Smaller particles resulting from the ecological response to a reduced nutrient supply would sink more slowly and therefore remineralize shallower in the water column. More regenerated nutrients would then accumulate within shallower waters and thus recirculate more quickly to the surface. In isolation, a shift to smaller particles would therefore ultimately lead to greater surface nutrient supply and larger export rates (Fig. 2.2a, blue arrow), represented by the positive slope of the blue export-versus-β line in Fig. 2.2d. In the presence of this sinking

speed effect (SSE), changes in export and β under slowed circulation must fall along the blue sinking speed-related export-versus-β line (Fig. 2.2d). In the absence of this sinking speed effect (i.e., particle size does not affect sinking rates/remineralization depths), there is no such requirement, and the initial stratification-induced export decrease would remain unaltered ("SC without SSE, with EE" point in Fig. 2.2d).

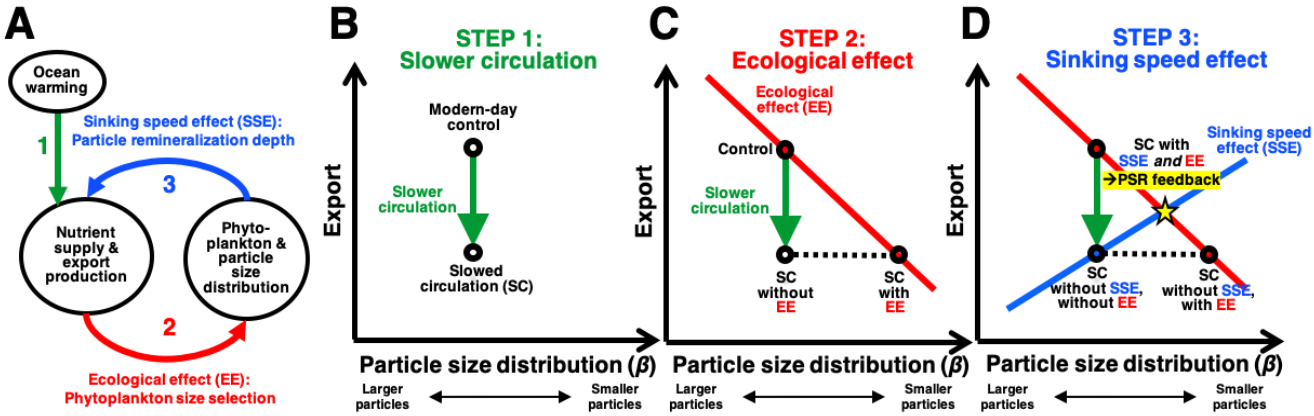

Figure 2.2 | (A) Schematic diagram of the particle size-remineralization (PSR) negative feedback on export production. A change in circulation rates induced by climate change alters surface nutrient supply and subsequent export production (green arrow). Changes in surface nutrient supply also drive changes in phytoplankton and resultant sinking particle sizes (red arrow). Changes in sinking particle sizes in turn alter remineralization depth and consequently, surface nutrient supply and export (blue arrow). (B) Schematic depicting decreased export production with decreases in circulation rates and surface nutrient supply. (C) Schematic depicting a theoretical relationship between export and β, here termed the phytoplankton size selection ecological effect (EE), in which smaller phytoplankton dominate in low-nutrient, low-export conditions. (D) Schematic depicting all previous components of the PSR feedback, in addition to the crucial final component: the particle remineralization depth sinking speed effect (SSE), in which smaller particles tend to get remineralized shallower, leading to a greater recycled surface nutrient supply and therefore greater export.

Only in the presence of both the ecological and sinking speed effects will the PSR feedback function; in this case, after circulation is slowed, export and β must reach a new steady-state at the intersection of the red and blue lines ("SC with SSE *and* EE" yellow star in Fig. 2.2d). Thus, the overall decrease in POC export would be smaller than predicted from decreased circulation rates and surface nutrient supply alone. That is, the net effect of phytoplankton selection and particle size-dependent remineralization depths provides a negative

feedback on, or dampening of, changes in export. Though the above description focuses on export decreases under decreased circulation rates, the PSR feedback would result in an analogous dampening of export increases under increased circulation rates and surface nutrient supply.

To quantify the strength of this hypothesized feedback, we employ a 3-D global ocean biogeochemical model and remotely-sensed estimates of carbon export and particle size distributions. To isolate the effects of the feedback, we take an idealized approach using empirical relationships and a simple model that allows responses to be easily traced back to assumptions made at each step. In doing so, we produce a first-order estimate of the particle size-remineralization (PSR) feedback strength throughout the ocean.

2.2 Methods

2.2.1 Ocean biogeochemical and particle remineralization model

2.2.1.1 Model setup

We examine the PSR feedback within the context of an idealized ocean biogeochemical model, which comprises a simple nutrient cycle (DeVries et al., 2014) embedded within the Ocean Circulation Inverse Model (OCIM) (DeVries, 2014). OCIM assimilates passive and transient tracer observations to constrain the time-mean, large-scale circulation at 2-degree horizontal resolution on 24 vertical layers. Nutrient cycling comprises phosphate (PO_4^{3-}) uptake and export in the surface ocean (<75m), particle remineralization in the subsurface (>75m), and production and decomposition of dissolved organic phosphorus.

Remineralization is represented implicitly based on the attenuation of the particle flux, as predicted by the 1-D mechanistic Particle Remineralization and Sinking Model (PRiSM). PRiSM computes particle flux profiles as a function of particle size distribution (β) at the surface, microbial remineralization rates, and physical relationships between particle size, mass, and sinking velocity. Using PRiSM, variations in annual mean β of the magnitude observed by satellite can lead to large differences in particle fluxes at depth (Supp. Fig. 2.1; Fig. 2.1a,d; DeVries et al 2014). Model configuration and parameter values used here are listed in Supp. Table 2.1; further model details and validation are described in DeVries et al. (2014). Here we extend the original PRiSM-enabled biogeochemical model in two important ways:

1.) We add the ability to enable or disable the PSR feedback by optionally allowing the particle size distribution to respond to changes in nutrient supply (Section 2.2.1.2).

2.) The original diagnostic nutrient uptake term (i.e., nutrient-restoring production) is replaced by the prognostic organic matter production scheme developed by Weber and Deutsch (2012) with minor parameter updates (see Supp. Table 2.2). This scheme calculates phytoplankton growth rates as a function of observed annual-mean temperatures (Locarnini et al., 2010) and solar radiation levels (Rossow & Schiffer, 1999), along with modeled PO_4^{3-}. We thus explicitly model phytoplankton production in terms of phosphorus consumption and regeneration. We then use an empirical, spatially variable relationship between particulate C-to-P ratios and phosphate concentrations (Galbraith & Martiny, 2015) to convert phytoplankton production into units of carbon. It is assumed that 10% of phytoplankton production is routed directly

to dissolved organic matter in the euphotic zone, with the remainder becoming particulate organic matter (Thornton, 2013).

2.2.1.2 Model representation of the PSR feedback

When the PSR feedback is disabled within our model, nutrient supply changes drive changes in export, but β remains constant over time. With the PSR feedback enabled, nutrient supply changes drive changes in export and β via an empirically-derived, spatially variable relationship between export and β that is detailed in Section 2.2.2. In this way, β can respond dynamically to a change in nutrient supply, leading to changes in remineralization depth, and initiating the feedback described in Section 2.1.2. Mathematically, β is updated at a given grid point as follows between timesteps t and $t+1$:

$$\beta_{t+1} = \beta_t + \frac{d\beta_{obs}}{dE_{n,obs}} \frac{E_{t+1} - E_t}{E_t} \text{, (Eqn. 2.1)}$$

where E is model-derived export and $\frac{d\beta_{obs}}{dE_{n,obs}}$ is the empirically-derived, time-independent fractional change in observed β (β_{obs}) per change in observed time-mean normalized export ($E_{n,obs}$) (i.e., absolute export divided by time-mean export at a given grid point).

To disable the feedback, $\frac{d\beta_{obs}}{dE_{n,obs}}$ is set equal to zero so that modeled β remains constant over time. To enable the feedback, $\frac{d\beta_{obs}}{dE_{n,obs}}$ is set equal to the linear temporal regression coefficient between β_{obs} and $E_{n,obs}$, which is computed from remotely-sensed time series of the two variables over the global ocean (Section 2.2.2). Thus, when the feedback is enabled, changes in modeled β

over time are dictated by the magnitude of modeled export change as well as the strength of the relationship between observed β and export, which can vary spatially.

2.2.2 Empirical analyses of phytoplankton size, β, and export from satellite data

Because the strength of our modeled PSR feedback depends strongly on the observed relationship between β and export ($\frac{d\beta_{obs}}{dE_{n,obs}}$ in Eqn. 2.1), we sought a robust empirical constraint on this relationship. Sections 2.2.2.1 and 2.2.2.2 respectively describe the global satellite-derived time series maps of β and export used here. Section 2.2.2.3 then describes how these monthly-mean β and export maps are used to compute a range of possible global $\frac{d\beta_{obs}}{dE_{n,obs}}$ relationships.

2.2.2.1 Global satellite-derived particle size distribution map

Global 1/12°-by-1/12° monthly maps of β observed by the SeaWiFS satellite sensor (in operation from September 1997 – December 2010) were downloaded from ftp://ftp.oceancolor.ucsb.edu//pub/org/oceancolor/MEaSUREs/PSD/. These β maps were derived from remotely-sensed particulate backscatter validated with *in situ* near-surface Coulter counter measurements (Kostadinov et al., 2009). To enable more efficient computation, we reduced the resolution of the original monthly β maps to 1°-by-1° degree via spatial averaging. At this resolution, time-mean β ranges from ~3.3 in coastal high-latitude regions (where high nutrient conditions favor larger phytoplankton) to ~5.3 in the subtropics (where low macronutrient concentrations favor small phytoplankton) (Fig. 2.1a).

2.2.2.2 Global satellite-derived export maps

Export is computed here as the product of net primary production (NPP) and the particle export ratio (export/NPP, or e-ratio), both of which can be derived from satellite. To create a range of plausible global monthly export maps, we multiplied all possible permutations of three monthly NPP and e-ratio maps, yielding nine distinct monthly time series of global export (Supp. Fig. 2.2). All three sets of monthly satellite NPP maps were downloaded from http://sites.science.oregonstate.edu/ocean.productivity/ and derived from SeaWiFS observations processed through the following algorithms: (i) the chlorophyll-based Vertically Generalized Production Model (VGPM) (Behrenfeld & Falkowski, 1997); (ii) the Eppley-VGPM model (VGPME), containing a modified relationship between temperature and production compared to the original VGPM (Carr et al., 2006); and (iii) the Carbon-based Production Model (CbPM), which uses particulate backscatter-derived carbon rather than chlorophyll to measure phytoplankton biomass (Behrenfeld et al., 2005). The three sets of monthly-mean e-ratio maps were computed from empirical relationships derived by L2000 (Laws et al., 2000), D2005 (Dunne et al., 2005), and L2011 (Laws et al., 2011). L2000 computes e-ratios from SST alone; D2005 computes e-ratios from NPP, SST, and euphotic zone depths; and L2011 computes e-ratios from SST and NPP. The *in situ*, statistically interpolated monthly SST dataset used here was NOAA's Extended Reconstructed Sea Surface Temperature (ERSST) v3b, downloaded from https://www1.ncdc.noaa.gov/pub/data/cmb/ersst/v3b/netcdf/ (Smith et al., 2008). Euphotic zone depths needed to compute D2005 e-ratios were derived from SeaWiFS-sensed chlorophyll concentrations (downloaded from the same website as NPP) according to Equation 10 in Lee et

al. (2007). As with β, all variables were computed and stored on a 1°-by-1° degree grid over the entirety of the SeaWiFS period (September 1997 – December 2010, 160 months long).

In the following analyses (Section 2.3), we employ all nine sets of global monthly export maps to propagate uncertainty in our results. When reporting most-likely values, we weight the nine map sets according to how well each map set's annual mean export matches *in situ* observations within each region defined here (Supp. Table 2.3; see Weber et al. (2016) for derivation of weighting factors). Fig. 2.3 shows the weighted annual mean carbon export flux over the nine map sets, as well as the regions used for weighting, which are delineated based on biogeochemical characteristics such as sea surface temperature and surface phosphate concentrations (Weber et al., 2016). The Atlantic and Pacific Oceans are divided into warm subtropics dominated by smaller picophytoplankton (STA, STP), cold subarctic regions dominated by blooms of larger microphytoplankton in the north (NA, NP), and cool tropical upwelling zones dominated by larger phytoplankton in the east (ETA, ETP). The Indian Ocean is kept intact (IND), while the Southern Ocean is divided into the productive, diatom-dominated Subantarctic Zone (SAZ) and the high-nutrient, low-chlorophyll Antarctic Zone (AAZ). The Indian Ocean region (IND) did not contain a sufficient number of *in situ* observations of export to enable comparison to the satellite export maps, so all nine maps are weighted equally there.

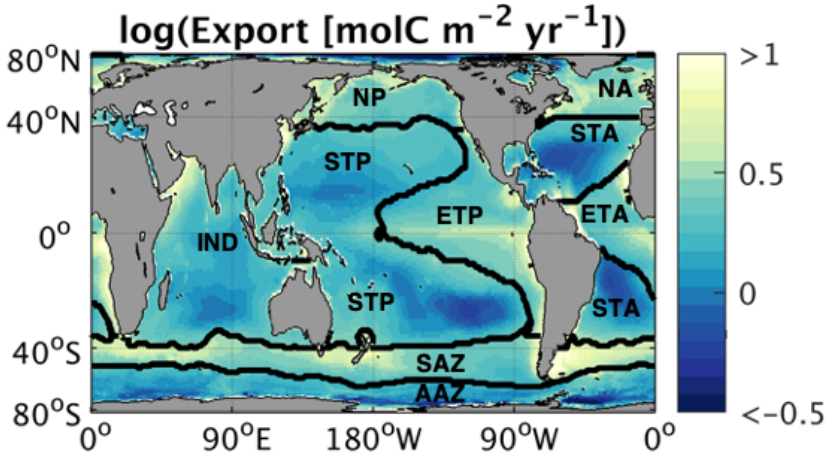

Figure 2.3 | Global map of regionally-weighted annual mean export, averaged over nine different export maps (detailed in Section 2.2.2.2). Contours indicate biogeochemical regions used for weighting and spatial averaging.

2.2.2.3 Regionally variable empirical β versus export relationships ($\frac{d\beta_{obs}}{dE_{n,obs}}$)

We quantify the empirical relationship between β and export individually for each grid cell by extracting the monthly time series of β and normalized export (E_n) from the satellite products described above, and then applying linear regression. This process produces a spatially variable, 1°-by-1° degree global map of the best-fit linear slopes ($\frac{d\beta_{obs}}{dE_{n,obs}}$) relating β and E_n. To capture the range of plausible $\frac{d\beta_{obs}}{dE_{n,obs}}$ maps, we repeat this process for each of the nine export products to generate nine distinct global $\frac{d\beta_{obs}}{dE_{n,obs}}$ maps (Supp. Fig. 2.3). To smooth out small-scale noise and illuminate larger-scale relationships, we then spatially average the slopes in each of the nine $\frac{d\beta_{obs}}{dE_{n,obs}}$ maps over the ocean biogeochemical regions defined in Fig. 2.3 (Fig. 2.4a). Lastly, we set the slopes at all grid points within a given region equal to that region's weighted (Supp. Table 2.3; Section 2.2.2.2) mean value (Fig. 2.4b) to generate the final $\frac{d\beta_{obs}}{dE_{n,obs}}$ map used in our PSR feedback-on runs (Fig. 2.4c).

To quantify the sensitivity of $\frac{d\beta_{obs}}{dE_{n,obs}}$ to the choice of export map used, we computed upper and lower-bound $\frac{d\beta_{obs}}{dE_{n,obs}}$ maps by adding and subtracting one standard deviation (error bars in Fig. 2.4b) to the weighted regional mean $\frac{d\beta_{obs}}{dE_{n,obs}}$ values. Conducting PSR feedback-on runs using upper and lower-bound $\frac{d\beta_{obs}}{dE_{n,obs}}$ maps establishes the range of PSR feedback strengths we can reasonably expect from our model forced with empirically-derived relationships.

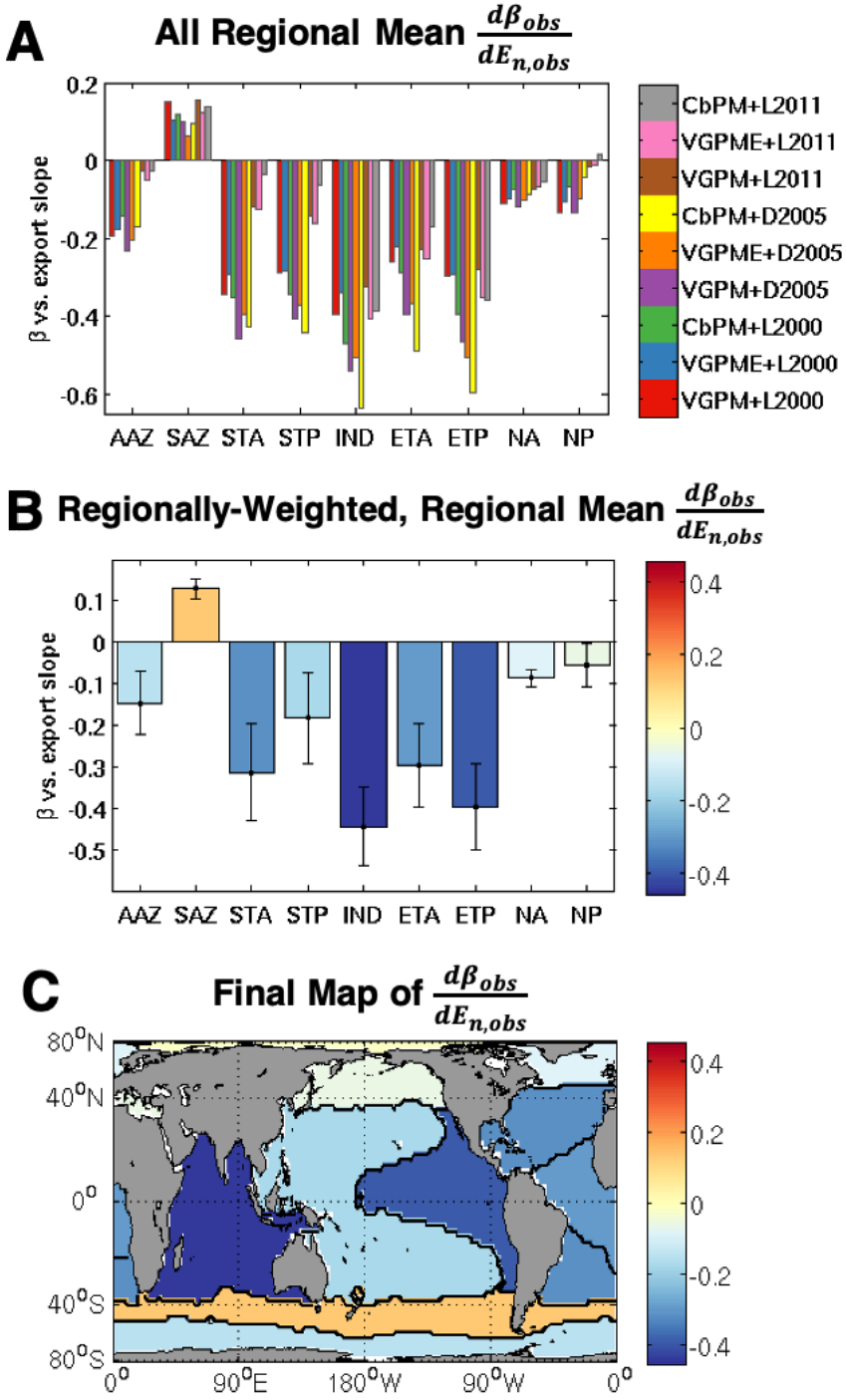

Figure 2.4 | (A) Regional mean changes in particle size slope for a given change in time-mean normalized export, $\frac{d\beta_{obs}}{dE_{n,obs}}$ (i.e., spatial averages of each map in Supp. Fig. 2.3 over regions shown in Fig. 2.3b), colored by corresponding export map. Colorbar labels indicate the NPP and e-ratio algorithms used to generate the given export map (see Section 2.2.2.2 for full descriptions of the algorithms). (B) Regionally-weighted mean $\frac{d\beta_{obs}}{dE_{n,obs}}$, averaged

over the nine possibilities for each region shown in Fig. 2.4a. Error bars represent one weighted standard deviation. (C) Global map of regionally variable $\frac{d\beta_{obs}}{dE_{n,obs}}$ used in model runs with the PSR feedback on.

2.2.3 Model runs to simulate future ocean warming and quantify the PSR feedback effect

To represent present-day conditions, we run a baseline simulation with modern-day circulation rates to steady-state. To simulate increased water column stratification and reduced vertical exchange due to warming, we uniformly and instantaneously reduce circulation and diffusion rates by 10% throughout the ocean. For comparison, observations show that the Atlantic meridional overturning circulation (AMOC) has weakened by about 15% since the mid-20th century due to anthropogenic warming (Caesar et al., 2018), while ESMs project that AMOC will weaken by 11-34% over the 21st century, depending on the chosen radiative forcing scenario (11% assumes the "high mitigation" RCP2.6 scenario, while 34% assumes the "business-as-usual" RCP8.5 scenario) (Collins et al., 2019). A 10% decrease in circulation rates is therefore a relatively conservative estimate of the effects of anthropogenic warming. Although modulation of ocean circulation rates in response to climate change will be more complicated and variable than the uniform 10% decrease applied here (e.g., Toggweiler and Russell, 2008), we seek only a simple, idealized way to approximate the reduced surface nutrient supply that is expected in a warmer future ocean.

To quantify the impact of the global PSR feedback on export changes with future warming, we run the slower-circulation rate simulation with and without the PSR feedback effect enabled. In feedback-off runs, β is set equal to annual mean values (Fig. 2.1a) for the entire duration of the run. In feedback-on runs, β is initially set equal to annual mean values, but is

allowed to change according to Eqn. 2.1, with $\frac{d\beta_{obs}}{dE_{n,obs}}$ defined as in Fig. 2.4c for the entire duration of the run. Additional feedback-on runs were conducted using the upper and lower-bound $\frac{d\beta_{obs}}{dE_{n,obs}}$ maps (described in Section 2.2.2.3).

All of the above described runs were also repeated with 10% faster circulation rates to determine whether the PSR feedback strength is symmetrical with regard to the direction of circulation change. Within all runs, β is constrained to realistically remain between 2 and 6.5 at all grid points, though these extremes are rarely reached. We run all experimental simulations for 100 years (initializing with conditions from the end of the present-day spin-up) to study near-future changes in export production and nutrient distributions, and to facilitate comparison with 100-year changes projected by the state-of-the-art Earth System Models discussed above.

2.3 Results and discussion

2.3.1 Spatial patterns in empirically-derived β versus export relationships ($\frac{d\beta_{obs}}{dE_{n,obs}}$)

No matter which maps are used (Section 2.2.2), satellite-derived β and export are strongly negatively correlated. Export thus tends to be high when β is small (particles are large) and low when β is large (particles are small) (Fig. 2.4; Supp. Fig. 2.3), as hypothesized in Section 2.1.2 and highlighted by the negatively-sloped red "Ecological Effect" line in Fig. 2.2c-d. Regions that are more nutrient-limited (i.e., the subtropics) exhibit especially strong negative relationships between β and export (Fig. 2.4; Supp. Fig. 2.3), as both β and export are predominantly driven

(in opposite directions) by surface nutrient supply in these areas. The counterintuitive weakly positive relationship between β and export in the SAZ is in line with findings from Lam and Bishop (2007), who showed that in the Southern Ocean, areas with higher biomass and larger particles at the surface were actually associated with lower rates of export out of the euphotic zone and at 200 m depth. In these diatom-dominated regions, zooplankton may be more active and have higher particle grazing efficiencies, leading to faster attenuation of particulate carbon fluxes with depth. The unique relationship between β and export in the SAZ and potentially the Southern Ocean at large is worth further exploration outside of this study.

2.3.2 Predicted export changes in the presence of the global PSR feedback effect

In this section, we discuss differences in predicted export production changes under altered circulation rates with and without the PSR feedback effect applied globally. Sections 2.3.2.1 and 2.3.2.2/2.3.2.3 respectively examine resultant global and zonal/regional mean changes in export.

2.3.2.1 Predicted global mean export changes with and without the global PSR feedback

To examine the global strength of the PSR feedback within our model under climate change conditions, we compare global mean export changes over time in the PSR feedback-on and off runs after a 10% decrease in circulation rates (Fig. 2.5, comparing slower circulation dashed and solid lines). In both the feedback-on and off cases, instantaneously decreasing

circulation rates reduces surface nutrient supply and immediately leads to a sharp decrease in global mean export of ~0.2 molC m^{-2} yr^{-1} from 3.54 molC m^{-2} yr^{-1}. After this initial plunge, global mean export declines by an additional 0.09 molC m^{-2} yr^{-1} over the next 100 years with the feedback off (for a total decrease of 0.29 molC m^{-2} yr^{-1} or 8.1%), versus an additional 0.05 molC m^{-2} yr^{-1} with the feedback on (for a total decrease of 0.25 molC m^{-2} yr^{-1} or 7.0%) (Fig. 2.5, slower circulation lines and bars). ESMs without the PSR feedback effect project global mean export decreases of around 7-18% between 2090-2099 and 1990-1999 under a "business-as-usual" radiative forcing scenario (RCP8.5). In the absence of the PSR feedback, the 100-year global mean export decrease of 8.1% predicted by our model is comparable to, but on the low-end of, these ESM projections, likely because of the conservative 10% decrease in circulation rates applied here.

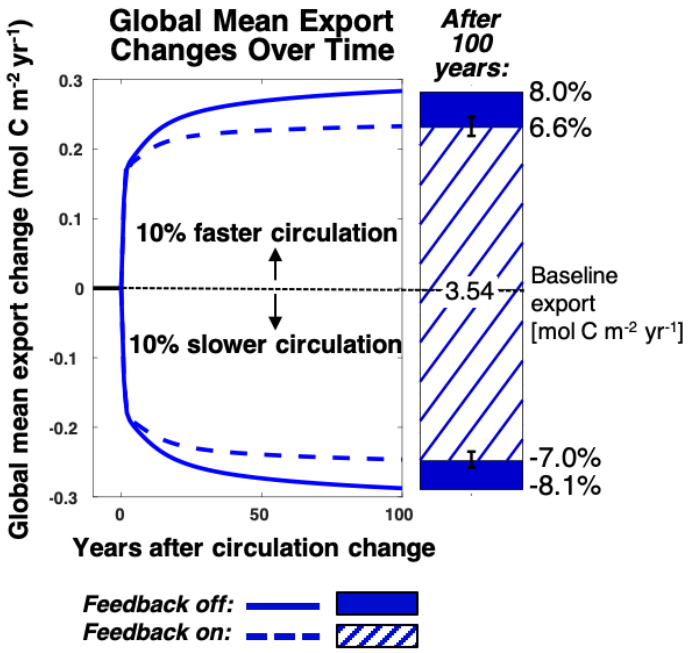

Figure 2.5 | Changes in global mean export over time from baseline conditions (current-day circulation, ran to steady-state) after increasing or decreasing circulation rates by 10%. Dashed and solid lines represent runs with the PSR feedback turned off and on, respectively. The bars on the right show absolute changes in global mean export from the baseline case 100 years after changing circulation rates. Corresponding relative changes (calculated as absolute changes from the baseline over the baseline mean) are listed in black. Global mean export in the baseline case is listed on the zero line. Hatched and solid patterns represent runs with the PSR feedback turned off and on,

respectively. The error bars represent export decreases generated when employing the upper and lower-bound $\frac{d\beta_{obs}}{dE_{n,obs}}$ maps described in Section 2.2.2.3.

Turning the PSR feedback on in our model reduced the total 100-year predicted decrease in export by ~14% (visually, the ratio of the solid-colored bar length to the full bar length below zero in Fig. 2.5). At equilibrium (when global mean export stabilizes ~500 years after decreasing circulation rates), this feedback effect increases to ~16%. With the feedback turned on, particle sizes shrink and remineralization depths shoal in response to an initial circulation-driven decrease in surface nutrient supply, thereby moderating this initial decrease by keeping more recycled nutrients at the surface. In particular, global mean β increases by 0.03 units (from 4.34 to 4.37) under 10% decreased circulation rates after 100 years with the PSR feedback on (Fig. 2.6a,b), corresponding to a 17 m global mean shoaling (from 595 to 578 m) of e-folding remineralization depths (Fig. 2.6b). The greatest regional mean β increase of 0.06 occurs in the Indian Ocean (IND), resulting in a 41 m shoaling of remineralization depths there (Fig. 2.6b). Results from runs employing upper and lower-bound $\frac{d\beta_{obs}}{dE_{n,obs}}$ maps (defined in Section 2.2.2.3, represented by the error bars in Fig. 2.4b) lend further support to our findings and indicate that the modeled global PSR feedback effect size is relatively insensitive to the choice of export maps used to compute $\frac{d\beta_{obs}}{dE_{n,obs}}$ (Fig 2.5, black error bars).

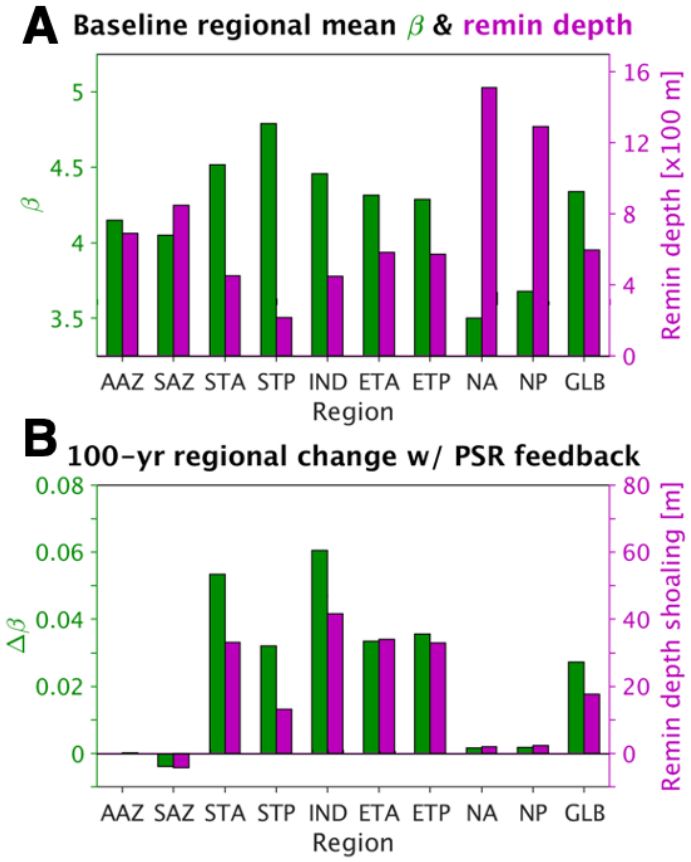

Figure 2.6 | (A) Baseline (current-day circulation, ran to steady-state) regional mean β (shown in green) and e-folding remineralization depth (shown in purple). (B) Absolute change in regional mean β (shown in green) and absolute shoaling of regional mean remineralization depth (shown in purple) 100 years after decreasing circulation rates by 10% with the PSR feedback turned on.

The PSR feedback also dampens the response of global-mean carbon export to an instantaneous *increase* in ocean circulation rates (Fig. 2.5). One hundred years after circulation rates are increased by 10%, global mean carbon export increases from 3.54 molC m^{-2} yr^{-1} by 0.28 molC m^{-2} yr^{-1} (8.0%) with the feedback off, whereas it increases by ~0.23 molC m^{-2} yr^{-1} (6.6%) with the feedback on (Fig. 2.5, faster circulation lines and bars). Thus increasing circulation rates by 10% with the PSR feedback on reduces the 100-year increase in export production by ~18% (visually, the ratio of the solid-colored bar length to the full bar length above zero in Fig. 2.5). At equilibrium, this feedback effect increases to ~20%. With the feedback turned on, particle sizes

grow and remineralization depths deepen in response to an initial circulation-driven increase in surface nutrient supply, thereby moderating this initial increase by transferring more nutrients to deeper waters where they recirculate more slowly to the surface. In particular, global mean β decreases by 0.03 units (from 4.34 to 4.31) under 10% increased circulation rates, corresponding to a 20 m global mean deepening (from 595 to 615 m) of e-folding remineralization depths (not shown). The greatest regional mean β decrease of 0.07 occurs in the Indian Ocean (IND), resulting in a 54 m shoaling of remineralization depths there. Compared with the decreased circulation case, absolute changes in remineralization depths are slightly larger under increased circulation rates because remineralization depth changes are more sensitive to variations in β when particles are larger (that is, at smaller values of β). Because remineralization depth changes are greater under increased circulation rates, so too is the global PSR feedback strength (14% with decreased circulation rates versus 18% with increased circulation rates). Again, results from PSR feedback-on runs constrained by upper and lower-bound $\frac{d\beta_{obs}}{dE_{n,obs}}$ maps further support the notion that the PSR feedback size is relatively insensitive to the choice of export maps used to compute $\frac{d\beta_{obs}}{dE_{n,obs}}$ (Fig 2.5, error bars). Thus, the effect of the PSR feedback is to buffer changes in export production in response to any physical perturbation in nutrient supply, regardless of the direction.

2.3.2.2 Predicted zonal and regional mean export changes *without* the global PSR feedback

In our baseline simulation under current-day circulation rates, POC export covaries tightly throughout the low to mid-latitudes with nutrient concentrations in shallow subsurface

waters beneath the euphotic zone, quantified here as [PO_4] at 200m depth (P_{200m}) (Fig. 2.7a,b; Fig. 2.8a). South of ~40°S and north of ~40°N, other factors such as light and/or temperature become limiting; as a result, export does not vary as tightly with P_{200m} in these higher-latitude regions. The spatial structure of the relationship between export and P_{200m} confirms that nutrient supply from subsurface layers is the primary driver of export rates throughout the nutrient-limited low- to mid-latitudes. Therefore, in these regions, the following balance approximately holds:

$$Export = E \approx w \times P_{200m}, \text{ (Eqn. 2.2)}$$

where w is the local upwards nutrient supply velocity, which represents the net effect of all vertical exchange processes, including diffusion, upwelling, entrainment, and mixing.

This balance can in turn be used to derive a simple diagnostic for understanding changes in export under altered circulation rates at any given location:

$$\Delta E = \Delta w \times P_{200m,\, baseline} + w_{baseline} \times \Delta P_{200m}$$

where *baseline* denotes variables from the baseline simulation ran to steady-state with current-day circulation rates and Δ denotes change from the baseline simulation under altered circulation rates. (Note that we ignore the "perturbation product" term, $\Delta w^* \Delta P_{200m}$, because it is negligible.)

When ocean circulation is slowed, Eqn. 2.3 allows us to identify two different contributions to the resultant reduction in export through the low to mid-latitudes. First, and most intuitively, when circulation rates are uniformly decreased, w is reduced across the entire ocean ($\Delta w < 0$) and the supply of "baseline" nutrients is curtailed. Second, a decrease in circulation rates also reduces phosphate concentrations throughout the shallow subsurface layer in the low to mid-latitudes ($\Delta P_{200m} < 0$) (solid lines and bars in Fig 2.7c,d; Fig. 2.8b). This decrease in P_{200m} is largely driven by enhanced biological nutrient utilization in the surface of the Southern Ocean in response to slower circulation, which is then propagated into the low to mid-latitude interior through Antarctic Intermediate and Subantarctic Mode Waters, as observed in future climate simulations by more complex ESMs (e.g., Moore et al., 2018).

Together, the decreases in shallow subsurface nutrient concentrations (P_{200m}) and vertical exchange rates (w) result in substantial reductions in export throughout most of the ocean under our decreased circulation simulations as dictated by Eqn. 2.3, with the greatest reductions occurring in nutrient-limited areas. In the absence of the PSR feedback, the 10% decrease we imposed on circulation rates leads to 100-year zonal mean export decreases of >15% at 35°N and S and ~10% between 35°N and S (solid line in Fig. 2.7e). Regionally, the oligotrophic subtropics (especially the STP) exhibit the largest relative decreases in export (~10-13%), followed closely by the tropics (ETA, ETP) with export decreases around 8-10% (solid bars in Fig. 2.7f). As expected, the decrease in export mirrors the pattern of ΔP_{200m} in low to mid-latitude regions due to a strong dependence of export on nutrient supply from the shallow subsurface here.

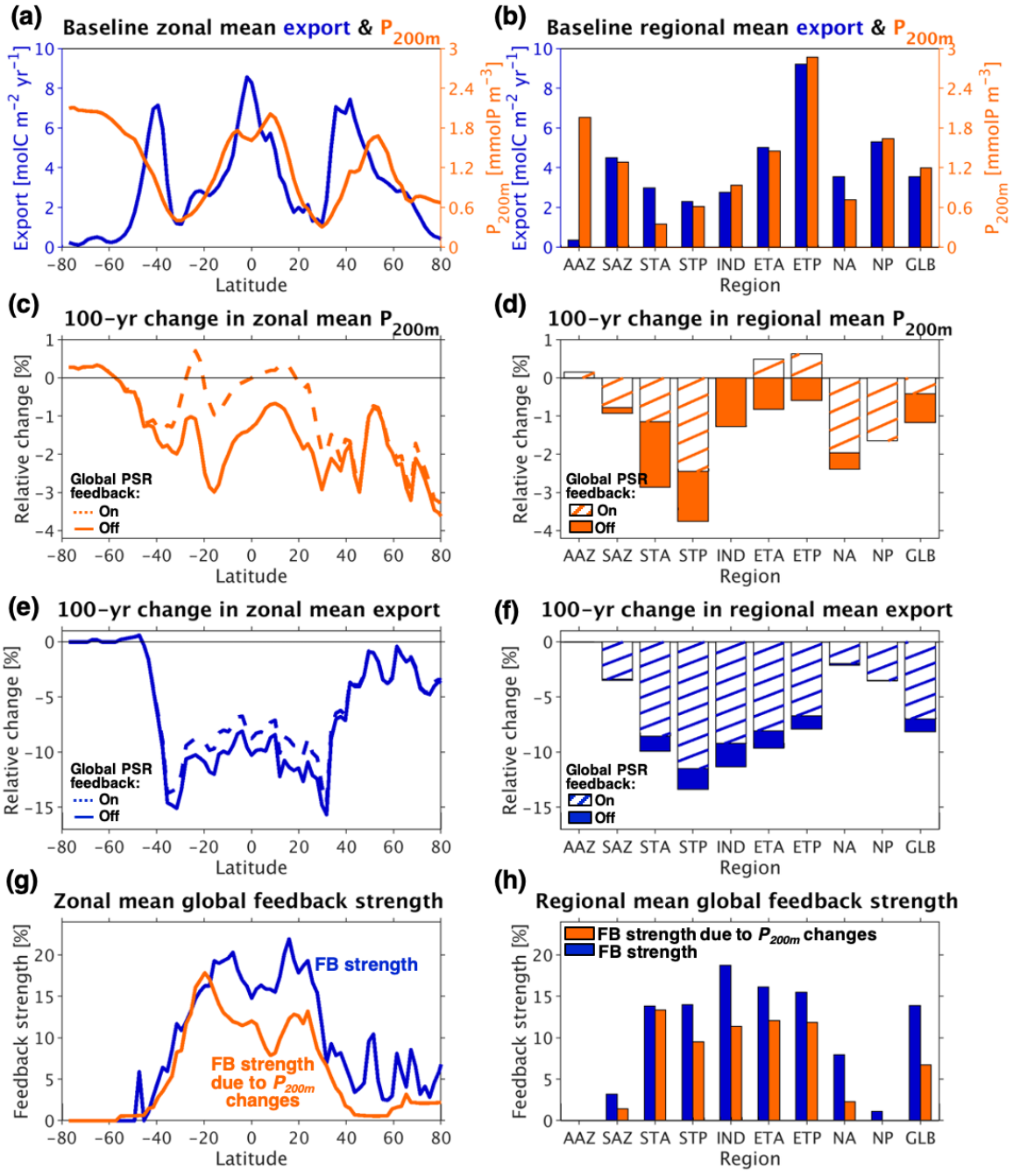

Figure 2.7 | (A) Baseline (current-day circulation, ran to steady-state) zonal mean export and shallow subsurface (200 m) phosphate concentration. (B) Same as (A), but with regional and global rather than zonal means. (C) Relative changes (calculated as absolute changes from the baseline over the baseline mean) in zonal mean phosphate concentration at 200 m depth 100 years after decreasing circulation rates by 10%. (D) Same as (C), but with regional and global means. (E) Relative changes in zonal mean export 100 years after decreasing circulation rates by 10%. (F) Same as (E), but with regional and global means. (G) Zonal mean PSR feedback strength, calculated as the difference in zonal mean export change from baseline between the feedback-off and on cases divided by the zonal mean export change in the feedback-off case alone (left-hand side of Eqn. 2.4; shown in blue). Predicted zonal mean PSR feedback strength from changes in circulation and shallow subsurface phosphate concentration (right-hand side of Eqn. 2.4; shown in orange). (H) Same as (G), but with regional and global means.

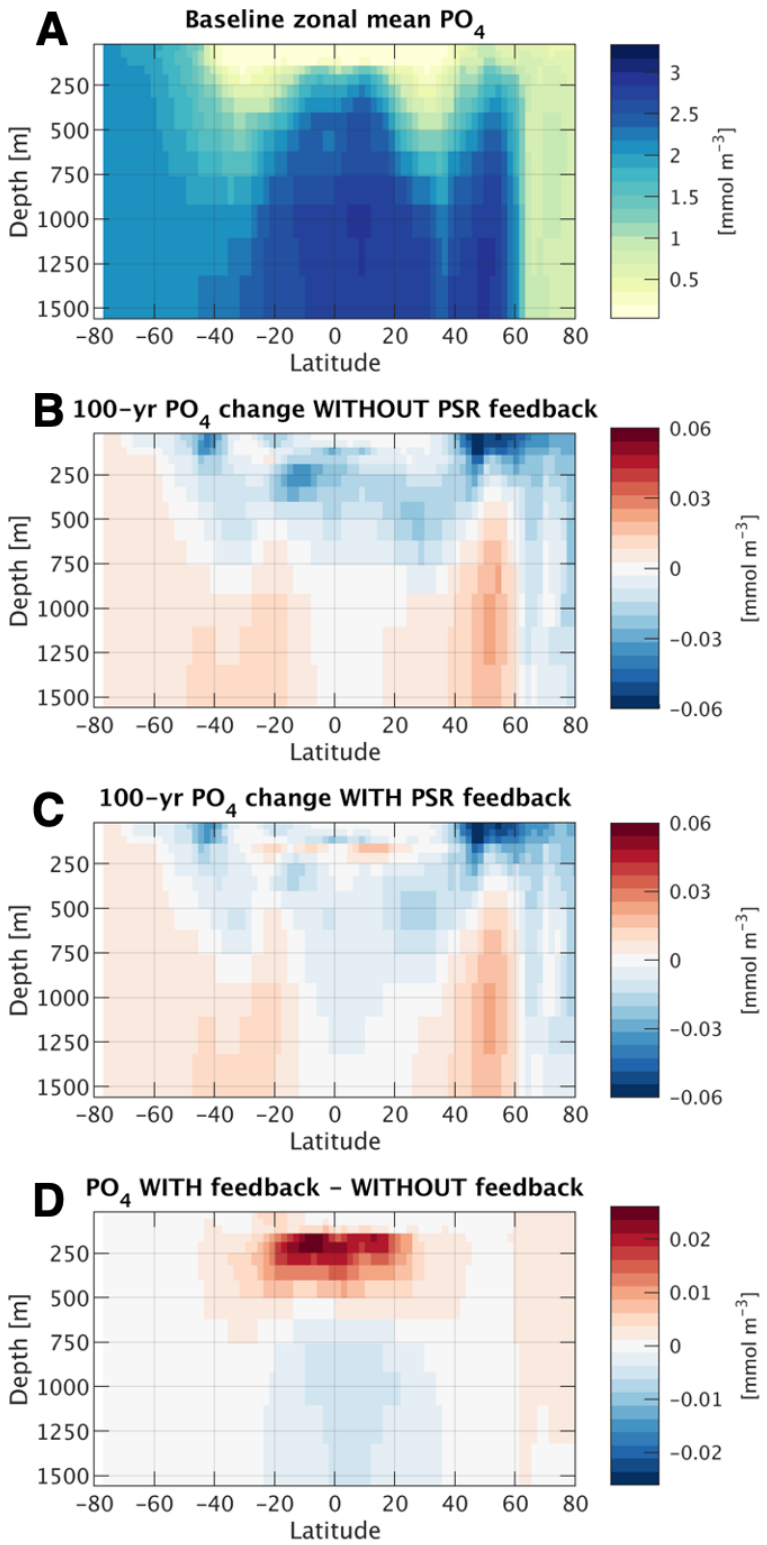

Figure 2.8 | (A) Baseline (current-day circulation, ran to steady-state) zonal mean phosphate concentration. (B) Absolute change in zonal mean phosphate concentration 100 years after decreasing circulation rates by 10% with the PSR feedback turned off. (C) Same as (B), but with the PSR feedback turned on. (D) Difference in zonal mean phosphate concentration between PSR feedback-on and -off runs (i.e., (B) minus (C)).

2.3.2.3 Predicted zonal and regional mean export changes *with* the global PSR feedback

As with the global mean (Section 2.3.2.1), we quantify zonal and regional mean PSR feedback strength as the difference in circulation-driven export change from baseline between the feedback-on and -off runs, normalized by the change from baseline in the feedback-off run. In other words, the PSR feedback strength is the percentage by which turning on the PSR feedback reduces (dampens) the response of carbon export to changes in ocean circulation (blue line and bars in Fig. 2.7g,h). Visually, the zonal mean feedback strength (blue line in Fig. 2.7g) is equal to the difference between the dashed and solid lines divided by the solid line in Fig. 2.7e, while the regional mean PSR feedback strength (blue bars in Fig. 2.7h) is equal to the length of the solid-colored portion of the bars divided by the entire length of the bars in Fig. 2.7f. The PSR feedback strength is greatest (most strongly damping) in the low to mid-latitudes and in the tropics (ETA, ETP) and subtropics (STA, STP, IND), with the feedback able to reduce zonal and regional mean export changes by up to 20% in these regions (blue lines and bars in Fig. 2.7g,h). To understand this spatial pattern, we combine Eqn. 2.3 with our definition of PSR feedback strength to yield the following diagnostic:

$$PSR\,feedback\,strength = \frac{\Delta E_{on} - \Delta E_{off}}{\Delta E_{off}} \approx \frac{\frac{\Delta P_{200m,\,on} - \Delta P_{200m,\,off}}{P_{200m,\,baseline}}}{\frac{\Delta w}{w_{baseline}} + \frac{\Delta P_{200m,\,off}}{P_{200m,\,baseline}}}, \text{ (Eqn. 2.4)}$$

where *on/off* denotes whether the PSR feedback was turned on or off under the altered circulation rates.

This expression reveals that the PSR feedback effect is strongest wherever activating the feedback leads to the greatest dampening of changes in P_{200m}, compared to the changes that occur in the feedback-off case. In the decreased circulation simulations ($\frac{\Delta w}{w_{baseline}}$ = -10% everywhere), the low to mid-latitude regions display the greatest differences in P_{200m} changes between feedback-on and off runs (Fig. 2.7c,d; Fig. 2.8b-d); these regions undergo the greatest reductions in circulation-driven export change due to the PSR feedback (Fig. 2.7e,f) and thus exhibit the largest PSR feedback effects (blue lines and bars in Fig. 2.7g,h).

The degree to which the PSR feedback dampens P_{200m} changes is in turn driven by the strength of the relationship between β and export. The low to mid-latitudes exhibit the most negative $\frac{d\beta_{obs}}{dE_{n,obs}}$ values and therefore, the tightest coupling between β and export (Fig. 2.4c). In these regions, where macronutrient limitation is the dominant constraint on productivity, a given circulation-driven decrease in surface nutrient supply causes a relatively large drop in both export and phytoplankton/particle size (leading to an increase in β) in the presence of the PSR feedback. This then allows significantly more nutrients to be recycled at the surface, resulting in greatly dampened decreases in P_{200m} and subsequent export production.

Our simple diagnostic (Eqn. 2.4) can explain PSR feedback strengths quite well over the global ocean, as seen by comparing total feedback strengths (blue lines/bars in Fig. 2.7g,h) with the approximation based on w and P_{200m} (right-hand side of Eqn. 2.4, represented by orange lines/bars in Fig. 2.7g,h). However, because new production can be fed by local upwelling as well as lateral advection, changes in P_{200m} and vertical exchange rates alone (orange lines/bars in Fig. 2.7g,h) cannot perfectly predict all changes in export (blue lines/bars in Fig. 2.7g,h),

especially in regions where lateral advection plays a relatively large role in supplying nutrients to the surface (i.e., recall that Eqn. 2.2 is only a close approximation).

2.3.3 Predicted export changes in the presence of regional PSR feedback effects

In this section, we discuss each individual ocean region's contribution to the global PSR feedback effect. To isolate the PSR feedback effect coming from each region, we conduct a set of model runs in which we decrease the circulation rate globally, but only activate the PSR feedback within one region at a time. In these feedback-on runs, we set $\frac{d\beta_{obs}}{dE_{n,obs}}$ in Eqn. 2.1 equal to zero at all grid points outside of the region we are isolating; within the isolated region, we set $\frac{d\beta_{obs}}{dE_{n,obs}}$ equal to the corresponding empirically-derived value (as shown in Fig. 2.4b). These simulations are then compared to the same feedback-off run discussed in Section 2.3.2 (i.e., no changes in β anywhere) to determine the impact of enabling the feedback within one region at a time. Sections 2.3.3.1. and 2.3.3.2 respectively describe the global and regional mean export changes resulting from this set of experiments.

2.3.3.1 Predicted global mean export changes with and without regional PSR feedbacks

Analysis of the regional feedback-on runs show that tropical (ETA, ETP) and subtropical (STA, STP, IND) regions contribute most significantly to the global PSR feedback (Fig. 2.9). Turning the feedback on in the ETP alone, for instance, leads to a 3.9% reduction in global mean

export change compared to the feedback-off case (Fig. 2.9a – row 7, last column); the ETP alone thus accounts for 38.6% of the global PSR feedback strength (Fig. 2.9b – row 7, last column), while spanning only 10.3% of total ocean area. Turning the feedback on in the subtropical (STA, STP, IND) and tropical (ETA, ETP) regions one at a time and then summing their individual contributions (11.7%, 11.6%, 22.3%, 13.3%, 38.6% respectively; Fig. 2.9b – last column) accounts for 97.5% of the global PSR feedback effect, while all other regions (AAZ, SAZ, NA, NP) account for only a negligible fraction of the effect (or even act to decrease the overall effect in the case of the SAZ) (Fig. 2.9b – last column). The dominant contributions of the tropical/subtropical regions to the global PSR feedback can once again be understood via spatial patterns in $\frac{d\beta_{obs}}{dE_{n,obs}}$ (Fig. 2.4c), with large changes in β and remineralization depth associated with relatively small changes in export in the nutrient-limited tropical/subtropical regions.

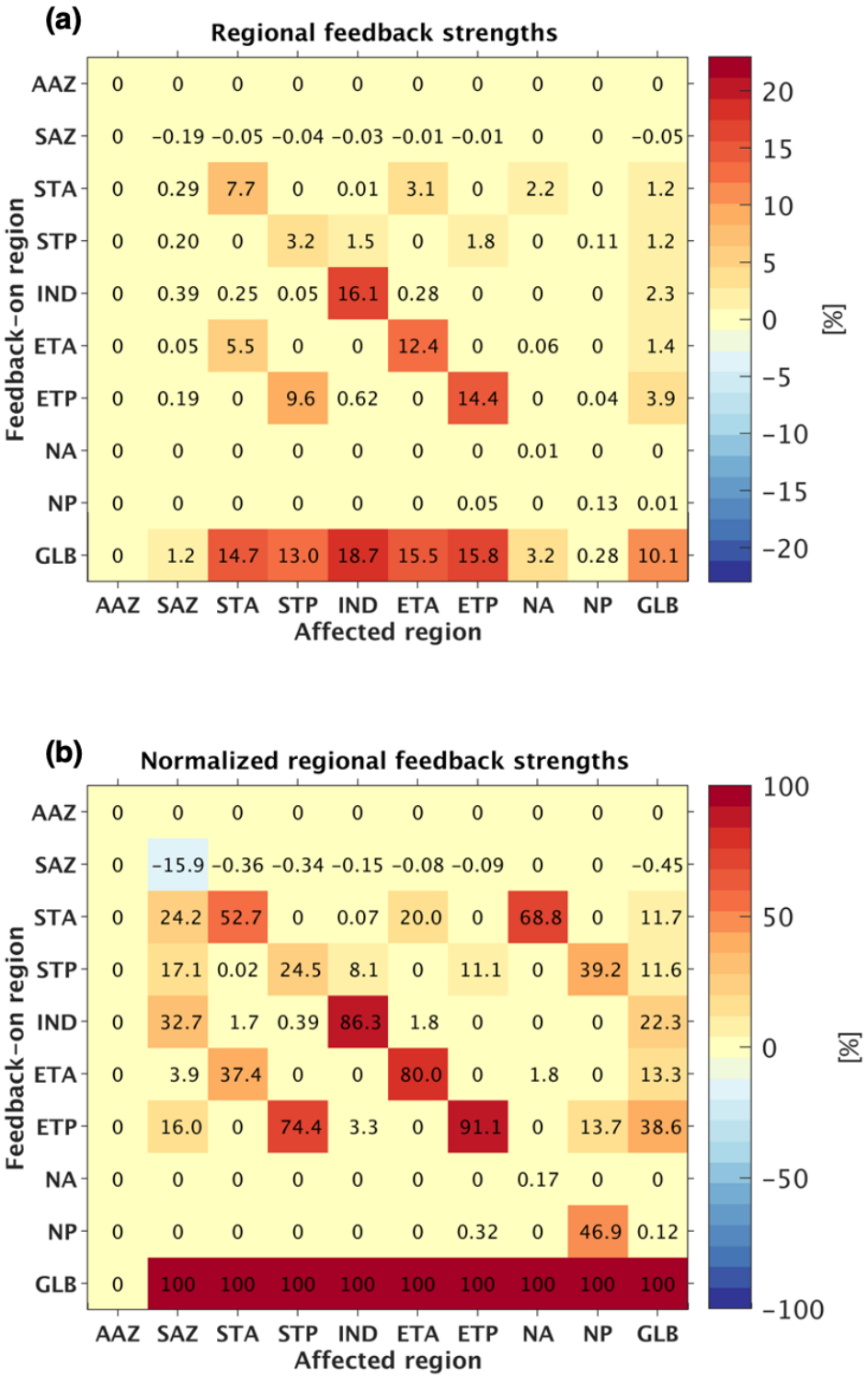

Figure 2.9 | (A) Regional mean PSR feedback strength due to the PSR feedback effect within each individual region. The y-axis denotes the single region (or the entire ocean in the case of "GLB" or "global") within which the PSR feedback was turned on, while the x-axis denotes the region affected. (B) Percent contribution of each individual region to each region's total PSR feedback strength, computed as the regionally-derived feedback strength within an affected region divided by the globally-derived feedback strength in the same affected region (i.e., each given grid cell in (A) is divided by the corresponding column's bottom-most grid cell).

2.3.3.2 Predicted regional mean export changes with and without regional PSR feedbacks

The significant tropical/subtropical contribution to the PSR feedback can also be seen by examining export changes within individual regions. Activating the PSR feedback in the STA, for example, dampens regional mean export decreases within the STA, the ETA, and the NA by 7.7%, 3.1%, and 2.2%, respectively (Fig. 2.9a – row 3). Turning on the feedback in the STP (Fig. 2.9a – row 4), ETA (Fig. 2.9a – row 6), or ETP (Fig. 2.9a – row 7) alone have similarly large effects on surrounding regions. In contrast, activating the feedback within higher-latitude regions (AAZ, SAZ, NA, NP) neither significantly moderates export decreases in any individual regions nor globally (Fig. 2.9a – rows 1-2, 8-9). The AAZ uniquely undergoes near-zero decreases in export for all runs with the feedback on or off; PSR feedback strength here is therefore negligible (Fig. 2.9a,b – row 1).

When the PSR feedback is turned on within a given region, the effect is typically felt most strongly within that same region, as would reasonably be expected given that export production and resultant remineralization are spatially co-occurring (Fig. 2.9a,b – diagonal going from upper left to lower right corner). However, depending on the local magnitude of $\frac{d\beta_{obs}}{dE_{n,obs}}$ compared to that of neighboring regions, as well as the connectivity of nutrient supplies between them, there can be substantial PSR feedback effects originating from afar. For example, in the Pacific basin, switching on the PSR feedback in the ETP has a stronger buffering effect on export in the STP region than switching on the feedback in the STP itself (Fig. 2.9b – row 7, column 4). This is because the relationship between β and export is much stronger in the ETP (with a

regional mean $\frac{d\beta_{obs}}{dE_{n,obs}}$ of -0.40; see Fig. 2.4c) than in the STP (with a regional mean $\frac{d\beta_{obs}}{dE_{n,obs}}$ of -0.18; see Fig. 2.4c), and because remineralized surface nutrients in the ETP are readily carried into the STP by wind-driven Ekman transport. In this way, PSR feedback-driven buffering of surface nutrient supply changes within the ETP indirectly buffers surface nutrient supply changes in the STP as well. This indirect effect also operates in the reverse direction, in that activating the PSR feedback in the STP also has a relatively strong impact back on the ETP (Fig. 2.9b – row 4, column 7). In this case, nutrients remineralized shallower in the STP thermocline are directed along sloping isopycnals that eventually upwell into the ETP surface, thus buffering decreases in export there. The STP also has a relatively large PSR feedback effect on the subpolar NP (Fig. 2.9b – row 4, column 9), due to the intense flow of the Kuroshio Current, which carries surface nutrients from the STP northward.

Similar relationships hold in the Atlantic basin between the tropics, subtropics, and subpolar regions. However, the PSR feedback effect of the ETA on the STA is smaller (Fig. 2.9b – row 6, column 3), while the effect of the STA on the ETA is larger (Fig. 2.9b – row 3, column 6) compared to their Pacific counterparts, presumably due to less pronounced Ekman divergence along the equatorial Atlantic. The STA's PSR feedback effect on the subpolar NA (Fig. 2.9b – row 3, column 8) is also substantially more pronounced than the STP's effect on the NP, indicating a stronger nutrient supply pathway between subtropical and subpolar gyres in the Atlantic Ocean via the Gulf Stream.

An interesting phenomenon that arises in the Southern Ocean is the negative (dampening) overall PSR feedback effect on the SAZ (Fig. 2.9a – row 10, column 2), despite a positive (amplifying) local feedback effect (Fig. 2.9a,b – row 2, column 2) and relationship between β

and export here (regional mean $\frac{d\beta_{obs}}{dE_{n,obs}}$ of +0.13; see Fig. 2.4c). Additive negative (dampening) PSR feedback effects from surrounding regions (STA, STP, IND, ETA, ETP) (Fig. 2.9a,b – rows 3-7, column 2) overcome the small positive (amplifying) local feedback effect here (Fig. 2.9a,b – row 2, column 2), such that the total feedback effect still reduces the magnitude of the regional mean export decrease by 1.2% compared to the feedback-off case (Fig. 2.9a – last row, column 2). Because the SAZ spans the entire width of the ocean and touches every other basin, additional remineralized surface nutrients collected in the many connected regions are quickly and easily circulated into the SAZ when the global PSR feedback is active, thus buffering larger would-be decreases in export here.

2.4 Conclusions

Surface nutrient supply drives export production and shapes phytoplankton communities and particle size distributions throughout the low to mid-latitude oceans. Large phytoplankton and particles are prevalent in nutrient replete conditions, while smaller phytoplankton and particles dominate in oligotrophic conditions (Litchman et al., 2007; Guidi et al., 2007; 2008; 2009). A reduction in surface nutrient supply stemming from increased water column stratification in a warming ocean (Bopp et al., 2013; Anna Cabré et al., 2015b; Capotondi et al., 2012) thus leads to a decrease in global export production (Fig 2.2, green arrows; Fig. 2.5, slower circulation solid lines/bars) *and* sinking particle size (Fig 2.2a, red arrow; Fig. 2.2c-d, red line; Fig. 2.6b). Smaller particles in turn drive shallower nutrient remineralization and thus faster resupply of those nutrients to the surface, dampening the initial circulation-driven change in export (Fig. 2.2a, blue arrow; Fig. 2.2d, blue line; Fig. 2.5, slower circulation dashed

lines/hatched bars; Fig. 2.6b; Fig. 2.7c-f; Fig. 2.8b-c). This study has shown that these mechanisms can give rise to a negative feedback loop that moderates the response of carbon export to changes in ocean circulation, which we term the particle size-remineralization (PSR) feedback.

Many global models ignore the effects of nutrient supply on particle size and/or the effects of particle size on remineralization depths (Laufkötter et al., 2016 and references therein). Within our model, including these effects reduces the magnitude of predicted 100-year changes in global export production by ~14% when circulation rates are decreased by a conservative 10% (Fig. 2.5). This implies that global models without the PSR feedback may be overestimating 100-year climate-driven export decreases by ~1.16 times. Under a relatively extreme ESM-projected decrease of 18% by 2100 (Bopp et al., 2013), absolute global export would be reduced by ~0.7-2.9 GtC/yr, assuming a present rate in the range of 4-16 GtC/yr (Boyd & Trull, 2007; DeVries & Weber, 2017; Dunne et al., 2005, 2007; Falkowski et al., 1998; Henson et al., 2011; Laws et al., 2000; Siegel et al., 2014; Yamanaka & Tajika, 1996); with the PSR feedback in effect, this predicted decrease would be reduced by ~14% to ~0.6-2.3 GtC/yr.

The PSR feedback is strongest (moderating export changes by up to 20%; Fig. 2.7g,h; Fig. 2.9) and export decreases are thus likely to be most overestimated in the low-latitude tropical and subtropical regions, where current models also predict some of the largest future export decreases (Bopp et al., 2013; Anna Cabré et al., 2015b). Within these regions, primary and export production are highly nutrient-limited, such that a given stratification-induced decrease in nutrient supply leads to relatively large decreases in export and sinking particle size (Fig. 2.4), with correspondingly large effects on remineralization depth (Fig. 2.6) and surface

nutrient recycling. Because these regions exhibit the greatest projected decreases in export as well as the strongest PSR feedback effects, spatial variations in projected export decrease may also be less pronounced than currently expected.

The PSR feedback operates on increases in surface nutrient supply as well. Under surface nutrient supply increases, phytoplankton/particles grow larger and remineralization depths deepen, which sends more nutrients out of the shallow subsurface and thereby moderates initial circulation-driven increases in export. This PSR feedback reduces the magnitude of predicted 100-year changes in global export production by about 18% when circulation rates are increased by 10% (Fig. 2.5, faster circulation dashed lines/hatched bars). In scenarios of global cooling (resulting in water column destratification, enhanced mixing, and increased surface nutrient supply), centennial-scale projections of export increase in models lacking the PSR feedback would therefore be >1.2 times too big, again with the largest overestimates in the low to mid-latitude regions. The PSR feedback thus moderates export changes in response to any physical perturbation to surface nutrient supply, whether driven by increasing or decreasing circulation rates. Of particular note, the strength of the PSR feedback does not depend on the size of circulation rate changes (i.e., PSR feedback strength remains relatively constant whether circulation rates are increased/decreased by 10% or 50% - results not shown).

The exact strength of the PSR feedback hinges on the empirical relationship between carbon export and particle size, which may differ depending on the datasets used to constrain it. To address this uncertainty, we correlated β against a range of different global export datasets and found that our results were relatively insensitive to the choice of export dataset. Unfortunately, well-grounded alternative global and temporally-resolved datasets for β were not

readily available, so uncertainty in the PSR feedback strength due to uncertainties in observed β could not be quantified here. Analysis of *in situ* Underwater Visual Profiler (UVP) data suggests that β may actually be smaller (thus particles, larger) and less variable (Cram et al., 2018) than the backscatter-derived values (Kostadinov et al., 2009) used in this study. This would potentially imply less variability in particle size-driven remineralization depths, weakening the PSR feedback strength calculated here. On the other hand, differences in remineralization depths are greater at smaller values of β (Supp. Fig. 2.1; Fig. 2 in Devries et al., 2014), such that any given increase in β associated with a decrease in export would lead to greater shoaling of remineralization depths and a larger PSR feedback effect than calculated here. More *in situ* observations of β are clearly needed to better resolve these competing effects. One potential explanation for these β discrepancies is that the algorithm used to derive β from remotely-sensed particulate backscatter sometimes misses the largest particles in high-productivity areas such as the Southern Ocean (Kostadinov et al., 2009). In addition to the theories proposed in Lam and Bishop (2007), this may partly explain why $\frac{d\beta_{obs}}{dE_{n,obs}}$ is weakly positive in the Subantarctic Zone (SAZ); particles may actually get larger with increasing export here, but because they are already quite large, the satellite β sensor/algorithm may not be able to capture the particles becoming any larger. The result would be an underestimation of the negative (dampening) PSR feedback effect in this region. Another caveat of our study is that very simple phytoplankton biology and growth dependent on only one macronutrient was assumed. Furthermore, explicit zooplankton and the effects of particle fragmentation via grazing (e.g. Cavan et al., 2017) or particle aggregation via fecal pellet production (e.g. Steinberg et al., 2012; Turner, 2015 and references therein) were not included. Despite the aforementioned shortcomings, the results presented here represent a

reasonable first attempt to quantify the strength of the PSR feedback effect on export changes within a global model.

Future work should test the PSR feedback effect in more complex models that better resolve phytoplankton/zooplankton biology, particle dynamics, and/or circulation changes. These models could include particle aggregation-disaggregation with prognostic sinking speeds (Gehlen et al., 2006), empirically-driven food-webs (Siegel et al., 2014), explicit phytoplankton and grazers of different sizes (Buesseler & Boyd, 2009), and/or spatiotemporally-resolved circulation changes that respond directly to atmospheric forcing. Additionally, future work should analyze the downstream effects of the PSR feedback on climate-driven projections of fisheries productivity, dissolved oxygen availability, and carbon sequestration in the deep ocean over centennial to millennial timescales. A smaller-than-currently-projected decrease in surface nutrient supply and export rates would be beneficial for maintaining fisheries, for example, but perhaps detrimental for deep ocean carbon sequestration. In particular, a decrease in circulation rates should enable enhanced carbon sequestration, as nutrients and CO_2 collect in the deep ocean (Fig. 2.8), but the PSR feedback may potentially moderate this increased sequestration effect. Other remineralization depth-related feedbacks not studied here may also be important for modulation of future changes in carbon export and its downstream effects; these should be investigated in future work as well. For instance, temperature increases may speed up bacterial remineralization rates (Cavan et al., 2019; Cram et al., 2018; John et al., 2014; Marsay et al., 2015; Matsumoto, 2007) and enhance recycling of nutrients near the surface, which would result in an additional negative feedback on export acting in the same direction as the PSR feedback. Oxygen concentrations, on the other hand, are predicted to decrease with future warming (Bopp

et al., 2002; Cabré et al., 2015a; Keeling et al., 2010; Long et al., 2016; Matear & Hirst, 2003; Schmidtko et al., 2017), resulting in depressed bacterial remineralization and zooplankton grazing rates (Cavan et al., 2017; Devol & Hartnett, 2001; Hartnett & Devol, 2003; Van Mooy et al., 2002), which would further exacerbate circulation-driven nutrient supply decreases in the surface ocean and create a positive feedback on export production changes. A decrease in mineral ballasting of sinking particles with ocean acidification may also feedback positively on export production decreases (Hofmann and Schellnhuber, 2009). Ensuring that the PSR and other remineralization feedbacks are adequately represented in ESMs should be a priority of the modeling community to enable robust predictions of carbon export fluxes in the future ocean.

2.5 Code availability

The MATLAB code required to make the figures generated here can be found at https://doi.org/10.5281/zenodo.3785725.

2.6 Data availability

Data in the form of *.mat files required to make the figures generated here can be found at http://doi.org/10.5281/zenodo.3785724.

2.7 Supporting information

Model configuration	
Particle parameters	
DL(z′ = 0)	2000 um
DS(z′ = 0)	20 um
cw	2.2e5 $m^{(1-\eta)}$ day^{-1}
η	1.17
cr	29^{-1} day^{-1}
ζ	1.62
Biogeochemical parameters	
τ	30 days
κ	0.5 $year^{-1}$
σ	0.1
Zs	115 m

Supporting Table 2.1 | PRiSM parameter values (reproduced from Table 1 in DeVries et al., 2014a – see DeVries et al., 2014a for the equations in which the parameters are used)

Parameter	Definition	Units	Value
T_o	Reference temperature	°C	25
μ_{max}	Maximum growth rate at reference temperature	$year^{-1}$	365.25
K_p	Half-saturation coefficient for PO_4 uptake	mmol m^{-3}	0.1
K_I	Saturating light level	W m^{-2}	40
k_T	Temperature sensitivity of growth	Unitless	0.03
m_1	Linear mortality rate	$year^{-1}$	36.525
m_2	Quadratic mortality rate	$year^{-1}$ $mmol^{-1}$ m^3	3652.5

Supporting Table 2.2 | Prognostic production scheme parameter values, with minor differences from those used in Weber and Deutsch (2012). These parameter values were re-derived by matching model surface PO_4 values with World Ocean Atlas observations on a 2-degree horizontal grid, in contrast with the 4-degree grid used in Weber and Deutsch (2012).

Region:	AAZ	SAZ	STA	STP	ETA	ETP	NA	NP
Satellite								
VGPM								
+Laws 2000	0.1139	0.3207	0.2308	0.0504	0.0656	0.0656	0.0478	0.0000
+Dunne 2005	0.1508	0.2328	0.1677	0.0300	0.0729	0.0729	0.0697	0.0026
+Laws 2011	0.0927	0.0454	0.0975	0.0208	0.0445	0.0445	0.1169	0.1855
VGPM-Eppley								
+Laws 2000	0.1507	0.0420	0.1419	0.0663	0.1213	0.1213	0.1184	0.1197
+Dunne 2005	0.1349	0.0212	0.0993	0.0435	0.1516	0.1516	0.1294	0.2379
+Laws 2011	0.0622	0.0036	0.0636	0.0292	0.1080	0.1080	0.1308	0.1211
CbPM								
+Laws 2000	0.0478	0.2014	0.0900	0.2688	0.1667	0.1667	0.1263	0.0107
+Dunne 2005	0.1215	0.1141	0.0640	0.2695	0.1047	0.1047	0.1322	0.0978
+Laws 2011	0.1255	0.0188	0.0451	0.2216	0.1648	0.1648	0.1286	0.2247
Sum	1.00	1.00	1.00	1.00	1.00	1.00	1.00	1.00

Supporting Table 2.3 | Regional weights for export map calculation (reproduced from Table S2 in Weber et al., 2016)

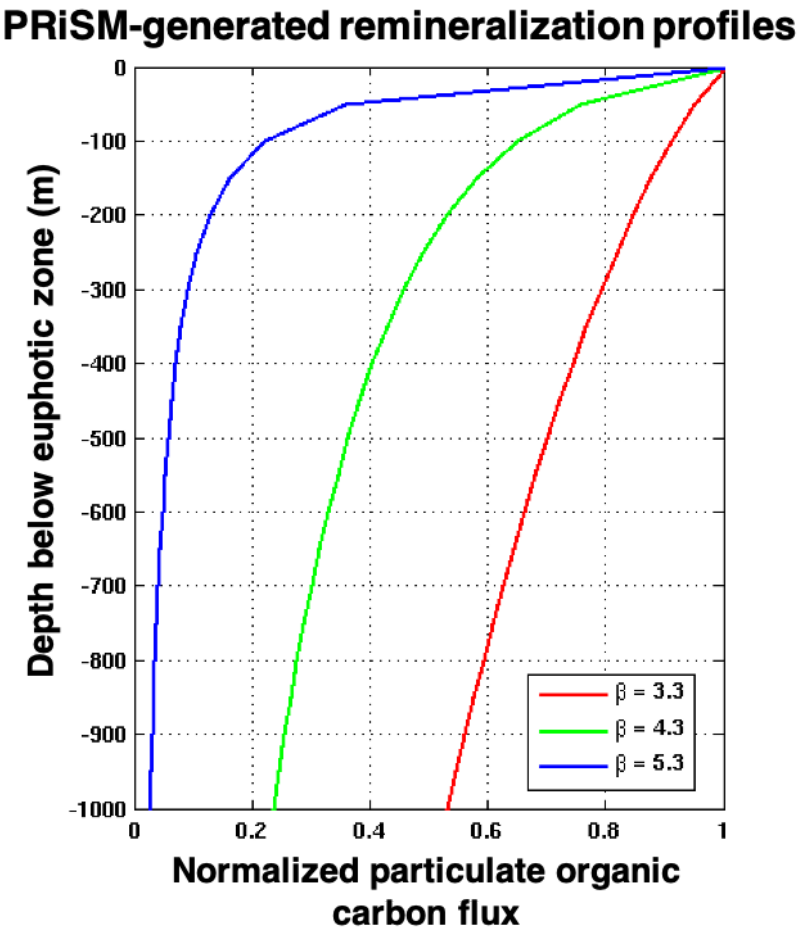

Supporting Figure 2.1 | PRiSM-calculated particle flux profiles with varying surface β values.

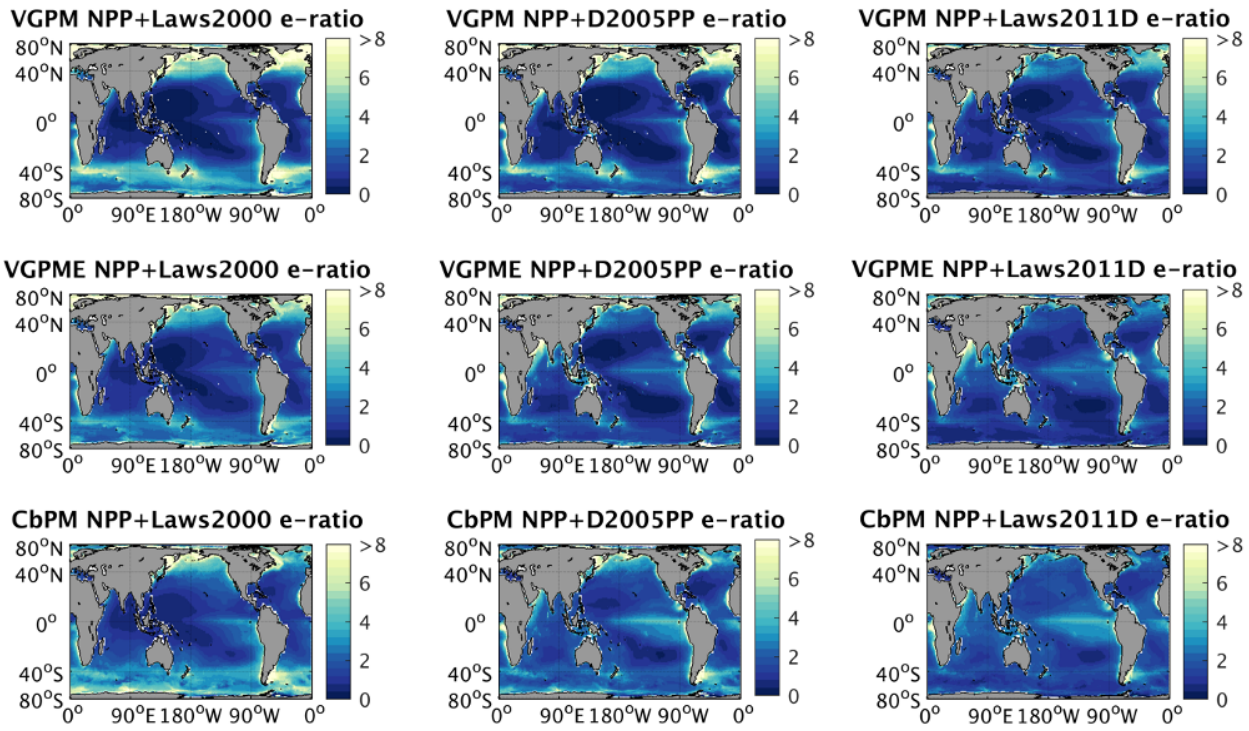

Supporting Figure 2.2 | Annual means of all nine monthly time series of global export considered here, computed from all possible permutations of three net primary productivity (NPP) and three e-ratio (export/NPP) algorithms (described in Section 2.2.2.2). Units are molC m^{-2} yr^{-1}.

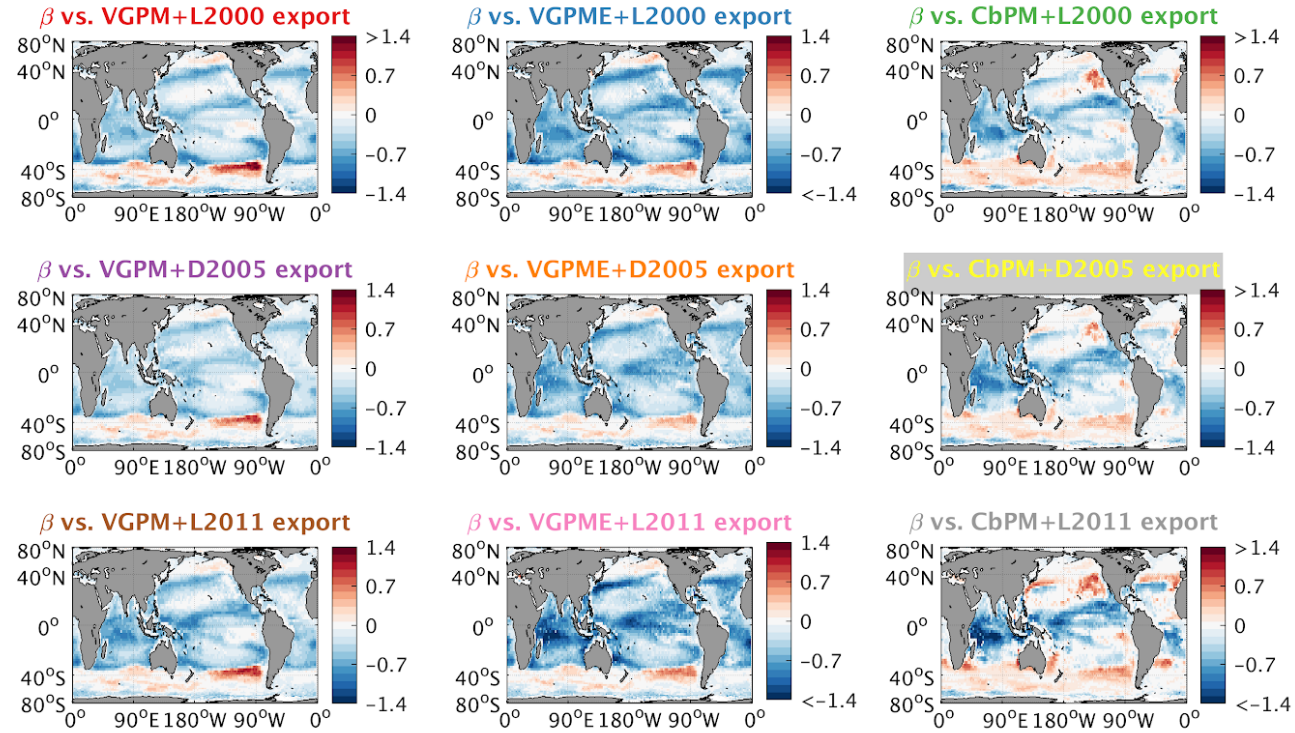

Supporting Figure 2.3. All nine monthly β versus time-mean normalized export ($\frac{d\beta_{obs}}{dE_{n,obs}}$, unitless) maps considered here. Title colors correspond to the NPP and e-ratio export combinations in Fig. 2.4a.

2.8 References

Alldredge, A. L., & Gotschalk, C. (1988). In situ settling behavior of marine snow. *Limnology and Oceanography*, *33*(3), 339–351. https://doi.org/10.4319/lo.1988.33.3.0339

Aumont, O., & Bopp, L. (2006). Globalizing results from ocean in situ iron fertilization studies. *Global Biogeochemical Cycles*, *20*(2). https://doi.org/10.1029/2005GB002591

Bach, L. T., Boxhammer, T., Larsen, A., Hildebrandt, N., Schulz, K. G., & Riebesell, U. (2016). Influence of plankton community structure on the sinking velocity of marine aggregates. *Global Biogeochemical Cycles*, *30*(8), 1145–1165. https://doi.org/10.1002/2016GB005372

Behrenfeld, M. J., & Falkowski, P. G. (1997). Photosynthetic rates derived from satellite-based chlorophyll concentration. *Limnology and Oceanography*, *42*(1), 1–20. https://doi.org/10.4319/lo.1997.42.1.0001

Behrenfeld, M. J., Boss, E., Siegel, D. A., & Shea, D. M. (2005). Carbon-based ocean productivity and phytoplankton physiology from space. *Global Biogeochemical Cycles*, *19*(1). https://doi.org/10.1029/2004GB002299

Bopp, Monfray, P., Aumont, O., Dufresne, J.-L., Treut, H. L., Madec, G., et al. (2001). Potential impact of climate change on marine export production. *Global Biogeochemical Cycles*, *15*(1), 81–99. https://doi.org/10.1029/1999GB001256

Bopp, Resplandy, L., Orr, J. C., Doney, S. C., Dunne, J. P., Gehlen, M., et al. (2013). Multiple stressors of ocean ecosystems in the 21st century: projections with CMIP5 models. *Biogeosciences*, *10*(10), 6225–6245. https://doi.org/10.5194/bg-10-6225-2013

Bopp, L., Quéré, C. L., Heimann, M., Manning, A. C., & Monfray, P. (2002). Climate-induced oceanic oxygen fluxes: Implications for the contemporary carbon budget. *Global Biogeochemical Cycles*, *16*(2), 6-1-6–13. https://doi.org/10.1029/2001GB001445

Bopp, L., Aumont, O., Cadule, P., Alvain, S., & Gehlen, M. (2005). Response of diatoms distribution to global warming and potential implications: A global model study. *Geophysical Research Letters*, *32*(19). https://doi.org/10.1029/2005GL023653

Boss, E., Twardowski, M. S., & Herring, S. (2001). Shape of the particulate beam attenuation spectrum and its inversion to obtain the shape of the particulate size distribution. *Applied Optics*, *40*(27), 4885–4893. https://doi.org/10.1364/AO.40.004885

Boyd, P. W., & Trull, T. W. (2007). Understanding the export of biogenic particles in oceanic waters: Is there consensus? *Progress in Oceanography*, *72*(4), 276–312. https://doi.org/10.1016/j.pocean.2006.10.007

Boyd, Philip W., Claustre, H., Levy, M., Siegel, D. A., & Weber, T. (2019). Multi-faceted particle pumps drive carbon sequestration in the ocean. *Nature*, *568*(7752), 327–335. https://doi.org/10.1038/s41586-019-1098-2

Buesseler, K. O., & Boyd, P. W. (2009). Shedding light on processes that control particle export and flux attenuation in the twilight zone of the open ocean. *Limnology and Oceanography*, *54*(4), 1210–1232. https://doi.org/10.4319/lo.2009.54.4.1210

Cabré, A., Marinov, I., Bernardello, R., & Bianchi, D. (2015). Oxygen minimum zones in the tropical Pacific across CMIP5 models: mean state differences and climate change trends. *Biogeosciences*, *12*(18), 5429–5454. https://doi.org/10.5194/bg-12-5429-2015

Cabré, Anna, Marinov, I., & Leung, S. (2015). Consistent global responses of marine ecosystems to future climate change across the IPCC AR5 earth system models. *Climate Dynamics*, *45*(5), 1253–1280. https://doi.org/10.1007/s00382-014-2374-3

Caesar, L., Rahmstorf, S., Robinson, A., Feulner, G., & Saba, V. (2018). Observed fingerprint of a weakening Atlantic Ocean overturning circulation. *Nature*, *556*(7700), 191–196. https://doi.org/10.1038/s41586-018-0006-5

Capotondi, A., Alexander, M. A., Bond, N. A., Curchitser, E. N., & Scott, J. D. (2012). Enhanced upper ocean stratification with climate change in the CMIP3 models. *Journal of Geophysical Research: Oceans*, *117*(C4). https://doi.org/10.1029/2011JC007409

Carr, M.-E., Friedrichs, M. A. M., Schmeltz, M., Noguchi Aita, M., Antoine, D., Arrigo, K. R., et al. (2006). A comparison of global estimates of marine primary production from ocean color. *Deep Sea Research Part II: Topical Studies in Oceanography*, *53*(5), 741–770. https://doi.org/10.1016/j.dsr2.2006.01.028

Cavan, E. L., Trimmer, M., Shelley, F., & Sanders, R. (2017). Remineralization of particulate organic carbon in an ocean oxygen minimum zone. *Nature Communications*, *8*(1), 1–9. https://doi.org/10.1038/ncomms14847

Cavan, Emma Louise, Henson, S. A., & Boyd, P. W. (2019). The Sensitivity of Subsurface Microbes to Ocean Warming Accentuates Future Declines in Particulate Carbon Export. *Frontiers in Ecology and Evolution*, *6*. https://doi.org/10.3389/fevo.2018.00230

Codispoti, L. A. (2010). Interesting Times for Marine N2O. *Science*, *327*(5971), 1339–1340. https://doi.org/10.1126/science.1184945

Collins, M., Sutherland, M., Bouwer, L., Cheong, S.-M., Frölicher, T., Jacot Des Combes, H., et al. (2019). *Chapter 6: Extremes, Abrupt Changes and Managing Risks — Special Report on the Ocean and Cryosphere in a Changing Climate* (IPCC Special Report on the Ocean and Cryosphere in a Changing Climate). Retrieved from https://www.ipcc.ch/srocc/chapter/chapter-6/

Collins, Mat, An, S.-I., Cai, W., Ganachaud, A., Guilyardi, E., Jin, F.-F., et al. (2010). The impact of global warming on the tropical Pacific Ocean and El Niño. *Nature Geoscience*, *3*(6), 391–397. https://doi.org/10.1038/ngeo868

Cram, J. A., Weber, T., Leung, S. W., McDonnell, A. M. P., Liang, J.-H., & Deutsch, C. (2018). The Role of Particle Size, Ballast, Temperature, and Oxygen in the Sinking Flux to the Deep Sea. *Global Biogeochemical Cycles*, *32*(5), 858–876. https://doi.org/10.1029/2017GB005710

Devol, A. H., & Hartnett, H. E. (2001). Role of the oxygen-deficient zone in transfer of organic carbon to the deep ocean. *Limnology and Oceanography*, *46*(7), 1684–1690. https://doi.org/10.4319/lo.2001.46.7.1684

DeVries, T., Liang, J.-H., & Deutsch, C. (2014). A mechanistic particle flux model applied to the oceanic phosphorus cycle. *Biogeosciences*, *11*(19), 5381–5398. https://doi.org/10.5194/bg-11-5381-2014

DeVries, Tim. (2014). The oceanic anthropogenic CO2 sink: Storage, air-sea fluxes, and transports over the industrial era. *Global Biogeochemical Cycles*, *28*(7), 631–647. https://doi.org/10.1002/2013GB004739

DeVries, Tim, & Primeau, F. (2011). Dynamically and Observationally Constrained Estimates of Water-Mass Distributions and Ages in the Global Ocean. *Journal of Physical Oceanography*, *41*(12), 2381–2401. https://doi.org/10.1175/JPO-D-10-05011.1

DeVries, Tim, & Weber, T. (2017). The export and fate of organic matter in the ocean: New constraints from combining satellite and oceanographic tracer observations. *Global Biogeochemical Cycles*, *31*(3), 535–555. https://doi.org/10.1002/2016GB005551

Ducklow, H., Steinberg, D., & Buesseler, K. (2001). Upper Ocean Carbon Export and the Biological Pump. *Oceanography*, *14*(4), 50–58. https://doi.org/10.5670/oceanog.2001.06

Dugdale, R., & Wilkerson, F. (1992). Nutrient Limitation of New Production in the Sea. In P. G. Falkowski, A. D. Woodhead, & K. Vivirito (Eds.), *Primary Productivity and Biogeochemical Cycles in the Sea* (pp. 107–122). Boston, MA: Springer US. https://doi.org/10.1007/978-1-4899-0762-2_7

Dunne, J. P., Armstrong, R. A., Gnanadesikan, A., & Sarmiento, J. L. (2005). Empirical and mechanistic models for the particle export ratio. *Global Biogeochemical Cycles*, *19*(4). https://doi.org/10.1029/2004GB002390

Dunne, J. P., Sarmiento, J. L., & Gnanadesikan, A. (2007). A synthesis of global particle export from the surface ocean and cycling through the ocean interior and on the seafloor. *Global Biogeochemical Cycles*, *21*(4). https://doi.org/10.1029/2006GB002907

Falkowski, P. G., Barber, R. T., & Smetacek, V. (1998). Biogeochemical Controls and Feedbacks on Ocean Primary Production. *Science*, *281*(5374), 200–206. https://doi.org/10.1126/science.281.5374.200

Friedland, K. D., Stock, C., Drinkwater, K. F., Link, J. S., Leaf, R. T., Shank, B. V., et al. (2012). Pathways between Primary Production and Fisheries Yields of Large Marine Ecosystems. *PLoS ONE*, *7*(1). https://doi.org/10.1371/journal.pone.0028945

Galbraith, E. D., & Martiny, A. C. (2015). A simple nutrient-dependence mechanism for predicting the stoichiometry of marine ecosystems. *Proceedings of the National Academy of Sciences of the United States of America*, *112*(27), 8199–8204. https://doi.org/10.1073/pnas.1423917112

Gehlen, M., Bopp, L., Emprin, N., Aumont, O., Heinze, C., & Ragueneau, O. (2006). Reconciling surface ocean productivity, export fluxes and sediment composition in a global biogeochemical ocean model. *Biogeosciences*, *3*(4), 521–537. https://doi.org/10.5194/bg-3-521-2006

Gregg, W. W., Ginoux, P., Schopf, P. S., & Casey, N. W. (2003). Phytoplankton and iron: validation of a global three-dimensional ocean biogeochemical model. *Deep Sea Research Part II: Topical Studies in Oceanography*, *50*(22), 3143–3169. https://doi.org/10.1016/j.dsr2.2003.07.013

Guidi, L., Stemmann, L., Legendre, L., Picheral, M., Prieur, L., & Gorsky, G. (2007). Vertical distribution of aggregates (>110 µm) and mesoscale activity in the northeastern Atlantic: Effects on the deep vertical export of surface carbon. *Limnology and Oceanography*, *52*(1), 7–18. https://doi.org/10.4319/lo.2007.52.1.0007

Guidi, L., Jackson, G. A., Stemmann, L., Miquel, J. C., Picheral, M., & Gorsky, G. (2008). Relationship between particle size distribution and flux in the mesopelagic zone. *Deep Sea Research Part I: Oceanographic Research Papers*, *55*(10), 1364–1374. https://doi.org/10.1016/j.dsr.2008.05.014

Guidi, L., Stemmann, L., Jackson, G. A., Ibanez, F., Claustre, H., Legendre, L., et al. (2009). Effects of phytoplankton community on production, size, and export of large aggregates: A world-ocean analysis. *Limnology and Oceanography*, *54*(6), 1951–1963. https://doi.org/10.4319/lo.2009.54.6.1951

Hartnett, H. E., & Devol, A. H. (2003). Role of a strong oxygen-deficient zone in the preservation and degradation of organic matter: a carbon budget for the continental margins of northwest Mexico and Washington State. *Geochimica et Cosmochimica Acta*, *67*(2), 247–264. https://doi.org/10.1016/S0016-7037(02)01076-1

Henson, S. A., Sanders, R., Madsen, E., Morris, P. J., Moigne, F. L., & Quartly, G. D. (2011). A reduced estimate of the strength of the ocean's biological carbon pump. *Geophysical Research Letters*, *38*(4). https://doi.org/10.1029/2011GL046735

Hirata, T., Hardman-Mountford, N. J., Brewin, R. J. W., Aiken, J., Barlow, R., Suzuki, K., et al. (2011). Synoptic relationships between surface Chlorophyll-*a* and diagnostic pigments specific to phytoplankton functional types. *Biogeosciences*, *8*(2), 311–327. https://doi.org/10.5194/bg-8-311-2011

Hofmann, M., & Schellnhuber, H.-J. (2009). Oceanic acidification affects marine carbon pump and triggers extended marine oxygen holes. *Proceedings of the National Academy of Sciences*, *106*(9), 3017–3022. https://doi.org/10.1073/pnas.0813384106

John, E. H., Wilson, J. D., Pearson, P. N., & Ridgwell, A. (2014). Temperature-dependent remineralization and carbon cycling in the warm Eocene oceans. *Palaeogeography, Palaeoclimatology, Palaeoecology*, *413*, 158–166. https://doi.org/10.1016/j.palaeo.2014.05.019

Keeling, R. F., Körtzinger, A., & Gruber, N. (2010). Ocean Deoxygenation in a Warming World. *Annual Review of Marine Science*, *2*(1), 199–229. https://doi.org/10.1146/annurev.marine.010908.163855

Kostadinov, T. S., Siegel, D. A., & Maritorena, S. (2009). Retrieval of the particle size distribution from satellite ocean color observations. *Journal of Geophysical Research: Oceans*, *114*(C9). https://doi.org/10.1029/2009JC005303

Kriest, I., & Oschlies, A. (2008). On the treatment of particulate organic matter sinking in large-scale models of marine biogeochemical cycles. *Biogeosciences*, *5*(1), 55–72. https://doi.org/10.5194/bg-5-55-2008

Kwon, E. Y., Primeau, F., & Sarmiento, J. L. (2009). The impact of remineralization depth on the air–sea carbon balance. *Nature Geoscience*, *2*(9), 630–635. https://doi.org/10.1038/ngeo612

Lam, P. J., & Bishop, J. K. B. (2007). High biomass, low export regimes in the Southern Ocean. *Deep Sea Research Part II: Topical Studies in Oceanography*, *54*(5), 601–638. https://doi.org/10.1016/j.dsr2.2007.01.013

Laufkötter, C., Vogt, M., Gruber, N., Aumont, O., Bopp, L., Doney, S. C., et al. (2016). Projected decreases in future marine export production: the role of the carbon flux through the upper ocean ecosystem. *Biogeosciences*, *13*(13), 4023–4047. https://doi.org/10.5194/bg-13-4023-2016

Laws, E. A., Falkowski, P. G., Smith, W. O., Ducklow, H., & McCarthy, J. J. (2000). Temperature effects on export production in the open ocean. *Global Biogeochemical Cycles*, *14*(4), 1231–1246. https://doi.org/10.1029/1999GB001229

Laws, E. A., D'Sa, E., & Naik, P. (2011). Simple equations to estimate ratios of new or export production to total production from satellite-derived estimates of sea surface temperature and primary production. *Limnology and Oceanography: Methods*, *9*(12), 593–601. https://doi.org/10.4319/lom.2011.9.593

Le Quéré, C., Harrison, S. P., Prentice, I. C., Buitenhuis, E. T., Aumont, O., Bopp, L., et al. (2005). Ecosystem dynamics based on plankton functional types for global ocean biogeochemistry models. *Global Change Biology*, *11*(11), 2016–2040. https://doi.org/10.1111/j.1365-2486.2005.1004.x

Lee, Z., Weidemann, A., Kindle, J., Arnone, R., Carder, K. L., & Davis, C. (2007). Euphotic zone depth: Its derivation and implication to ocean-color remote sensing. *Journal of Geophysical Research: Oceans*, *112*(C3). https://doi.org/10.1029/2006JC003802

Letscher, R. T., Primeau, F., & Moore, J. K. (2016). Nutrient budgets in the subtropical ocean gyres dominated by lateral transport. *Nature Geoscience*, *9*(11), 815–819. https://doi.org/10.1038/ngeo2812

Litchman, E., Klausmeier, C. A., Schofield, O. M., & Falkowski, P. G. (2007). The role of functional traits and trade-offs in structuring phytoplankton communities: scaling from cellular to ecosystem level. *Ecology Letters*, *10*(12), 1170–1181. https://doi.org/10.1111/j.1461-0248.2007.01117.x

Locarnini, R. A., Mishonov, A. V., Antonov, J. I., Boyer, T. P., Garcia, H. E., Baranova, O. K., et al. (2010). World Ocean Atlas 2009, Volume 1: Temperature. (S. Levitus, Ed.). U.S. Government Printing Office.

Long, M. C., Deutsch, C., & Ito, T. (2016). Finding forced trends in oceanic oxygen. *Global Biogeochemical Cycles*, *30*(2), 381–397. https://doi.org/10.1002/2015GB005310

Maier−Reimer, E. (1993). Geochemical cycles in an ocean general circulation model. Preindustrial tracer distributions. *Global Biogeochemical Cycles*, *7*(3), 645–677. https://doi.org/10.1029/93GB01355

Marsay, C. M., Sanders, R. J., Henson, S. A., Pabortsava, K., Achterberg, E. P., & Lampitt, R. S. (2015). Attenuation of sinking particulate organic carbon flux through the mesopelagic ocean. *Proceedings of the National Academy of Sciences*, *112*(4), 1089–1094. https://doi.org/10.1073/pnas.1415311112

Martin, J. H., Knauer, G. A., Karl, D. M., & Broenkow, W. W. (1987). VERTEX: carbon cycling in the northeast Pacific. *Deep Sea Research Part A. Oceanographic Research Papers*, *34*(2), 267–285. https://doi.org/10.1016/0198-0149(87)90086-0

Martínez-García, A., Sigman, D. M., Ren, H., Anderson, R. F., Straub, M., Hodell, D. A., et al. (2014). Iron Fertilization of the Subantarctic Ocean During the Last Ice Age. *Science*, *343*(6177), 1347–1350. https://doi.org/10.1126/science.1246848

Matear, R. J., & Hirst, A. C. (2003). Long-term changes in dissolved oxygen concentrations in the ocean caused by protracted global warming. *Global Biogeochemical Cycles*, *17*(4). https://doi.org/10.1029/2002GB001997

Matsumoto, K. (2007a). Biology-mediated temperature control on atmospheric pCO2 and ocean biogeochemistry. *Geophysical Research Letters*, *34*(20). https://doi.org/10.1029/2007GL031301

Matsumoto, K. (2007b). Radiocarbon-based circulation age of the world oceans. *Journal of Geophysical Research: Oceans*, *112*(C9). https://doi.org/10.1029/2007JC004095

McDonnell, A. M. P., Boyd, P. W., & Buesseler, K. O. (2015). Effects of sinking velocities and microbial respiration rates on the attenuation of particulate carbon fluxes through the mesopelagic zone. *Global Biogeochemical Cycles*, *29*(2), 175–193. https://doi.org/10.1002/2014GB004935

McDonnell, Andrew M. P., & Buesseler, K. O. (2010). Variability in the average sinking velocity of marine particles. *Limnology and Oceanography*, *55*(5), 2085–2096. https://doi.org/10.4319/lo.2010.55.5.2085

Michaels, A. F., & Silver, M. W. (1988). Primary production, sinking fluxes and the microbial food web. *Deep Sea Research Part A. Oceanographic Research Papers*, *35*(4), 473–490. https://doi.org/10.1016/0198-0149(88)90126-4

Moore, J. K., Fu, W., Primeau, F., Britten, G. L., Lindsay, K., Long, M., et al. (2018). Sustained climate warming drives declining marine biological productivity. *Science*, *359*(6380), 1139–1143. https://doi.org/10.1126/science.aao6379

Najjar, R. G., Sarmiento, J. L., & Toggweiler, J. R. (1992). Downward transport and fate of organic matter in the ocean: Simulations with a general circulation model. *Global Biogeochemical Cycles*, *6*(1), 45–76. https://doi.org/10.1029/91GB02718

Oschlies, A., Schulz, K. G., Riebesell, U., & Schmittner, A. (2008). Simulated 21st century's increase in oceanic suboxia by CO2-enhanced biotic carbon export. *Global Biogeochemical Cycles*, *22*(4). https://doi.org/10.1029/2007GB003147

Passow, U., & Carlson, C. A. (2012). The biological pump in a high CO2 world. *Marine Ecology Progress Series*, *470*, 249–271. https://doi.org/10.3354/meps09985

Picheral, M., Guidi, L., Stemmann, L., Karl, D. M., Iddaoud, G., & Gorsky, G. (2010). The Underwater Vision Profiler 5: An advanced instrument for high spatial resolution studies of particle size spectra and zooplankton. *Limnology and Oceanography: Methods*, *8*(9), 462–473. https://doi.org/10.4319/lom.2010.8.462

Rossow, W. B., & Schiffer, R. A. (1999). Advances in Understanding Clouds from ISCCP. *Bulletin of the American Meteorological Society*, *80*(11), 2261–2288. https://doi.org/10.1175/1520-0477(1999)080<2261:AIUCFI>2.0.CO;2

Sarmiento, J. L., & Siegenthaler, U. (1992). New Production and the Global Carbon Cycle. In P. G. Falkowski, A. D. Woodhead, & K. Vivirito (Eds.), *Primary Productivity and*

Biogeochemical Cycles in the Sea (pp. 317–332). Boston, MA: Springer US. https://doi.org/10.1007/978-1-4899-0762-2_18

Schmidtko, S., Stramma, L., & Visbeck, M. (2017). Decline in global oceanic oxygen content during the past five decades. *Nature*, *542*(7641), 335–339. https://doi.org/10.1038/nature21399

Schmittner, A., Oschlies, A., Giraud, X., Eby, M., & Simmons, H. L. (2005). A global model of the marine ecosystem for long-term simulations: Sensitivity to ocean mixing, buoyancy forcing, particle sinking, and dissolved organic matter cycling. *Global Biogeochemical Cycles*, *19*(3). https://doi.org/10.1029/2004GB002283

Sheldon, R. W., Prakash, A., & Sutcliffe, W. H. (1972). The Size Distribution of Particles in the Ocean1. *Limnology and Oceanography*, *17*(3), 327–340. https://doi.org/10.4319/lo.1972.17.3.0327

Siegel, D. A., Buesseler, K. O., Doney, S. C., Sailley, S. F., Behrenfeld, M. J., & Boyd, P. W. (2014). Global assessment of ocean carbon export by combining satellite observations and food-web models. *Global Biogeochemical Cycles*, *28*(3), 181–196. https://doi.org/10.1002/2013GB004743

Smayda, T. J. (1971). Normal and accelerated sinking of phytoplankton in the sea. *Marine Geology*, *11*(2), 105–122. https://doi.org/10.1016/0025-3227(71)90070-3

Smith, T. M., Reynolds, R. W., Peterson, T. C., & Lawrimore, J. (2008). Improvements to NOAA's Historical Merged Land–Ocean Surface Temperature Analysis (1880–2006). *Journal of Climate*, *21*(10), 2283–2296. https://doi.org/10.1175/2007JCLI2100.1

Steinberg, D. K., Lomas, M. W., & Cope, J. S. (2012). Long-term increase in mesozooplankton biomass in the Sargasso Sea: Linkage to climate and implications for food web dynamics and biogeochemical cycling. *Global Biogeochemical Cycles*, *26*(1). https://doi.org/10.1029/2010GB004026

Thornton, D. C. O. (2014). Dissolved organic matter (DOM) release by phytoplankton in the contemporary and future ocean. *European Journal of Phycology*, *49*(1), 20–46. https://doi.org/10.1080/09670262.2013.875596

Toggweiler, J. R., & Russell, J. (2008). Ocean circulation in a warming climate. *Nature*, *451*(7176), 286–288. https://doi.org/10.1038/nature06590

Turner, J. T. (2015). Zooplankton fecal pellets, marine snow, phytodetritus and the ocean's biological pump. *Progress in Oceanography*, *130*, 205–248. https://doi.org/10.1016/j.pocean.2014.08.005

Van Mooy, B. A. S., Keil, R. G., & Devol, A. H. (2002). Impact of suboxia on sinking particulate organic carbon: Enhanced carbon flux and preferential degradation of amino acids via

denitrification. *Geochimica et Cosmochimica Acta*, *66*(3), 457–465. https://doi.org/10.1016/S0016-7037(01)00787-6

Weber, T., & Deutsch, C. (2014). Local versus basin-scale limitation of marine nitrogen fixation. *Proceedings of the National Academy of Sciences*, *111*(24), 8741–8746. https://doi.org/10.1073/pnas.1317193111

Weber, Thomas, & Deutsch, C. (2012). Oceanic nitrogen reservoir regulated by plankton diversity and ocean circulation. *Nature*, *489*(7416), 419–422. https://doi.org/10.1038/nature11357

Weber, Thomas, Cram, J. A., Leung, S. W., DeVries, T., & Deutsch, C. (2016). Deep ocean nutrients imply large latitudinal variation in particle transfer efficiency. *Proceedings of the National Academy of Sciences*, *113*(31), 8606–8611. https://doi.org/10.1073/pnas.1604414113

Yamanaka, Y., & Tajika, E. (1996). The role of the vertical fluxes of particulate organic matter and calcite in the oceanic carbon cycle: Studies using an ocean biogeochemical general circulation model. *Global Biogeochemical Cycles*, *10*(2), 361–382. https://doi.org/10.1029/96GB00634

Chapter 3: ENSO drives near-surface oxygen and vertical habitat variability in the Tropical Pacific

This chapter is an edited version of the following publication: Leung, S., Thompson, L., McPhaden, M. J., & Mislan, K. A. S. (2019). ENSO drives near-surface oxygen and vertical habitat variability in the Tropical Pacific. *Environmental Research Letters*, *14*(6), 064020. https://doi.org/10.1088/1748-9326/ab1c13

3.1 Summary

El Niño-Southern Oscillation (ENSO) is the leading cause of sea surface temperature variability in the Tropical Pacific with known impacts on tuna geographic range, but its effects on oxygen and available oxygenated habitat space are less clear. Variations in oxygenated vertical habitat space in the upper ocean can alter interactions between predator and prey, as well as drive changes in the vulnerability of economically important tuna and other pelagic fish to surface fishing gear. Using *in situ* measurements, we show that ENSO is the primary driver of upper-ocean oxygen partial pressure (pO_2) variability on year-to-year time scales in the Tropical Pacific. Mechanistically, these pO_2 variations are primarily caused by vertical shifts in thermocline depth, which alternately elevate and depress cold, hypoxic waters from the ocean interior depending on the ENSO phase and location. Transport-driven, isopycnal pO_2 variations within the thermocline also play an important but secondary role. In the western Tropical Pacific, waters within the exclusive economic zones of Palau, Micronesia, Nauru, and the Marshall Islands undergo the greatest variations in oxygenated tuna vertical habitat extent: approximately 19.5 m, 23.9 m, 19.5 m, and 19.3 m, respectively, between El Niño and La Niña phases. Oxygen

thus plays an important role in altering available tuna vertical habitat space between different phases of ENSO.

3.2 Introduction

As the dominant mode of year-to-year climate variability over the globe (McPhaden et al., 2006; Deser et al., 2010; Kenyon and Hegerl, 2010; Viron et al., 2013), El Niño-Southern Oscillation (ENSO) generates large swings in Tropical Pacific climate, often with widespread socioeconomic impacts (Cochrane et al., 2009; Badjeck et al., 2010; Barnett, 2011). In addition to severe droughts in Pacific island states (Barnett, 2001) and coral bleaching across ocean basins (Hughes et al., 2018), ENSO has been linked to marked variations in tuna catches and landings throughout the Tropical Pacific (Lehodey et al., 1997). Because of the critical role that tuna fisheries play in ensuring economic development and food security in the region (e.g., Barnett, 2011), it is important to better understand how tuna respond to ENSO-driven changes in their habitats. Past work has focused on temperature-related variations in observed tuna habitat extents associated with ENSO (Lehodey et al., 1997), but habitat favorability can also be affected by changes in oxygen availability (e.g., Barkley et al., 1978; Brill, 1994; Bushnell and Brill, 1991). With predicted declines in global oceanic oxygen content under greenhouse warming (Frölicher et al., 2009; Keeling et al., 2009; Bopp et al., 2013; Cocco et al., 2013; Cabré et al., 2015; Schmidtko et al., 2017), oxygen-driven constraints on available habitat will likely become even more important.

Changes in oxygenated vertical habitat space may have particularly important and far-reaching effects on tuna fisheries and ecosystem dynamics. Hypoxia-induced vertical habitat

compression can lead to crowding of tuna closer to the surface, where they are more easily captured and potentially overfished (Green, 1967; Barkley et al., 1978; Prince and Goodyear, 2006). Differential variations in vertical habitat extent among organisms with different oxygen requirements can decouple or enhance predator-prey interactions, altering previously established food webs (Prince et al., 2010; Bertrand et al., 2011; Koslow et al., 2011; Mislan et al., 2017). Horizontal migrations away from traditional fishing grounds can also result from changes in vertical habitat suitability (Block et al., 2011; Pinsky et al., 2013). A better understanding of ENSO-driven variations in vertical habitat extent can therefore help improve seasonal predictions of species spatial distributions, allowing both fishers and fisheries managers to make better informed short-term decisions (Hobday et al., 2016). Quantifying the impacts of ENSO on vertical habitat extent can also inform strategies to address longer-term future changes, which include projected increases in the frequency of extreme ENSO phases (Cai et al., 2014; Cai et al., 2015). More frequent and/or intense extremes could lead to pronounced year-to-year changes in available tuna habitat that may swamp projections of relatively modest long-term mean trends (Mislan et al., 2017). Thus, a deeper understanding of oxygen-defined vertical habitat variability could also increase the accuracy of current and future tuna stock assessments, which are frequently based on Catch Per Unit Effort (CPUE) estimates normalized by climatological habitat favorability maps that do not take interannual oxygen variability into account (Brill and Lutcavage, 2001; Bigelow et al., 2002; Goodyear, 2003; Prince and Goodyear, 2006; Maunder et al., 2006; Maunder and Piner, 2015).

More recent ecological tuna models do account for the effects of oxygen on tuna movements and populations, using either energy budgets of individual organisms (Dueri et al.,

2014) or habitat favorability indices computed with theoretical functions bounded by thresholds measured in the lab or field (e.g., Lehodey et al., 2008; Lehodey et al., 2010; Lehodey et al., 2013; Lehodey et al., 2015). However, a lack of knowledge regarding oxygen variability and movements within real-world tuna habitats makes it difficult to precisely judge the accuracy of oxygen-influenced spatial dynamics within these models. Coupled ocean-atmosphere models with biogeochemistry can provide some insight into oxygen variability within the Tropical Pacific (e.g., Frölicher et al., 2009; Cabré et al., 2015; Resplandy et al., 2015), but without a comprehensive mechanistic understanding of observed variability, these models can only be judged by their skill in reproducing (approximate) climatological signals. These coupled models are also used to project changes in ocean oxygen content with future warming, where the statistical significance of future trends is typically determined by how large the trends are compared to natural variability within the models. If the magnitude of natural, short-term variability such as ENSO in these models is not in line with observations, then their ability to provide robust projections of future conditions may be diminished. Oxygen variability and trends within the Tropical Pacific have proven to be especially difficult to model, given the complicated ENSO dynamics, ocean circulation patterns, and particle export fluxes in this region (e.g., Cabré et al., 2015). Quantification of observed present-day oxygen variability within the Tropical Pacific is therefore needed to better evaluate and improve both ecological and coupled ocean-atmosphere models.

Here we quantify observed ENSO-driven upper-ocean (0-300 m) oxygen variability and analyze its mechanistic drivers throughout the Tropical Pacific. The impact of these ENSO-driven oxygen variations on hypoxia-defined tuna vertical habitat extent is then examined

and related to potential effects on fisheries, food security, and economic development mainly in the western Tropical Pacific, where tuna catches are greatest.

3.3 Methods

3.3.1 Oxygen partial pressure (pO2) and tuna hypoxic depth (THD) calculations

To accurately represent the oxygen conditions experienced by marine animals such as tuna, we report oxygen content in terms of partial pressures (pO_2) because it is pO_2, rather than dissolved oxygen concentration (O_2), that drives oxygen transfer and provision to animal tissue (Seibel, 2011; Hofmann et al., 2011). To compute pO_2 from input variables of temperature, salinity, and O_2, we first convert O_2 to percent oxygen saturation (Garcia and Gordon, 1992). We then divide percent oxygen saturation by the fractional atmospheric concentration of oxygen (21%) and as a final step, correct for hydrostatic pressure at depth (Enns et al., 1965). An additional advantage of using pO_2 is that because it is a function of percent oxygen saturation, it automatically accounts for changes in surface oxygen solubility owing to changes in sea surface temperatures (SST); in other words, pO_2 is not affected by variations in solubility, allowing us to rule out this potential confounding factor driving variations in oxygen content. To describe changes in the availability of oxygenated vertical habitat in the upper ocean to tuna and other pelagic predators with similar physiologies, we use tuna hypoxic depth (THD), defined as the shallowest depth at which pO_2 first falls below 15 kPa. This 15 kPa pO_2 threshold is approximately equivalent to the 3.5 ml l^{-1} dissolved concentration threshold (assuming a salinity

of 32.5 psu, a temperature of 23.5°C, and depth of 0 m, as in the tank experiment by Gooding et al., 1981) typically used to describe hypoxic conditions considered dangerous for skipjack and yellowfin tuna (Ingham et al., 1977; Barkley et al., 1978; Evans et al., 1981; Gooding et al., 1981; Bushnell et al., 1990; Prince and Goodyear, 2006; Arrizabalaga et al., 2015), which make up the vast majority of tuna caught in the western and central Tropical Pacific (Pons et al., 2017) (see Supp. Fig. 3.1, which shows more precisely how this 15 kPa pO_2 threshold translates into dissolved oxygen concentrations in units of both ml l^{-1} and umol kg^{-1} as a function of temperature, salinity, and depth across values of these properties that are typically encountered by skipjack and yellowfin tuna).

3.3.2 Data collection, binning, and averaging

In situ profiles of near-surface (0-700 m) temperature, salinity, and O_2 collected between January 1955 and May 2017 were downloaded from the World Ocean Database (WOD) at https://www.nodc.noaa.gov/OC5/SELECT/dbsearch/dbsearch.html on June 25th, 2017. WOD compiles uniform and quality-controlled data throughout the global ocean from buoys, ships, gliders, and floats (Boyer et al., 2013). All available datasets within WOD were collected and used including data from ocean stations, high resolution CTDs, expendable bathythermographs (XBT), mechanical bathythermographs (MBT), profiling floats (including Argo), drifting buoys, moored buoys, autonomous pinniped bathythermographs, undulating oceanographic recorders, buckets, thermosalinographs, and gliders. XBT/MBT temperatures were corrected using Levitus et al. (2009). Any flagged data were excluded.

Raw profiles of temperature, salinity, and O_2 were binned onto 5-by-5 horizontal degree, monthly mean maps with standard WOD vertical levels (5 m depth resolution down to 100 m, 25 m depth resolution between 100-500 m, and 100 m depth resolution beneath 500 m). These monthly mean maps were then used to calculate corresponding pO_2 maps at grid points where all three input variables were available. The mean seasonal cycle was then computed at each grid point for all variables. No lower threshold was placed on the number of years required to compute a climatological monthly mean (e.g., if a given grid cell had only one monthly mean data point in January over the entire time series, then that data point became January's climatological mean at that grid cell). Anomalies were then calculated by subtracting the mean seasonal cycle at each corresponding grid point. The resulting 4-D (x, y, z, time) anomaly maps were used for all subsequent map-based analyses (Fig. 3.1-3.4; Supp. Fig. 3.3-3.6, 3.8-3.9), where missing data is denoted with empty grid cells.

For all other analyses (Table 3.1; Fig. 3.5; Supp. Fig. 3.7), raw profiles of the variables were grouped by month and region of interest, including the Western Equatorial Pacific box (WEP), the Eastern Equatorial Pacific box (EEP), and Exclusive Economic Zones (EEZs) (defined in Fig. 3.2a and c). Raw profiles of pO_2 were computed whenever corresponding raw profiles of all three input variables were available. The mean seasonal cycle was then computed within each region of interest, and anomaly profiles were subsequently calculated by subtracting the mean seasonal cycle within each corresponding region.

All aforementioned mapped and regional anomalies were also computed by subtracting out World Ocean Atlas 2013 climatologies (Locarnini et al., 2013; Zweng et al., 2013; Garcia et al., 2014), which did not yield any notable differences in our results. To maintain data source

consistency, we thus show only anomalies computed by subtracting out the WOD-computed climatologies discussed above. See Supporting Information - Data Coverage for a discussion of the effects of spatially and temporally variable amounts of data on our results.

3.3.3 Thermocline depth (TCD) calculations

One potential driver of near-surface oxygen variability is changes in the vertical structure of differentiated water masses. Subsurface temperature data is much more plentiful than that of O_2 (see Supporting Information - Data Coverage), and thermo- and oxycline depths covary strongly throughout the Tropical Pacific; we therefore use variations in thermocline depth (TCD) alone to represent the vertical movements of water masses with distinct temperature and oxygen signatures. TCD was calculated from depth-resolved monthly mean temperature maps (Fig. 3.1, 3.3-3.4; Supp. Fig. 3.4, 3.6d, 3.9b,d,f,h) and profiles (Table 3.1) using the variable representative isotherm method, as recommended for tropical waters by Fiedler (2010), who compared several objective methods of computing TCD with empirical TCD estimates made by eye. Other objective methods of computing TCD, such as the depth of the 20°C isotherm or the depth of the maximum vertical gradient in temperature, led to similar results here. In addition to its computational efficiency, the advantage of the variable representative isotherm method is that it accounts for the wide range of temperatures in which the thermocline occurs, since there is no single isotherm that well represents empirical TCDs (e.g., empirical thermocline temperatures range from 16 to 26°C within the Tropical Pacific alone) (Fiedler, 2010). According to the variable representative isotherm method, the thermocline spans the water column from the base of the mixed layer to the depth at which temperature has dropped halfway toward the

temperature at 400 m; TCD is then defined as the midpoint of this layer. Mathematically, the isotherm at which the TCD occurs is as follows:

T(thermocline representative isotherm) = T(MLD) – 0.25 [T(MLD) – T(400 m)], where T(MLD) = SST – 0.8°C.

3.3.4 ENSO definition and index

All variables (either binned onto 5°-by-5° monthly mean maps or spatially averaged over specified regions) were examined for ENSO-related variability using the Oceanic Niño Index (ONI). ONI is calculated as the three-month running mean of sea surface temperature anomalies in the Niño 3.4 region (5°N-5°S, 120°-170°W) (Huang et al., 2016). El Niño and La Niña periods occur when ONI is greater than 0.5°C and less than -0.5°C, respectively, for at least five consecutive three-month running-mean periods (Supp. Fig. 3.2). Time series of the Oceanic Niño Index (ONI) were downloaded from http://origin.cpc.ncep.noaa.gov/products/analysis_monitoring/ensostuff/ONI_v5.php on June 4th, 2018.

3.3.5 Statistical significance of spatial data

To avoid incorrect or overstated interpretations, we control our false discovery rate (FDR) whenever analyzing the results of multiple hypothesis tests. The FDR is defined as the statistically expected fraction of local (i.e., at a single grid point in the case of map analyses or within a single region in the case of comparisons across EEZs or other specified areas) null hypothesis test rejections for which the respective null hypotheses are actually true. Controlling

FDR in the context of multiple hypothesis tests thus requires smaller *p*-values compared to single hypothesis testing in order to reject local null hypotheses. The procedure for determining significance under a controlled FDR is as follows (Wilks, 2016): 1.) Sort the collection of *p*-values from *N* (i.e., the total number of grid points in the case of map analyses and the total number of regions in the case of comparisons across EEZs or other specified areas) local hypothesis tests p_i, with $i = 1, \ldots, N$, in ascending order. 2.) Reject local null hypotheses if their respective *p*-values are no larger than a threshold level p_{FDR}, which is equal to the largest p_i that is no larger than the fraction of α_{FDR} specified by i/N. p_{FDR} is thus calculated as follows: $p_{FDR} = \max[\, p_i : p_i \leq (i/N)\alpha_{FDR}]$, where α_{FDR} is the chosen FDR (expressed as a fraction). This method assumes that the multiple local tests are statistically independent, but is also valid even when the results of the multiple tests are strongly correlated (such as is the case with geospatial data). Indeed, when spatial correlations are high, the achieved FDR will be even smaller (stricter) than the chosen FDR (Ventura et al., 2004; Wilks, 2006), so that the chosen α_{FDR} should be approximately double the desired level when analyzing highly spatially correlated data grids (Wilks, 2016).

3.3.6 Code availability

The MATLAB code required to make all of the figures and tables generated here can be found at https://doi.org/10.5281/zenodo.2648131.

3.3.7 Data availability

Data in the form of *.mat files required to make all of the figures and tables generated here can be found at http://doi.org/10.5281/zenodo.2648124.

3.4 Results and discussion

3.4.1 ENSO-driven upper-ocean pO_2 and oxygenated vertical habitat variability

In the equatorial Pacific (between 7.5°N and 7.5°S), mean near-surface pO_2 differs substantially from east to west, with higher pO_2 values at any given depth in the west compared to the east (Fig. 3.1a; Supp. Fig. 3.3a-b). The mean oxycline, where pO_2 changes most quickly with depth, is located at around 100 m depth near the western boundary, descends to 150 m near the dateline, and shoals to around 50 m near the eastern boundary (Fig. 3.1a). Mean tuna hypoxic depth (THD; Fig. 3.1 solid gray contour) lies close to the oxycline across the entire basin. The within-oxycline vertical pO_2 gradient is strongest in the east, coincident with the top of the shallow oxygen minimum zone there.

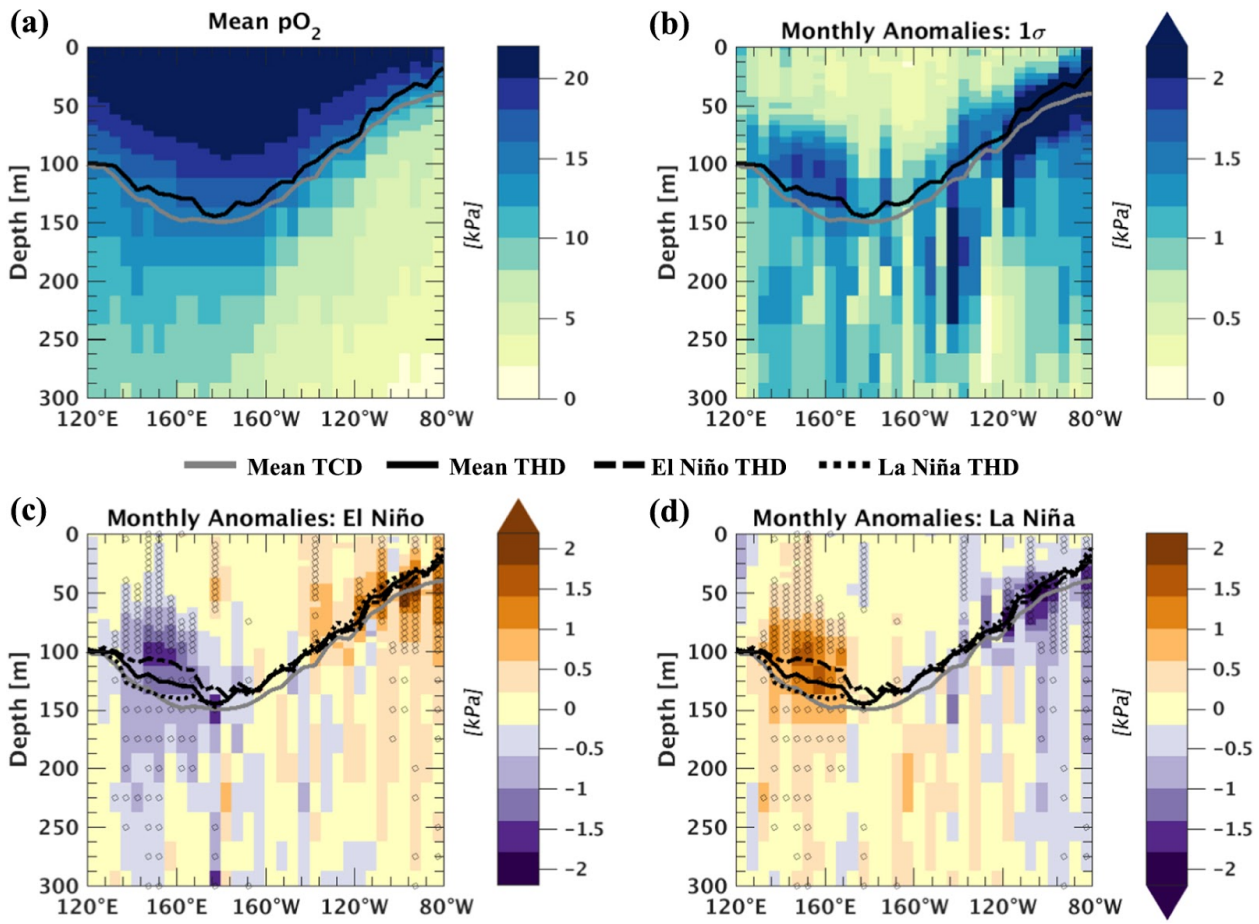

Figure 3.1 | Equatorial (7.5°N - 7.5°S) Pacific pO_2 means and variability between Jan 1955 and May 2017. a, Mean pO_2. b, Temporal standard deviation of monthly pO_2 anomalies. c, El Niño (ONI mean composite) pO_2 anomalies. d, La Niña (ONI mean composite) pO_2 anomalies. Contours of mean thermocline depth (TCD) are shown in gray. Contours of mean, El Niño, and La Niña tuna hypoxic depth (THD) are shown in black. Stippling (circles) on c and d indicate grid points where El Niño and La Niña composite pO_2 are significantly different from one another using a two-sided Wilcoxon rank-sum test and a multiple-hypothesis-test false discovery rate of 0.1 (see Methods – Statistical significance of spatial data for details).

Monthly variability in equatorial Pacific pO_2 shows distinct east-west differences as well (Fig. 3.1b; Supp. Fig. 3.3c-d). Near-surface pO_2 variability is greater in the east due to the presence of sharp vertical gradients in pO_2, with maximum variability occurring within the relatively shallow oxycline between 140°W and 80°W (Fig. 3.1b; Supp. Fig. 3.3c-d). pO_2 variability in the west, between the western boundary and 160°W, is about half as large as that in the east and is again greatest surrounding the local oxycline (Fig. 3.1b; Supp. Fig. 3.3c-d).

Interannual variability in near-surface pO_2 is driven primarily by ENSO throughout the Tropical Pacific. During El Niño, pO_2 decreases to the west of 160°W and increases to the east of 160°W throughout the upper water column (Fig. 3.1c; Supp. Fig. 3.3e-f). The opposite occurs during La Niña (Fig. 3.1d; Supp. Fig. 3.3g-h). In the east above the oxygen minimum zone, these results are in agreement with both field (Gutiérrez et al., 2008; Czeschel et al., 2012; Llanillo et al., 2013; Stramma et al., 2016; Graco et al., 2016) and model-based studies (Yang et al., 2017). In the west, the effects of ENSO on near-surface oxygen conditions have not been well-characterized before this study. In both the east and west, ENSO-driven pO_2 variability is greatest within the vicinity of the oxycline (around 100-150 m depth in the west and 50 m depth in the east) (Fig. 3.1c-d), as is the case for total interannual pO_2 variability (Fig. 3.1b). The ENSO-associated pO_2 variability dominates the total variability, in agreement with model results from Resplandy et al. (2015), who showed that ENSO is the major driver of interannual variations in Tropical Pacific air-sea oxygen fluxes within three Coupled Model Intercomparison Project 5 (CMIP5) Earth System Models (CESM1-BGC, GFDL-ESM2G, and GFDL-ESM2M).

Interannual variability in Tropical Pacific THD is also driven primarily by ENSO. Relative ENSO-driven THD variations are greatest from the western boundary (around 125°E) to 160°W and from 130°W to the eastern boundary (around 80°W) (Fig. 3.2b-c). Within the western region (125°E to 160°W), THD is as much as 22 m shallower during El Niño versus mean conditions, and 34 m shallower during El Niño versus La Niña conditions (Fig. 3.1c-d contours). Averaged over the Western Equatorial Pacific box (WEP) defined in Fig. 3.2a, THD variations compress vertical habitat space by 10.3% (14.5 m) during El Niño (Fig. 3.2b; Table 3.1) and expand it by 9.5% (13.3 m) during La Niña (Fig. 3.2c; Table 3.1), compared to mean

conditions. Vertical habitat space is thus compressed by 27.8 m during El Niño relative to La Niña within the WEP ($p<0.05$, unequal variances t-test). In the east, ENSO acts in the opposite direction, shoaling THD during La Niña and deepening it during El Niño. Averaged over the Eastern Equatorial Pacific box (EEP) defined in Fig. 3.2a and compared to mean conditions, hypoxia-induced vertical habitat compression of 2.9% (1.1 m) occurs during La Niña (Fig. 3.2c; Table 3.1), while expansion of 12.9% (4.9 m) occurs during El Niño (Fig. 3.2b; Table 3.1). Vertical habitat space is thus compressed by about 6 m during La Niña relative to El Niño within the EEP ($p<0.05$, unequal variances t-test).

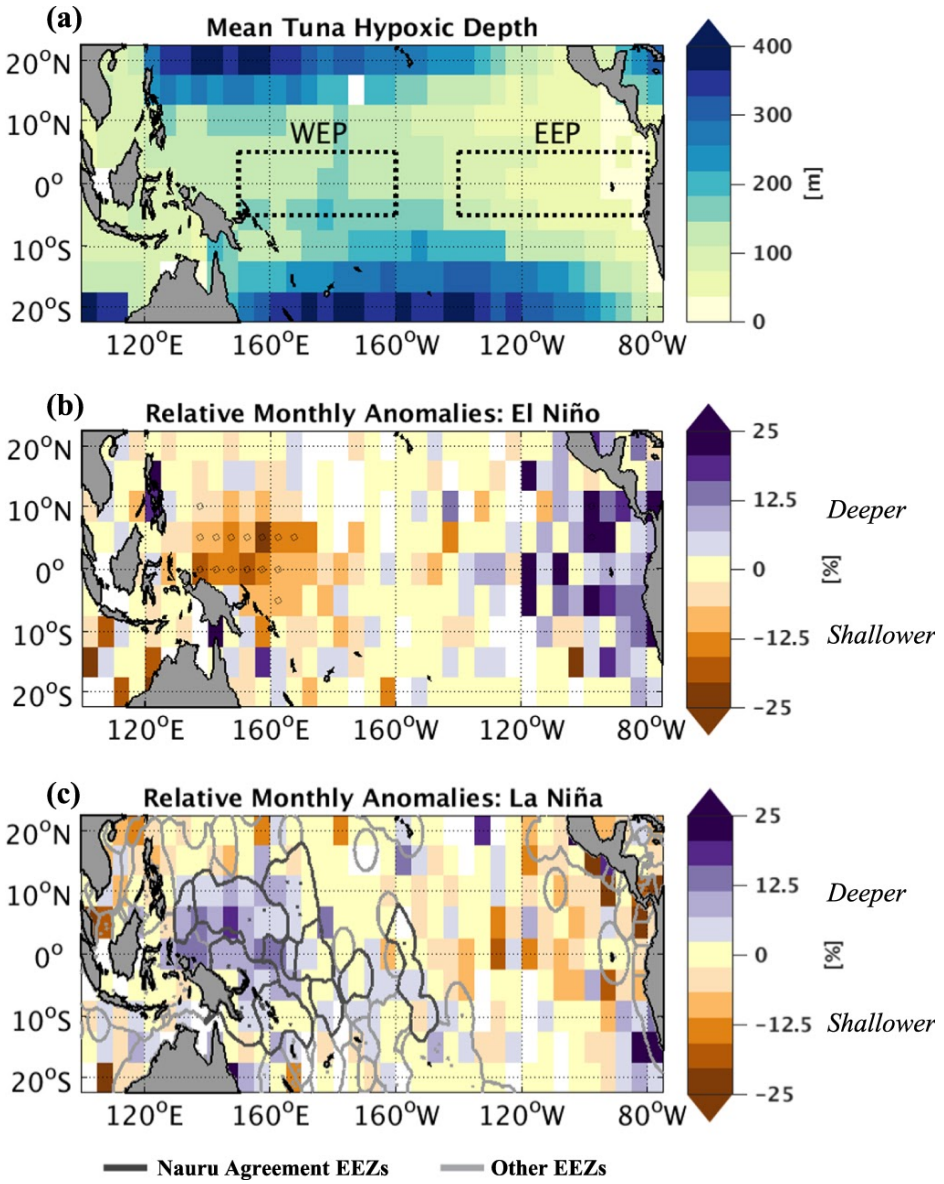

Figure 3.2 | ENSO-driven variations in tuna hypoxic depth (THD). a, Mean THD. Definitions of the Western Equatorial Pacific (WEP) and Eastern Equatorial Pacific (EEP) regions are denoted by the dashed black boxes. **b,** Relative El Niño (ONI mean composite) THD anomalies. Stippling (circles) on **c** and **d** indicate grid points where El Niño and La Niña composite pO_2 are significantly different from one another using a two-sided Wilcoxon rank-sum test and a multiple-hypothesis-test false discovery rate of 0.1. **c,** Relative La Niña (ONI mean composite) THD anomalies. Dark gray outlines denote the exclusive economic zones (EEZs) of the eight Parties to the Nauru Agreement (PNA). Light gray outlines denote the EEZs of all other countries in the region.

	WEP	EEP
Overall mean	THD: 140.5 m TCD: 148.7 m	THD: 38.3 m TCD: 51.7 m
El Niño mean (% change from overall mean)	THD: 126.0 m (-10.3%) TCD: 130.5 m (-12.2%)	THD: 43.2 m (+12.9%) TCD: 62.2 m (+20.4%)
La Niña mean (% change from overall mean)	THD: 153.8 m (+9.5%) TCD: 162.0 m (+9.0%)	THD: 37.2 m (-2.9%) TCD: 43.7 m (-15.6%)
All-profile THD vs. TCD regression coefficient	0.86 m/m (R^2 = 0.65)	0.94 m/m (R^2 = 0.67)
ENSO-driven THD vs. TCD regression coefficient	0.88 m/m	0.33 m/m

Table 3.1 | Thermocline depth (TCD) and tuna hypoxic depth (THD) variations and relationships. Mean and ENSO composite TCD and THD values within the Western Equatorial Pacific (WEP) and Eastern Equatorial Pacific (EEP) regions, as defined in Fig. 3.2a. All-profile THD vs. TCD regression coefficients are computed by relating THD and TCD anomalies from all simultaneous profiles (using iteratively reweighted least-squares with a bisquare weighting function and corresponding pseudo R^2 values – see Willett and Singer, 1988), and thus represent the magnitude of THD changes driven primarily by TCD changes alone. ENSO-driven THD vs. TCD regression coefficients are computed as the difference between El Niño and La Niña THD values divided by the difference between El Niño and La Niña TCD values, and thus represent the magnitude of ENSO-related THD changes driven by both ENSO-associated TCD and isopycnal pO_2 changes.

3.4.2 ENSO-associated mechanistic drivers of oxygen variability

Based on the observations analyzed here, ENSO-related variations in oxygenated tuna vertical habitat space appear to be driven primarily by the up-and-down motions of distinct water masses separated by well-defined thermo- and oxyclines. ENSO has different effects on the vertical positioning of these water masses and therefore thermocline depths (TCDs) depending on the region. In the WEP (as defined in Fig. 3.2a), El Niño shoals TCD by 12.2% (18.1 m) (Supp. Fig. 3.4b; Table 3.1), while La Niña deepens TCD by 9.0% (13.3 m) compared to mean

conditions (Supp. Fig. 3.4c; Table 3.1). TCD is thus approximately 31.5 m shallower during El Niño relative to La Niña within the WEP ($p<0.05$, unequal variances t-test). Within the EEP (as defined in Fig. 3.2a), El Niño deepens TCD by 20.4% (10.5 m) (Supp. Fig. 3.4b; Table 3.1), while La Niña shoals TCD by 15.6% (8.1 m) compared to mean conditions (Supp. Fig. 3.4c; Table 3.1). TCD is thus about 18.5 m shallower during La Niña relative to El Niño within the EEP ($p<0.05$, unequal variances t-test).

The strongest temporal correlations between pO_2 and TCD (Fig. 3.3a) occur at depths surrounding the mean thermocline, where both pO_2 and TCD variability are largest (Fig. 3.1b-d; Fig. 3.3a). The prevalence of these strong positive correlations between pO_2 and TCD, in addition to the strong positive correlations between THD and TCD throughout the Tropical Pacific (Fig. 3.3b; Table 3.1), suggest the following: as the thermocline deepens, hypoxic waters beneath the thermocline are pushed downward, expanding oxygenated vertical habitat space and increasing pO_2 in the upper water column; conversely, as the thermocline shoals, hypoxic waters beneath the thermocline are pulled upward, compressing oxygenated vertical habitat space and decreasing pO_2 in the upper water column.

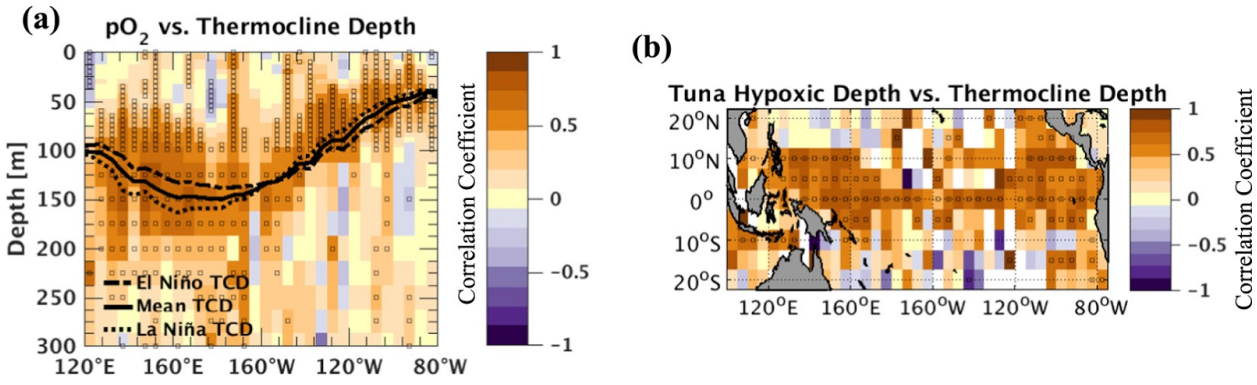

Figure 3.3 | Thermocline depth (TCD)-driven pO_2 and tuna hypoxic depth (THD) variations. a, Equatorial (7.5°N - 7.5°S) temporal correlation coefficients between monthly pO_2 (varies with depth) and TCD (constant with depth) anomalies. Contours of mean, El Niño (ONI mean composite), and La Niña (ONI mean composite) TCD are shown in black. **b,** Temporal correlation coefficients between monthly THD and TCD anomalies. Stippling (circles) on **a** and **b** indicate grid points where the correlation coefficient is significantly different from zero using a multiple-hypothesis-test false discovery rate of 0.1.

Though first-order variations in THD anomalies are well-explained by the up-and-down motions of the thermocline and accompanying water masses, concurrent changes in pO_2 along isopycnals within the thermocline—caused by changes in primary production and physical transport—can either reinforce or dampen this primary effect (isopycnals are roughly equivalent to isothermals in the Tropical Pacific because density below the mixed layer is primarily determined by temperature there). During El Niño, decreases in equatorial primary and export production in the east should decrease microbial oxygen consumption and thus *increase* pO_2 along isopycnals; in the west, increases in local production and export should lead to a *decrease* in pO_2 along isopycnals. During La Niña, these conditions should reverse (Chavez et al., 1999; Behrenfeld, et al., 2001; Lehodey, 2001). Contrary to these expectations, however, isopycnal pO_2 within the thermocline *decreases* in the east and *increases* in the west during El Niño (Fig. 3.4b; Supp. Fig. 3.5b), with the opposite occurring during La Niña (Fig. 3.4c; Supp. Fig. 3.5c). The isopycnal pO_2 variations observed here are therefore likely caused by ENSO-associated changes in lateral ventilation and transport within the thermocline rather than local changes in primary production. ENSO-associated lateral transport changes are, in turn, likely driven by variations in the strength of subsurface zonal currents, the most important being the Equatorial Undercurrent (EUC). The EUC carries oxygen-rich water from the subtropics and western Pacific to the central and eastern Pacific along the thermocline (Stramma et al., 2010), and undergoes large variations in strength associated with ENSO (Johnson et al., 2000; Izumo, 2005). During the 1997/98 El Niño, for instance, EUC mass transport (measured along the equator at 140°W) dropped to nearly zero from a mean of around 34 Sv (Izumo, 2005). Decreases in EUC strength of this magnitude greatly reduce within-thermocline transport of oxygen from the western to the

central and eastern equatorial Pacific during El Niño. Increases in EUC strength during La Niña, on the other hand, bring anomalously large amounts of oxygen from the west to the east, raising and lowering within-thermocline isopycnal pO_2 values in the east and west, respectively. During both ENSO phases, these transport-driven isopycnal oxygen changes dampen and oppose the effects of TCD variations, but because they have much a weaker impact on pO_2 and THD, the vertical movement of water masses remains the dominant factor influencing ENSO-associated pO_2 and THD anomalies.

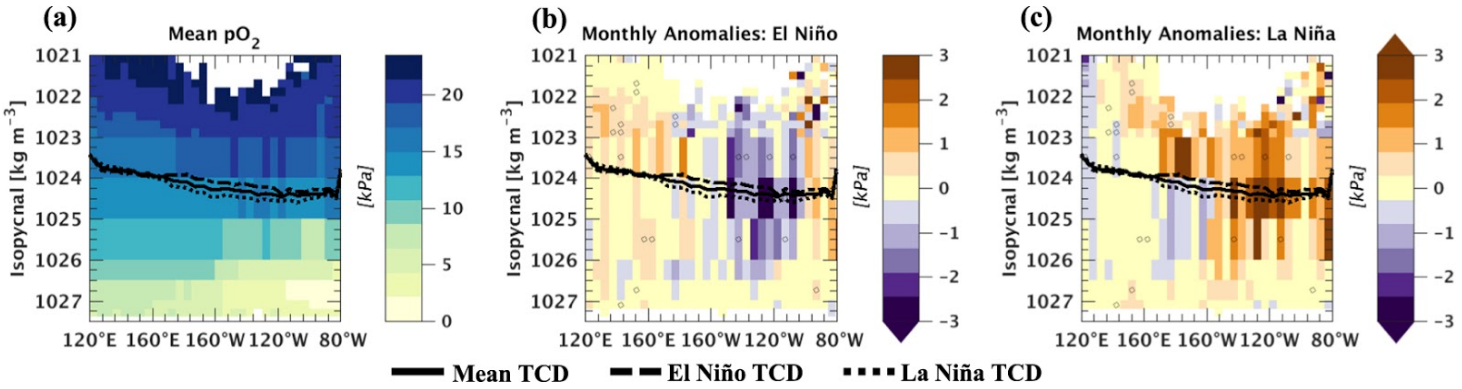

Figure 3.4 | Equatorial (7.5°N - 7.5°S) Pacific isopycnal pO_2 means and variability (analogous to Figure 1 plotted in depth space). a, Mean pO_2 along isopycnals. **b,** El Niño (ONI mean composite) isopycnal pO_2 anomalies. **d,** La Niña (ONI mean composite) isopycnal pO_2 anomalies. Contours of mean, El Niño, and La Niña thermocline depth (TCD) are shown in black. Stippling (circles) on **b** and **c** indicate isopycnal grid points where El Niño and La Niña composite pO_2 are significantly different from one another using a two-sided Wilcoxon rank-sum test and a multiple-hypothesis-test false discovery rate of 0.1.

The effects of transport-driven changes on ENSO-related THD and pO_2 variations are particularly small in the western Pacific (Fig. 3.4b-c). As a result, ENSO-induced TCD variations alone can accurately predict concomitant THD variations, leading to comparable all-profile and ENSO-driven THD vs. TCD regression coefficients within the WEP (Table 3.1). All-profile THD vs. TCD regression coefficients are computed by relating THD and TCD anomalies from all simultaneous profiles, and thus represent the magnitude of THD changes driven primarily by changes in TCD. ENSO-driven THD vs. TCD regression coefficients are

computed as the difference between El Niño and La Niña THD values divided by the difference between El Niño and La Niña TCD values, and thus represent the magnitude of ENSO-related THD changes driven by both ENSO-associated TCD *and* isopycnal pO_2 changes. In contrast to the situation in the west, ENSO-driven variations in eastern Pacific, within-thermocline isopycnal pO_2 noticeably dampen the THD variations induced by vertical shifts in water masses and TCD (Fig. 3.4b-c). Because of this, variations in TCD alone (that is, not accounting for within-thermocline isopycnal pO_2 changes) slightly overpredict differences in THD between ENSO phases within the EEP, as evidenced by a larger all-profile THD vs. TCD regression coefficient compared to the ENSO-driven one here (Table 3.1). Despite the noticeable dampening effect of physical transport changes on pO_2 and THD variations in the EEP, the up-and-down movements of water masses remain the primary factor driving ENSO-related pO_2 and THD variations, as can be seen from the net direction and sign of these variations. In sum, based on observations alone, the vertical motions of the thermocline appear to be the main driver of ENSO-induced variations in near-surface pO_2 and THD throughout the Tropical Pacific, while ventilation-driven variations in isopycnal pO_2 within the thermocline play an important (especially in the east) but secondary role. This is again in agreement with model results from Resplandy et al. (2015), who found that the main drivers of interannual variations in Tropical Pacific air-sea oxygen flux were changes in physical circulation and vertical transport rather than primary production.

3.4.3 Asymmetries between El Niño and La Niña

In both the WEP and EEP regions (as defined in Fig. 3.2a), El Niño induces greater deviations of tuna hypoxic depth (THD) from mean conditions compared to La Niña (Table 3.1), which is consistent with observed asymmetrical effects of ENSO on other well-studied climate phenomena (Hoerling et al., 1997; Kang and Kug, 2002; An et al., 2005). Averaged over the WEP, El Niño shoals THD by 14.5 m, while La Niña only deepens THD by 13.3 m (Table 3.1). In the EEP, El Niño deepens THD by 4.9 m, while La Niña only shoals THD and thus compresses tuna vertical habitat space by 1.1 m (Table 3.1). These asymmetric variations in THD are caused by corresponding asymmetric variations in thermocline depth (TCD) between opposing ENSO phases, such that ENSO-driven TCD changes are also larger during El Niño compared to La Niña within both the WEP and EEP regions (Table 3.1).

3.4.4 Oxygenated vertical habitat variability within western Tropical Pacific Exclusive Economic Zones (EEZs)

We now narrow our focus to the western Tropical Pacific both because it is the most tuna-rich region in the world and ENSO-driven oxygenated vertical habitat variations are most pronounced here. Tuna hypoxic depth (THD) variations of the magnitude observed here can significantly affect catchability and CPUE using common industrial surface fishing gear such as longlines and purse seines, potentially resulting in overfishing in years when vertical habitat space is compressed (Green, 1967; Barkley et al., 1978; Evans et al., 1981; Nakano et al., 1997; Prince and Goodyear, 2006; Bigelow and Maunder, 2007; Prince et al., 2010). Though tuna

occur throughout the Western and Central Pacific Ocean, approximately 60% of the total tuna catch in this region is taken from within the exclusive economic zones (EEZs) of only eight Pacific island nations that jointly enacted the Nauru Agreement to better manage their fisheries (Havice, 2013). Of the eight Parties to the Nauru Agreement (PNA), the EEZs belonging to Micronesia and the Marshall Islands undergo the greatest reductions in mean vertical habitat space during El Niño (14.0 m or 9.9% and 13.4 m or 7.9%, respectively), while the EEZs belonging to Palau, Papua New Guinea, and Nauru exhibit the greatest expansions in mean vertical habitat space during La Niña (14.3 m or 12.5%, 11.2 m or 8.1%, and 14.5 m or 11.1%, respectively) (Fig. 3.5). The EEZs of Palau, Micronesia, Nauru, and the Marshall Islands undergo the largest total mean ENSO-driven variations in vertical habitat space, with 19.5 m, 23.9 m, 19.5 and 19.3 m differences in THD between El Niño and La Niña, respectively (Fig. 3.5).

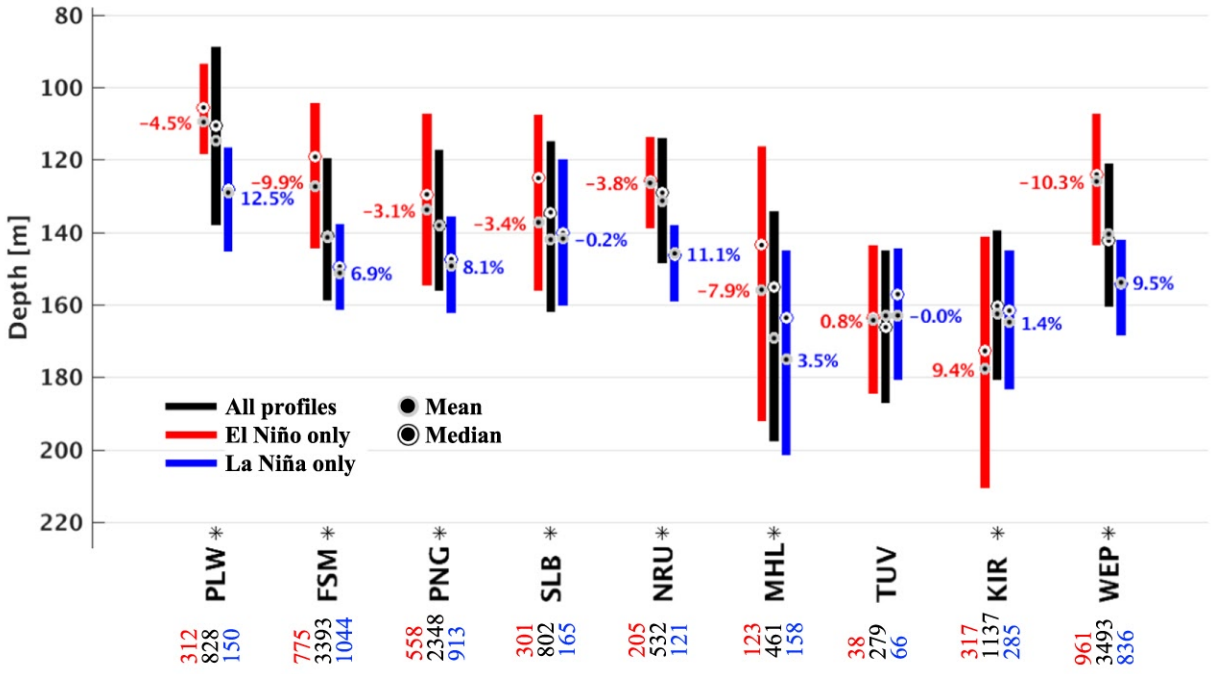

Figure 3.5 | ENSO-induced tuna hypoxic depth (THD) variations within Parties to the Nauru Agreement (PNA) exclusive economic zones (EEZs). Boxplot (without the whiskers) of THD distributions within the EEZ of

each PNA country (shown in Fig. 3.2c), as well as within the Western Equatorial Pacific (WEP) region (defined in Fig. 3.2a). From left to right, the PNA countries are roughly arranged from east to west. Percentage labels indicate relative deviations of El Niño (red) and La Niña (blue) composite means from the overall mean. Asterisks indicate when El Niño and La Niña composite THD are significantly different from one another within a given country's EEZ, using a two-sided Wilcoxon rank-sum test and a multiple-hypothesis-test false discovery rate of 0.05. The total number of THD measurements available from individual profiles in each EEZ is listed in black below the country names, while the number of measurements available during El Niño and La Niña are listed in red and blue, respectively.

3.5 Conclusions

Past work has demonstrated that temperature is an important predictor of Tropical Pacific tuna habitat suitability and migration towards the east during El Niño years (Lehodey et al., 1997), but the role of oxygen was previously underappreciated due to a lack of knowledge regarding its large-scale ENSO-driven variability. Here we have shown that oxygen-induced vertical habitat expansion in the east and compression in the west acts in the same direction as temperature to potentially push skipjack and yellowfin tuna eastward in times of El Niño (and especially so during an extreme El Niño), as they seek out available food sources and more favorable oxygen conditions. Temperature as well as pO_2 therefore likely play important roles in determining tuna spatial distributions with ENSO. The large ENSO-driven variations in oxygen content within the Tropical Pacific suggests that it may be important to account for interannual oxygen variability in predictions of skipjack and yellowfin tuna spatial distributions and stock assessments calculated from CPUE. Depending on the level of accuracy needed, the use of climatological mean oxygen values or long-term mean oxygen trends, may not be accurate or representative enough to capture ongoing tuna spatial dynamics, thresholds, or preferences of interest.

Here we have specifically defined vertical habitat availability in the Tropical Pacific using tuna hypoxic depth (THD) computed with a minimum oxygen threshold applicable to

skipjack and yellowfin tuna (15 kPa). THD can, however, also be used to define vertical habitats in other areas of the ocean and for other tuna species when computed with different species-specific thresholds. Bigeye tuna, for example, can spend considerably longer in low-oxygen waters than skipjack and yellowfin tuna (e.g., Lowe et al., 2000; Evans et al., 2008; Schaefer and Fuller, 2010), while albacore tuna have oxygen requirements more similar to those of skipjack and yellowfin tuna (e.g., Laurs and Lynn, 1977; Childers et al., 2011; Williams et al., 2015). THD variability for these other species may look very different from those for skipjack and yellowfin tuna, with variations in ocean oxygen content impacting their vertical habitats, catch rates, and stock assessments in different ways within different ocean regions. Within the Tropical Pacific, however, it is likely that ENSO impacts the oxygenated vertical habitat suitability of many tuna species, given its large effects on oxygen throughout the region.

With climate change, the frequency of extreme ENSO events is predicted to increase (Cai et al., 2014; Cai et al., 2015), potentially leading to greater variability in oxygenated vertical habitat space and therefore less stable year-to-year supplies of tuna and other large pelagic fish. Future warming may also shift the Tropical Pacific towards a more El Niño-like mean state (Vecchi et al., 2006; Zhang and Song, 2006; Vecchi and Soden, 2007; Collins et al., 2010; Huang and Ying, 2015; Ying et al., 2016). If these predictions are accurate, vertical habitat space will shrink in the west, pushing skipjack and yellowfin tuna eastward and upward and rendering them more vulnerable to overfishing with industrial surface fishing gear.

In the western Tropical Pacific, whether during El Niño years or more permanently under future climate change scenarios, habitat suitability changes and eastward migration of skipjack and yellowfin tuna out of western EEZs threaten food security from local tuna catch, economic

development from lucrative tuna canning and port operations, and government income from licensing fees paid by foreign fishing interests to access EEZ waters (Hamnett and Anderson, 2000; Moss, 2007; Guillotreau et al., 2012). Continued and increased *in situ* monitoring of oxygen in the Tropical Pacific is therefore crucial for detecting current and future changes in oxygen conditions that will affect the spatial distributions and populations of tuna and other pelagic fish. Because of the oftentimes dramatic societal impacts brought about by ENSO, changes in ENSO frequency and intensity, on top of changes in mean conditions, are of great immediate concern for Tropical Pacific societies. Future work should therefore analyze model-projected, climate warming-driven changes in ENSO-related oxygen variability and extremes.

3.6 Acknowledgements

This study was supported by a NASA Earth and Space Science Fellowship to S.L. L.T. also acknowledges support from NASA (Grant NNX17AH56G). M.J.M. is supported by NOAA. K.A.S. was supported by the Washington Research Foundation Fund for Innovation in Data-Intensive Discovery and the Moore/Sloan Data Science Environments Project. PMEL contribution no. 4953.

3.7 Supporting information

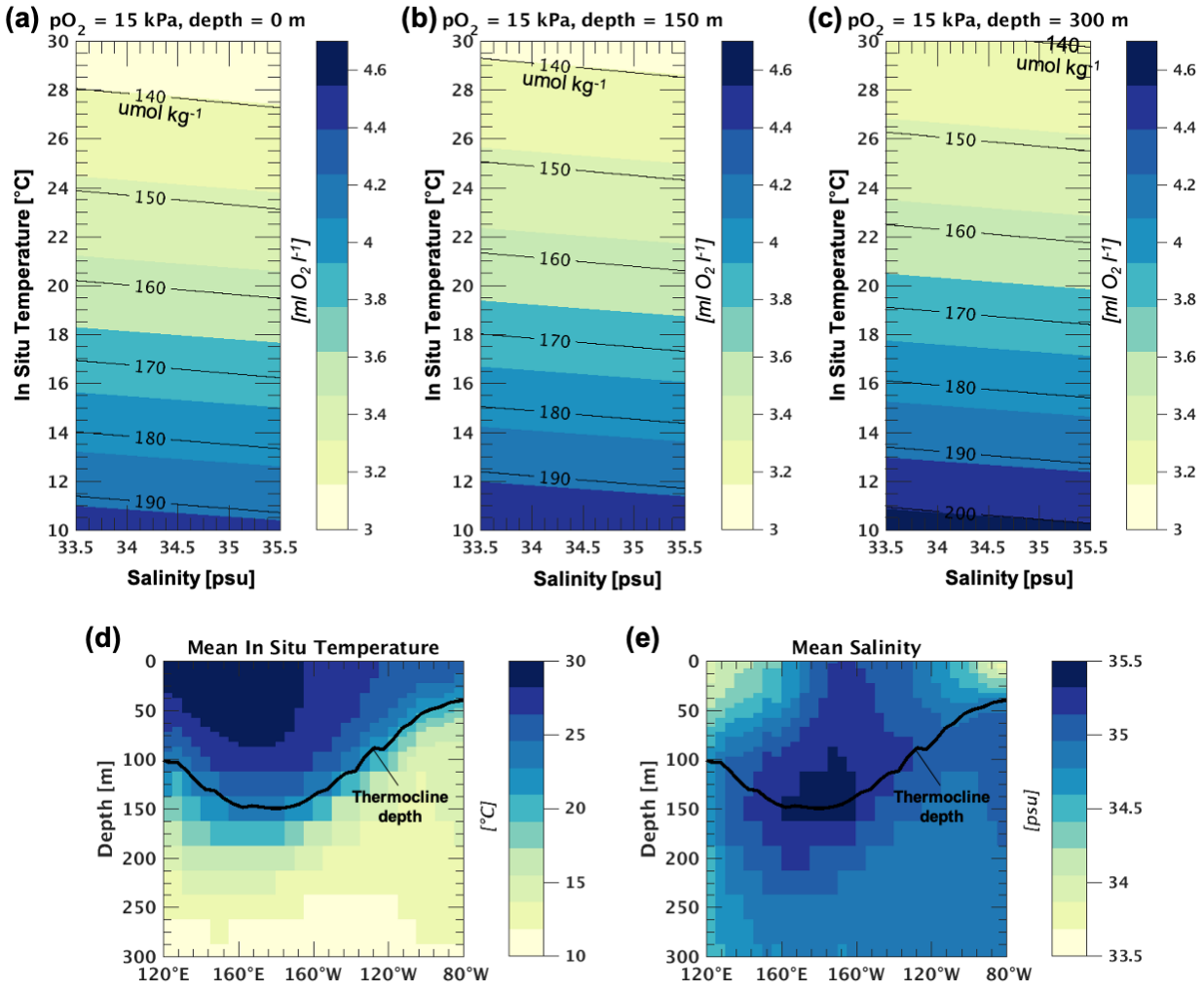

Supporting Figure 3.1 | Skipjack and yellowfin tuna hypoxic depth (THD) threshold (pO_2 = 15 kPa) expressed in dissolved oxygen concentrations across commonly encountered water column conditions. a,b,c, 15 kPa expressed in units of ml O_2 l^{-1} (colors) and umol O_2 kg^{-1} (contour lines) between *in situ* temperatures of 15-30°C and salinities of 33-36 psu, and at depths of 0 (**a**), 150 (**b**), and 300 m (**c**). pO_2 is converted to dissolved oxygen concentrations in units of ml l^{-1} using equations from Garcia and Gordon (1992) and Enns et al. (1965) (see Section 2.1 for details). Dissolved oxygen concentrations in units of ml l^{-1} are then converted to units of umol kg^{-1} by dividing the former by the molar volume of O_2 (22.3916 L mol^{-1}) and the potential density of seawater at the given *in situ* temperature and salinity. **d,e,** Equatorial (7.5°N - 7.5°S) Pacific mean (between Jan 1955 and May 2017) *in situ* temperature (**d**) and (**e**) salinity within the approximate depth ranges of skipjack and yellowfin tuna.

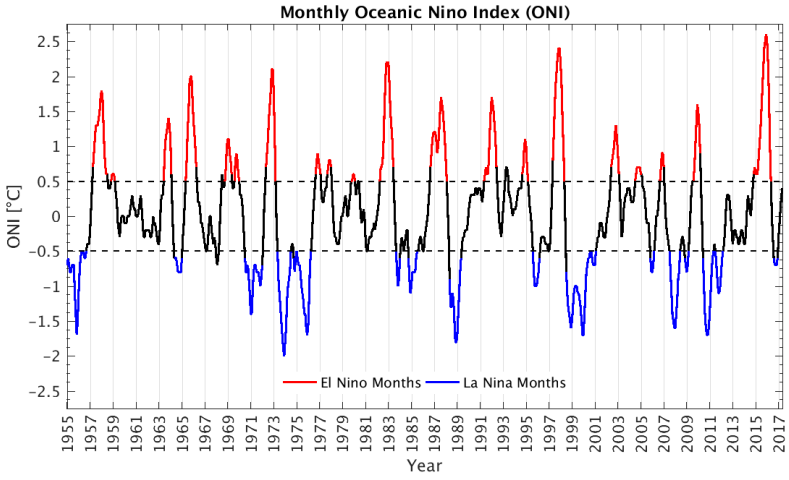

Supporting Figure 3.2 | Monthly Oceanic Niño Index (ONI) time series between Jan 1955 and May 2017. ONI is calculated as the three-month running mean of SST anomalies in the Niño 3.4 region (5°N-5°S, 120°-170°W). Five or more consecutive months with ONI>0.5°C and ONI<-0.5°C are classified as El Niño and La Niña periods, respectively.

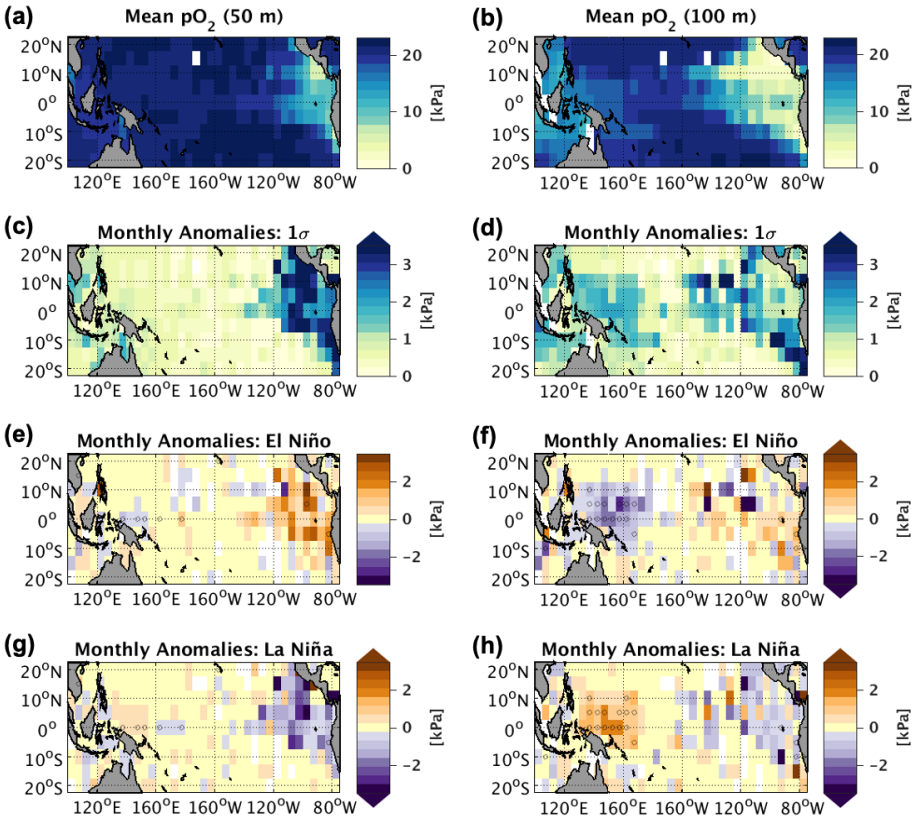

Supporting Figure 3.3 | Tropical Pacific pO_2 means and variability. a,b, Mean pO_2 at 50 (**a**) and 100 m depth (**b**). **c,d,** Temporal standard deviation of monthly pO_2 anomalies at 50 (**c**) and 100 m depth (**d**). **e,f,** Relative El Niño (ONI mean composite) pO_2 anomalies at 50 (**e**) and 100 m depth (**f**). **g,h,** Relative La Niña (ONI mean composite) pO_2 anomalies at 50 (**g**) and 100 m depth (**h**). Stippling (circles) on **e-h** indicate grid points where El Niño and La Niña composite pO_2 are significantly different from one another at the same depth, using a two-sided Wilcoxon rank-sum test and a multiple-hypothesis-test false discovery rate of 0.1.

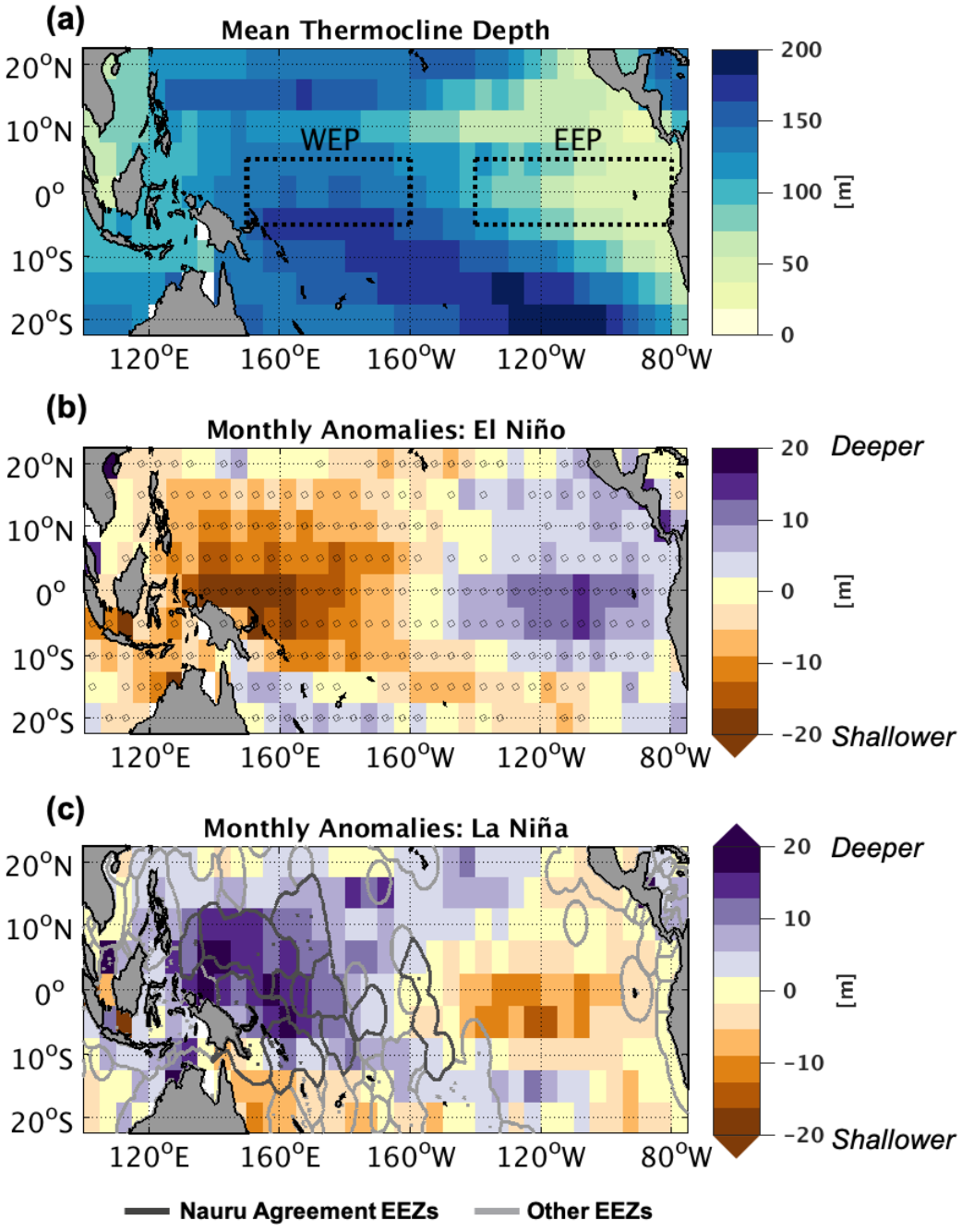

Supporting Figure 3.4 | ENSO-driven variations in thermocline depth (TCD). a, Mean TCD. **b,** Relative El Niño (ONI mean composite) TCD anomalies. **c,** Relative La Niña (ONI mean composite) TCD anomalies. Stippling (circles) on **b** and **c** indicate grid points where El Niño and La Niña composite TCD are significantly different from one another using a two-sided Wilcoxon rank-sum test and a multiple-hypothesis-test false discovery rate of 0.1.

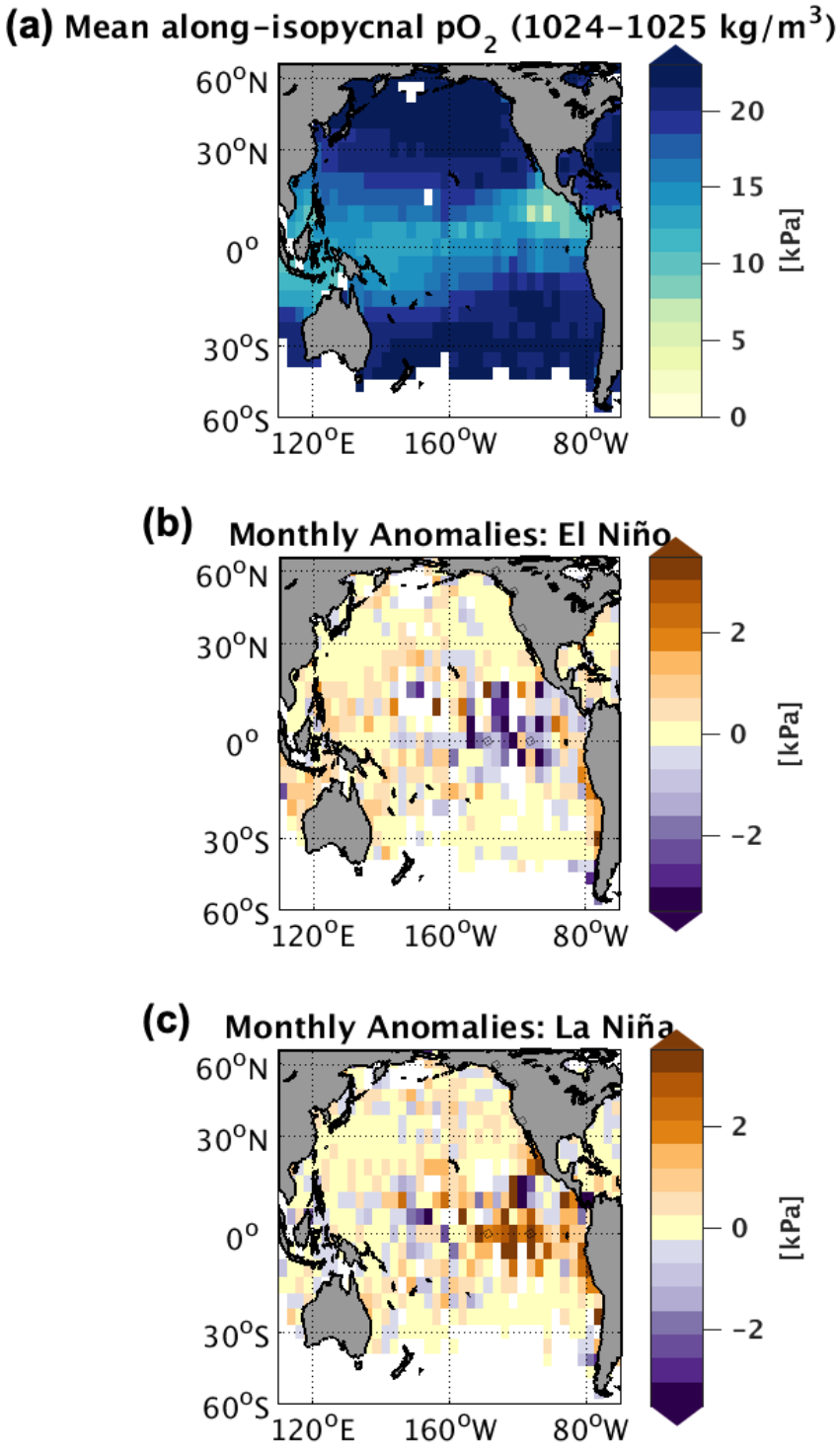

Supporting Figure 3.5 | ENSO-driven pO_2 variations along isopycnals within the thermocline (between 1024 and 1025 kg m^{-3}). a, Mean pO_2. **b,** Relative El Niño (ONI mean composite) pO_2 anomalies. **c,** Relative La Niña (ONI mean composite) pO_2 anomalies. Stippling (circles) on **b** and **c** indicate grid points where El Niño and La Niña composite isopycnal pO_2 are significantly different from one another using a two-sided Wilcoxon rank-sum test and a multiple-hypothesis-test false discovery rate of 0.1.

3.7.1 Data coverage

Supp. Fig. 3.6 gives an overview of data coverage in the equatorial Pacific over time, while Supp. Fig. 3.7, Supp. Fig. 3.8 and Supp. Fig. 3.9 show the number of data points specifically used to compute Table 3.1/Fig. 3.5's WEP values, Fig. 3.1/Fig. 3.3a, and Fig. 3.2/Supp. Fig. 3.4/Fig. 3.3b, respectively. There are many more measurements of temperature and salinity compared to O_2 at virtually all times and locations. Because O_2 measurements are sparse, calculated pO_2 data are, too, though they are relatively evenly distributed in time between 1955 and 2017 (Supp. Fig. 3.6a-c). Overall, there are similar numbers of pO_2 measurements made during El Niño and La Niña (Supp. Fig. 3.7a-b; Supp. Fig. 3.8b; Supp. Fig. 3.9g). In general, there are more pO_2 data points close to land, near the eastern and western boundaries (Supp. Fig. 3.6a-c; Supp. Fig. 3.8a,c-d; Supp. Fig. 3.9a,c,e).

Unlike pO_2, temperature measurements in the Tropical Pacific are relatively unevenly distributed in time with the majority of temperature measurements taken after 1980 (Supp. Fig. 3.6d). As was alluded to above, there are many more measurements of temperature than pO_2 at essentially all times and locations (Supp. Fig. 3.6; Supp. Fig. 3.7; Supp. Fig. 3.9a-f), such that the amount of data used in analyses of relationships between pO_2 and temperature-derived variables are typically limited by the availability of O_2 rather than temperature measurements. The number of temperature observations taken during El Niño are similar to those taken during La Niña (Supp. Fig. 3.7a-b; Supp. Fig. 3.9h). Spatially, observations of temperature are more evenly distributed than those of pO_2 and do not necessarily favor regions closer to land (Supp. Fig. 3.6d; Supp. Fig. 3.9b,d,f).

Taken together, the spatiotemporal distribution of observations discussed above suggests the following: 1) Uncertainties associated with composite or average pO_2 and pO_2-derived variables are greater than those associated with temperature and temperature-derived variables because there are many more measurements of temperature than pO_2; 2) Composites and averages of temperature and temperature-derived variables may be more representative of conditions since 1980, whereas pO_2 composites and averages may be more representative of conditions over a longer period (i.e., 1955-2017) because the relatively even distribution of O_2 measurements in time; 3) Uncertainties associated with El Niño and La Niña temperature and temperature-derived composites are similar in magnitude, owing to a similar number of temperature observations during the two opposing phases; 4) Uncertainties associated with El Niño and La Niña pO_2 and pO_2-derived composites are similar in magnitude, owing to a similar number of O_2 observations during the two phases; 5) Composite pO_2 and pO_2-derived values closer to land in the far eastern and western edges of the Tropical Pacific are less uncertain due to the greater availability of measurements there; 6) pO_2 averages over the WEP and EEP regions are slightly weighted towards the coastal regions due to the increasing number of O_2 observations as one approaches land.

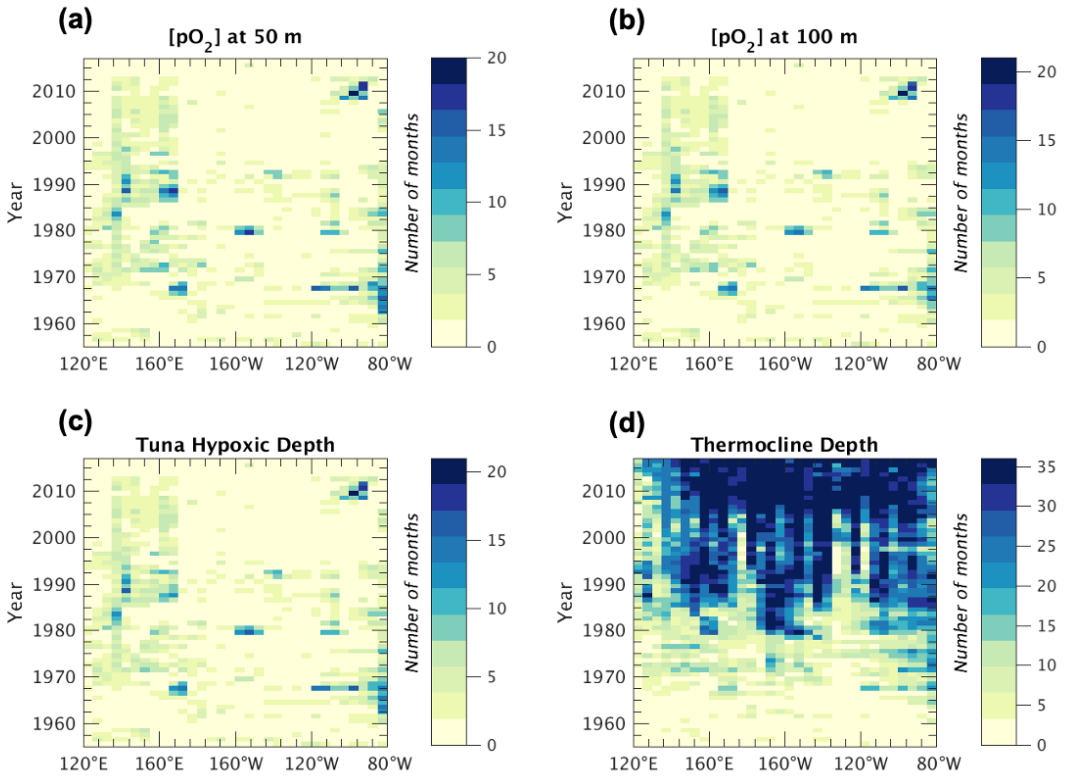

Supporting Figure 3.6 | Spatiotemporal distribution of measurements in the equatorial Pacific (7.5°N - 7.5°S). **a-d,** Number of months of available data between 7.5°N and 7.5°S as a function of time and longitude for pO_2 at 50 m depth (**a**), pO_2 at 100 m depth (**b**), tuna hypoxic depth (THD) (**c**), and thermocline depth (TCD) (**d**).

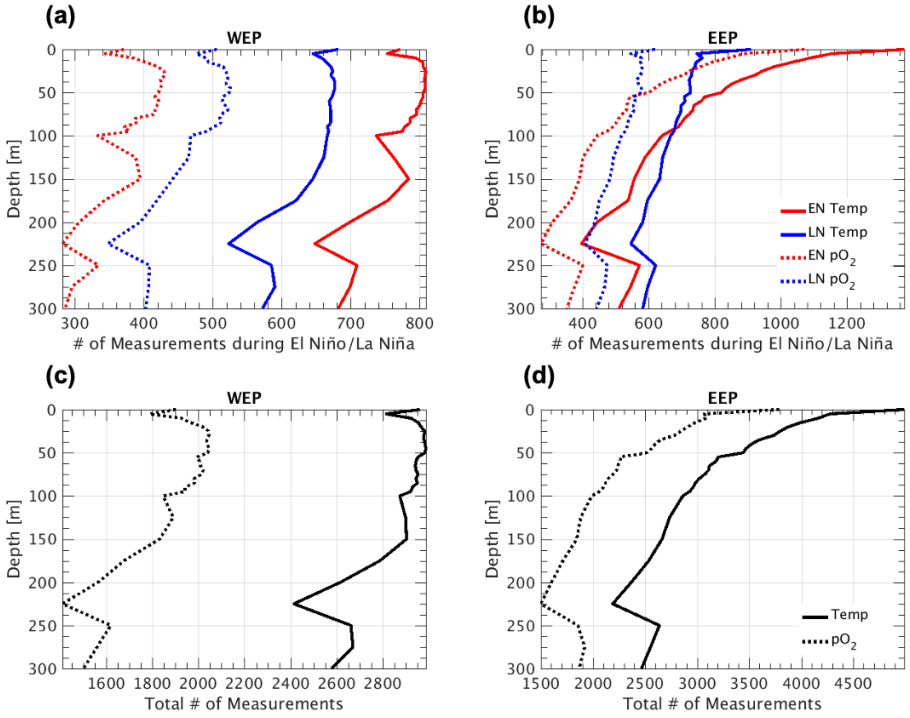

Supporting Figure 3.7 | pO_2 and temperature data availability in the West (WEP) and East (EEP) Equatorial Pacific (corresponding to Table 3.1 and Fig. 3.5). a,b, The number of pO_2 and temperature measurements used to compute El Niño and La Niña composite pO_2 and temperature profiles in the WEP (**a**) and EEP (**b**). **c,d,** The number of pO_2 and temperature measurements used to compute mean pO_2 and temperature profiles in the WEP (**e**) and EEP (**f**).

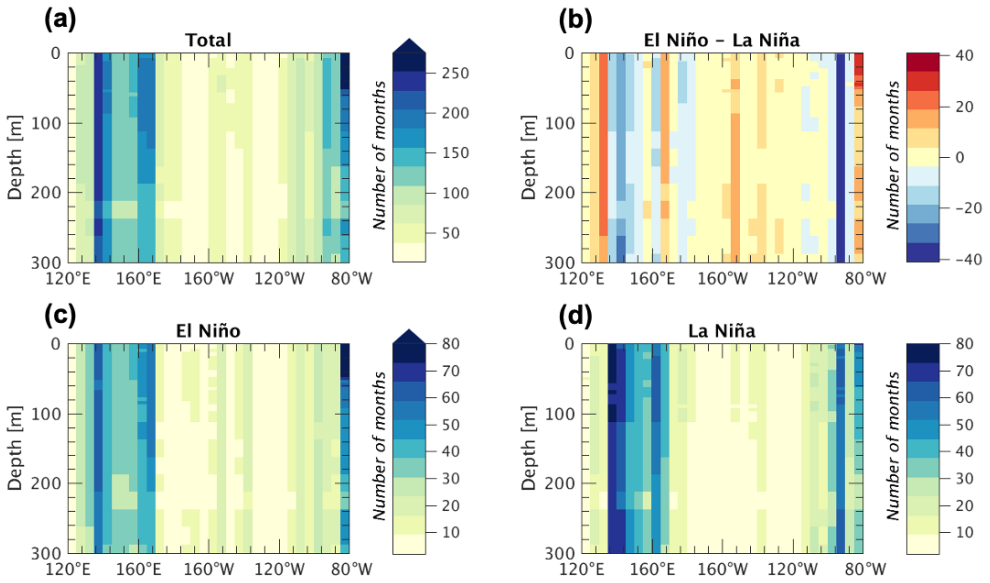

Supporting Figure 3.8 | Equatorial Pacific (7.5°N - 7.5°S) pO_2 data availability (corresponding to Fig. 3.1 and Fig. 3.3a). a,c,d, Number of months of data available between 7.5°N and 7.5°S as a function of depth and longitude for pO_2 in total (**a**), during El Niño (**c**), and during La Niña (**d**). **b,** Difference in the number of months of pO_2 data available during El Niño and La Niña (**c** minus **d**).

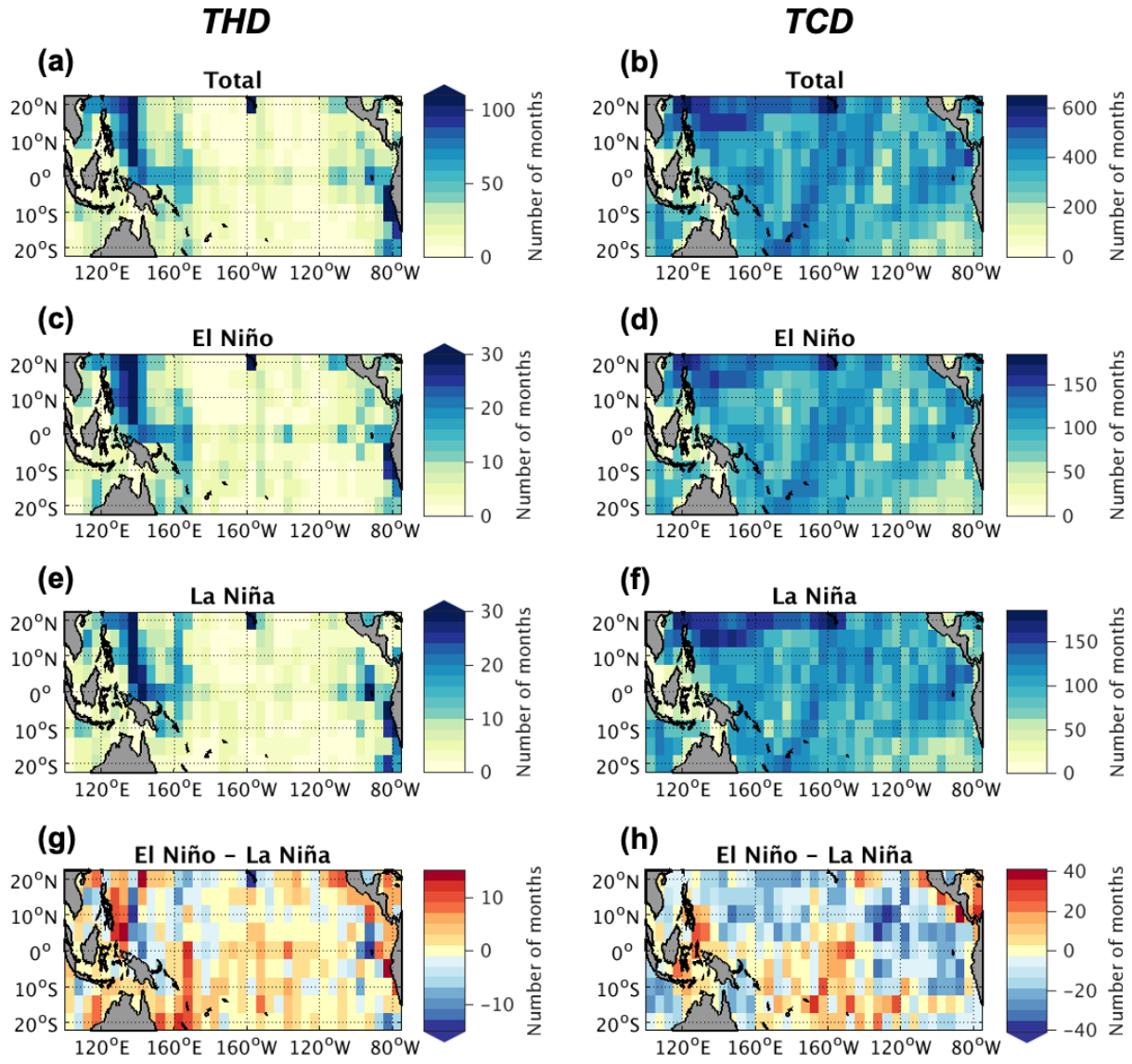

Supporting Figure 3.9 | Tropical Pacific tuna hypoxic depth (THD) and thermocline depth (TCD) data availability (corresponding to Fig. 3.2, Supp. Fig. 3.3, and Fig. 3.3b). a-f, Number of months of data available as a function of latitude and longitude for THD and TCD, respectively, in total (**a,b**), during El Niño (**c,d**), and during La Niña (**e,f**). **g,h,** Difference in the number of months of data available for THD (**g**) and TCD (**h**) during El Niño and La Niña (**c** minus **d, d** minus **f**).

3.8 References

An, S.-I., Ham, Y.-G., Kug, J.-S., Jin, F.-F., & Kang, I.-S. (2005). El Niño–La Niña Asymmetry in the Coupled Model Intercomparison Project Simulations. *Journal of Climate*, *18*(14), 2617–2627. https://doi.org/10.1175/JCLI3433.1

Arrizabalaga, H., Dufour, F., Kell, L., Merino, G., Ibaibarriaga, L., Chust, G., et al. (2015). Global habitat preferences of commercially valuable tuna. *Deep Sea Research Part II: Topical Studies in Oceanography*, *113*, 102–112. https://doi.org/10.1016/j.dsr2.2014.07.001

Badjeck, M.-C., Allison, E. H., Halls, A. S., & Dulvy, N. K. (2010). Impacts of climate variability and change on fishery-based livelihoods. *Marine Policy*, *34*(3), 375–383. https://doi.org/10.1016/j.marpol.2009.08.007

Barkley, R. A., Neill, W. H., & Gooding, R. M. (1978). Skipjack tuna, Katsuwonus pelamis, habitat based on temperature and oxygen requirements. *Fishery Bulletin*, *76*(3). Retrieved from https://swfsc.noaa.gov/publications/CR/1978/7804.PDF

Barnett, J. (2011). Dangerous climate change in the Pacific Islands: food production and food security. *Regional Environmental Change*, *11*(1), 229–237. https://doi.org/10.1007/s10113-010-0160-2

Behrenfeld, M. J., Randerson, J. T., McClain, C. R., Feldman, G. C., Los, S. O., Tucker, C. J., et al. (2001). Biospheric Primary Production During an ENSO Transition. *Science*, *291*(5513), 2594–2597. https://doi.org/10.1126/science.1055071

Bertrand, A., Chaigneau, A., Peraltilla, S., Ledesma, J., Graco, M., Monetti, F., & Chavez, F. P. (2011). Oxygen: A Fundamental Property Regulating Pelagic Ecosystem Structure in the Coastal Southeastern Tropical Pacific. *PLOS ONE*, *6*(12), e29558. https://doi.org/10.1371/journal.pone.0029558

Bigelow, K. A., & Maunder, M. N. (2007). Does habitat or depth influence catch rates of pelagic species? *Canadian Journal of Fisheries and Aquatic Sciences*, *64*(11), 1581–1594. https://doi.org/10.1139/f07-115

Bigelow, K. A., Hampton, J., & Miyabe, N. (2002). Application of a habitat-based model to estimate effective longline fishing effort and relative abundance of Pacific bigeye tuna (Thunnus obesus). *Fisheries Oceanography*, *11*(3), 143–155. https://doi.org/10.1046/j.1365-2419.2002.00196.x

Block, B. A., Jonsen, I. D., Jorgensen, S. J., Winship, A. J., Shaffer, S. A., Bograd, S. J., et al. (2011). Tracking apex marine predator movements in a dynamic ocean. *Nature*, *475*(7354), 86–90. https://doi.org/10.1038/nature10082

Bopp, Resplandy, L., Orr, J. C., Doney, S. C., Dunne, J. P., Gehlen, M., et al. (2013). Multiple stressors of ocean ecosystems in the 21st century: projections with CMIP5 models. *Biogeosciences*, *10*(10), 6225–6245. https://doi.org/10.5194/bg-10-6225-2013

Boyer, T. P., Antonov, J. I., Baranova, O. K., Coleman, C., Garcia, H. E., Grodsky, A., et al. (2013). World Ocean Database 2013. National Environmental Satellite and Data Information Service (NESDIS). Retrieved from http://doi.org/10.7289/V5NZ85MT

Brill, R. W., & Lutcavage, M. E. (2001). Understanding Environmental Influences on Movements and Depth Distributions of Tunas and Billfishes Can Significantly Improve Population Assessments. *American Fisheries Society Symposium*, *25*, 179–198.

Brill, Richard W. (1994). A review of temperature and oxygen tolerance studies of tunas pertinent to fisheries oceanography, movement models and stock assessments. *Fisheries Oceanography*, *3*(3), 204–216. https://doi.org/10.1111/j.1365-2419.1994.tb00098.x

Bushnell, P. G., & Brill, R. W. (1991). Responses of Swimming Skipjack (Katsuwonus pelamis) and Yellowfin (Thunnus albacares) Tunas to Acute Hypoxia, and a Model of Their Cardiorespiratory Function. *Physiological Zoology*, *64*(3), 787–811.

Bushnell, Peter. G., Brill, R. W., & Bourke, R. E. (1990). Cardiorespiratory responses of skipjack tuna (Katsuwonus pelamis), yellowfin tuna (Thunnus albacares), and bigeye tuna (Thunnus obesus) to acute reductions of ambient oxygen. *Canadian Journal of Zoology*, *68*(9), 1857–1865. https://doi.org/10.1139/z90-265

Cabré, A., Marinov, I., Bernardello, R., & Bianchi, D. (2015). Oxygen minimum zones in the tropical Pacific across CMIP5 models: mean state differences and climate change trends. *Biogeosciences*, *12*(18), 5429–5454. https://doi.org/10.5194/bg-12-5429-2015

Cai, W., Borlace, S., Lengaigne, M., van Rensch, P., Collins, M., Vecchi, G., et al. (2014). Increasing frequency of extreme El Niño events due to greenhouse warming. *Nature Climate Change*, *4*(2), 111–116. https://doi.org/10.1038/nclimate2100

Cai, W., Wang, G., Santoso, A., McPhaden, M. J., Wu, L., Jin, F.-F., et al. (2015). Increased frequency of extreme La Niña events under greenhouse warming. *Nature Climate Change*, *5*(2), 132–137. https://doi.org/10.1038/nclimate2492

Chavez, F. P., Strutton, P. G., Friederich, G. E., Feely, R. A., Feldman, G. C., Foley, D. G., & McPhaden, M. J. (1999). Biological and Chemical Response of the Equatorial Pacific Ocean to the 1997-98 El Niño. *Science*, *286*(5447), 2126–2131. https://doi.org/10.1126/science.286.5447.2126

Childers, J., Snyder, S., & Kohin, S. (2011). Migration and behavior of juvenile North Pacific albacore (Thunnus alalunga). *Fisheries Oceanography*, *20*(3), 157–173. https://doi.org/10.1111/j.1365-2419.2011.00575.x

Cocco, V., Joos, F., Steinacher, M., Frölicher, T. L., Bopp, L., Dunne, J., et al. (2013). Oxygen and indicators of stress for marine life in multi-model global warming projections. *Biogeosciences*, *10*(3), 1849–1868. https://doi.org/info:doi:10.5194/bg-10-1849-2013

Cochrane, K., De Young, C., Soto, D., & Bahri, T. (2009). *Climate change implications for fisheries and aquaculture*. Rome: Food and Agriculture Organization of the United Nations. Retrieved from http://www.fao.org/fileadmin/user_upload/newsroom/docs/FTP530.pdf

Collins, M., An, S.-I., Cai, W., Ganachaud, A., Guilyardi, E., Jin, F.-F., et al. (2010). The impact of global warming on the tropical Pacific Ocean and El Niño. *Nature Geoscience*, *3*(6), 391–397. https://doi.org/10.1038/ngeo868

Czeschel, R., Stramma, L., & Johnson, G. C. (2012). Oxygen decreases and variability in the eastern equatorial Pacific. *Journal of Geophysical Research: Oceans*, *117*(C11). https://doi.org/10.1029/2012JC008043

Deser, C., Alexander, M. A., Xie, S.-P., & Phillips, A. S. (2010). Sea Surface Temperature Variability: Patterns and Mechanisms. *Annual Review of Marine Science*, *2*(1), 115–143. https://doi.org/10.1146/annurev-marine-120408-151453

Dueri, S., Bopp, L., & Maury, O. (2014). Projecting the impacts of climate change on skipjack tuna abundance and spatial distribution. *Global Change Biology*, *20*(3), 742–753. https://doi.org/10.1111/gcb.12460

Dufresne, J.-L., Foujols, M.-A., Denvil, S., Caubel, A., Marti, O., Aumont, O., et al. (2013). Climate change projections using the IPSL-CM5 Earth System Model: from CMIP3 to CMIP5. *Climate Dynamics*, *40*(9), 2123–2165. https://doi.org/10.1007/s00382-012-1636-1

Enns, T., Scholander, P. F., & Bradstreet, E. D. (1965). Effect of Hydrostatic Pressure on Gases Dissolved in Water. *The Journal of Physical Chemistry*, *69*(2), 389–391. https://doi.org/10.1021/j100886a005

Evans, K., Langley, A., Clear, N. P., Williams, P., Patterson, T., Sibert, J., et al. (2008). Behaviour and habitat preferences of bigeye tuna (Thunnus obesus) and their influence on longline fishery catches in the western Coral Sea. *Canadian Journal of Fisheries and Aquatic Sciences*, *65*(11), 2427–2443. https://doi.org/10.1139/F08-148

Evans, R. H., McLain, D. R., & Bauer, R. A. (1981). Atlantic skipjack tuna: influences of mean environmental conditions on their vulnerability to surface fishing gear. *Marine Fisheries Review*, *43*(6). Retrieved from https://spo.nmfs.noaa.gov/sites/default/files/pdf-content/MFR/mfr436/mfr4361.pdf

Fiedler, P. C. (2010). Comparison of objective descriptions of the thermocline. *Limnology and Oceanography: Methods*, *8*(6), 313–325. https://doi.org/10.4319/lom.2010.8.313

Frölicher, T. L., Joos, F., Plattner, G.-K., Steinacher, M., & Doney, S. C. (2009). Natural variability and anthropogenic trends in oceanic oxygen in a coupled carbon cycle–climate model ensemble. *Global Biogeochemical Cycles*, *23*(1). https://doi.org/10.1029/2008GB003316

Garcia, H. E., Locarnini, R. A., Boyer, T. P., Antonov, J. I., Mishonov, A. V., Baranova, O. K., et al. (2013). *World Ocean Atlas Volume 3: Dissolved Oxygen, Apparent Oxygen Utilization, and Oxygen Saturation* (No. NOAA Atlas NESDIS 75) (p. 40). Silver Spring, Maryland: National Oceanographic Data Center. Retrieved from https://data.nodc.noaa.gov/woa/WOA13/DOC/woa13_vol3.pdf

Garcia, Herncin E., & Gordon, L. I. (1992). Oxygen solubility in seawater: Better fitting equations. *Limnology and Oceanography*, *37*(6), 1307–1312. https://doi.org/10.4319/lo.1992.37.6.1307

Gooding, R. M., Neill, W. H., & Dizon, A. E. (1981). Respiration rates and low-oxygen tolerance limits in skipjack tuna, Katsuwonus pelamis. *Fishery Bulletin*, *79*(1). Retrieved from https://spo.nmfs.noaa.gov/sites/default/files/pdf-content/1981/791/gooding.pdf

Goodyear, C. P. (2003). Tests of the robustness of habitat-standardized abundance indices using simulated blue marlin catch–effort data. *Marine and Freshwater Research*, *54*(4), 369–381. https://doi.org/10.1071/mf01253

Graco, M. I., Purca, S., Dewitte, B., Castro, C. G., Morón, O., Ledesma, J., et al. (2017). The OMZ and nutrient features as a signature of interannual and low-frequency variability in the Peruvian upwelling system. *Biogeosciences*, *14*(20), 4601–4617. https://doi.org/10.5194/bg-14-4601-2017

Green, R. E. (1967). Relationship of the Thermocline to Success of Purse Seining for Tuna. *Transactions of the American Fisheries Society*, *96*(2), 126–130. https://doi.org/10.1577/1548-8659(1967)96[126:ROTTTS]2.0.CO;2

Guillotreau, P., Campling, L., & Robinson, J. (2012). Vulnerability of small island fishery economies to climate and institutional changes. *Current Opinion in Environmental Sustainability*, *4*(3), 287–291. https://doi.org/10.1016/j.cosust.2012.06.003

Gutiérrez, D., Enríquez, E., Purca, S., Quipúzcoa, L., Marquina, R., Flores, G., & Graco, M. (2008). Oxygenation episodes on the continental shelf of central Peru: Remote forcing and benthic ecosystem response. *Progress in Oceanography*, *79*(2), 177–189. https://doi.org/10.1016/j.pocean.2008.10.025

Hamnett, M. P., & Anderson, C. L. (n.d.). *Impact of ENSO events on tuna fisheries in the US affiliated Pacific islands* (No. SOEST 00-03, JIMAR Contribution 00-330). Honolulu, HI: Joint Institute for Marine and Atmospheric Research. Retrieved from http://www.soest.hawaii.edu/pfrp/soest_jimar_rpts/hamnett_enso00.pdf

Havice, E. (2013). Rights-based management in the Western and Central Pacific Ocean tuna fishery: Economic and environmental change under the Vessel Day Scheme. *Marine Policy*, *42*, 259–267. https://doi.org/10.1016/j.marpol.2013.03.003

Hobday, A. J., Spillman, C. M., Eveson, J. P., & Hartog, J. R. (2016). Seasonal forecasting for decision support in marine fisheries and aquaculture. *Fisheries Oceanography*, *25*(S1), 45–56. https://doi.org/10.1111/fog.12083

Hoerling, M. P., Kumar, A., & Zhong, M. (1997). El Niño, La Niña, and the Nonlinearity of Their Teleconnections. *Journal of Climate*, *10*(8), 1769–1786. https://doi.org/10.1175/1520-0442(1997)010<1769:ENOLNA>2.0.CO;2

Hofmann, A. F., Peltzer, E. T., Walz, P. M., & Brewer, P. G. (2011). Hypoxia by degrees: Establishing definitions for a changing ocean. *Deep Sea Research Part I: Oceanographic Research Papers*, *58*(12), 1212–1226. https://doi.org/10.1016/j.dsr.2011.09.004

Huang, B., L'Heureux, M., Hu, Z.-Z., & Zhang, H.-M. (2016). Ranking the strongest ENSO events while incorporating SST uncertainty. *Geophysical Research Letters*, *43*(17), 9165–9172. https://doi.org/10.1002/2016GL070888

Huang, P., & Ying, J. (2015). A Multimodel Ensemble Pattern Regression Method to Correct the Tropical Pacific SST Change Patterns under Global Warming. *Journal of Climate*, *28*(12), 4706–4723. https://doi.org/10.1175/JCLI-D-14-00833.1

Hughes, T. P., Anderson, K. D., Connolly, S. R., Heron, S. F., Kerry, J. T., Lough, J. M., et al. (2018). Spatial and temporal patterns of mass bleaching of corals in the Anthropocene. *Science*, *359*(6371), 80–83. https://doi.org/10.1126/science.aan8048

Ingham, M. C., Cook, S. K., & Hausknecht, K. A. (1977). Oxycline characteristics and skipjack tuna distribution in the southeastern tropical Atlantic. *Fishery Bulletin*, *75*(4). Retrieved from https://spo.nmfs.noaa.gov/sites/default/files/pdf-content/1977/754/ingham.pdf

Izumo, T. (2005). The equatorial undercurrent, meridional overturning circulation, and their roles in mass and heat exchanges during El Niño events in the tropical Pacific ocean. *Ocean Dynamics*, *55*(2), 110–123. https://doi.org/10.1007/s10236-005-0115-1

Johnson, G. C., McPhaden, M. J., Rowe, G. D., & McTaggart, K. E. (2000). Upper equatorial Pacific Ocean current and salinity variability during the 1996–1998 El Niño–La Niña cycle. *Journal of Geophysical Research: Oceans*, *105*(C1), 1037–1053. https://doi.org/10.1029/1999JC900280

Kang, I.-S., & Kug, J.-S. (2002). El Niño and La Niña sea surface temperature anomalies: Asymmetry characteristics associated with their wind stress anomalies. *Journal of Geophysical Research: Atmospheres*, *107*(D19), ACL 1-1-ACL 1-10. https://doi.org/10.1029/2001JD000393

Keeling, R. F., Körtzinger, A., & Gruber, N. (2010). Ocean Deoxygenation in a Warming World. *Annual Review of Marine Science*, *2*(1), 199–229. https://doi.org/10.1146/annurev.marine.010908.163855

Kenyon, J., & Hegerl, G. C. (2010). Influence of Modes of Climate Variability on Global Precipitation Extremes. *Journal of Climate*, *23*(23), 6248–6262. https://doi.org/10.1175/2010JCLI3617.1

Koslow, J. A., Goericke, R., Lara-Lopez, A., & Watson, W. (2011). Impact of declining intermediate-water oxygen on deepwater fishes in the California Current. *Marine Ecology Progress Series*, *436*, 207–218. https://doi.org/10.3354/meps09270

Laurs, R. M., & Lynn, R. J. (1977). Seasonal migration of north Pacific albacore, thunnus alalunga, into north American coastal waters: distribution, relative abundance, and association with transition zone waters. *Fishery Bulletin*, *75*(4), 795–822.

Lehodey, P., Bertignac, M., Hampton, J., Lewis, A., & Picaut, J. (1997). El Niño Southern Oscillation and tuna in the western Pacific. *Nature*, *389*(6652), 715–718. https://doi.org/10.1038/39575

Lehodey, P., Senina, I., Sibert, J., Bopp, L., Calmettes, B., Hampton, J., & Murtugudde, R. (2010). Preliminary forecasts of Pacific bigeye tuna population trends under the A2 IPCC scenario. *Progress in Oceanography*, *86*(1), 302–315. https://doi.org/10.1016/j.pocean.2010.04.021

Lehodey, Patrick. (2001). The pelagic ecosystem of the tropical Pacific Ocean: dynamic spatial modelling and biological consequences of ENSO. *Progress in Oceanography*, *49*(1), 439–468. https://doi.org/10.1016/S0079-6611(01)00035-0

Lehodey, Patrick, Senina, I., & Murtugudde, R. (2008). A spatial ecosystem and populations dynamics model (SEAPODYM) – Modeling of tuna and tuna-like populations. *Progress in Oceanography*, *78*(4), 304–318. https://doi.org/10.1016/j.pocean.2008.06.004

Lehodey, Patrick, Senina, I., Calmettes, B., Hampton, J., & Nicol, S. (2013). Modelling the impact of climate change on Pacific skipjack tuna population and fisheries. *Climatic Change*, *119*(1), 95–109. https://doi.org/10.1007/s10584-012-0595-1

Lehodey, Patrick, Senina, I., Nicol, S., & Hampton, J. (2015). Modelling the impact of climate change on South Pacific albacore tuna. *Deep Sea Research Part II: Topical Studies in Oceanography*, *113*, 246–259. https://doi.org/10.1016/j.dsr2.2014.10.028

Levitus, S., Antonov, J. I., Boyer, T. P., Locarnini, R. A., Garcia, H. E., & Mishonov, A. V. (2018). Global ocean heat content 1955–2008 in light of recently revealed instrumentation problems. *Geophysical Research Letters*. https://doi.org/10.1029/2008GL037155@10.1002/(ISSN)1944-8007.GRL40

Llanillo, P. J., Karstensen, J., Pelegrí, J. L., & Stramma, L. (2013). Physical and biogeochemical forcing of oxygen and nitrate changes during El Niño/El Viejo and La Niña/La Vieja

upper-ocean phases in the tropical eastern South Pacific along 86° W. *Biogeosciences (BG)*, *10*, 6339–6355. http://dx.doi.org/10.5194/bg-10-6339-2013

Locarnini, R. A., Mishonov, A. V., Antonov, J. I., Boyer, T. P., Garcia, H. E., Baranova, O. K., et al. (2013). *World Ocean Atlas 2013, Volume 1: Temperature* (No. NOAA Atlas NESDIS 73). Silver Spring, Maryland: National Oceanographic Data Center. Retrieved from https://data.nodc.noaa.gov/woa/WOA13/DOC/woa13_vol1.pdf

Lowe, T. E., Brill, R. W., & Cousins, K. L. (2000). Blood oxygen-binding characteristics of bigeye tuna (Thunnus obesus), a high-energy-demand teleost that is tolerant of low ambient oxygen. *Marine Biology*, *136*(6), 1087–1098. https://doi.org/10.1007/s002270000255

Maunder, M. N., & Piner, K. R. (2015). Contemporary fisheries stock assessment: many issues still remain. *ICES Journal of Marine Science*, *72*(1), 7–18. https://doi.org/10.1093/icesjms/fsu015

Maunder, M. N., Sibert, J. R., Fonteneau, A., Hampton, J., Kleiber, P., & Harley, S. J. (2006). Interpreting catch per unit effort data to assess the status of individual stocks and communities. *ICES Journal of Marine Science*, *63*(8), 1373–1385. https://doi.org/10.1016/j.icesjms.2006.05.008

McPhaden, M. J., Zebiak, S. E., & Glantz, M. H. (2006). ENSO as an Integrating Concept in Earth Science. *Science*, *314*(5806), 1740–1745. https://doi.org/10.1126/science.1132588

Mislan, K. a. S., Deutsch, C. A., Brill, R. W., Dunne, J. P., & Sarmiento, J. L. (2017). Projections of climate-driven changes in tuna vertical habitat based on species-specific differences in blood oxygen affinity. *Global Change Biology*, *23*(10), 4019–4028. https://doi.org/10.1111/gcb.13799

Moss, R. M. (2007). Environment and development in the Republic of the Marshall Islands: Linking climate change with sustainable fisheries development. *Natural Resources Forum*, *31*(2), 111–118. https://doi.org/10.1111/j.1477-8947.2007.00147.x

Nakano, H., Okazaki, M., & Okamoto, H. (1997). Analysis of catch depth by species for tuna longline fishery based on catch by branch lines. *Bulletin of National Research Institute of Far Seas Fisheries*, *34*, 43–62.

Pinsky, M. L., Worm, B., Fogarty, M. J., Sarmiento, J. L., & Levin, S. A. (2013). Marine Taxa Track Local Climate Velocities. *Science*, *341*(6151), 1239–1242. https://doi.org/10.1126/science.1239352

Pons, M., Branch, T. A., Melnychuk, M. C., Jensen, O. P., Brodziak, J., Fromentin, J. M., et al. (2017). Effects of biological, economic and management factors on tuna and billfish stock status. *Fish and Fisheries*, *18*(1), 1–21. https://doi.org/10.1111/faf.12163

Prince, E. D., & Goodyear, C. P. (2006). Hypoxia-based habitat compression of tropical pelagic fishes. *Fisheries Oceanography*, *15*(6), 451–464. https://doi.org/10.1111/j.1365-2419.2005.00393.x

Prince, E. D., Luo, J., Goodyear, C. P., Hoolihan, J. P., Snodgrass, D., Orbesen, E. S., et al. (2010). Ocean scale hypoxia-based habitat compression of Atlantic istiophorid billfishes. *Fisheries Oceanography*, *19*(6), 448–462. https://doi.org/10.1111/j.1365-2419.2010.00556.x

Resplandy, L., Séférian, R., & Bopp, L. (2015). Natural variability of CO2 and O2 fluxes: What can we learn from centuries-long climate models simulations? *Journal of Geophysical Research: Oceans*, *120*(1), 384–404. https://doi.org/10.1002/2014JC010463

Schaefer, K. M., & Fuller, D. W. (2010). Vertical movements, behavior, and habitat of bigeye tuna (Thunnus obesus) in the equatorial eastern Pacific Ocean, ascertained from archival tag data. *Marine Biology*, *157*(12), 2625–2642. https://doi.org/10.1007/s00227-010-1524-3

Schmidtko, S., Stramma, L., & Visbeck, M. (2017). Decline in global oceanic oxygen content during the past five decades. *Nature*, *542*(7641), 335–339. https://doi.org/10.1038/nature21399

Seibel, B. A. (2011). Critical oxygen levels and metabolic suppression in oceanic oxygen minimum zones. *Journal of Experimental Biology*, *214*(2), 326–336. https://doi.org/10.1242/jeb.049171

Stramma, L., Johnson, G. C., Firing, E., & Schmidtko, S. (2010). Eastern Pacific oxygen minimum zones: Supply paths and multidecadal changes. *Journal of Geophysical Research: Oceans*, *115*(C9). https://doi.org/10.1029/2009JC005976

Stramma, L., Fischer, T., Grundle, D. S., Krahmann, G., Bange, H. W., & Marandino, C. A. (2016). Observed El Niño conditions in the eastern tropical Pacific in October 2015. *Ocean Science*, *12*(4), 861–873. https://doi.org/10.5194/os-12-861-2016

Vecchi, G. A., & Soden, B. J. (2007). Global Warming and the Weakening of the Tropical Circulation. *Journal of Climate*, *20*(17), 4316–4340. https://doi.org/10.1175/JCLI4258.1

Vecchi, G. A., Soden, B. J., Wittenberg, A. T., Held, I. M., Leetmaa, A., & Harrison, M. J. (2006). Weakening of tropical Pacific atmospheric circulation due to anthropogenic forcing. *Nature*, *441*(7089), 73–76. https://doi.org/10.1038/nature04744

Ventura, V., Paciorek, C. J., & Risbey, J. S. (2004). Controlling the Proportion of Falsely Rejected Hypotheses when Conducting Multiple Tests with Climatological Data. *Journal of Climate*, *17*(22), 4343–4356. https://doi.org/10.1175/3199.1

Viron, O. de, Dickey, J. O., & Ghil, M. (2013). Global modes of climate variability. *Geophysical Research Letters*, *40*(9), 1832–1837. https://doi.org/10.1002/grl.50386

Wilks, D. S. (2006). On “Field Significance” and the False Discovery Rate. *Journal of Applied Meteorology and Climatology*, *45*(9), 1181–1189. https://doi.org/10.1175/JAM2404.1

Wilks, D. S. (2016). “The Stippling Shows Statistically Significant Grid Points”: How Research Results are Routinely Overstated and Overinterpreted, and What to Do about It. *Bulletin of the American Meteorological Society*, *97*(12), 2263–2273. https://doi.org/10.1175/BAMS-D-15-00267.1

Willett, J. B., & Singer, J. D. (1988). Another Cautionary Note about R 2: Its Use in Weighted Least-Squares Regression Analysis. *The American Statistician*, *42*(3), 236–238. https://doi.org/10.1080/00031305.1988.10475573

Williams, A. J., Allain, V., Nicol, S. J., Evans, K. J., Hoyle, S. D., Dupoux, C., et al. (2015). Vertical behavior and diet of albacore tuna (Thunnus alalunga) vary with latitude in the South Pacific Ocean. *Deep Sea Research Part II: Topical Studies in Oceanography*, *113*, 154–169. https://doi.org/10.1016/j.dsr2.2014.03.010

Yang, S., Gruber, N., Long, M. C., & Vogt, M. (2017). ENSO-Driven Variability of Denitrification and Suboxia in the Eastern Tropical Pacific Ocean. *Global Biogeochemical Cycles*, *31*(10), 1470–1487. https://doi.org/10.1002/2016GB005596

Ying, J., Huang, P., & Huang, R. (2016). Evaluating the formation mechanisms of the equatorial Pacific SST warming pattern in CMIP5 models. *Advances in Atmospheric Sciences*, *33*(4), 433–441. https://doi.org/10.1007/s00376-015-5184-6

Zhang, M., & Song, H. (2006). Evidence of deceleration of atmospheric vertical overturning circulation over the tropical Pacific. *Geophysical Research Letters*, *33*(12). https://doi.org/10.1029/2006GL025942

Zweng, M. M., Reagan, J. R., Antonov, J. I., Locarnini, R. A., Mishonov, A. V., Boyer, T. P., et al. (2013). *World Ocean Atlas 2013, Volume 2: Salinity* (No. NOAA Atlas NESDIS 74). Silver Spring, Maryland. Retrieved from https://data.nodc.noaa.gov/woa/WOA13/DOC/woa13_vol2.pdf

Chapter 4: The significance of ocean deoxygenation for open ocean tunas and billfishes

This chapter is an edited version of a peer-reviewed chapter in a 2019 International Union for Conservation of Nature and Natural Resources report. The citation is as follows: Leung, S., Mislan, K. A. S., Muhling, B., & Brill, R. (2019). Section 8.2: The significance of ocean deoxygenation for open ocean tunas and billfishes. *Ocean deoxygenation: everyone's problem: causes, impacts, consequences*. https://doi.org/10.2305/IUCN.CH.2019.13.en

4.1 Summary

Tunas and billfishes should be especially sensitive to low ambient oxygen conditions given their high metabolic rates as well as the large differences between their resting and maximum metabolic rates. Although there are many behavioural similarities among the different species, there are also clear and demonstrable differences in growth rates, maximum adult size, physiological abilities, low-oxygen tolerances, and preferred environmental conditions. This section aims to summarize the main species-specific effects of projected changes in ocean oxygen content on tunas and billfishes, as well as the resulting ecosystem and societal consequences.

Climate change is projected to alter oxygen concentrations throughout the open-ocean, with most regions undergoing decreases due to a slowdown in ocean ventilation and a decline in surface oxygen solubility. Between 200 and 700 m depth (a vertical range including depths to which tunas and billfishes commonly descend to forage), the greatest and most certain decreases in oxygen concentrations are projected to occur in the North Pacific and much of the Southern Ocean, while the smallest and least certain changes are projected to occur within the Tropical Pacific Ocean. Along a north-south line through the middle of the Pacific Ocean (160°W

longitude), projected oxygen concentration decreases are most pronounced from 15°N to 50°N between 250 and 750 m depth and south of 50°S between 50 and 300 m depth.

The depth at which oxygen concentrations drop below 3.5 ml l^{-1} (a threshold hypoxic concentration for several tuna and billfish species including yellowfin and skipjack tunas, marlins, and sailfish) is projected to shoal throughout the global oceans, which may lead to widespread vertical habitat compression and changes in vertical movement patterns. Projected shoaling of the 3.5 ml l^{-1} threshold depth is especially pronounced within subtropical and mid-latitude Pacific Ocean regions. Oxycline depth is also projected to shoal by over 150 m in these same Pacific Ocean regions and throughout much of the Southern Ocean. Species residing in the temperate North Pacific, such as swordfish and yellowfin, bigeye, Pacific bluefin, and albacore tunas, may therefore be impacted by future oxygen changes more greatly than other species, as projected decreases in oxygen concentrations are greatest within their present-day ranges.

Changes in temperature and oxygen content have the potential to alter the distribution and catchability of tunas and billfishes in three dimensions. Because they are highly mobile, tunas and billfishes can exhibit complex shifts in their distributions in response to changing environmental conditions. Where surface layer temperatures become too warm, they may spend more time at depth (assuming oxygen concentrations are sufficient); where low-oxygen layers shoal or expand, they may spend more time near the oxygenated surface (assuming temperatures are not too warm), increasing their vulnerability to surface fishing gears. If no vertical refuge from unsuitable conditions is available, they may shift their distributions horizontally. Because temperature and hypoxia tolerances of tunas and billfishes are species-specific, any changes in

temperature and oxygen content within the water column may modify competition among different species as their vertical and horizontal habitats shift in different ways, potentially altering established food web dynamics, ecosystem structures, and bycatch rates. Differential responses of prey species to changes in environmental conditions could also affect food web structures, the ability of tunas and billfishes to find food, age at first reproduction, and mean body sizes.

Future changes in the distributions of tunas and billfishes are likely to complicate stock assessments and to have important socioeconomic effects. As spatial habitats of targeted tuna and billfish species shift, the ability of fishery-dependent, catch per unit effort (CPUE)-based abundance indices to capture stock dynamics accurately will be compromised, unless CPUE-standardization methods can adapt. Where populations of targeted tuna and billfish species decrease in abundance or move away from traditional fishing grounds, fishers will have to spend more resources to locate and catch these species or reconfigure their gear to target new ones. Economic, political, and regulatory constraints can, however, hinder the ability of fishers to effectively adapt, particularly if species move across management boundaries. Smaller-scale fisheries in developing nations and fisheries relying on vessels with limited range and low technological capabilities are likely to be most vulnerable to shifts in range or migratory patterns.

Ocean hypoxia effect	Potential Consequences
Decreasing oxygen concentrations in current habitats may result in species-specific shifts in range and migratory patterns.	● Alters the ecological relationships between some tuna and billfish species and their prey. ● Geographically redistributes catches and societal benefits from fisheries. ● Complicates stock assessment and management, as changes in environmental conditions alter fish availability and subsequent fishery data-derived estimates of abundance.
Shallower oxyclines and hypoxic layers may result in species-specific changes in vertical movement patterns and compression of vertical habitat.	● Decreases vertical separation among tuna species, resulting in future increases in the frequency of competitive species interactions. ● Alters coupling between predator and prey and thus foraging success. ● Increases vulnerability to capture by surface fishing gears.
Changing oxygen concentrations may lead to changes in locations of spawning grounds.	● Alters spawning success and year class strength, which could modify the ability of tuna and billfish populations to withstand high rates of fishing mortality. ● Albacore tuna in the South Pacific may be negatively affected by oxygen concentration decreases on their spawning grounds; other species may be either negatively or positively affected.
The temperate North Pacific Ocean is projected to undergo large decreases in oxygen content within the upper water column (above 1000 m).	● Species currently residing in this region (which include swordfish and yellowfin, bigeye, Pacific bluefin, and albacore tunas) are expected to experience the most dramatic decreases in oxygen concentrations and shoaling of hypoxic layers within their habitat.

4.2 Introduction

The effects of temperature and ambient oxygen on the behaviours and physiology of tunas (members of the family Scombridae, tribe Thunnini) and billfishes (members of the family Istiophoridae and Xiphiidae) (Fig. 4.1) have been actively investigated over five decades (e.g., Barkley et al., 1978; Blackburn, 1965; Bushnell and Brill, 1991; 1992; Bushnell et al., 1990; Dizon, 1977; Dizon et al., 1974; 1976; Gooding et al., 1981; Sharp, 1975; 1978; 1983; Stevens, 1972; Stevens and Fry, 1972; Sund et al., 1981). Variations in temperature and ambient oxygen with depth have long been known to influence species-specific vertical movement patterns which, in turn, affect vulnerability to different types of fishing gear (Fig. 4.2). Understanding changes in the vulnerability of fish to specific gear types under different oceanographic conditions defined by temperature and oxygen content is important for standardizing catch-per-unit effort (CPUE) indices used in stock assessments and management decisions (e.g., Brill, 1994; Bigelow et al., 2002; Bigelow and Maunder, 2006; Hinton and Deriso, 1998; Hinton and Nakano, 1996; Sharp, 1995; 2001). Horizontal migrations away from traditional habitats and fishing grounds can also result from changes in environmental conditions (Block et al., 2011; Pinsky et al., 2013), with important downstream effects on the food security and economic development of regions dependent on tuna and billfish fisheries.

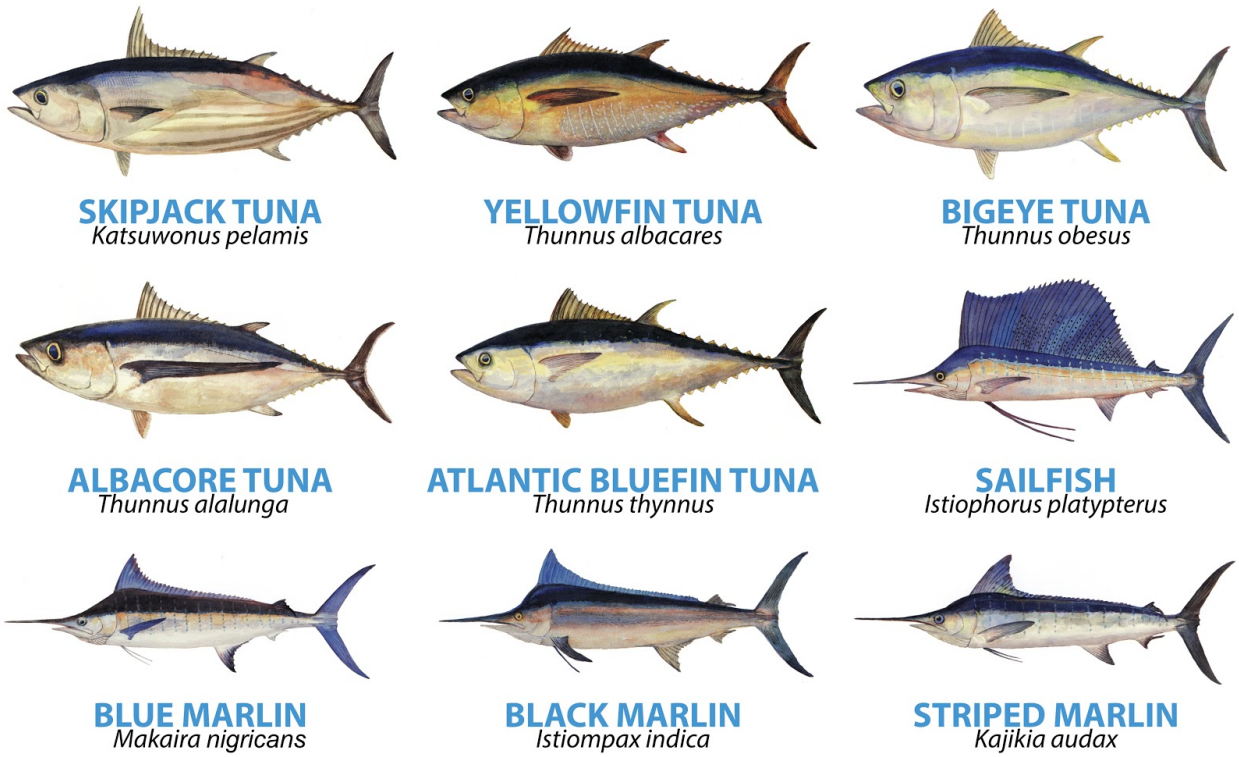

Figure 4.1 | Tuna and billfish species. (Paintings by George Mattson.)

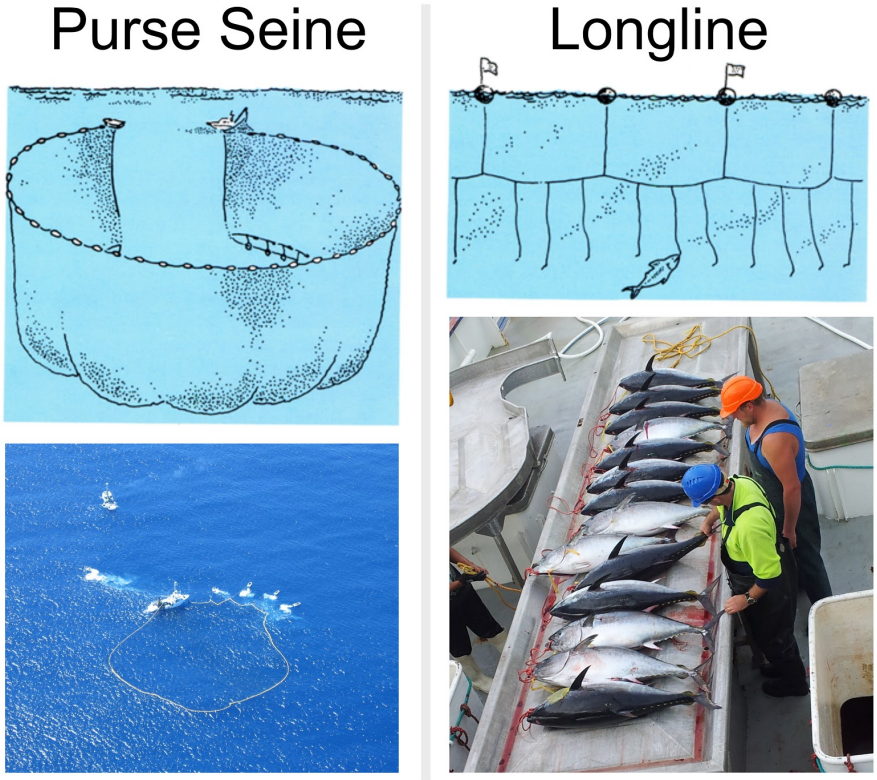

Figure 4.2 | Common types of fishing gear used to commercially capture tuna and billfish. (Conceptual drawings from Joseph et al., 1980. Top photograph by Jessica Farley. Bottom photograph by Alistair Hobday.)

On theoretical grounds alone, tunas and billfishes should be especially sensitive to low oxygen concentrations given their unique anatomical and physiological characteristics, which permit high routine and maximum metabolic rates and large absolute metabolic scopes (e.g., Bernal et al., 2009; Brill and Bushnell, 1991; 2001; Brill and Lai, 2016; Bushnell and Jones, 1994; Deutsch et al. 2015; Killen et al., 2016; Korsmeyer and Dewar, 2001; Stoffels, 2015; Wegner et al., 2013). Metabolic rates of billfishes have never been measured, but are assumed to be similar to those of tunas because of the high degree of convergent evolution (Bernal et al., 2001; 2009; Wegner et al., 2013). The limiting effects of hypoxia in the marine environment appear, however, to be highly species-specific (e.g., Childress and Seibel, 1998; Deutsch et al., 2015; Seibel, 2011; 2013). An understanding of basic mechanistic principles (i.e., species-specific physiological abilities and tolerances and the resultant behavioural responses to environmental conditions) is therefore needed to better predict species-specific movement patterns (e.g. Hobday et al., 2013; Horodysky et al., 2015; 2016; McKenzie et al., 2016). The ability to predict the effects of environmental conditions on the movements of large and economically important fish species is becoming even more critical as the effects of directional global climate change become increasingly apparent in the pelagic environment – including but not limited to increasing upper ocean temperature, expansion of oxygen minimum zones, and the resultant interaction of these two factors (e.g., Breitburg et al. 2018; Deutsch et al. 2015; Gilly et al., 2013; Mislan et al., 2017; Muhling et al., 2016; Prince and Goodyear, 2006; 2007; Prince et al., 2010, Stramma et al., 2010a; 2012).

This section aims to summarize the main effects of projected changes in ocean oxygen content on species-specific tuna and billfish habitats and populations, as well as the resulting

ecosystem and societal consequences. We begin by defining the tuna and billfish species of interest and comparing limits of hypoxia tolerance and resultant movement behaviours among these species. We then analyze projected changes in oxygen content within current habitat spaces and summarize projected oxygen-induced habitat suitability changes calculated from four different types of models. Lastly, we highlight the potential effects of these oxygen-induced habitat suitability changes on ecosystems and human society.

Throughout this section, we will discuss oxygen content and conditions in terms of either dissolved concentrations (units of ml l^{-1} or mg l^{-1}) or partial pressures (units of kPa), depending on the context. Oxygen content within the ocean has historically been expressed in terms of dissolved concentrations rather than partial pressures because unlike partial pressures, dissolved concentrations do not depend on temperature, salinity, or depth in the water column and are thus useful for mass balance calculations and numerical models. The driving force for molecular oxygen transfer (both from water to blood in the gills and from blood through tissues to the mitochondria) is, however, controlled by the partial pressure of oxygen (Hoffmann et al., 2011). To characterize the oxygen environment experienced by tunas and billfishes more completely, we therefore also report oxygen conditions in terms of partial pressures whenever possible. Because partial pressures depend on both dissolved oxygen concentrations and oxygen solubility (which in turn depends on temperature, salinity, and depth), we will avoid conversion to partial pressures when comparing results with historical thresholds or measurements expressed in dissolved concentration units and lacking simultaneous temperature, salinity, and depth data.

4.3 Definition of species group

We will discuss various species of billfish and tuna here, but emphasis will be placed on the seven principle market species of tunas (Table 4.1) both because of their importance and the availability of data. Tunas in aggregate support the world's largest fisheries with an economic value of ~US$9 billion, landing ~ 6.5 x 10^6 metric tons annually. The seven principle market species collectively account for ~66% of the global tuna landings (FAO 2014; Guillotreau et al., 2017; Sumaila et al., 2007) (Table 4.1). Yellowfin (*Thunnus albacares*) and skipjack (*Katsuwonus pelamis*) tunas collectively account for ~85% of the landings of the seven principle market species. Albacore (*Thunnus alalunga*), bigeye (*Thunnus obesus*), and bluefin tunas collectively account for >10% of the landings, but the latter two have high economic value because they dominate the fresh fish (i.e., sashimi-grade) market (Guillotreau et al., 2017). Because of the especially high political profile of Atlantic (*Thunnus thynnus*), Pacific (*Thunnus orientalis*), and Southern (*Thunnus maccoyii*) bluefin tunas (e.g., Safina, 2001), these three species have received significant scientific attention, especially with regard to the effects of climate change on their movements, distributions and spawning areas (e.g., Hazen et al., 2013; Kitagawa and Kimura, 2015; Muhling et al., 2015; 2016; 2017). The aggregate landings of billfishes (~136 x 10^3 metric tons in 2015) (FAO 2017) are approximately three orders of magnitude less than those of the primary market species of tunas, with swordfish (*Xiphias gladius*) constituting most of the billfish catch. Other billfishes are, however, highly prized by recreational anglers because of their acrobatic ability and because some species (e.g., blue and

black marlin, *Makaira nigricans* and *Istiompax indica*, respectively) achieve extraordinary body sizes.

Species	Percent of Total Tuna Catch
Skipjack tuna	58.1%
Yellowfin tuna	26.8%
Bigeye tuna	8.2%
Albacore	5.9%
Atlantic bluefin tuna	less than 1%
Pacific bluefin tuna	less than 1%
Southern bluefin tuna	less than 1%

Table 4.1 | Relative importance of the principal market species of tunas based on annual landings (FAO. Fishery Statistical Collections. Global Tuna Catches by Stock. 2014; Available at: http://www.fao.org/fishery/statistics/tuna-catches/en. Accessed: 30/12/2014.)

Tunas and billfishes are highly mobile, top-level carnivores (though trophic level varies with age class) that live predominately in the energy-depauperate pelagic environment, where rates of primary productivity (per unit area) are approximately one-tenth of those in coastal areas (e.g., Antoine et al., 1996; Westberry et al., 2008) and where forage-species are highly aggregated (such as at fronts) and these aggregations are heterogeneously distributed (e.g., Lehodey et al., 1998; Polovina et al., 2001). Though several tuna species also inhabit coastal waters where productivity is higher overall, it is tunas' unique anatomical, biological, and physiological attributes (e.g., Block and Stevens, 2001; Brill, 1996; Brill and Hobday, 2017) that allow their now well-documented extraordinary growth and reproductive rates (Gaertner et al., 2008; Gaikov et al., 1980; Schaefer, 2001; Wild, 1986). These extraordinary growth and reproductive rates in turn permit simultaneous high rates of natural (Murphy and Sakagawa, 1977) and fisheries mortality. Less is known about the physiological abilities of billfishes because, in contrast to tunas (Farwell et al., 2001), they have never been maintained in shore-side

facilities and therefore have never been available for laboratory studies involving whole animals. There is, however, considerable evidence for rapid somatic and gonadal growth rates and high fecundity in billfishes (e.g., Hopper, 1990; Prince and Pulos, 1983).

Although there are many behavioural similarities among the principle market species of tunas, there are also clear and demonstrable species-specific differences in growth rates (Fromentin and Fonteneau, 2001; Murua et al., 2017), maximum adult size, physiological abilities, and tolerances of temperature and oxygen reductions that occur with increasing depth (e.g., Blank et al., 2004; Galli et al., 2009, 2011; Lowe et al., 2000; Shiels et al., 1999; 2015; Bernal et al., 2009; 2017; Sibert et al., 2006; Table 4.2; Table 4.3). It is primarily differences in adult body size, thermoregulatory ability, and cardio-respiratory function that determine species-specific thermal and hypoxic tolerances, which in turn account for documented differences in daily vertical mobility patterns (Fig. 4.3; Fig. 4.4), spatial distributions (Fig. 4.5), migratory patterns (which take some species from temperate feeding areas to tropical spawning areas), and apparent resource partitioning (e.g., Bernal et al., 2009; 2017; Block et al., 2001; Boustany et al., 2010; Carey 1990; Carey and Robison, 1981; Muhling et al., 2017; Musyl et al., 2003; Schaefer and Fuller, 2002; Schaefer et al., 2009a; Wilson et al., 2005; 2015). These species-specific movements have been reviewed extensively for tunas, billfishes and sharks by Bernal et al., (2009), and more recently and specifically for tunas and billfishes by Horodysky et al. (2016) and Bernal et al. (2017). These reviews show that tuna species can be categorized into groups exhibiting distinct vertical movement behaviours (Fig. 4.4). For example, the extensive vertical movements of bigeye tuna (and other species in Group 3, Fig. 4.4) and their ability to remain at depth for extended periods are in stark contrast to the vertical movement patterns of

skipjack and yellowfin tunas (Schaefer and Fuller, 2002; 2007; 2010; Schaefer et al., 2007; 2009a; 2009b; 2014). The latter species also make forays to depths of ~500 m, but times spent in these cold and hypoxic waters are brief compared to time spent at depth by bigeye tuna, which include long periods (~45-60 minutes) below the thermocline (~500 m depth) during daylight hours, where water temperatures may be below 6°C and oxygen levels ~1 mg l^{-1} (~0.7 ml l^{-1}, assuming 5°C) (Fig. 4.3) (Evans et al., 2008; Fuller et al., 2015; Hanamoto, 1987; Musyl et al., 2003; Schaefer and Fuller, 2002; 2010). Albacore also exhibit vertical movements to depths below 400 m, but their vertical forays are generally brief (<32 minutes), like those of skipjack and yellowfin tunas (Childers et al., 2011; Williams et al., 2015). Tracking data show that albacore usually experience oxygen levels >5 mg l^{-1} (> ~3.7 ml l^{-1}, assuming 15°C) (Laurs and Lynn, 1977) and shipboard experiments on swimming showed that aerobic metabolism declined below this oxygen level, all of which imply that albacore are relatively hypoxia-intolerant compared to bigeye tuna (Bushnell et al., 1990; Graham et al., 1989). Similarly, although there are extensive records of the vertical movements of both Atlantic and Pacific bluefin tunas, these data do not allow inferences with respect to the hypoxia tolerance of these species. Both species do, however, make forays to depth where water temperature is ~10°C and lower (Bauer et al., 2017; Block et al., 2005; Boustany et al., 2010; Kitagawa et al., 2004; 2007a; 2007b; Patterson et al., 2008). Atlantic bluefin tuna reportedly reach depths of ~1000 m and water temperatures of ~5°C (Block et al., 2001), but the accompanying oxygen levels at the depths and areas routinely occupied by Atlantic bluefin tuna are unlikely to be limiting (Gilly et al., 2013; Teo and Boustany, 2016). Southern bluefin tuna can also spend periods of over 10 hours below ~400 m at

temperatures <10°C (Patterson et al., 2008), but oxygen levels in these same areas are relatively high (Mislan et al., 2017).

	Fork length (cm)	Lower lethal oxygen levels		
		mg l^{-1}	**ml l^{-1}**	**% saturation**
Skipjack tuna	50	2.45	1.87	37
	75	2.83	2.16	43
Yellowfin tuna	50	1.49	1.14	23
	75	2.32	1.77	35
Bigeye tuna	50	0.52	0.40	8
	75	0.65	0.50	10
Albacore	50	1.67	1.23	21
	75	1.39	1.03	18

Table 4.2 (from Lehodey et al., 2011) | Lower lethal oxygen levels for four of the seven principal market species of tunas based on the ratio of minimum speed needed to sustain hydrostatic equilibrium (i.e., to keep these negatively buoyant fish from sinking) (Magnuson 1978; Magnuson and Weininger 1978). Values are shown for a 50 cm and 75 cm skipjack, yellowfin, bigeye, and albacore tuna. Percent saturation data for skipjack, yellowfin, and bigeye tunas were calculated using oxygen solubility in sea water at 25°C and data for albacore using oxygen solubility in sea water at 15°C.

Common Name	Scientific Name	Frequented Depth Range (m)	Minimum pO_2 (kPa)	Depth of Minimum pO_2 (m)	Depth of Oxycline (m)
Skipjack Tuna	*Katsuwonus pelamis*	0 - 260	12±6	236±37	117±94
Albacore Tuna	*Thunnus alalunga*	0 - 600	9±5	533±107	128±95
Yellowfin Tuna	*Thunnus albacares*	0 - 464	9±5	407±82	121±95
Blackfin Tuna	*Thunnus atlanticus*	0 - 200	15±3	185±46	99±39
Southern Bluefin Tuna	*Thunnus maccoyii*	0 - 600	15±2	575±90	106±97
Bigeye Tuna	*Thunnus obesus*	0 - 500	9±5	454±82	122±93
Pacific Bluefin Tuna	*Thunnus orientalis*	0 - 550	7±4	522±75	178±146
Atlantic Bluefin Tuna	*Thunnus thynnus*	0 - 500	13±4	460±109	80±31
Longtail Tuna	*Thunnus tonggol*	0 - 25	21±1	20±8	77±50
Black Marlin	*Istiompax indica*	0 - 100	17±5	98±12	127±102
Sailfish	*Istiophorus platypterus*	0 - 40	21±2	29±15	118±92
White Marlin	*Kajikia albida*	0 - 150	16±4	146±18	88±42
Striped Marlin	*Kajikia audax*	0 - 289	11±6	255±45	126±101
Blue Marlin	*Makaira nigricans*	0 - 40	21±2	28±15	124±94
Shortbill Spearfish	*Tetrapturus angustirostris*	0 - 200	12±6	196±13	133±104
Roundscale Spearfish	*Tetrapturus georgii*	0 - 200	14±4	195±23	93±44
Longbill Spearfish	*Tetrapturus pfluegeri*	0 - 240	13±5	218±30	93±44
Swordfish	*Xiphias gladius*	0 - 550	10±6	494±98	117±93

Table 4.3 | Summary of oxygen conditions encountered in present-day, species-specific tuna and billfish habitats. For simplicity, we assumed a constant, frequently-visited vertical range throughout each species' horizontal extent to delineate present-day, three-dimensional habitat. Species-specific horizontal ranges were taken directly from the IUCN Red List (IUCN 2011, 2014), while depth ranges were taken from the IUCN Red List (IUCN 2011, 2014) with six modifications as follows: (1) IUCN lists 10 m as the lower depth limit for longtail tuna, but the minimum depth interval for our analysis was 25 m depth, which is therefore the frequently-visited lower depth used here. (2) IUCN lists 2743 m as the absolute lower depth limit for Southern bluefin tuna, but we deemed 600 m to be a more reasonable frequently-visited lower depth based on tagging data (Patterson et al., 2008). (3) IUCN lists 50 m as the upper depth limit for Southern bluefin tuna, but there is evidence that they spend large amounts of time much closer to the surface (Patterson et al., 2008); we therefore used 0 m as the frequently-visited upper depth here. (4) IUCN lists 1500 m as the absolute lower depth limit for bigeye tuna, but mention that they are mostly found above 500 m, which is therefore the frequently-visited lower depth used here. (5) IUCN lists 1000 m as the absolute lower depth limit for blue marlin, but mention that they remain mostly within the upper 40 m, which is therefore the frequently-visited lower depth used here. (6) IUCN lists 2878 m as the absolute lower depth limit for swordfish, but mention that its typical range is from the surface to 550 m, which is therefore the frequently-visited lower depth used here. Next, we computed present-day annual mean oxygen partial pressure (pO_2) values over the entire ocean using data from World Ocean Atlas 2013 (WOA 2013) on a 1^o x 1^o horizontal grid at 25-m depth intervals. From these gridded pO_2 values analyzed over each species' assumed three-dimensional range, we then calculated the spatial means and standard deviations of minimum pO_2 values in the water column encountered by each species and

the depths at which these minimum pO_2 values occur. Lastly, we also calculated the spatial mean and standard deviation of the oxycline depth within each species' assumed habitat. For reference, 1 kPa = 7.5 mmHg.

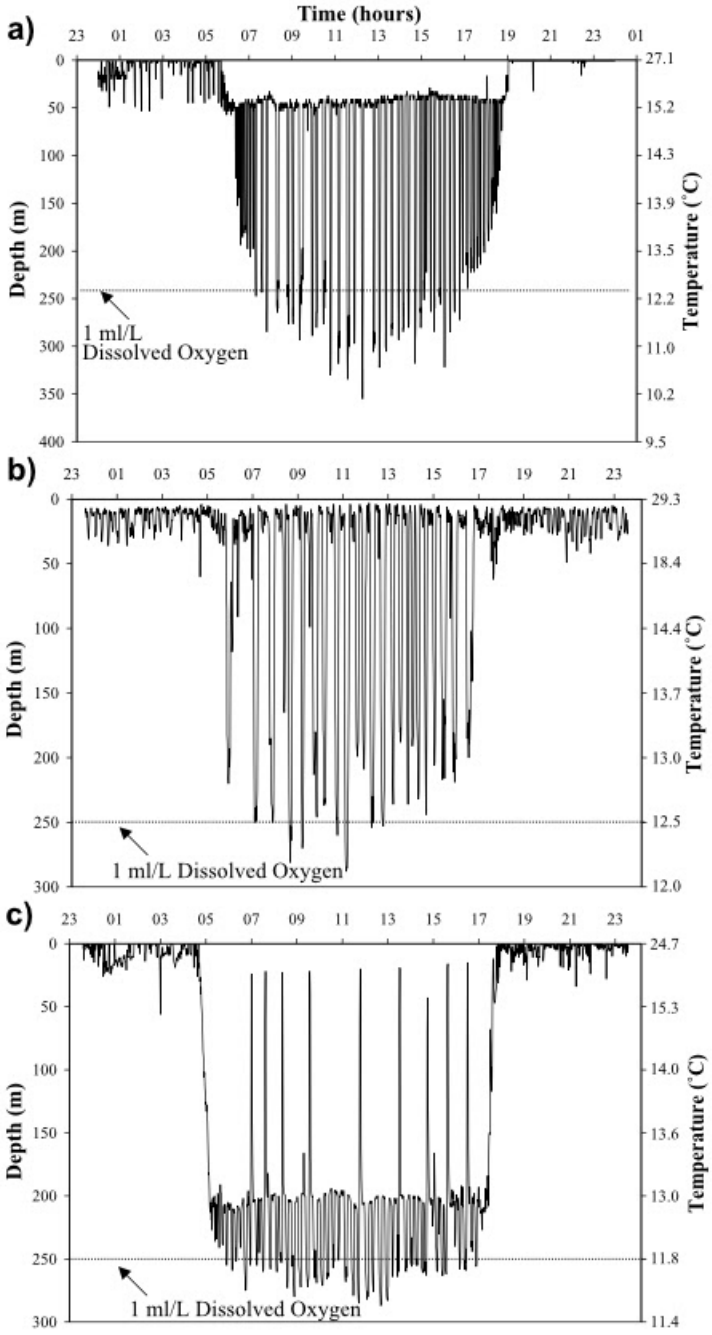

Figure 4.3 | Representative daily vertical movement patterns of a) skipjack tuna (66-cm), b) yellowfin tuna (52-cm), c) bigeye (88-cm) tunas. Tuna dive to deep depths during the day to forage for prey in the deep sound scattering layer. Skipjack and yellowfin tunas stay for short periods <15 minutes whereas bigeye tuna remain for much longer periods (>2 hours). The 1 ml l^{-1} oxygen line indicates a tuna hypoxic threshold. At 12°C, 1 ml l^{-1} = 1.3 mg l^{-1}. Adapted from Schaefer et al. (2009a).

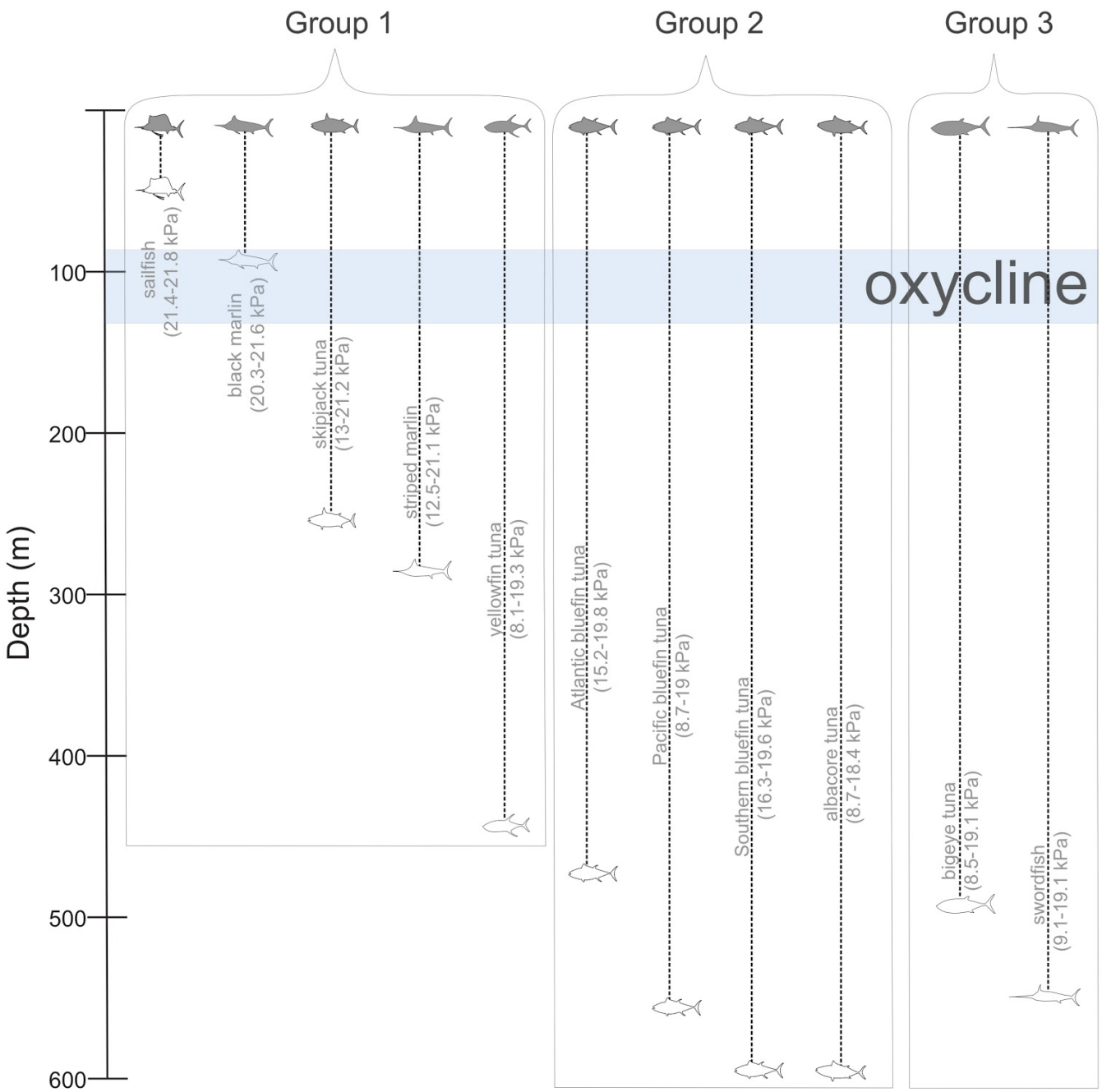

Figure 4.4 | Schematic diagram of approximate depth ranges frequented by various tuna and billfish species. Depth ranges were taken and sometimes modified (see Table 4.3 caption) from the IUCN Red List (IUCN 2011, 2014). Species are grouped by relative hypoxia tolerance, with Group 1 being least hypoxia-tolerant and Group 3 being most hypoxia-tolerant. The range (25th through 75th percentile) of oxygen partial pressure (pO_2) values encountered by each species within their assumed present-day habitats (delineated by the constant depth ranges listed in Table 4.3 and IUCN Red List horizontal distributions) is shown. Note that the amounts of time spent at depth by each species, as well as the environmental conditions within each species' range, differ. Drawing adapted from Figure 1 in Bernal et al. (2009).

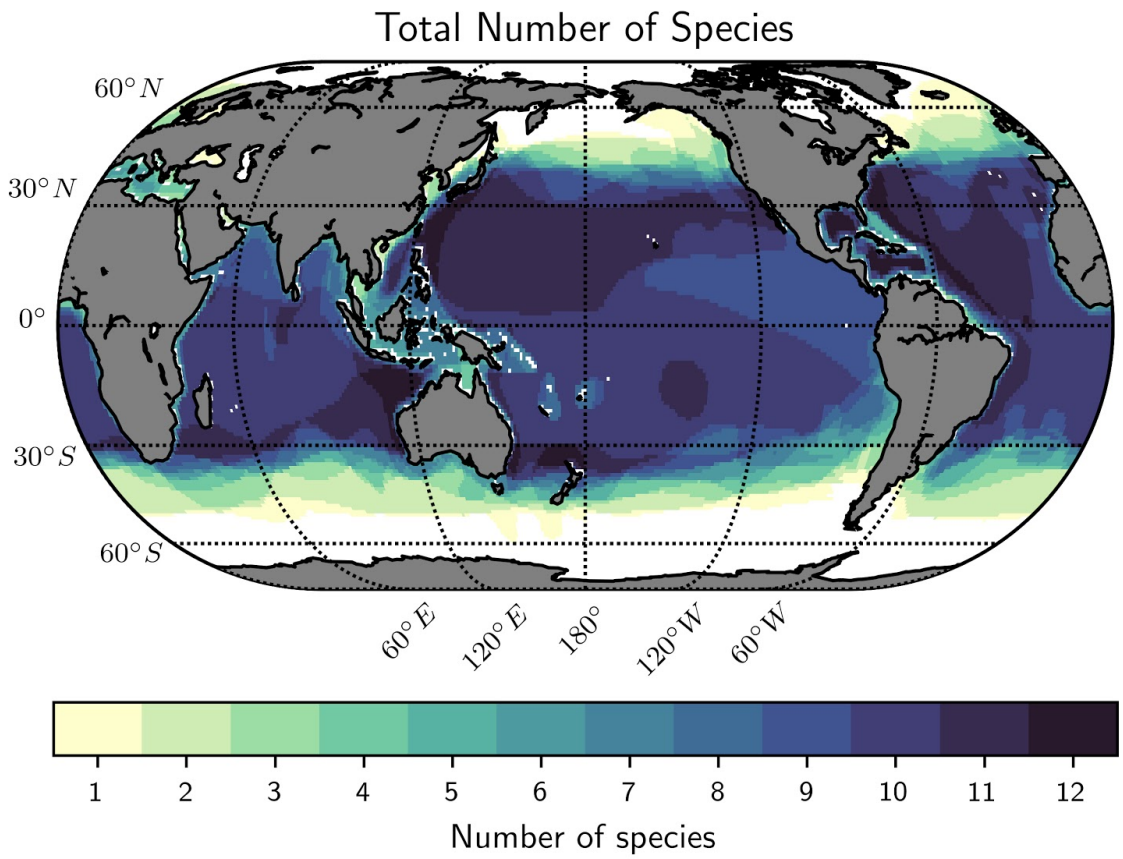

Figure 4.5 | Global distribution of the number of species of tuna and billfish based on horizontal range data from the IUCN Red List (IUCN 2011, 2014).

Tracking studies employing sonic telemetry and electronic data recording tags have shown that billfishes likewise display species-specific vertical movement patterns. Marlins and sailfishes (*Istiophorus platypterus*) largely remain in the uniform temperature surface layer, although like skipjack and yellowfin tunas, they do make brief descents below the thermocline (Block et al., 1993; Brill et al., 1993; Holland et al., 1990; Hoolihan et al., 2005; Horodysky et al., 2007; Pepperell and Davis, 1999; Pohlot and Ehrhardt, 2017; Prince and Goodyear, 2006; 2007; Prince et al., 2010). Their vertical movements do, however, appear to be strongly constrained to water with oxygen concentrations >3.5 ml l^{-1} (Braun et al., 2015). In contrast, swordfish tracked in the Pacific and Atlantic Oceans and Mediterranean Sea have been shown to

regularly descend and stay for up to eight hours below 550-600 m, where temperatures are ~5°C and oxygen levels are below ~1.4 mg l^{-1} (~1 ml l^{-1}, assuming 5°C) (Fig. 4.4) (Abascal et al., 2010; Canese et al., 2008; Carey, 1990; Carey and Robison, 1981; Dewar et al., 2011; Evans et al., 2014; Sepulveda et al., 2010; Takahashi et al., 2003). This result is congruent with the vertical movement patterns of bigeye tuna described above. The maximum depths reached by bigeye tuna and swordfish, and the concomitant reductions in temperature and low ambient oxygen, obviously imply similarly extraordinary physiological tolerances of both species; some convergent evolution in cardiac function between the two species has indeed been confirmed (Galli et al., 2009).

4.4 Trends and impacts

In this section, we summarize projected changes in oxygen content (and other variables influencing oxygen balance) affecting tuna and billfish specifically, and then examine how these changes will alter future habitat suitability and populations. Climate change is projected to alter oxygen concentrations throughout the ocean, with most regions undergoing projected decreases owing to a slowdown in ocean ventilation and a decline in surface oxygen solubility (e.g., Frölicher et al., 2009; Keeling et al., 2010; Bopp et al., 2013; Cocco et al., 2013; Cabré et al., 2015). Agreement among models over how oxygen concentrations will change is greatest in the North Pacific and much of the Southern Ocean, and lowest in the Tropical Pacific (Bopp et al., 2013; Cabré et al., 2015), though observations in the latter region indicate that oxygen concentrations have been decreasing there over the last several decades (Stramma et al., 2008; Stramma et al., 2010a; Stramma et al., 2010b; Helm et al., 2011; Czeschel et al., 2012;

Schmidtko et al., 2017; Ito et al., 2017). [Chapter 3: “Oxygen Projections for the Future” in this report provides a more detailed overview of projected changes in global oxygen content.]

4.4.1 Projecting oxygen changes in present-day tuna and billfish habitats

We use output from Earth System Models included in the Coupled Model Intercomparison Project 5 (CMIP5) (Taylor et al., 2012) to project changes in global oceanic oxygen content set to occur by the end of the 21st century. These models, which simulate physical, chemical and biological processes, are run into the future under various plausible greenhouse gas emissions scenarios. We utilize model output from years 2071–2100 within the RCP8.5 scenario, which represents a “business-as-usual” situation in which climate change goes unmitigated. To simulate present-day conditions, we use output from years 1971–2000 within the historical scenario, which is forced with historically observed atmospheric CO_2 emissions and concentrations. To calculate projected future changes, we compute multi-model mean simulated differences between the RCP8.5 and historical scenarios. The six models included here were CESM1-BGC (Gent et al., 2011; Lindsay et al., 2014), GFDL-ESM2G, GFDL-ESM2M (Dunne et al., 2012; 2013), HadGEM2-ES (Palmer and Totterdell, 2001; Collins et al., 2011; Jones et al., 2011), IPSL-CM5A-LR (Dufresne et al., 2013), and MPI-ESM-LR (Giorgetta et al., 2013; Ilyina et al., 2013).

Average oxygen concentrations between 200 and 700 m depth, where many tuna and billfish species forage, are projected to decrease throughout the mid- and high-latitudes (Fig. 4.6a-b). The greatest and most coherent decreases are projected to occur in the eastern North Pacific Ocean (Fig. 4.6a-b), which already has lower mean oxygen concentrations compared to

the western half of the basin (Fig. 4.6a). Within the eastern North Pacific between 20-40°N, average oxygen concentrations between 200-700 m depth are projected to decrease by as much as 0.6 ml l^{-1} from 1971–2000 to 2071–2100 (Fig. 4.6b). The depth at which oxygen concentrations drop to 3.5 ml l^{-1} (a threshold hypoxic concentration for several species of tuna and billfish including yellowfin and skipjack tunas, marlins, and sailfish) is also projected to shoal throughout most of the global oceans, reducing available oxygenated vertical habitat space for many species (Fig. 4.6c-d). By 2071-2100, projected shoaling of the 3.5 ml l^{-1} oxygen level is greatest in the North Pacific and parts of the Southern Ocean, moving upward by 60-100 m from a historical average of about 450-600 m depth in the former and by over 150 m from a historical average of >1,000 m depth in the latter. Projected changes in oxycline depth are spatially similar to those of the 3.5 ml l^{-1} hypoxic depth, with a predicted shoaling of over 150 m in some places within the North Pacific and Southern Oceans (Fig. 4.6, bottom row). Along 160°W in the North Pacific, the largest projected decreases in oxygen concentration (between 0.8-1 ml l^{-1}) are centred around ~450 m depth, with the greatest potential impacts on swordfish and yellowfin, bigeye, Pacific bluefin, and albacore tunas residing in the area (Fig. 4.7). Oxygen concentrations are projected to decrease greatly throughout most of the present-day range of Pacific bluefin tuna in particular. Comparisons between current and future oxygen conditions experienced by Pacific bluefin tuna within their present-day habitats (based on depth limits listed in Table 4.3) further support the notion that this species will likely experience some of the largest decreases in oxygen content, assuming that they maintain their present-day range (Fig. 4.8).

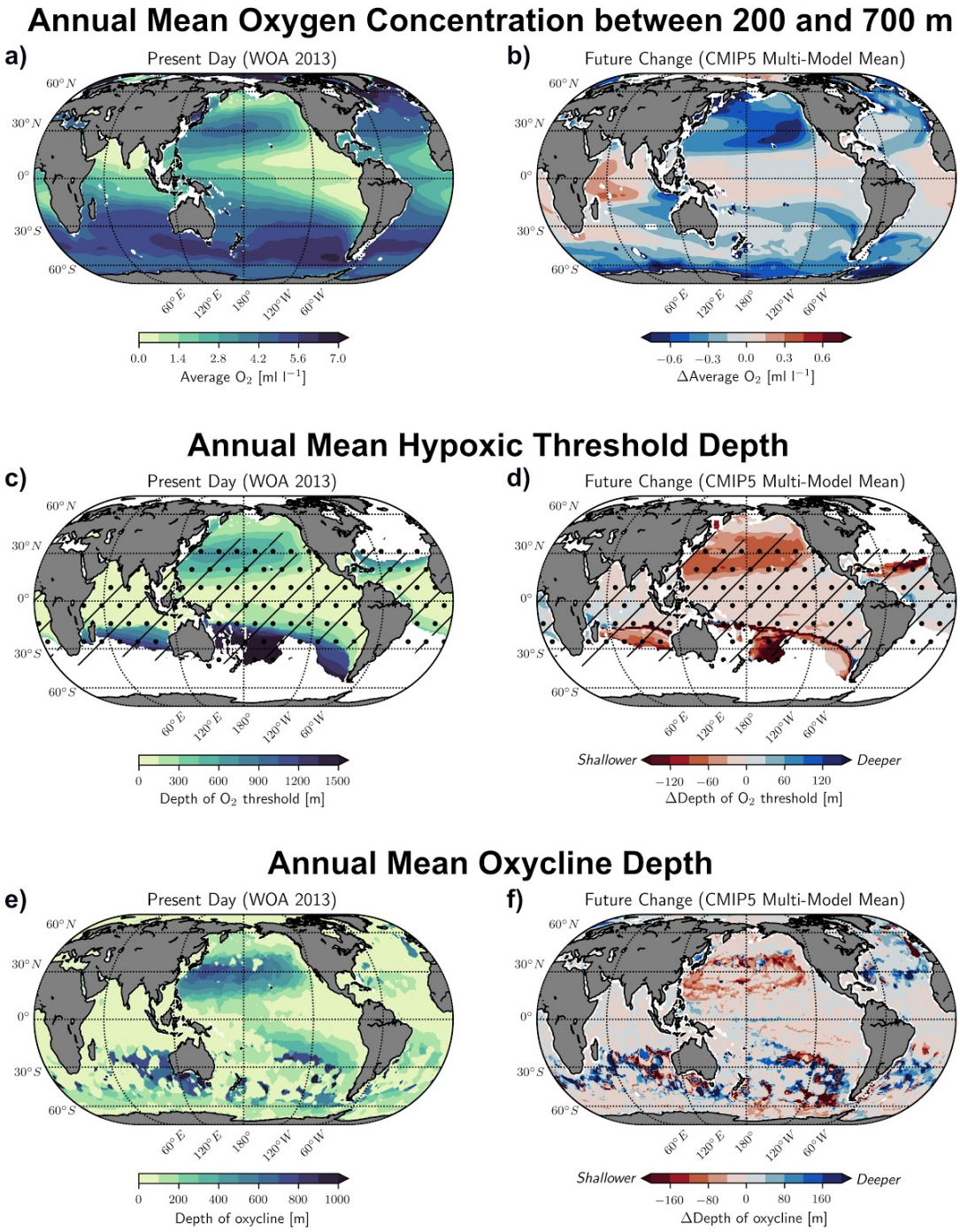

Figure 4.6 | Historical and projected changes in annual mean (a-b) average oxygen concentrations between 200 and 700 m, (c-d) threshold hypoxic depths (where oxygen concentrations decrease below 3.5 ml l^{-1}), and (e-f) upper oxycline depths (lower row). Historical oxygen data are from WOA 2013. Projected changes (RCP8.5 scenario, 2071–2100 minus 1971–2000) are from six Earth System Models included in the Coupled Model Intercomparison Project Phase 5 (CMIP5), interpolated onto the same grid as WOA 2013 (1º x 1º horizontal grid with 25-m depth intervals). Hatching and stippling denote skipjack and yellowfin tuna habitat, respectively (IUCN 2011, 2014). Threshold hypoxic and upper oxycline depths are shallowest in tropical regions and deepest in temperate regions. They are projected to be shallower in the North and South Pacific and the Southern Indian Ocean by 2100.

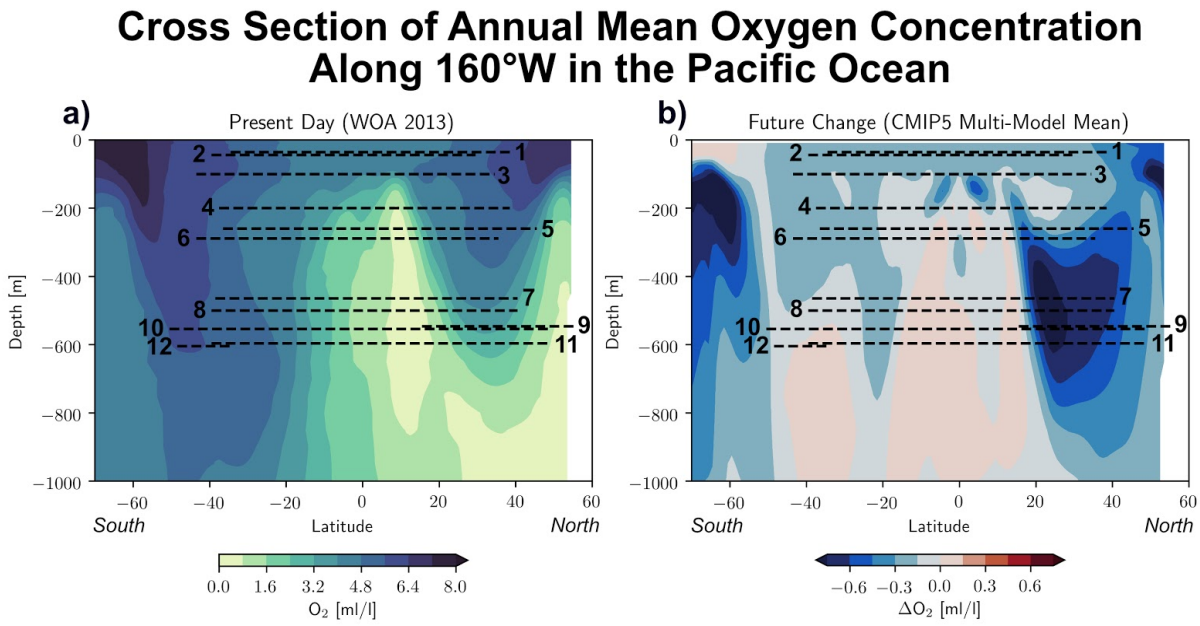

1) Sailfish, **2)** Blue Marlin, **3)** Black Marlin, **4)** Shortbill Spearfish, **5)** Skipjack Tuna
6) Striped Marlin, **7)** Yellowfin Tuna, **8)** Bigeye Tuna, **9)** Pacific Bluefin Tuna, **10)** Swordfish,
11) Albacore Tuna, **12)** Southern Bluefin Tuna

Figure 4.7 | Historical (a) and projected changes in (b) annual mean oxygen concentrations along 160°W in the Pacific. Each species' present-day, frequently-visited lower depth range (as described in the caption of Table 4.3) is plotted across its latitudinal extent at this longitude. Historical oxygen data are from WOA 2013. Projected changes (RCP8.5 scenario, 2071–2100 minus 1971–2000) are from six Earth System Models included in CMIP5, interpolated onto the same grid as WOA 2013. Oxygen concentrations are the lowest in the tropics. The greatest decreases in oxygen concentrations by 2100 are projected to occur at temperate latitudes within the depth ranges of various tuna and billfish species.

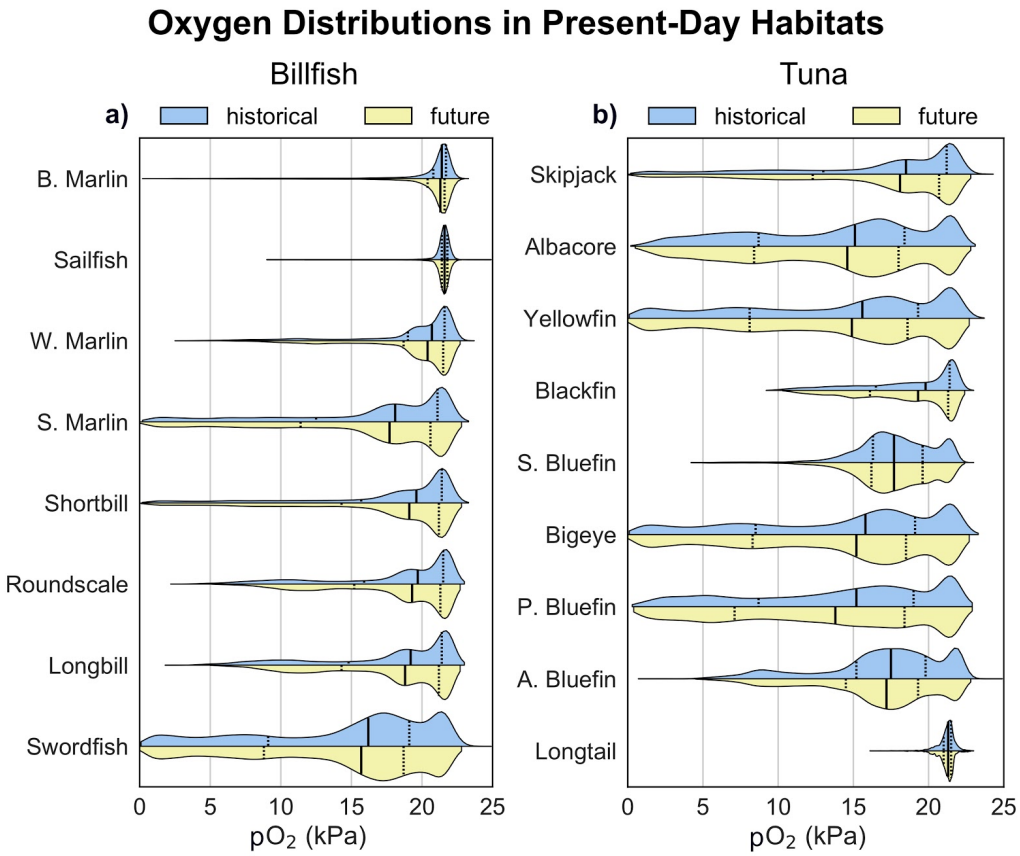

Figure 4.8 | Historical and projected oxygen distributions encountered in present-day, species-specific tuna (a) and billfish (b) habitats. For simplicity, we assumed a constant, frequently-visited vertical range throughout each species' horizontal extent to delineate present-day, three-dimensional habitat. Species-specific horizontal ranges were taken directly from the IUCN Red List (IUCN 2011, 2014), while depth ranges were taken from the IUCN Red List (IUCN 2011, 2014) with six modifications, as detailed in the caption of Table 4.3. Historical oxygen partial pressure (pO_2) data are from WOA 2013. Future pO_2 projections were generated by adding CMIP5-modelled changes (RCP8.5 scenario, 2071–2100 minus 1971–2000) to WOA 2013 historical values. The two vertical dashed black lines within each distribution curve indicate the 25th and 75th percentiles of pO_2 encountered (as listed for each species in Fig. 4.4), while the vertical solid black line indicates the 50th percentile. Oxygen partial pressures encountered vary greatly among the different species. Oxygen pressures are projected to decrease in the habitats of most tuna and billfish species by 2100.

It is important to note here (specifically, in the discussion of Section 4.4.1 and in generating Table 4.3, Fig. 4.4, Fig. 4.7, and Fig. 4.8) that all species-specific, present-day habitats are assumed to be rectangular boxes. In other words, we apply a single static, oft-frequented depth range (listed in Table 4.3) over each species' horizontal habitat to represent its three-dimensional distribution (using data from IUCN 2011; 2014 with minor modifications).

In reality, each species-specific depth range (as well as the amount of time spent at each depth) varies greatly over space and time (e.g., Barkley et al., 1978; Block et al., 2001; Schaefer and Fuller, 2002; 2007; 2010; Schaefer et al., 2009a, 2009b; 2014; Wilson et al., 2005; 2015). This is because temperature and oxygen levels also exhibit large spatio-temporal variabilities, and vertical movements are constrained by temperature and oxygen levels themselves rather than depth *per se* (Prince et al., 2010; Bernal et al., 2017). There are, however, currently not enough data to properly resolve the spatial and temporal variations of each species' vertical movements over its entire horizontal range. For simplicity, we therefore choose a spatio-temporally constant, oft-frequented depth range throughout each species' horizontal distribution to define its present-day three-dimensional habitat. Without more and better standardized data, it is also difficult to distinguish between the absolute maximum depth to which each species can descend, the deepest average descent, and the depth above which they spend the majority of their time. Within these constraints, we attempt to define a reasonable depth range that each species frequently occupies, based on IUCN data and results from tagging studies (Table 4.3). We acknowledge, however, that there may be minor inconsistencies among species in how the depth range most frequently occupied is defined.

4.4.2 Projecting oxygen-induced habitat suitability changes with statistical models

One of the most straightforward and common approaches for projecting future habitat changes is to use statistical methods to relate present-day species distributions to observed environmental conditions, and to then apply these relationships to projections of future

environmental conditions (Hartog et al., 2011; Stock et al., 2011; Hazen et al., 2013; Muhling et al., 2015; Coro et al., 2016; Peck et al., 2016). The main advantages of these models are that they allow for multivariate, non-linear relationships among variables; require relatively few input variables; and are conceptually simple as they require no explicit parametrizations of physiology, behaviour, or ecosystem dynamics (Dormann et al., 2012; Peck et al., 2016). Because key mechanistic processes are not included in the models, however, present-day empirical relationships are assumed to hold into the future, which may not be a valid assumption in all cases (Dormann et al., 2012; Horodysky et al., 2015; 2016; Peck et al., 2016). Most statistical models also rely more on temperature than oxygen, due to the greater availability of temperature data (both environmental and from electronic tracks), and the abundance of studies showing the importance of thermal limits in determining the distributions of tuna and billfish species. Muhling et al. (2017) were, however, able to use temperature and chlorophyll measurements at the surface, temperature and oxygen concentrations at 100 m depth, and concurrent data on the presence or absence of adult Atlantic bluefin tuna to create a statistical model capable of predicting this species' distributions in the North Atlantic Ocean. They found that oxygen concentration at 100 m depth was the most important predictor of habitat suitability out of the four variables considered. Application of the model to future projections from GFDL-ESM2M (one of the CMIP5 Earth System Models, using the RCP8.5 scenario and comparing 1971–2000 to 2071–2100) showed a general loss of habitat with climate change, especially south of ~40°N as well as in the region south of Greenland, which was in agreement with projections from an oxygen balance model (as discussed in Section 4.4.4) applied to the same GFDL-ESM2M projections.

4.4.3 Projecting Oxygen-Induced Habitat Suitability Changes with a P_{50} Depth-Based Trait Analysis Model

Blood oxygen affinity (quantified by the partial pressure of oxygen required to bring blood oxygen content to 50% of the maximum oxygen carrying capacity, and commonly referred to as the "P_{50}") can predict hypoxia tolerance in a range of fish species (Farrell and Richards, 2009; Mandic et al., 2009; Wells, 2009). Hypoxia-tolerant species (including bigeye tuna) have blood with high oxygen affinity (i.e., low P_{50}) (Lowe et al., 2000). While this high blood oxygen affinity allows species like bigeye to be more tolerant of low ambient oxygen conditions, it may also lead to slower rates of oxygen delivery if blood oxygen affinity remains too high at the tissues (Yang et al., 1992). Blood oxygen affinity at tissues also depends, however, on whether arterial blood undergoes temperature changes as it passes through gills (i.e., "open system" temperature changes where the blood is free to exchange oxygen and CO_2 with the respiratory medium) or as it passes through the vascular countercurrent heat exchangers possessed by tunas (i.e., "closed system" temperature changes where blood is not free to exchange oxygen and CO_2 with the respiratory medium) (Brill and Bushnell, 1991; 2006; Carey and Gibson, 1977; 1983; Clark et al., 2008; Jones et al., 1986; Lowe et al., 2000; Stevens, 1982; Stevens and Carey, 1981; Rossi-Fanellai and Antoninie, 1960). These countercurrent heat exchangers allow tunas to maintain muscle temperatures significantly above ambient water temperatures and can therefore help lower blood oxygen affinity at muscles, where oxygen off-loading and delivery is required. Bigeye tuna are particularly adept at maintaining elevated muscle temperatures during deep descents (into water as cold as ~5°C) by controlling the efficacy of their vascular countercurrent

heat exchangers before making rapid ascents back to the warm uniform temperature surface layer to get a "gulp" of heat in a way analogous to a marine mammal returning to the surface to get a breath (Boye et al., 2009; Holland and Sibert, 1994). At depth where muscle temperatures are significantly above ambient temperature, arterial blood in bigeye tuna is thus subjected to "closed system" temperature changes. The net result is large decreases in blood oxygen affinity from high (low P_{50}) to low (high P_{50}) values that are more characteristic of less hypoxia-tolerant species such as skipjack, yellowfin, and bluefin tunas (Brill and Bushnell 1991; 2006; Clark et al., 2008). These large decreases in blood oxygen affinity (increases in P_{50}) as the blood travels from gills to warm tissues ensures adequate rates of oxygen delivery in the swimming muscles of bigeye tuna. Studies quantifying the oxygen affinity of isolated haemoglobin (Sharp, 1975; 1983) and whole blood (Cech et al., 1984) from albacore all suggest that this species is relatively hypoxia-intolerant (although more hypoxia-tolerant than yellowfin or skipjack tunas).

P_{50} depth is the shallowest depth in the water column where the partial pressure of oxygen (pO_2) drops below the minimum value required for blood to reach its P_{50} value. It thus denotes the depth below which oxygen becomes limiting and serves as a mechanistic way of estimating species-specific vertical habitat range in regions where hypoxic conditions exist at depths reachable by tunas (Mislan et al., 2016). The spatial distribution and extent of P_{50} depths vary greatly among tuna species. For example, the vertical movements of more hypoxia-tolerant species (e.g., bigeye tuna) are constrained by P_{50} depth over smaller geographic areas than less hypoxia-tolerant species (e.g., yellowfin or Pacific bluefin tunas) (Mislan et al., 2017) (Fig. 4.9). The shallowest P_{50} depths are in the tropics, occurring above 100 m in some areas for the least hypoxia-tolerant tuna species, including yellowfin tuna (Fig. 4.9) (Mislan et al., 2017).

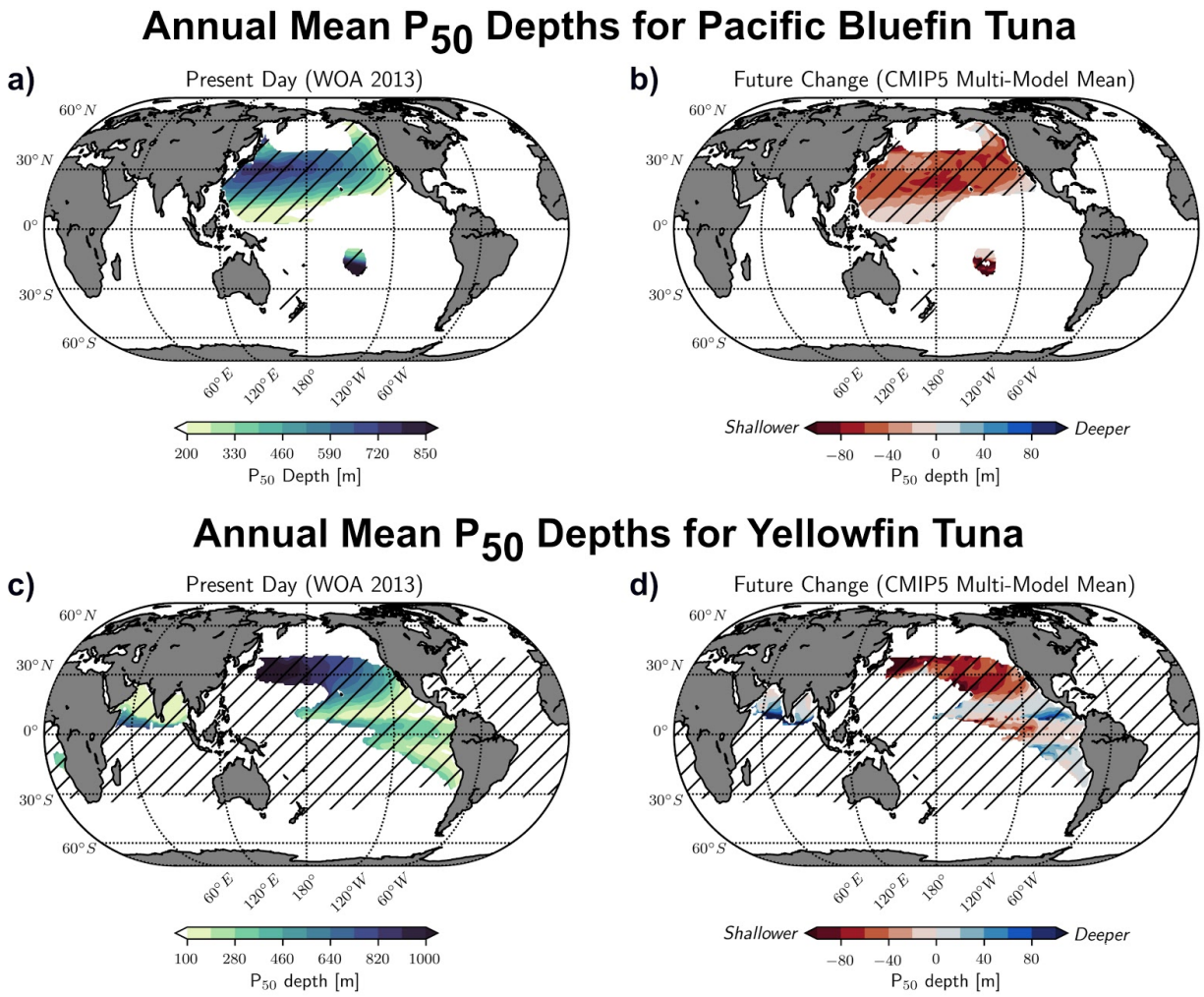

Figure 4.9 | Historical and projected changes in P_{50} depths within the present-day habitats of Pacific bluefin tuna (a-b) and yellowfin tuna (c-d). P_{50} depth is the shallowest depth at which blood is <50% oxygenated. Historical data are from WOA 2013. Projected changes (RCP8.5 scenario, 2071–2100 minus 1971–2000) are from six Earth System Models included in CMIP5, interpolated onto the same grid as WOA 2013. White regions of the ocean do not contain P_{50} depths for the given species. Hatching denotes the given species' habitat, based on IUCN geographic ranges (IUCN 2011, 2014). P_{50} depths in Pacific bluefin tuna habitats are projected to be universally shallower in 100 years. Changes in P_{50} depths within yellowfin tuna habitats are projected to vary spatially.

By the end of the 21st century, P_{50} depths of multiple tuna species are projected (under the RCP8.5 scenario, using the six CMIP5 models listed in Section 4.4.1) to shoal in temperate regions, and to either shoal or deepen within the tropics depending on the specific location. Multi-species P_{50} depths are projected to become shallower in the subtropical and mid-latitude North Pacific Ocean in particular (Fig. 4.9), where the greatest decreases in oxygen content are

projected to occur (Mislan et al., 2017; Bopp et al., 2013). For Pacific bluefin tuna, whose geographic range is almost entirely in the North Pacific, P_{50} depths are projected to be shallower throughout its range (Fig. 4.9). Yellowfin tuna, on the other hand, have a broader geographic range than Pacific bluefin tuna, with populations in the temperate and Tropical Pacific as well as the Arabian Sea and the Bay of Bengal. The P_{50} depths of yellowfin tuna are very shallow in the tropics, but are projected to become deeper by 2100 in the areas where they are currently shallowest (i.e., between 5°N-20°N and 5°S-20°S in the eastern Pacific) (Fig. 4.9). In other regions within the eastern Pacific (poleward of 20°N and within 5° of the Equator), P_{50} depths of yellowfin tuna are projected to be shallower by 2100. These bidirectional changes could potentially alter the vertical range of yellowfin tuna over large geographic areas. Projections of oxygen levels in the eastern Pacific within 20° of the Equator are not considered to be robust (Bopp et al., 2013; Cabre et al., 2015) however, and may change as models are improved. Changes in spawning regions are another factor that needs to be considered. P_{50} depths of Southern bluefin tuna are projected to be 80 to 600 m shallower by 2100 in their main spawning region off the west coast of Australia (Mislan et al., 2017). P_{50} depths are likely key in determining billfish habitat use as well, but physiological parameters needed to calculate species-specific P_{50} depths for billfish are not available. Based on their similar vertical ranges and hypoxic tolerances (Fig. 4.4), however, we hypothesize that future changes in P_{50} depths of marlin will be closer to those of yellowfin tuna and those of swordfish will be closer to those of bigeye tuna. In summary, P_{50} depth analysis is important for understanding how climate change-driven alterations in oxygen levels within the pelagic environment will impact individual species with different hypoxic tolerances.

4.4.4 Projecting oxygen-induced habitat suitability changes with metabolic oxygen balance models

The oxygen balance model used to evaluate future changes in Atlantic bluefin tuna habitat by Muhling et al. (2016) includes three sub-components: an oxygen demand model, an oxygen supply model, and a cardiac transport model. Overall "oxygen balance" is calculated by subtracting metabolic oxygen demand from estimates of oxygen supply, both of which are influenced by water temperature, the amount of dissolved oxygen in the water, and fish swimming speed. All three sub-models were parameterized using published studies on captive tunas (yellowfin, skipjack and bluefin tunas). Muhling et al. (2016) show a case study for Atlantic bluefin tuna, but the oxygen balance model has also been modified for yellowfin tuna. Projections for both species groups (i.e., combined bluefin tunas, yellowfin tuna) are thus shown here. As experimental data are from juvenile fish (due to difficulties keeping adults in captivity), the oxygen balance models may be overly conservative at cooler temperatures (Graham and Dickson, 2001).

Metabolic oxygen demand (MO_2) with water temperature and swimming speed is estimated from Generalized Additive Models (GAMs) trained on experimental data (Blank et al., 2007; Brill, 1987; Clark et al., 2010; Dewar and Graham, 1994). Yellowfin tuna MO_2 is assumed to be constant when temperature is <15°C, as no measurements are available from lower temperatures. Bluefin tuna MO_2 increases when temperatures fall below ~15°C, but there is no evidence that tuna species predominantly caught in tropical and subtropical areas (e.g., skipjack and yellowfin tunas) respond similarly. The oxygen supply model is adapted from equations

reported by Bushnell and Brill (1991). The volume of water passing through the gills (ventilation volume) depends on swimming speed and mouth gape, with the latter increasing under hypoxic conditions. Oxygen delivery is then dependent on ambient dissolved oxygen concentration, ventilation volume, and percent utilization (i.e., the percent of the oxygen content in the inhaled water stream removed by the cardio-respiratory system). Delivery of oxygen to tissues is dependent on cardiac output, and the difference in oxygen content of arterial and venous blood (Brill and Bushnell, 2001). These equations are parameterized by combining results from Blank et al. (2002; 2004), Korsmeyer et al. (1997 a, b), and Clark et al. (2008, 2013b) into a multivariate exponential relationship, where both temperature and swimming speed determine heart rate, and thus cardiac output (assuming the volume of blood pumped per heartbeat remains constant, which is true in tunas; Brill and Bushnell 2001). Oxygen balance (i.e., surplus or deficit) is determined by subtracting metabolic demand from the lesser of oxygen delivery through the gills, and oxygen delivery via the circulatory system.

Application of the oxygen balance model (Muhling et al., 2016) to annual temperature and dissolved oxygen climatologies from the World Ocean Atlas (Garcia et al., 2014; Locarni et al., 2013) shows that regions of highest oxygen balance in the upper 50 m of the water column correspond closely to regions of highest catch for both yellowfin and bluefin tunas (FAO, 2017). In particular, favourable conditions are present on Atlantic bluefin tuna fishing grounds in the north-east Atlantic Ocean and Mediterranean Sea (Teo and Boustany, 2016), on Southern bluefin tuna fishing grounds along 40°S between South Africa and New Zealand (Hobday et al., 2016), and along migratory pathways used by Pacific bluefin tuna to cross between Japan and the California Current region (Fujioka et al., 2016) (Fig. 4.10a,c). Metabolic stress in the upper

ocean is thought to be higher on Atlantic and Pacific bluefin tunas' spawning grounds in the Gulf of Mexico, south of Indonesia, and between Taiwan and Japan, due to warm upper ocean conditions in these areas. Conditions at 200 m are, however, more favourable and it has been proposed that adult Atlantic bluefin tuna may thermoregulate by descending to cooler depths in these areas (Teo et al., 2007).

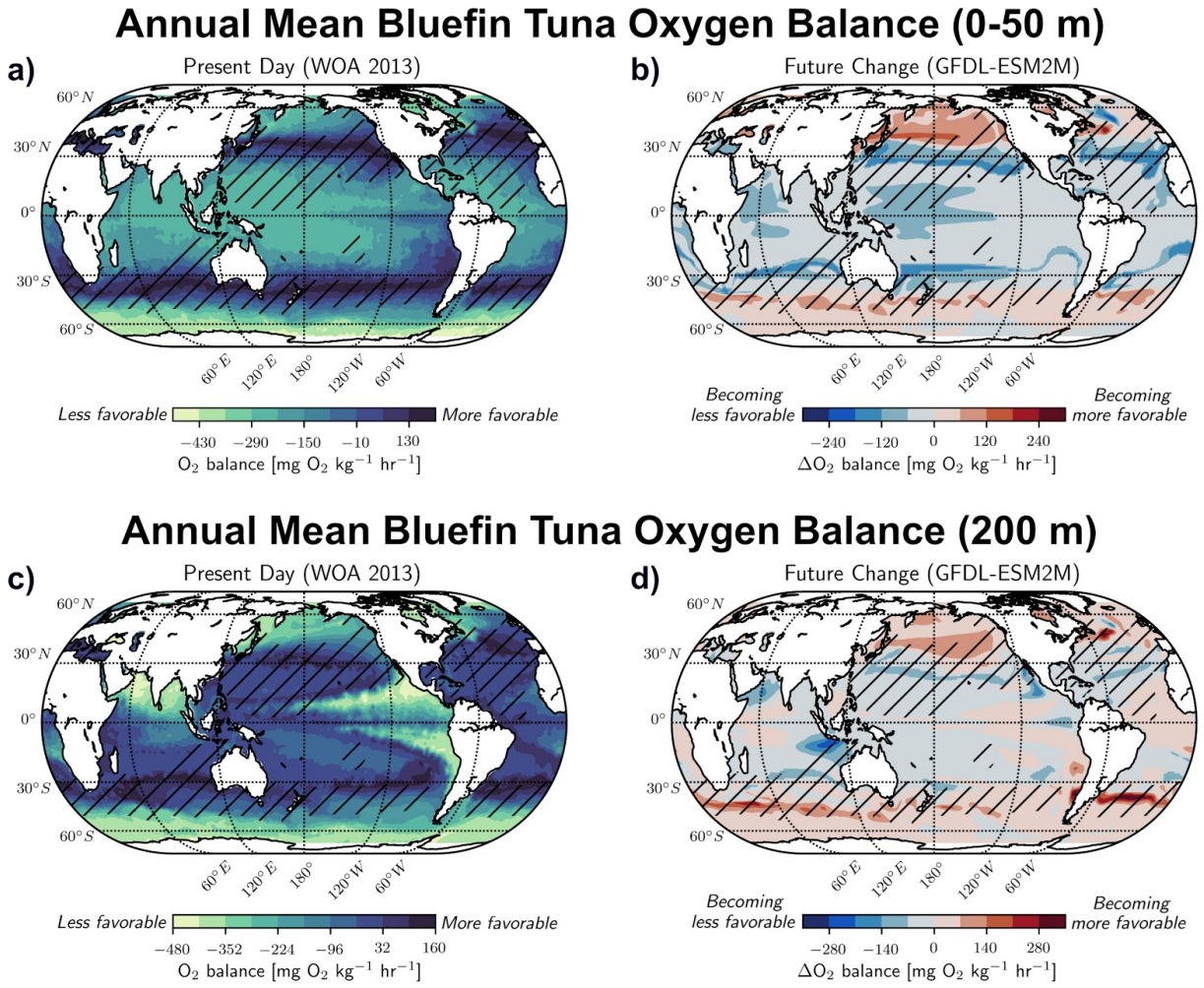

Figure 4.10 | Annual mean bluefin tuna (all three species combined) oxygen balance. Hatching represents current bluefin (all three species) tuna habitat (IUCN 2011, 2014). a.) 0-50 m depth oxygen balance in recent historical past (from World Ocean Atlas, temperature climatology 1995–2012, oxygen climatology 1900–2012). b.) Future change in 0-50 m depth oxygen balance from GFDL-ESM2M (RCP8.5 scenario, 2071–2100 minus 1971–2000). c.) Same as a, but at 200 m depth. d.) Same as b, but at 200 m depth.

Projections from GFDL-ESM2M (one of the CMIP5 Earth System Models, using the RCP8.5 scenario and comparing 1971–2000 to 2071–2100) show poleward shifts in annual mean favourable metabolic habitat for all three species of bluefin tunas in the upper 50 m of the water column as a result of warming and deoxygenation (Fig. 4.10b). There is also a projected reduction in suitability at 200 m depth on Southern bluefin tuna spawning grounds south of Indonesia and in Pacific bluefin tuna habitat in the southern California Current, primarily due to stronger deoxygenation at depth in these areas (Fig. 4.10d). Conversely, some parts of the Southern Ocean may become more favourable, both in the upper 50 m of the water column and at 200 m depth. The P_{50} depth-based trait analysis model discussed in Section 4.4.3 projected a shoaling of Pacific bluefin tuna P_{50} depth throughout the North Pacific, while the oxygen balance model discussed here suggests that habitat suitability in the upper water column may decline as a result of warming and deoxygenation. In some parts of the North Pacific, it is therefore possible that certain species, such as Pacific bluefin tuna, may experience habitat loss at both the upper and lower bounds of their vertical habitat within their current range.

In contrast to the three species of bluefin tunas, present-day favourable metabolic habitat for yellowfin tuna covers most of the tropics and subtropics between 40°N and 40°S, with some lower suitability near the equator (Fig. 4.11a). This corresponds well with the observed distribution of yellowfin tuna, which are caught on various fishing gears between these latitudes in all oceans, except for some parts of the eastern Pacific Ocean (FAO, 2017). Conditions at 200 m depth also appear to be favourable for yellowfin tuna throughout much of the subtropics, with the exception of the oxygen minimum zones in the eastern equatorial Atlantic and Pacific Oceans as well as the northern Indian Ocean (Fig. 4.11c). Projections of future conditions suggest a loss

of yellowfin tuna habitat in near-surface waters within the tropics, due to warming and deoxygenation, though this may be partially offset by poleward habitat expansion (Fig. 4.11b). Habitat suitability at 200 m depth of some subtropical regions may improve, with warming temperatures and weaker deoxygenation. The area south of Indonesia may, however, become less habitable in association with stronger deoxygenation (Fig. 4.11d).

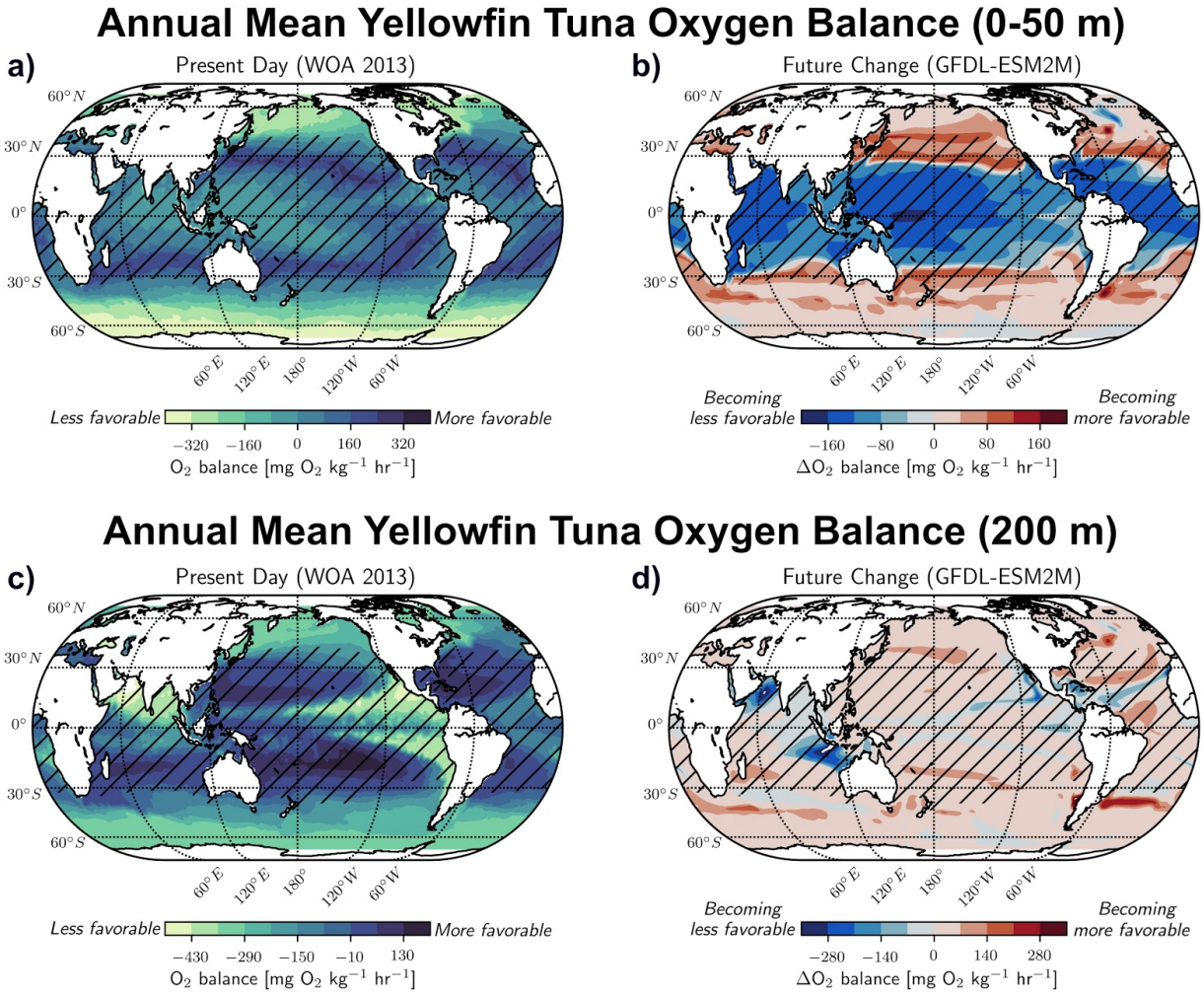

Figure 4.11 | Annual mean yellowfin tuna oxygen balance. Hatching represents current yellowfin tuna habitat (IUCN 2011, 2014). a.) 0-50 m depth oxygen balance in recent historical past (from World Ocean Atlas, temperature climatology 1995–2012, oxygen climatology 1900–2012). b.) Future change in 0-50 m depth oxygen balance from GFDL-ESM2M (RCP8.5 scenario, 2071–2100 minus 1971–2000). c.) Same as a, but at 200 m depth. d.) Same as c, but at 200 m depth.

4.4.5 Projecting Oxygen-Induced Habitat Suitability Changes with Process-Based Models (SEAPODYM and APECOSM-E)

Based on advection-diffusion-reaction equations, the spatial ecosystem and population dynamics model (SEAPODYM) was developed to investigate spatial tuna population dynamics under the influence of both environmental conditions and fishing (Lehodey et al., 2003). It has undergone various refinements since its initial development and includes all of the following features: (1) forcing by temperature, currents, primary production, and oxygen concentration; (2) predictions of spatio-temporal distributions of mid-trophic level micronekton; (3) predictions of spatio-temporal distributions of tuna populations by age; (4) predictions of total catch size by fleet; and (5) parameter estimation (Lehodey et al., 2010; Lehodey et al., 2013; Lehodey et al., 2015). Tunas' spatial and population dynamics are determined using modelled habitat indices, growth rates, and mortality rates. Feeding habitat is determined by the accessibility of prey, while spawning habitat is determined by temperature preferences, availability of food suitable for larvae, and predator pressure. Larval recruitment is assumed to be a function of spawning stock biomass, the extent of spawning habitat, larval food availability, and larval mortality during advection by currents.

Using SEAPODYM and future biogeochemical changes from IPSL-CM4 (an older CMIP3, rather than CMIP5, Earth System Model) under scenario A2 (similar to scenario RCP8.5, but reaching ~850 ppm CO_2 rather than ~950 ppm by 2100), Lehodey et al. (2013) projected that skipjack tuna habitat will expand within the central and eastern Pacific as well as towards higher latitudes, but will shrink within the increasingly warm and decreasingly

productive west-central Tropical Pacific by the end of the 21st century. A simulation replacing projected oxygen concentrations with present-day climatologies did not change these results, indicating that the projected changes in skipjack tuna habitat are principally driven by changes in temperature, primary productivity, and currents (Lehodey et al., 2013). Similar projections of future albacore habitat, on the other hand, indicate that oxygen concentration decreases in the South Pacific projected by IPSL-CM4 in the next half-century will lead to weaker recruitment here, with a strong negative impact on the abundance of young south Pacific albacore (Lehodey et al., 2015). Projected changes in bigeye tuna habitats and populations are also likely to be heavily influenced by spatially variable changes in oxygen concentrations by 2100 (Lehodey et al., 2010). For example, the feeding habitat of adult bigeye tuna is projected to improve in the eastern Tropical Pacific because subsurface increases in dissolved oxygen concentrations will allow for access to deeper prey. At the same time, natural mortality rates of older bigeye tuna are projected to increase within the western-central Pacific due to decreasing oxygen concentrations (along with overly warm temperatures and decreases in food supply) (Lehodey et al., 2010). This increase in mortality, coupled with the migration of surviving fish to more favourable habitat in the east, may lead to declining adult biomass in the western Pacific by the end of the 21st century.

Like SEAPODYM, the Apex Predator ECOSystem Model - Estimation (APECOSM-E) simulates both spatial and temporal dynamics of skipjack tuna biomass and abundance. Unlike SEAPODYM, however, APECOSM-E mechanistically (rather than empirically) links environmental factors, metabolic rates, and behavioural responses via dynamic energy budget theory. This technique involves tracking the energy budget of an individual organism throughout

its life stages (Dueri et al., 2014). Despite their different methods of representing biological processes and the slightly different Earth System Models driving their ocean biogeochemistry (APECOSM-E uses CMIP5 model IPSL-CM5A-MR and scenario RCP8.5), both models exhibit similar changes in skipjack tuna distribution within the Pacific Ocean by 2100, projecting shifts away from the western Pacific and expansions into the eastern Pacific and towards higher latitudes. In both models, changes in temperature and access to food were the dominant factors driving these distribution shifts, while changes in oxygen content played a relatively minor or insignificant role.

4.5 Ecosystem consequences

A thorough understanding of the ecological relationships that exist within the modern-day ocean is needed to better predict how species-specific responses to three-dimensional changes in temperature and oxygen will affect ecosystem structure and dynamics. Currently available data suggest that species-specific vertical movements result in niche partitioning in areas where different species are sympatric (e.g., Bernal et al., 2009; 2017). For example, the vertical movement patterns of swordfish and bigeye tuna appear to directly follow the diurnal vertical movements of the squid, euphausiids, and mesopelagic fish that are associated with the deep sound scattering layer (SSL) (Bertrand et al., 1999; 2002a; 2002b; Carey, 1990; Carey and Robison, 1981; Dagorn et al., 2000a; 2000b; 2000c; Grudinin, 1989; Josse et al., 1998; Longhurst, 1976; Marchal et al., 1993; Marchal and Lebourges, 1996; Nakamura, 1993; Roger and Grandperrin, 1976; Yatsu et al., 1999). This is in contrast to the shallower habitat use of yellowfin and skipjack tunas, although both of these species do appear

to make descents, albeit brief, to depths occupied by SSL organisms during the daytime (Schaefer and Fuller 2007; Schaefer et al. 2007; 2009a; 2009b). This apparent resource partitioning is supported by stomach content analyses, which show that bigeye tuna generally select mesopelagic prey from the SSL, while yellowfin tuna feed primarily on epipelagic prey from the mixed layer when the two tuna species are caught in the same areas (Holland and Grubbs 2007; King and Ikehara, 1956; Kornilova, 1981; Pelczarski, 1988; Portier et al., 2004; 2007). The fishes and crustaceans of the SSL migrate downward during the day into cold, dark, low-oxygen waters as a refuge against predation, and can do so due to a suite of morphological, physiological, and biochemical adaptations (e.g., Childress and Nygaard, 1974; Belman and Childress, 1975; Childress, 1971; Sanders and Childress, 1990). Bigeye tuna and swordfish have, however, also obviously evolved physiological abilities to sustain extended forays into the SSL organisms' predator refuge.

Tunas and billfishes are likely to display species-specific three-dimensional habitat changes due to future climate change, just as they currently display species-specific movement patterns and ecological niches. Differential changes in hypoxia-induced vertical habitat extents, in particular, can either decouple or enhance competition among different species. For example, in the North Pacific Ocean, projected decreases in vertical separation among several pairs of tuna species due to species-specific changes in P_{50} depths suggest future increases in the frequency of competitive interactions between tuna here (Mislan et al., 2017). Species-specific responses to climate-driven changes in oxygen and other environmental conditions may also impact bycatches (i.e., unintended catches) of tunas, billfishes, and other species (Hobday et al., 2015; Komoroske and Lewison, 2015). To our knowledge, there are currently no studies exploring the effects of

climate-driven oxygen changes on bycatches of tuna and billfish in fisheries targeting other species, nor on bycatches of other non-targeted species in tuna and billfish fisheries. Hartog et al. (2011), however, suggests that a temperature-driven increase in overlapping habitats of yellowfin and Southern bluefin tunas in the yellowfin-targeting, eastern Australian longline fishery may lead to increased bycatches of Southern bluefin tuna if current management policies do not adapt.

Future oxygen-driven changes in vertical movements and spatial distributions of prey species exploited by tunas and billfish will also play an important role in determining the overall ecosystem effects induced by oxygen changes. As is the case for tunas and billfishes, changing oxygen concentrations may impact prey in species-specific ways, potentially altering established ecosystem structures and food web dynamics (e.g., Koslow et al., 2011; Gallo and Levin, 2016). Koslow et al. (2011) showed that the abundance of mesopelagic prey species decreased by 63% during periods of reduced oxygen concentration within the oxygen minimum zone of the southern California Current. This likely occurred because the prey species were forced to occupy better-oxygenated shallow (and subsequently more well-lit) waters, rendering them more vulnerable to visually orienting predators such as tunas and billfishes. Changes in populations of these mid-trophic level mesopelagic prey species (which are both major consumers of zooplankton and major food sources for tunas, billfishes, and a wide range of other fish, squids, seabirds, and marine mammals) could have far-reaching impacts on the abundance of tunas and billfishes in particular, and the structure of pelagic food webs in general, which may be either positive or negative. Future changes in vertical habitat usage driven by changes in oxygen content may also alter population structures via changes in species size and productivity. For

example, Prince and Goodyear (2006) showed that enhanced coupling between predator and prey likely leads to increased foraging opportunities and therefore larger mean body sizes of sailfish in the hypoxia-compressed habitats of the eastern Tropical Pacific and Atlantic Oceans, as compared to the well-oxygenated western North Atlantic Ocean. Whether climate change will lead to enhanced or decreased coupling between predator and prey will depend on region-specific changes in oxygen and temperature distributions, as well as species-specific differences in hypoxic and thermal tolerances.

4.6 Societal consequences

Different tuna and billfish species are fished by different gears, depending on targeted species size and depth range, vessel capacity, and applicable regulations, among other factors (ICCAT, 2016; Ward and Hindmarsh, 2007; Williams and Terawasi, 2011). Skipjack and yellowfin tunas (the two tuna species dominating worldwide landings, Table 4.1) are primarily taken by purse seine fisheries (Fig. 4.2), which are concentrated in the tropical waters of the Pacific, Atlantic, and Indian Oceans (FAO Fisheries & Aquaculture "Global Capture Production" and "Global Catches by Stock" databases consulted on 20/12/2017). Purse seines largely target the upper water column, and may fish down to ~200 – 300 m depth depending on the target species (ICCAT, 2016; Lennert-Cody et al., 2008). Purse seining thus depends on oxycline and/or thermocline depths (below which skipjack and yellowfin tunas do not frequently dive) being shallower than ~200 – 300 m. Pelagic longline gear primarily catches larger fish (ICCAT, 2016) and can be placed in different configurations in order to set the majority of hooks at the desired depths. For example, hooks are set to occupy 50 – 100 m depth to target swordfish (at

night, when this species occupies the upper water column) and 200 – 300 m depth to target tunas (Bigelow et al. 2006; Nakano et al., 1997; Ward and Myers, 2005). In general, skipjack tuna and billfishes are caught on shallower set hooks, while albacore and bigeye tunas are more likely to be caught on deep-set gear, due to their species-specific vertical movement patterns (described in Section 4.3). Yellowfin tuna longline catchability is less correlated with depth within their vertical range (above about 300-500 m) (Nikolic et al., 2017; Prince et al., 2010; Ward and Myers, 2005). Surface gears including trolling and hook-and-line are used to catch smaller or juvenile tunas in some areas, such as the juvenile albacore fishery off of the western United States and the juvenile Atlantic bluefin tuna fishery in the north-eastern Atlantic Ocean (Fromentin, 2009; Xu et al., 2015; Nikolic et al., 2017). Other gears, such as fixed traps, drift gillnets, and harpoons, are also used to target tunas and billfishes, but fishing effort and landings are generally small compared to purse seine and longline fisheries (Miyake et al., 2010).

Ocean warming and deoxygenation have the potential to change the distribution and catchability of tunas and billfishes in three dimensions. Because tunas and billfishes are highly mobile and patchily aggregated, they are likely to exhibit complex shifts in their distributions in response to changing environmental conditions. Where surface layer temperatures become too warm, they may spend more time at depth (assuming oxygen concentrations are sufficient), potentially decreasing their vulnerability to surface-oriented fishing gears. In contrast, if oxygen minimum layers expand and shoal, relatively hypoxia-intolerant species (e.g., skipjack and yellowfin tunas) may be pushed towards the surface (assuming temperatures are not too warm), potentially increasing their vulnerability to surface-oriented fishing gears (e.g. Stramma et al., 2012). If no vertical refuge from unsuitable conditions is available, the fish may shift their

distributions horizontally, moving towards areas with temperatures or oxygen levels that are more tolerable. To maintain their livelihoods, fishers will need to adapt to potential changes in species distributions, vulnerabilities to different gear types or fishing fleets, and efficiencies of supply chains, which can be further exacerbated by factors such as rising fuel prices and decreasing government subsidies (Jones et al., 2015). Where populations of target species decrease or move away from traditional fishing grounds, fishers will have to spend more resources to catch the same species, or adapt their gear and vessel configurations to target new ones. Economic and regulatory constraints can, however, hamper the ability of fishers to effectively adapt to changing species availability, particularly if species movements cross management boundaries (Pinsky and Fogarty, 2012). Smaller-scale fisheries in developing nations and fisheries relying on vessels with limited range and low technological capabilities are likely to be most vulnerable, particularly if their exposures to the effects of climate change are also high (Ommer et al., 2009; Guillotreau et al., 2012). Communities that are strongly economically dependent on these types of small-scale fisheries for livelihoods and incomes are therefore likely to be hardest hit by climate-driven changes to fish distributions.

Climate-driven changes in habitat suitability and population structures are also likely to complicate stock assessment and management. Most current stock assessment models use standardized indices of abundance derived from fishery-dependent catch per unit effort (CPUE) data to infer changes in stock size. Environmentally-driven changes in species distribution, range, or population structure can, however, lead to trends in catchability and subsequently CPUE data that are unrelated to abundance (Bigelow and Maunder, 2006; Link et al., 2011). If not accounted for, these types of changes in CPUE data can bias estimates of abundance used in

population assessment models (Wilberg et al., 2010). Some newer stock assessment methods can incorporate effects of time-varying selectivity (Methot and Wetzel, 2013), however, and spatio-temporal models are becoming more feasible (Berger et al., 2017). In addition, indices derived from survey or fisheries data can be standardized to account for environmental effects (e.g., Lynch et al., 2012; Cao et al., 2017). Misspecification of these processes can, however, lead to biases (Hulson et al., 2013). Increasing model complexity to deal with changing environmental factors thus requires caution. Managers will have to carefully adapt their stock assessment strategies in the face of climate change in order to remain effective and ensure resource sustainability.

4.7 Conclusions and recommendations

We conclude (as have numerous other authors cited here) that climate change occurring over the next 100 years will drive species-specific changes in the population structures and (more importantly) the horizontal and vertical movement patterns of tunas and billfishes in the open ocean through changes in habitat suitability. We contend that a major factor contributing to these changes will be altered oxygen distributions throughout the global ocean. The temperate North Pacific Ocean is projected to undergo some of the largest overall decreases in oxygen content within the upper water column across ocean basins, as well as some of the most pronounced shoaling of hypoxic layers (Section 4.4.1). Species which currently reside in this region (e.g., swordfish and yellowfin, bigeye, Pacific bluefin, and albacore tunas) are thus expected to experience the most dramatic decreases in oxygen content and shoaling of P_{50} depths in their present-day habitat (Section 4.4.3). In response to these changes in oxygen (and

temperature), Pacific bluefin tuna are expected to shift northward toward more favourable oxygen conditions and to adjust their vertical habitat usage to avoid oxygen limitation from shoaling P_{50} depths (Sections 4.4.3 and 4.4.4). Atlantic bluefin tuna are projected to shift northward as well, propelled by warming, unfavourable oxygen balances (Section 4.4.4), and a loss of habitat south of ~40°N (Section 4.4.2). Yellowfin tuna are likewise expected to shift poleward toward habitats with more favourable temperature and oxygen balances (Section 4.4.4), as well as to potentially move upward in the water column within the temperate North Pacific due to shoaling P_{50} depths (Section 4.4.3). Skipjack tuna, on the other hand, are less likely to be affected by future changes in oxygen concentrations at depth because they generally remain within the well-oxygenated surface layer (Section 4.4.5). The combined effects of warming and slight deoxygenation of the upper mixed layer in tropical regions on species such as skipjack tuna remain uncertain, however. The effects of future oxygen changes on bigeye tuna population dynamics are more mixed, in that projected changes in subsurface oxygen concentrations in the eastern and western Tropical Pacific drive both increases and decreases, respectively, in SEAPODYM-predicted adult biomass (Section 4.4.5). In the South Pacific, SEAPODYM projects that younger cohorts of South Pacific albacore will be negatively affected by decreases in oxygen concentrations within their spawning grounds (Section 4.4.5). These projected changes are summarized in Fig. 4.12.

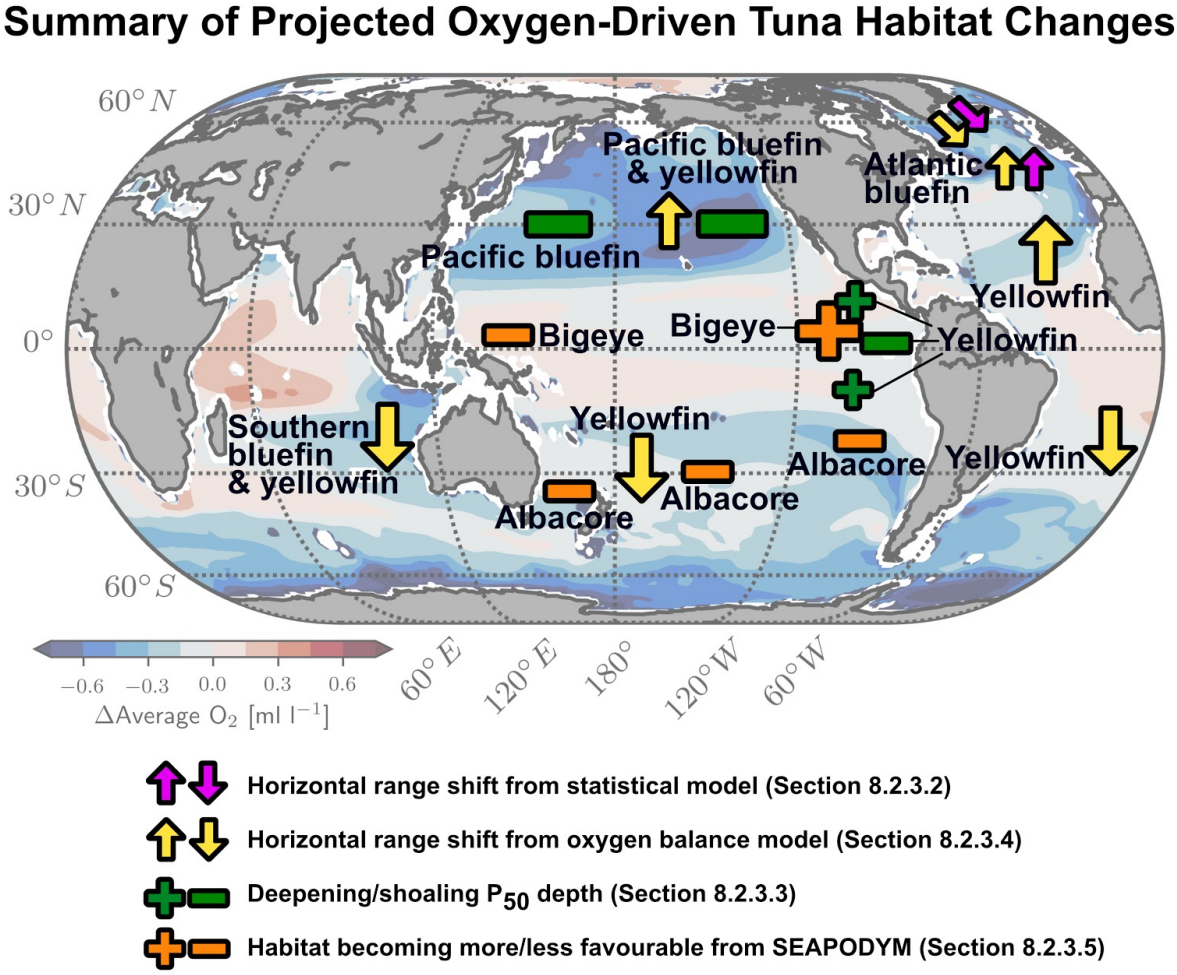

Figure 4.12 | Summary of projected changes in species-specific tuna habitats by the end of the 21st century, driven (at least partially) by projected changes in oxygen content. The background map of projected changes in average oxygen concentrations between 200 and 700 m depth is taken from Fig. 4.6b. Changes in habitat driven by factors unrelated to or not including oxygen are not shown here. For example, changes in skipjack tuna distributions within the Pacific Ocean are expected to be driven primarily by temperature and access to food; because oxygen plays an insignificant role in this case, these projected distributional shifts are not depicted here. It is important to note that there are substantial uncertainties associated with each habitat projection. Uncertainties are especially large in the eastern Tropical Pacific, due mainly to lack of model agreement on how oxygen concentrations will change within this region. For more information on uncertainties, see the sections cited in the legend.

Each type of model used to predict the effects of future oxygen changes on tunas and billfishes has its own advantages and disadvantages. The trait-based, oxygen balance, and statistical models we describe here account for only the direct effects of oxygen (and temperature) changes on tuna and billfish physiology and therefore movements. The more

complex process-based models (SEAPODYM and APECOSM-E), on the other hand, account for these direct effects as well as the indirect effects of potential oxygen-driven food-web and population structure changes. Additionally, the trait analysis, oxygen balance, and statistical models are distribution models that only consider climate change impacts in terms of potential horizontal and vertical range shifts, while SEAPODYM and APECOSM-E takes into account life histories and phenologies to produce more detailed projections of population and age structures. More complex models can be more difficult to parameterize, however, which can lead to greater uncertainty in projections. Continued work on all types of species-specific models will therefore be necessary for generating more accurate projections and reducing uncertainties.

Improvements in Earth System Models used to project future environmental conditions will also help increase the accuracy of projections related to tuna and billfish distributions in response to climate change. Current Earth System Models, including the ones used in this report, typically have horizontal resolutions of 1° or coarser. This coarse resolution cannot distinguish many important meso- and sub-mesoscale processes that can oftentimes drive observed species distributions. Furthermore, projections of biogeochemical variables (such as oxygen concentration) can be highly uncertain within these models compared to projections of purely physical variables (such as temperature). Projections of changes in oxygen concentrations in the Tropical Pacific Ocean, where the interactions between biology and the physics of ocean circulation are complicated, are especially uncertain. Part of the reason for these uncertainties is the relative lack of actual biogeochemical measurements that can be used for calibration and improvements in mechanistic understanding. Increased *in situ* monitoring of oxygen

concentrations throughout the global oceans is therefore crucial for improving Earth System Model predictions of biogeochemistry.

To further improve projections of future habitat and population changes, greater numbers of *in situ* observations of tuna and billfish habitat use are also needed. More *in situ* habitat observations, along with more laboratory studies of physiological traits, will lead to a better understanding of the environmental conditions that can predict species-specific movement patterns and therefore species-specific responses to climate change. Data products that synthesize and standardize multiple sources of information would be particularly useful. For example, contradictory records for the depth ranges frequented by various tunas and billfishes sometimes occur because a standard method for calculating these ranges does not exist. In addition, the development of a four-dimensional (three spatial dimensions and time) gridded atlas documenting the spatio-temporally variable habitats of tunas and billfishes, derived from tagging data and species-specific physiological abilities and tolerances, would be invaluable for analyzing how regional and seasonal variations in habitat usage will be impacted by deoxygenation. More detailed *in situ* observations of prey abundances and behaviours would also help improve projections of future habitat suitability changes by improving our understanding of the effects of oxygen and other environmental conditions on prey distributions and predator-prey interactions.

The most obvious way to slow or prevent projected changes in global oxygen content and resultant changes in the populations and distributions of tunas and billfishes is to reduce greenhouse gas emissions. Besides preventing climate change, however, we can also adapt to and prepare for potential future effects. A sound mechanistic understanding of how tunas and

billfishes respond to their ocean environment is key to successful adaptation. We thus argue (as have others, e.g. Brill and Hobday, 2017; Hobday et al., 2013; Kimura et al., 2010; Lehodey et al., 2011; Mislan et al., 2016; Watters et al., 2003) that illuminating the interactions between fishes, fisheries, and climate change is, and will continue to be, critical for ensuring the sustainability of tunas and billfishes into the 21st century.

4.8 References

Abascal, F. J., Mejuto, J., Quintans, M., & Ramos-Cartelle, A. (2010). Horizontal and vertical movements of swordfish in the Southeast Pacific. *ICES Journal of Marine Science*, *67*(3), 466–474. https://doi.org/10.1093/icesjms/fsp252

Antoine, D., André, J.-M., & Morel, A. (1996). Oceanic primary production: 2. Estimation at global scale from satellite (Coastal Zone Color Scanner) chlorophyll. *Global Biogeochemical Cycles*, *10*(1), 57–69. https://doi.org/10.1029/95GB02832

Bauer, R. K., Fromentin, J.-M., Demarcq, H., Brisset, B., & Bonhommeau, S. (2015). Co-Occurrence and Habitat Use of Fin Whales, Striped Dolphins and Atlantic Bluefin Tuna in the Northwestern Mediterranean Sea. *PLoS ONE*, *10*(10). https://doi.org/10.1371/journal.pone.0139218

Bauer, R. K., Fromentin, J.-M., Demarcq, H., & Bonhommeau, S. (2017). Habitat use, vertical and horizontal behaviour of Atlantic bluefin tuna (Thunnus thynnus) in the Northwestern Mediterranean Sea in relation to oceanographic conditions. *Deep Sea Research Part II: Topical Studies in Oceanography*, *141*, 248–261. https://doi.org/10.1016/j.dsr2.2017.04.006

Belman, B. W., & Childress, J. J. (1976). Circulatory adaptations to the oxygen minimum layer in the bathypelagic mysid gnathophausia ingens. *The Biological Bulletin*, *150*(1), 15–37. https://doi.org/10.2307/1540586

Berger, A. M., Goethel, D. R., Lynch, P. D., Quinn, T., Mormede, S., McKenzie, J., & Dunn, A. (2017). Space oddity: The mission for spatial integration. *Canadian Journal of Fisheries and Aquatic Sciences*, *74*(11), 1698–1716. https://doi.org/10.1139/cjfas-2017-0150

Bernal, D., Dickson, K. A., Shadwick, R. E., & Graham, J. B. (2001). Review: Analysis of the evolutionary convergence for high performance swimming in lamnid sharks and tunas. *Comparative Biochemistry and Physiology. Part A, Molecular & Integrative Physiology*, *129*(2–3), 695–726. https://doi.org/10.1016/s1095-6433(01)00333-6

Bernal, D., Sepulveda, C., Musyl, M., & Brill, R. W. (2009). The Eco-physiology of Swimming and Movement Patterns of Tunas, Billfishes, and Large Pelagic Sharks. In *Fish Locomotion: An Eco-ethological Perspective* (1st ed.). Science Publishers.

Bernal, Diego, Brill, R. W., Dickson, K. A., & Shiels, H. A. (2017). Sharing the water column: physiological mechanisms underlying species-specific habitat use in tunas. *Reviews in Fish Biology and Fisheries*, *27*(4), 843–880. https://doi.org/10.1007/s11160-017-9497-7

Bertrand, A., Bard, F.-X., & Josse, E. (2002). Tuna food habits related to the micronekton distribution in French Polynesia. *Marine Biology*, *140*(5), 1023–1037. https://doi.org/10.1007/s00227-001-0776-3

Bertrand, Arnaud, Borgne, R. L., & Josse, E. (1999). Acoustic characterisation of micronekton distribution in French Polynesia. *Marine Ecology Progress Series*, *191*, 127–140. https://doi.org/10.3354/meps191127

Bertrand, Arnaud, Josse, E., Bach, P., Gros, P., & Dagorn, L. (2002). Hydrological and trophic characteristics of tuna habitat: consequences on tuna distribution and longline catchability. *Canadian Journal of Fisheries and Aquatic Sciences*, *59*(6), 1002–1013. https://doi.org/10.1139/f02-073

Bigelow, K., Musyl, M. K., Poisson, F., & Kleiber, P. (2006). Pelagic longline gear depth and shoaling. *Fisheries Research*, *77*(2), 173–183. https://doi.org/10.1016/j.fishres.2005.10.010

Bigelow, K. A., & Maunder, M. N. (2007). Does habitat or depth influence catch rates of pelagic species? *Canadian Journal of Fisheries and Aquatic Sciences*, *64*(11), 1581–1594. https://doi.org/10.1139/f07-115

Bigelow, K. A., Hampton, J., & Miyabe, N. (2002). Application of a habitat-based model to estimate effective longline fishing effort and relative abundance of Pacific bigeye tuna (Thunnus obesus). *Fisheries Oceanography*, *11*(3), 143–155. https://doi.org/10.1046/j.1365-2419.2002.00196.x

Blackburn, M. (1965). Oceanography and the ecology of tunas. *Oceanography and Marine Biology Annual Review*, *2*, 229–322.

Blank, J. M., Morrissette, J. M., Davie, P. S., & Block, B. A. (2002). Effects of temperature, epinephrine and Ca2+ on the hearts of yellowfin tuna (Thunnus albacares). *Journal of Experimental Biology*, *205*(13), 1881–1888.

Blank, J. M., Morrissette, J. M., Landeira-Fernandez, A. M., Blackwell, S. B., Williams, T. D., & Block, B. A. (2004). In situ cardiac performance of Pacific bluefin tuna hearts in response to acute temperature change. *Journal of Experimental Biology*, *207*(5), 881–890. https://doi.org/10.1242/jeb.00820

Blank, J. M., Farwell, C. J., Morrissette, J. M., Schallert, R. J., & Block, B. A. (2007). Influence of swimming speed on metabolic rates of juvenile pacific bluefin tuna and yellowfin

tuna. *Physiological and Biochemical Zoology: PBZ*, *80*(2), 167–177. https://doi.org/10.1086/510637

Block, B. A., & Stevens, E. D. (2001). *Tuna: Physiology, Ecology, and Evolution* (Vol. 19). San Diego: Academic Press. Retrieved from https://doi.org/10.1016/S1546-5098(01)19001-1

Block, B. A., Booth, D. T., & Carey, F. G. (1992). Depth and temperature of the blue marlin, Makaira nigricans, observed by acoustic telemetry. *Marine Biology*, *114*(2), 175–183. https://doi.org/10.1007/BF00349517

Block, B. A., Jonsen, I. D., Jorgensen, S. J., Winship, A. J., Shaffer, S. A., Bograd, S. J., et al. (2011). Tracking apex marine predator movements in a dynamic ocean. *Nature*, *475*(7354), 86–90. https://doi.org/10.1038/nature10082

Block, Barbara A., Dewar, H., Blackwell, S. B., Williams, T. D., Prince, E. D., Farwell, C. J., et al. (2001). Migratory Movements, Depth Preferences, and Thermal Biology of Atlantic Bluefin Tuna. *Science*, *293*(5533), 1310–1314. https://doi.org/10.1126/science.1061197

Block, Barbara A., Teo, S. L. H., Walli, A., Boustany, A., Stokesbury, M. J. W., Farwell, C. J., et al. (2005). Electronic tagging and population structure of Atlantic bluefin tuna. *Nature*, *434*(7037), 1121–1127. https://doi.org/10.1038/nature03463

Bopp, Resplandy, L., Orr, J. C., Doney, S. C., Dunne, J. P., Gehlen, M., et al. (2013). Multiple stressors of ocean ecosystems in the 21st century: projections with CMIP5 models. *Biogeosciences*, *10*(10), 6225–6245. https://doi.org/10.5194/bg-10-6225-2013

Boustany, A. M., Matteson, R., Castleton, M., Farwell, C., & Block, B. A. (2010). Movements of pacific bluefin tuna (Thunnus orientalis) in the Eastern North Pacific revealed with archival tags. *Progress in Oceanography*, *86*(1), 94–104. https://doi.org/10.1016/j.pocean.2010.04.015

Boye, J., Musyl, M., Brill, R., & Malte, H. (2009). Transectional heat transfer in thermoregulating bigeye tuna (Thunnus obesus) – a 2D heat flux model. *Journal of Experimental Biology*, *212*(22), 3708–3718. https://doi.org/10.1242/jeb.031427

Braun, C. D., Kaplan, M. B., Horodysky, A. Z., & Llopiz, J. K. (2015). Satellite telemetry reveals physical processes driving billfish behavior. *Animal Biotelemetry*, *3*(1), 2. https://doi.org/10.1186/s40317-014-0020-9

Breitburg, D., Levin, L. A., Oschlies, A., Grégoire, M., Chavez, F. P., Conley, D. J., et al. (2018). Declining oxygen in the global ocean and coastal waters. *Science*, *359*(6371). https://doi.org/10.1126/science.aam7240

Brill, R. W. (1987). On the standard metabolic rate of tropical tunas, including the effect of body size and acute temperature change. *Fishery Bulletin*, *85*, 25–35.

Brill, R. W., & Bushnell, P. G. (2006). Effects of open- and closed-system temperature changes on blood O2-binding characteristics of Atlantic bluefin tuna (Thunnus thynnus). *Fish*

Physiology and Biochemistry, *32*(4), 283–294. https://doi.org/10.1007/s10695-006-9104-7

Brill, R. W., Holts, D. B., Chang, R. K. C., Sullivan, S., Dewar, H., & Carey, F. G. (1993). Vertical and horizontal movements of striped marlin (Tetrapturus audax) near the Hawaiian Islands, determined by ultrasonic telemetry, with simultaneous measurement of oceanic currents. *Marine Biology*, *117*(4), 567–574. https://doi.org/10.1007/BF00349767

Brill, Richard W. (1994). A review of temperature and oxygen tolerance studies of tunas pertinent to fisheries oceanography, movement models and stock assessments. *Fisheries Oceanography*, *3*(3), 204–216. https://doi.org/10.1111/j.1365-2419.1994.tb00098.x

Brill, Richard W. (1996). Selective advantages conferred by the high performance physiology of tunas, billfishes, and dolphin fish. *Comparative Biochemistry and Physiology Part A: Physiology*, *113*(1), 3–15. https://doi.org/10.1016/0300-9629(95)02064-0

Brill, Richard W., & Bushnell, P. G. (1991). Metabolic and cardiac scope of high energy demand teleosts, the tunas. *Canadian Journal of Zoology*, *69*(7), 2002–2009. https://doi.org/10.1139/z91-279

Brill, Richard W., & Bushnell, P. G. (2001). The cardiovascular system of tunas. In *Fish Physiology* (Vol. 19, pp. 79–120). Academic Press. https://doi.org/10.1016/S1546-5098(01)19004-7

Brill, Richard W., & Hobday, A. J. (2017). Tunas and their fisheries: safeguarding sustainability in the twenty-first century. *Reviews in Fish Biology and Fisheries*, *27*(4), 691–695. https://doi.org/10.1007/s11160-017-9500-3

Brill, Richard W., & Lai, N. C. (2015). 1 - Elasmobranch Cardiovascular System. In R. E. Shadwick, A. P. Farrell, & C. J. Brauner (Eds.), *Fish Physiology* (Vol. 34, pp. 1–82). Academic Press. https://doi.org/10.1016/B978-0-12-801286-4.00001-0

Bushnell, P. G., & Brill, R. W. (1991). Responses of Swimming Skipjack (Katsuwonus pelamis) and Yellowfin (Thunnus albacares) Tunas to Acute Hypoxia, and a Model of Their Cardiorespiratory Function. *Physiological Zoology*, *64*(3), 787–811.

Bushnell, P. G., & Brill, R. W. (1992). Oxygen transport and cardiovascular responses in skipjack tuna (Katsuwonus pelamis) and yellowfin tuna (Thunnus albacares) exposed to acute hypoxia. *Journal of Comparative Physiology B*, *162*(2), 131–143. https://doi.org/10.1007/BF00398338

Bushnell, P. G., & Jones, D. R. (1994). Cardiovascular and respiratory physiology of tuna: adaptations for support of exceptionally high metabolic rates. *Environmental Biology of Fishes*, *40*(3), 303–318. https://doi.org/10.1007/BF00002519

Bushnell, Peter. G., Brill, R. W., & Bourke, R. E. (1990). Cardiorespiratory responses of skipjack tuna (Katsuwonus pelamis), yellowfin tuna (Thunnus albacares), and bigeye tuna

(Thunnus obesus) to acute reductions of ambient oxygen. *Canadian Journal of Zoology*, *68*(9), 1857–1865. https://doi.org/10.1139/z90-265

Cabré, A., Marinov, I., Bernardello, R., & Bianchi, D. (2015). Oxygen minimum zones in the tropical Pacific across CMIP5 models: mean state differences and climate change trends. *Biogeosciences*, *12*(18), 5429–5454. https://doi.org/10.5194/bg-12-5429-2015

Canese, S., Garibaldi, F., Relini, L. O., & Greco, S. (2008). Swordfish tagging with pop–up satellite tags in the Mediterranean Sea. *ICCAT Collective Volume of Scientific Papers*, *62*(4), 1052–1057.

Cao, J., Thorson, J. T., Richards, R. A., & Chen, Y. (2017). Spatiotemporal index standardization improves the stock assessment of northern shrimp in the Gulf of Maine. *Canadian Journal of Fisheries and Aquatic Sciences*, *74*(11), 1781–1793. https://doi.org/10.1139/cjfas-2016-0137

Carey, F. G. (1990). *Further acoustic telemetry observations on the biology of swordfish* (Planning the future of billfishes: research and management in the '90s and beyond) (pp. 103–122). Savannah, Georgia: National Coalition for Marine Conservation Inc.

Carey, F. G., & Robison, B. H. (1981). Daily patterns in the activities of swordfish, Xiphias gladius, observed by acoustic telemetry. *Fishery Bulletin*, *79*, 277–292.

Carey, Francis G., & Gibson, Q. H. (1977). Reverse temperature dependence of tuna hemoglobin oxygenation. *Biochemical and Biophysical Research Communications*, *78*(4), 1376–1382. https://doi.org/10.1016/0006-291X(77)91444-9

Carey, Francis G., & Gibson, Q. H. (1983). Heat and oxygen exchange in the rete mirabile of the bluefin tuna, Thunnus thynnus. *Comparative Biochemistry and Physiology Part A: Physiology*, *74*(2), 333–342. https://doi.org/10.1016/0300-9629(83)90612-6

Cech, J. J., Laurs, R. M., & Graham, J. B. (1984). Temperature-Induced Changes in Blood Gas Equilibria in the Albacore, Thunnus Alalunga, a Warm-Bodied Tuna. *Journal of Experimental Biology*, *109*(1), 21–34.

Childers, J., Snyder, S., & Kohin, S. (2011). Migration and behavior of juvenile North Pacific albacore (Thunnus alalunga). *Fisheries Oceanography*, *20*(3), 157–173. https://doi.org/10.1111/j.1365-2419.2011.00575.x

Childress, J. J., & Nygaard, M. (1974). Chemical composition and buoyancy of midwater crustaceans as function of depth of occurrence off Southern California. *Marine Biology*, *27*(3), 225–238. https://doi.org/10.1007/BF00391948

Childress, J. J., & Seibel, B. A. (1998). Life at stable low oxygen levels: adaptations of animals to oceanic oxygen minimum layers. *Journal of Experimental Biology*, *201*(8), 1223–1232.

Childress, James J. (1971). Respiratory adaptations to the oxygen minimum layer in the bathypelagic mysid gnathophausia ingens. *The Biological Bulletin*, *141*(1), 109–121. https://doi.org/10.2307/1539995

Clark, T. D., Seymour, R. S., Wells, R. M. G., & Frappell, P. B. (2008). Thermal effects on the blood respiratory properties of southern bluefin tuna, Thunnus maccoyii. *Comparative Biochemistry and Physiology Part A: Molecular & Integrative Physiology*, *150*(2), 239–246. https://doi.org/10.1016/j.cbpa.2008.03.020

Clark, T. D., Brandt, W. T., Nogueira, J., Rodriguez, L. E., Price, M., Farwell, C. J., & Block, B. A. (2010). Postprandial metabolism of Pacific bluefin tuna (Thunnus orientalis). *Journal of Experimental Biology*, *213*(14), 2379–2385. https://doi.org/10.1242/jeb.043455

Clark, T. D., Farwell, C. J., Rodriguez, L. E., Brandt, W. T., & Block, B. A. (2013). Heart rate responses to temperature in free-swimming Pacific bluefin tuna (Thunnus orientalis). *Journal of Experimental Biology*, *216*(17), 3208–3214. https://doi.org/10.1242/jeb.086546

Cocco, V., Joos, F., Steinacher, M., Frölicher, T. L., Bopp, L., Dunne, J., et al. (2013). Oxygen and indicators of stress for marine life in multi-model global warming projections. *Biogeosciences*, *10*(3), 1849–1868. https://doi.org/info:doi:10.5194/bg-10-1849-2013

Collins, W. J., Bellouin, N., Doutriaux-Boucher, M., Gedney, N., Halloran, P., Hinton, T., et al. (2011). Development and evaluation of an Earth-System model – HadGEM2. *Geoscientific Model Development*, *4*(4), 1051–1075. https://doi.org/10.5194/gmd-4-1051-2011

Coro, G., Magliozzi, C., Ellenbroek, A., Kaschner, K., & Pagano, P. (2016). Automatic classification of climate change effects on marine species distributions in 2050 using the AquaMaps model. *Environmental and Ecological Statistics*, *23*(1), 155–180. https://doi.org/10.1007/s10651-015-0333-8

Czeschel, R., Stramma, L., & Johnson, G. C. (2012). Oxygen decreases and variability in the eastern equatorial Pacific. *Journal of Geophysical Research: Oceans*, *117*(C11). https://doi.org/10.1029/2012JC008043

Dagorn, L., Bach, P., & Josse, E. (2000). Movement patterns of large bigeye tuna (Thunnus obesus) in the open ocean, determined using ultrasonic telemetry. *Marine Biology*, *136*(2), 361–371. https://doi.org/10.1007/s002270050694

Dagorn, Laurent, Josse, E., & Bach, P. (2000). Individual differences in horizontal movements of yellowfin tuna (Thunnus albacares) in nearshore areas in French Polynesia, determined using ultrasonic telemetry. *Aquatic Living Resources*, *13*(4), 193–202. https://doi.org/10.1016/S0990-7440(00)01063-9

Dagorn, Laurent, Josse, E., Bach, P., & Bertrand, A. (2000). Modeling tuna behaviour near floating objects: from individuals to aggregations. *Aquatic Living Resources*, *13*(4), 203–211. https://doi.org/10.1016/S0990-7440(00)01065-2

Deutsch, C., Ferrel, A., Seibel, B., Pörtner, H.-O., & Huey, R. B. (2015). Climate change tightens a metabolic constraint on marine habitats. *Science*, *348*(6239), 1132–1135. https://doi.org/10.1126/science.aaa1605

Dewar, H., & Graham, J. (1994). Studies of Tropical Tuna Swimming Performance in a Large Water Tunnel - Energetics. *Journal of Experimental Biology*, *192*(1), 13–31.

Dewar, Heidi, Prince, E. D., Musyl, M. K., Brill, R. W., Sepulveda, C., Luo, J., et al. (2011). Movements and behaviors of swordfish in the Atlantic and Pacific Oceans examined using pop-up satellite archival tags. *Fisheries Oceanography*, *20*(3), 219–241. https://doi.org/10.1111/j.1365-2419.2011.00581.x

Dizon, A. E. (1977). Effect of dissolved oxygen concentration and salinity on swimming speed of two species of tunas. *Fishery Bulletin*, *75*, 649–653.

Dizon, Andrew E, Don Stevens, E., Neill, W. H., & Magnuson, J. J. (1974). Sensitivity of restrained skipjack tuna (Katsuwonus pelamis) to abrupt increases in temperature. *Comparative Biochemistry and Physiology Part A: Physiology*, *49*(2), 291–299. https://doi.org/10.1016/0300-9629(74)90120-0

Dizon, Andrew E., Byles, T. C., & Don Stevens, E. (1976). Perception of abrupt temperature decrease by restrained skipjack tuna, Katsuwonus pelamis. *Journal of Thermal Biology*, *1*(3), 185–187. https://doi.org/10.1016/0306-4565(76)90012-7

Dormann, C. F., Schymanski, S. J., Cabral, J., Chuine, I., Graham, C., Hartig, F., et al. (2012). Correlation and process in species distribution models: bridging a dichotomy. *Journal of Biogeography*, *39*(12), 2119–2131. https://doi.org/10.1111/j.1365-2699.2011.02659.x

Dueri, S., Bopp, L., & Maury, O. (2014). Projecting the impacts of climate change on skipjack tuna abundance and spatial distribution. *Global Change Biology*, *20*(3), 742–753. https://doi.org/10.1111/gcb.12460

Dufresne, J.-L., Foujols, M.-A., Denvil, S., Caubel, A., Marti, O., Aumont, O., et al. (2013). Climate change projections using the IPSL-CM5 Earth System Model: from CMIP3 to CMIP5. *Climate Dynamics*, *40*(9), 2123–2165. https://doi.org/10.1007/s00382-012-1636-1

Dunne, J. P., John, J. G., Adcroft, A. J., Griffies, S. M., Hallberg, R. W., Shevliakova, E., et al. (2012). GFDL's ESM2 Global Coupled Climate–Carbon Earth System Models. Part I: Physical Formulation and Baseline Simulation Characteristics. *Journal of Climate*, *25*(19), 6646–6665. https://doi.org/10.1175/JCLI-D-11-00560.1

Dunne, J. P., John, J. G., Shevliakova, E., Stouffer, R. J., Krasting, J. P., Malyshev, S. L., et al. (2012). GFDL's ESM2 Global Coupled Climate–Carbon Earth System Models. Part II:

Carbon System Formulation and Baseline Simulation Characteristics. *Journal of Climate*, *26*(7), 2247–2267. https://doi.org/10.1175/JCLI-D-12-00150.1

Evans, K., Langley, A., Clear, N. P., Williams, P., Patterson, T., Sibert, J., et al. (2008). Behaviour and habitat preferences of bigeye tuna (Thunnus obesus) and their influence on longline fishery catches in the western Coral Sea. *Canadian Journal of Fisheries and Aquatic Sciences*, *65*(11), 2427–2443. https://doi.org/10.1139/F08-148

Evans, K., Abascal, F., Kolody, D., Sippel, T., Holdsworth, J., & Maru, P. (2014). The horizontal and vertical dynamics of swordfish in the South Pacific Ocean. *Journal of Experimental Marine Biology and Ecology*, *450*, 55–67. https://doi.org/10.1016/j.jembe.2013.10.025

FAO – Fisheries and Aquaculture Information and Statistics Branch. (2017). Retrieved December 19, 2017, from http://www.fao.org/figis/servlet/SQServlet?file=/usr/local/tomcat/8.5.16/figis/webapps/figis/temp/hqp_8098547457917812592.xml&outtype=html

FAO - Fishery Statistical Collections. (2014). FAO Fisheries & Aquaculture - Fishery Statistical Collections - Global Tuna Catches by Stock. Retrieved December 18, 2017, from http://www.fao.org/fishery/statistics/tuna-catches/en

Farrell, A. P., & Richards, J. G. (2009). Chapter 11 Defining Hypoxia: An Integrative Synthesis of the Responses of Fish to Hypoxia. In J. G. Richards, A. P. Farrell, & C. J. Brauner (Eds.), *Fish Physiology* (Vol. 27, pp. 487–503). Academic Press. https://doi.org/10.1016/S1546-5098(08)00011-3

Farwell, C. J. (2001). 10. Tunas in captivity. In *Fish Physiology* (Vol. 19, pp. 391–412). Academic Press. https://doi.org/10.1016/S1546-5098(01)19011-4

Frölicher, T. L., Joos, F., Plattner, G.-K., Steinacher, M., & Doney, S. C. (2009). Natural variability and anthropogenic trends in oceanic oxygen in a coupled carbon cycle–climate model ensemble. *Global Biogeochemical Cycles*, *23*(1). https://doi.org/10.1029/2008GB003316

Fromentin, J.-M. (2009). Lessons from the past: investigating historical data from bluefin tuna fisheries. *Fish and Fisheries*, *10*(2), 197–216. https://doi.org/10.1111/j.1467-2979.2008.00311.x

Fromentin, J.-M., & Fonteneau, A. (2001). Fishing effects and life history traits: a case study comparing tropical versus temperate tunas. *Fisheries Research*, *53*(2), 133–150. https://doi.org/10.1016/S0165-7836(00)00299-X

Fujioka, K., Masujima, M., Boustany, A. M., & Kitagawa, T. (2016). Horizontal movements of Pacific bluefin tuna. In *Biology and Ecology of Bluefin Tuna* (pp. 101–122). Boca Raton, FL: CRC Press. Retrieved from https://doi.org/10.1201/ b18714-9

Fuller, D. W., Schaefer, K. M., Hampton, J., Caillot, S., Leroy, B. M., & Itano, D. G. (2015). Vertical movements, behavior, and habitat of bigeye tuna (Thunnus obesus) in the

equatorial central Pacific Ocean. *Fisheries Research*, *172*, 57–70. https://doi.org/10.1016/j.fishres.2015.06.024

Gaertner, D., Molina, A. D. de, Ariz, J., Pianet, R., & Hallier, J. P. (2008). Variability of the growth parameters of the skipjack tuna (Katsuwonus pelamis) among areas in the eastern Atlantic: analysis from tagging data within a meta-analysis approach. *Aquatic Living Resources*, *21*(4), 349–356. https://doi.org/10.1051/alr:2008049

Gaikov, V. V., Chur, V. N., Zharov, V. L., & Fedoseev, P. Y. (1980). On age and growth of the Atlantic bigeye tuna. *International Commission for the Conservation of Atlantic Tunas, Collective Volume of Scientific Papers*, *9*, 294–302.

Galli, G. L. J., Shiels, H. A., & Brill, R. W. (2009). Temperature sensitivity of cardiac function in pelagic fishes with different vertical mobilities: yellowfin tuna (Thunnus albacares), bigeye tuna (Thunnus obesus), mahimahi (Coryphaena hippurus), and swordfish (Xiphias gladius). *Physiological and Biochemical Zoology: PBZ*, *82*(3), 280–290. https://doi.org/10.1086/597484

Galli, G. L. J., Lipnick, M. S., Shiels, H. A., & Block, B. A. (2011). Temperature effects on Ca2+ cycling in scombrid cardiomyocytes: a phylogenetic comparison. *The Journal of Experimental Biology*, *214*(7), 1068–1076. https://doi.org/10.1242/jeb.048231

Gallo, N. D., & Levin, L. A. (2016). Chapter Three - Fish Ecology and Evolution in the World's Oxygen Minimum Zones and Implications of Ocean Deoxygenation. In B. E. Curry (Ed.), *Advances in Marine Biology* (Vol. 74, pp. 117–198). Academic Press. https://doi.org/10.1016/bs.amb.2016.04.001

Garcia, H. E., Locarnini, R. A., Boyer, T. P., Antonov, J. I., Mishonov, A. V., Baranova, O. K., et al. (2013). *World Ocean Atlas Volume 3: Dissolved Oxygen, Apparent Oxygen Utilization, and Oxygen Saturation* (No. NOAA Atlas NESDIS 75) (p. 40). Silver Spring, Maryland: National Oceanographic Data Center. Retrieved from https://data.nodc.noaa.gov/woa/WOA13/DOC/woa13_vol3.pdf

Gent, P. R., Danabasoglu, G., Donner, L. J., Holland, M. M., Hunke, E. C., Jayne, S. R., et al. (2011). The Community Climate System Model Version 4. *Journal of Climate*, *24*(19), 4973–4991. https://doi.org/10.1175/2011JCLI4083.1

Gilly, W. F., Beman, J. M., Litvin, S. Y., & Robison, B. H. (2013). Oceanographic and biological effects of shoaling of the oxygen minimum zone. *Annual Review of Marine Science*, *5*, 393–420. https://doi.org/10.1146/annurev-marine-120710-100849

Gilman, E. L., Allain, V., Collette, B., Hampton, L., & Lehodey, P. (2016). Effects of Ocean Warming on Pelagic Tunas, A Review. In *Explaining Ocean Warming: Causes, Scale, Effects and Consequences* (pp. 254–270). Gland, Switzerland: IUCN – International Union for the Conservation of Nature. Retrieved from https://doi.org/10.2305/IUCN.CH.2016.08.en

Giorgetta, M. A., Jungclaus, J., Reick, C. H., Legutke, S., Bader, J., Böttinger, M., et al. (2018). Climate and carbon cycle changes from 1850 to 2100 in MPI-ESM simulations for the Coupled Model Intercomparison Project phase 5. *Journal of Advances in Modeling Earth Systems*, 572–597. https://doi.org/10.1002/jame.20038@10.1002/(ISSN)1942-2466.MPIESM1

Graham, J. B., & Dickson, K. A. (2001). Anatomical and physiological specializations for endothermy. In *Fish Physiology* (Vol. 19, pp. 121–165). Academic Press. https://doi.org/10.1016/S1546-5098(01)19005-9

Grundinin, V. (1989). On the ecology of yellowfin tuna (Thunnus albacares) and bigeye tuna (Thunnus obesus). *Ichthyol*, *29*, 22–29.

Guillotreau, P., Campling, L., & Robinson, J. (2012). Vulnerability of small island fishery economies to climate and institutional changes. *Current Opinion in Environmental Sustainability*, *4*(3), 287–291. https://doi.org/10.1016/j.cosust.2012.06.003

Guillotreau, P., Squires, D., Sun, J., & Compeán, G. A. (2017). Local, regional and global markets: what drives the tuna fisheries? *Reviews in Fish Biology and Fisheries*, *27*(4), 909–929. https://doi.org/10.1007/s11160-016-9456-8

Hanamoto, E. (1986). Effect of oceanographic environment on bigeye tuna distribution. *Special Report of the Kanagawa Prefectural Fishery Experimental Station*, *2*, 1–61.

Hartog, J. R., Hobday, A. J., Matear, R., & Feng, M. (2011). Habitat overlap between southern bluefin tuna and yellowfin tuna in the east coast longline fishery – implications for present and future spatial management. *Deep Sea Research Part II: Topical Studies in Oceanography*, *58*(5), 746–752. https://doi.org/10.1016/j.dsr2.2010.06.005

Hazen, E. L., Jorgensen, S., Rykaczewski, R. R., Bograd, S. J., Foley, D. G., Jonsen, I. D., et al. (2013). Predicted habitat shifts of Pacific top predators in a changing climate. *Nature Climate Change*, *3*(3), 234–238. https://doi.org/10.1038/nclimate1686

Helm, K. P., Bindoff, N. L., & Church, J. A. (2011). Observed decreases in oxygen content of the global ocean. *Geophysical Research Letters*, *38*(23). https://doi.org/10.1029/2011GL049513

Hinton, M. G., & Deriso, R. D. (1998). *Distribution and stock assessment of swordfish, Xiphias gladius, in the eastern Pacific Ocean from catch and effort data standardized on biological and environmental parameters* (Papers from the International Symposium on Pacific Swordfish No. NOAA Technical Report NMFS 142).

Hinton, M. G., & Nakano, H. (1996). Standardizing catch and effort statistics using physiological, ecological, or behavioral constraints and environmental data, with an application to blue marlin (Makaira nigricans) catch and effort data from Japanese longline fisheries in the Pacific. *Inter–American Tropical Tuna Commission Bulletin*, *21*, 171–200.

Hobday, A. J., Evans, K., Eveson, J. P., Farley, J. H., Hartog, J. R., Basson, M., & Patterson, T. A. (2016). Distribution and migration – Southern bluefin tuna (Thunnus maccoyii). In *Biology and Ecology of Bluefin Tuna* (pp. 189–210). Boca Raton, FL: CRC Press. Retrieved from https://doi.org/10.1201/ b18714-12

Hobday, Alistair J., Young, J. W., Abe, O., Costa, D. P., Cowen, R. K., Evans, K., et al. (2013). Climate impacts and oceanic top predators: moving from impacts to adaptation in oceanic systems. *Reviews in Fish Biology and Fisheries*, *23*(4), 537–546. https://doi.org/10.1007/s11160-013-9311-0

Hobday, Alistair J., Bell, J. D., Cook, T. R., Gasalla, M. A., & Weng, K. C. (2015). Reconciling conflicts in pelagic fisheries under climate change. *Deep Sea Research Part II: Topical Studies in Oceanography*, *113*, 291–300. https://doi.org/10.1016/j.dsr2.2014.10.024

Hobday, Alistair J., Arrizabalaga, H., Evans, K., Scales, K. L., Senina, I., & Weng, K. C. (2017). International collaboration and comparative research on ocean top predators under CLIOTOP. *Deep Sea Research Part II: Topical Studies in Oceanography*, *140*, 1–8. https://doi.org/10.1016/j.dsr2.2017.03.008

Hofmann, A. F., Peltzer, E. T., Walz, P. M., & Brewer, P. G. (2011). Hypoxia by degrees: Establishing definitions for a changing ocean. *Deep Sea Research Part I: Oceanographic Research Papers*, *58*(12), 1212–1226. https://doi.org/10.1016/j.dsr.2011.09.004

Holland, K., Brill, R. W., & Chang, R. K. C. (1990). Horizontal and vertical movements of Pacific blue marlin tagged and released using sportfishing gear. *Fishery Bulletin*, *88*, 397–402.

Holland, K. N., & Grubbs, R. D. (2008). Fish Visitors to Seamounts: Tunas and Bill Fish at Seamounts. In *Seamounts: Ecology, Fisheries & Conservation* (pp. 189–201). John Wiley & Sons, Ltd. https://doi.org/10.1002/9780470691953.ch10a

Holland, K. N., & Sibert, J. R. (1994). Physiological thermoregulation in bigeye tuna,Thunnus obesus. *Environmental Biology of Fishes*, *40*(3), 319–327. https://doi.org/10.1007/BF00002520

Hoolihan, J. P. (2005). Horizontal and vertical movements of sailfish (Istiophorus platypterus) in the Arabian Gulf, determined by ultrasonic and pop-up satellite tagging. *Marine Biology*, *146*(5), 1015–1029. https://doi.org/10.1007/s00227-004-1488-2

Hopper, C. N. (1990). Patterns of Pacific blue marlin reproduction in Hawaiian waters. *Planning the Future of Billfishes*, 123–136.

Horodysky, A. Z., Kerstetter, D. W., Latour, R. J., & Graves, J. E. (2007). Habitat utilization and vertical movements of white marlin (Tetrapturus albidus) released from commercial and recreational fishing gears in the western North Atlantic Ocean: inferences from short duration pop-up archival satellite tags. *Fisheries Oceanography*, *16*(3), 240–256. https://doi.org/10.1111/j.1365-2419.2007.00419.x

Horodysky, A. Z., Cooke, S. J., & Brill, R. W. (2015). Physiology in the service of fisheries science: Why thinking mechanistically matters. *Reviews in Fish Biology and Fisheries*, *25*(3), 425–447. https://doi.org/10.1007/s11160-015-9393-y

Horodysky, A. Z., Cooke, S. J., Graves, J. E., & Brill, R. W. (2016). Fisheries conservation on the high seas: linking conservation physiology and fisheries ecology for the management of large pelagic fishes. *Conservation Physiology*, *4*(1). https://doi.org/10.1093/conphys/cov059

Hulson, P.-J. F., Quinn, T. J., Hanselman, D. H., & Ianelli, J. N. (2013). Spatial modeling of Bering Sea walleye pollock with integrated age-structured assessment models in a changing environment. *Canadian Journal of Fisheries and Aquatic Sciences*, *70*(9), 1402–1416. https://doi.org/10.1139/cjfas-2013-0020

ICCAT. (2016). *ICCAT Manual*. International Commission for the Conservation of Atlantic Tuna.

Ilyina, T., Six, K. D., Segschneider, J., Maier−Reimer, E., Li, H., & Núñez−Riboni, I. (2013). Global ocean biogeochemistry model HAMOCC: Model architecture and performance as component of the MPI-Earth system model in different CMIP5 experimental realizations. *Journal of Advances in Modeling Earth Systems*, *5*(2), 287–315. https://doi.org/10.1029/2012MS000178

Ito, T., Minobe, S., Long, M. C., & Deutsch, C. (2017). Upper ocean O2 trends: 1958–2015. *Geophysical Research Letters*, *44*(9), 4214–4223. https://doi.org/10.1002/2017GL073613

IUCN. (2011). Thunnus maccoyii, Katsuwonus pelamis, Thunnus alalunga, Thunnus obesus, Thunnus thynnus, Thunnus albacares, Thunnus atlanticus, Thunnus tonggol spatial data, Version 2016-2. Retrieved from https://www.iucnredlist.org/

IUCN. (2014). Thunnus orientalis spatial data, Version 2016-2. Retrieved from https://www.iucnredlist.org/

Graham, J. B., Lowell, W. R., Lai, N. C., & Laurs, R. M. (1989). O2 tension, swimming-velocity, and thermal effects on the metabolic rate of the Pacific albacore Thunnus alalunga. *Experimental Biology*, *48*(2), 89–94.

Jones, C. D., Hughes, J. K., Bellouin, N., Hardiman, S. C., Jones, G. S., Knight, J., et al. (2011). The HadGEM2-ES implementation of CMIP5 centennial simulations. *Geoscientific Model Development*, *4*, 543–570. https://doi.org/10.5194/gmd-4-543-2011

Jones, D. R., Brill, R. W., & Mense, D. C. (1986). The Influence of Blood Gas Properties on Gas Tensions and pH of Ventral and Dorsal Aortic Blood in Free-Swimming Tuna, Euthynnus Affinis. *Journal of Experimental Biology*, *120*(1), 201–213.

Jones, M. C., Dye, S. R., Pinnegar, J. K., Warren, R., & Cheung, W. W. L. (2015). Using scenarios to project the changing profitability of fisheries under climate change. *Fish and Fisheries*, *16*(4), 603–622. https://doi.org/10.1111/faf.12081

Joseph, J., Klawe, W., & Murphy, P. (1980). *Tuna and Billfish — fish without a country*. La Jolla, California: Inter-American Tropical Tuna Commission.

Josse, E., Bach, P., & Dagorn, L. (1998). Simultaneous observations of tuna movements and their prey by sonic tracking and acoustic surveys. *Hydrobiologia*, *371*(0), 61–69. https://doi.org/10.1023/A:1017065709190

Keeling, R. F., Körtzinger, A., & Gruber, N. (2010). Ocean Deoxygenation in a Warming World. *Annual Review of Marine Science*, *2*(1), 199–229. https://doi.org/10.1146/annurev.marine.010908.163855

Killen, S. S., Glazier, D. S., Rezende, E. L., Clark, T. D., Atkinson, D., Willener, A. S. T., & Halsey, L. G. (2016). Ecological Influences and Morphological Correlates of Resting and Maximal Metabolic Rates across Teleost Fish Species. *The American Naturalist*, *187*(5), 592–606. https://doi.org/10.1086/685893

King, J. E., & Ikehara, I. I. (1956). Comparative study of food of bigeye and yellowfin tuna in the central Pacific. *Fishery Bulletin*, *57*, 61–85.

Kitagawa, T., & Kimura, S. (2015). *Biology and Ecology of Bluefin Tuna*. CRC Press.

Kitagawa, T., Kimura, S., Nakata, H., & Yamada, H. (2004). Diving behavior of immature, feeding Pacific bluefin tuna (Thunnus thynnus orientalis) in relation to season and area: the East China Sea and the Kuroshio–Oyashio transition region. *Fisheries Oceanography*, *13*(3), 161–180. https://doi.org/10.1111/j.1365-2419.2004.00282.x

Kitagawa, T., Boustany, A. M., Farwell, C. J., Williams, T. D., Castleton, M. R., & Block, B. A. (2007). Horizontal and vertical movements of juvenile bluefin tuna (Thunnus orientalis) in relation to seasons and oceanographic conditions in the eastern Pacific Ocean. *Fisheries Oceanography*, *16*(5), 409–421. https://doi.org/10.1111/j.1365-2419.2007.00441.x

Kitagawa, T., Kimura, S., Nakata, H., & Yamada, H. (2007). Why do young Pacific bluefin tuna repeatedly dive to depths through the thermocline? *Fisheries Science*, *73*(1), 98–106. https://doi.org/10.1111/j.1444-2906.2007.01307.x

Komoroske, L. M., & Lewison, R. L. (2015). Addressing fisheries bycatch in a changing world. *Frontiers in Marine Science*, *2*. https://doi.org/10.3389/fmars.2015.00083

Kornilova, G. N. (1980). Feeding of yellowfin tuna, Thunnus albacares, and bigeye tuna, Thunnus obesus, in the equatorial zone of the Indian Ocean. *Journal of Ichthyology*, *20*(6), 111–119.

Korsmeyer, K. E., Lai, N. C., Shadwick, R. E., & Graham, J. B. (1997a). Heart rate and stroke volume contribution to cardiac output in swimming yellowfin tuna: response to exercise and temperature. *Journal of Experimental Biology*, *200*(14), 1975–1986.

Korsmeyer, K. E., Lai, N. C., Shadwick, R. E., & Graham, J. B. (1997b). Oxygen transport and cardiovascular responses to exercise in the yellowfin tuna Thunnus albacares. *Journal of Experimental Biology*, *200*(14), 1987–1997.

Korsmeyer, Keith E., & Dewar, H. (2001). Tuna metabolism and energetics. In *Fish Physiology* (Vol. 19, pp. 35–78). Academic Press. https://doi.org/10.1016/S1546-5098(01)19003-5

Koslow, J. A., Goericke, R., Lara-Lopez, A., & Watson, W. (2011). Impact of declining intermediate-water oxygen on deepwater fishes in the California Current. *Marine Ecology Progress Series*, *436*, 207–218. https://doi.org/10.3354/meps09270

Laurs, R. M., & Lynn, R. J. (1977). Seasonal migration of north Pacific albacore, thunnus alalunga, into north American coastal waters: distribution, relative abundance, and association with transition zone waters. *Fishery Bulletin*, *75*(4), 795–822.

Lehodey, P., Senina, I., Sibert, J., Bopp, L., Calmettes, B., Hampton, J., & Murtugudde, R. (2010). Preliminary forecasts of Pacific bigeye tuna population trends under the A2 IPCC scenario. *Progress in Oceanography*, *86*(1), 302–315. https://doi.org/10.1016/j.pocean.2010.04.021

Lehodey, P., Hampton, J., Brill, R. W., Nicol, S., Senina, I., Calmettes, B., et al. (2011). Vulnerability of oceanic fisheries in the Tropical Pacific to climate change. In *Vulnerability of Tropical Pacific Fisheries and Aquaculture to Climate Change* (pp. 447–506). Noumea, New Caledonia: Secretariat of the Pacific Community.

Lehodey, Patrick, Andre, J.-M., Bertignac, M., Hampton, J., Stoens, A., Menkes, C., et al. (1998). Predicting skipjack tuna forage distributions in the equatorial Pacific using a coupled dynamical bio-geochemical model. *Fisheries Oceanography*, *7*(3–4), 317–325. https://doi.org/10.1046/j.1365-2419.1998.00063.x

Lehodey, Patrick, Chai, F., & Hampton, J. (2003). Modelling climate-related variability of tuna populations from a coupled ocean–biogeochemical-populations dynamics model. *Fisheries Oceanography*, *12*(4–5), 483–494. https://doi.org/10.1046/j.1365-2419.2003.00244.x

Lehodey, Patrick, Senina, I., Calmettes, B., Hampton, J., & Nicol, S. (2013). Modelling the impact of climate change on Pacific skipjack tuna population and fisheries. *Climatic Change*, *119*(1), 95–109. https://doi.org/10.1007/s10584-012-0595-1

Lehodey, Patrick, Senina, I., Nicol, S., & Hampton, J. (2015). Modelling the impact of climate change on South Pacific albacore tuna. *Deep Sea Research Part II: Topical Studies in Oceanography*, *113*, 246–259. https://doi.org/10.1016/j.dsr2.2014.10.028

Lennert-Cody, C. E., Roberts, J. J., & Stephenson, R. J. (2008). Effects of gear characteristics on the presence of bigeye tuna (Thunnus obesus) in the catches of the purse-seine fishery of the eastern Pacific Ocean. *ICES Journal of Marine Science*, *65*(6), 970–978. https://doi.org/10.1093/icesjms/fsn075

Lindsay, K., Bonan, G. B., Doney, S. C., Hoffman, F. M., Lawrence, D. M., Long, M. C., et al. (2014). Preindustrial-Control and Twentieth-Century Carbon Cycle Experiments with the Earth System Model CESM1(BGC). *Journal of Climate*, *27*(24), 8981–9005. https://doi.org/10.1175/JCLI-D-12-00565.1

Link, J. S., Nye, J. A., & Hare, J. A. (2011). Guidelines for incorporating fish distribution shifts into a fisheries management context. *Fish and Fisheries*, *12*(4), 461–469. https://doi.org/10.1111/j.1467-2979.2010.00398.x

Locarnini, R. A., Mishonov, A. V., Antonov, J. I., Boyer, T. P., Garcia, H. E., Baranova, O. K., et al. (2013). *World Ocean Atlas 2013, Volume 1: Temperature* (No. NOAA Atlas NESDIS 73). Silver Spring, Maryland: National Oceanographic Data Center. Retrieved from https://data.nodc.noaa.gov/woa/WOA13/DOC/woa13_vol1.pdf

Longhurst, A. R. (1976). Vertical migration. In *The Ecology of the Seas* (pp. 116–137). Philadelphia, Pennsylvania: WB Saunders.

Lowe, T. E., Brill, R. W., & Cousins, K. L. (2000). Blood oxygen-binding characteristics of bigeye tuna (Thunnus obesus), a high-energy-demand teleost that is tolerant of low ambient oxygen. *Marine Biology*, *136*(6), 1087–1098. https://doi.org/10.1007/s002270000255

Lynch, P. D., Shertzer, K. W., & Latour, R. J. (2012). Performance of methods used to estimate indices of abundance for highly migratory species. *Fisheries Research*, *125–126*, 27–39. https://doi.org/10.1016/j.fishres.2012.02.005

Mandic, M., Todgham, A. E., & Richards, J. G. (2009). Mechanisms and evolution of hypoxia tolerance in fish. *Proceedings of the Royal Society B: Biological Sciences*, *276*(1657), 735–744. https://doi.org/10.1098/rspb.2008.1235

Marchal, E., Gerlotto, F., & Stequert, B. (1993). On the relationship between scattering layer, thermal structure and tuna abundance in the eastern atlantic equatorial current system. *Oceanologica Acta*, *16*(3), 261–272.

Marchal, Emile, & Lebourges, A. (1996). Acoustic evidence for unusual diel behaviour of a mesopelagic fish (Vinciguerria nimbaria) exploited by tuna. *ICES Journal of Marine Science*, *53*(2), 443–447. https://doi.org/10.1006/jmsc.1996.0062

McKenzie, D. J., Axelsson, M., Chabot, D., Claireaux, G., Cooke, S. J., Corner, R. A., et al. (2016). Conservation physiology of marine fishes: state of the art and prospects for policy. *Conservation Physiology*, *4*(1). https://doi.org/10.1093/conphys/cow046

Methot, R. D., & Wetzel, C. R. (2013). Stock synthesis: A biological and statistical framework for fish stock assessment and fishery management. *Fisheries Research*, *142*, 86–99. https://doi.org/10.1016/j.fishres.2012.10.012

Mislan, K. a. S., Dunne, J. P., & Sarmiento, J. L. (2016). The fundamental niche of blood oxygen binding in the pelagic ocean. *Oikos*, *125*(7), 938–949. https://doi.org/10.1111/oik.02650

Mislan, K. a. S., Deutsch, C. A., Brill, R. W., Dunne, J. P., & Sarmiento, J. L. (2017). Projections of climate-driven changes in tuna vertical habitat based on species-specific differences in blood oxygen affinity. *Global Change Biology*, *23*(10), 4019–4028. https://doi.org/10.1111/gcb.13799

Miyake, M., Guillotreau, P., Sun, C.-H., & Ishimura, G. (2010). *Recent developments in the tuna industry: stocks, fisheries, management, processing, trade and markets* (No. FAO Fisheries and Aquaculture Technical Paper 543). Rome: FAO.

Muhling, B. A., Liu, Y., Lee, S.-K., Lamkin, J. T., Roffer, M. A., Muller-Karger, F., & Walter, J. F. (2015). Potential impact of climate change on the Intra-Americas Sea: Part 2. Implications for Atlantic bluefin tuna and skipjack tuna adult and larval habitats. *Journal of Marine Systems*, *148*, 1–13. https://doi.org/10.1016/j.jmarsys.2015.01.010

Muhling, B. A., Brill, R., Lamkin, J. T., Roffer, M. A., Lee, S.-K., Liu, Y., & Muller-Karger, F. (2017). Projections of future habitat use by Atlantic bluefin tuna: mechanistic vs. correlative distribution models. *ICES Journal of Marine Science*, *74*(3), 698–716. https://doi.org/10.1093/icesjms/fsw215

Muhling, B. A., Lamkin, J. T., Alemany, F., García, A., Farley, J., Ingram, G. W., et al. (2017). Reproduction and larval biology in tunas, and the importance of restricted area spawning grounds. *Reviews in Fish Biology and Fisheries*, *27*(4), 697–732. https://doi.org/10.1007/s11160-017-9471-4

Murphy, T. C., & Sakagawa, G. T. A. (1977). A review and evaluation of estimates of natural mortality rates in tunas. *International Commission for the Conservation of Atlantic Tunas, Collective Volume of Scientific Papers*, *6*, 117–123.

Murua, H., Rodriguez-Marin, E., Neilson, J. D., Farley, J. H., & Juan-Jordá, M. J. (2017). Fast versus slow growing tuna species: age, growth, and implications for population dynamics and fisheries management. *Reviews in Fish Biology and Fisheries*, *27*(4), 733–773. https://doi.org/10.1007/s11160-017-9474-1

Musyl, M. K., Brill, R. W., Boggs, C. H., Curran, D. S., Kazama, T. K., & Seki, M. P. (2003). Vertical movements of bigeye tuna (Thunnus obesus) associated with islands, buoys, and seamounts near the main Hawaiian Islands from archival tagging data. *Fisheries Oceanography*, *12*(3), 152–169. https://doi.org/10.1046/j.1365-2419.2003.00229.x

Nakamura, Y. (1993). Vertical and Horizontal Movements of mature females of Ommastrephes bartramii observed by ultrasonic telemetry. *Recent Advances in Cephalopod Fisheries Biology*. Retrieved from https://ci.nii.ac.jp/naid/10019925405/

Nakano, H., Okazaki, M., & Okamoto, H. (1997). Analysis of catch depth by species for tuna longline fishery based on catch by branch lines. *Bulletin of National Research Institute of Far Seas Fisheries*, *34*, 43–62.

Nikolic, N., Morandeau, G., Hoarau, L., West, W., Arrizabalaga, H., Hoyle, S., et al. (2017). Review of albacore tuna, Thunnus alalunga, biology, fisheries and management. *Reviews in Fish Biology and Fisheries*, *27*(4), 775–810. https://doi.org/10.1007/s11160-016-9453-y

Ommer, R. E., Jarre, A. C., Perry, R. I., Barange, M., Cochrane, K., & Moloney, C. (2009). Human dimensions of the fisheries under global change. In *Climate Change and Small Pelagic Fish* (pp. 275–284). Cambridge University Press. Retrieved from https://doi.org/10.1017/ CBO9780511596681.013

Palmer, J. R., & Totterdell, I. J. (2001). Production and export in a global ocean ecosystem model. *Deep Sea Research Part I: Oceanographic Research Papers*, *48*(5), 1169–1198. https://doi.org/10.1016/S0967-0637(00)00080-7

Patterson, T. A., Evans, K., Carter, T. I., & Gunn, J. S. (2008). Movement and behaviour of large southern bluefin tuna (Thunnus maccoyii) in the Australian region determined using pop-up satellite archival tags. *Fisheries Oceanography*, *17*(5), 352–367. https://doi.org/10.1111/j.1365-2419.2008.00483.x

Peck, M. A., Arvanitidis, C., Butenschön, M., Canu, D. M., Chatzinikolaou, E., Cucco, A., et al. (2018). Projecting changes in the distribution and productivity of living marine resources: A critical review of the suite of modelling approaches used in the large European project VECTORS. *Estuarine, Coastal and Shelf Science*, *201*, 40–55. https://doi.org/10.1016/j.ecss.2016.05.019

Pelczarski, W. (1988). Examination of food of yellowfin tuna (Thunnus albacares) and bigeye tuna (T. obesus) from the open waters of the central Atlantic. *Collective Scientific Papers ICCAT*, *28*(SCRS 87/55), 58–73.

Pepperell, J. G., & Davis, T. L. O. (1999). Post-release behaviour of black marlin, Makaira indica, caught off the Great Barrier Reef with sportfishing gear. *Marine Biology*, *135*(2), 369–380. https://doi.org/10.1007/s002270050636

Pinsky, M. L., & Fogarty, M. (2012). Lagged social-ecological responses to climate and range shifts in fisheries. *Climatic Change*, *115*(3), 883–891. https://doi.org/10.1007/s10584-012-0599-x

Pinsky, M. L., Worm, B., Fogarty, M. J., Sarmiento, J. L., & Levin, S. A. (2013). Marine Taxa Track Local Climate Velocities. *Science*, *341*(6151), 1239–1242. https://doi.org/10.1126/science.1239352

Pohlot, B. G., & Ehrhardt, N. (2018). An analysis of sailfish daily activity in the Eastern Pacific Ocean using satellite tagging and recreational fisheries data. *ICES Journal of Marine Science*, *75*(2), 871–879. https://doi.org/10.1093/icesjms/fsx082

Polovina, J. J., Howell, E., Kobayashi, D. R., & Seki, M. P. (2001). The transition zone chlorophyll front, a dynamic global feature defining migration and forage habitat for marine resources. *Progress in Oceanography*, *49*(1), 469–483. https://doi.org/10.1016/S0079-6611(01)00036-2

Potier, M., Marsac, F., Lucas, V., Sabatié, R., Hallier, J.-P., & Ménard, F. (2004). Feeding Partitioning among Tuna Taken in Surface and Mid-water Layers: The Case of Yellowfin (*Thunnus albacares*) and Bigeye (*T. obesus*) in the Western Tropical Indian Ocean. *Western Indian Ocean Journal of Marine Science*, *3*(1), 51–62. https://doi.org/10.4314/wiojms.v3i1.28447

Potier, Michel, Marsac, F., Cherel, Y., Lucas, V., Sabatié, R., Maury, O., & Ménard, F. (2007). Forage fauna in the diet of three large pelagic fishes (lancetfish, swordfish and yellowfin tuna) in the western equatorial Indian Ocean. *Fisheries Research*, *83*(1), 60–72. https://doi.org/10.1016/j.fishres.2006.08.020

Prince, E., & Goodyear, C. P. (2007). Consequences of Ocean Scale Hypoxia Constrained Habitat for Tropical Pelagic Fishes. *Gulf and Caribbean Research*, *19*(2), 17–20. https://doi.org/10.18785/gcr.1902.04

Prince, E. D., & Pulos, L. M. (1983). *Proceedings of the International Workshop on age determination of oceanic pelagic fishes: Tunas, billfishes, and sharks, Miami, Florida, February 15-18, 1982* (NOAA Technical Report NMFS No. 8). Miami, Florida: NOAA/National Marine Fisheries Service.

Prince, Eric D., & Goodyear, C. P. (2006). Hypoxia-based habitat compression of tropical pelagic fishes. *Fisheries Oceanography*, *15*(6), 451–464. https://doi.org/10.1111/j.1365-2419.2005.00393.x

Prince, Eric D., Luo, J., Goodyear, C. P., Hoolihan, J. P., Snodgrass, D., Orbesen, E. S., et al. (2010). Ocean scale hypoxia-based habitat compression of Atlantic istiophorid billfishes. *Fisheries Oceanography*, *19*(6), 448–462. https://doi.org/10.1111/j.1365-2419.2010.00556.x

Roger, C., & Grandperrin, R. (1976). Pelagic food webs in the tropical Pacific. *Limnology and Oceanography*, *21*(5), 731–735. https://doi.org/10.4319/lo.1976.21.5.0731

Rossi-Fanelli, A., & Antonini, E. (1960). Oxygen equilibrium of haemoglobin from Thunnus thynnus. *Nature*, *186*, 895–896. https://doi.org/10.1038/186895a0

Safina, C. (2001). 11. Tuna conservation. In *Fish Physiology* (Vol. 19, pp. 413–459). Academic Press. https://doi.org/10.1016/S1546-5098(01)19012-6

Sanders, N. K., & Childress, J. J. (1990). Adaptations to the Deep-Sea Oxygen Minimum Layer: Oxygen Binding by the Hemocyanin of the Bathypelagic Mysid, Gnathophausia ingens Dohrn. *The Biological Bulletin*, *178*(3), 286–294. https://doi.org/10.2307/1541830

Schaefer, K. M., & Fuller, D. W. (2002). Movements, behavior, and habitat selection of bigeye tuna (Thunnus obesus) in the eastern equatorial Pacific, ascertained through archival tags. *Fishery Bulletin*, *100*, 765–788.

Schaefer, K. M., & Fuller, D. W. (2007). Vertical movement patterns of skipjack tuna (Katsuwonus pelamis) in the eastern equatorial Pacific Ocean, as revealed with archival tags. *Fishery Bulletin*, *105*, 379–389.

Schaefer, Kurt M. (2001). Reproductive biology of tunas. In *Fish Physiology* (Vol. 19, pp. 225–270). Academic Press. https://doi.org/10.1016/S1546-5098(01)19007-2

Schaefer, Kurt M., & Fuller, D. W. (2010). Vertical movements, behavior, and habitat of bigeye tuna (Thunnus obesus) in the equatorial eastern Pacific Ocean, ascertained from archival tag data. *Marine Biology*, *157*(12), 2625–2642. https://doi.org/10.1007/s00227-010-1524-3

Schaefer, Kurt M., Fuller, D. W., & Block, B. A. (2007). Movements, behavior, and habitat utilization of yellowfin tuna (Thunnus albacares) in the northeastern Pacific Ocean, ascertained through archival tag data. *Marine Biology*, *152*(3), 503–525. https://doi.org/10.1007/s00227-007-0689-x

Schaefer, Kurt M., Fuller, D. W., & Block, B. A. (2009). Vertical Movements and Habitat Utilization of Skipjack (Katsuwonus pelamis), Yellowfin (Thunnus albacares), and Bigeye (Thunnus obesus) Tunas in the Equatorial Eastern Pacific Ocean, Ascertained Through Archival Tag Data. In J. L. Nielsen, H. Arrizabalaga, N. Fragoso, A. Hobday, M. Lutcavage, & J. Sibert (Eds.), *Tagging and Tracking of Marine Animals with Electronic Devices* (pp. 121–144). Dordrecht: Springer Netherlands. https://doi.org/10.1007/978-1-4020-9640-2_8

Schaefer, Kurt M., Fuller, D. W., & Block, B. A. (2011). Movements, behavior, and habitat utilization of yellowfin tuna (Thunnus albacares) in the Pacific Ocean off Baja California, Mexico, determined from archival tag data analyses, including unscented Kalman filtering. *Fisheries Research*, *112*(1), 22–37. https://doi.org/10.1016/j.fishres.2011.08.006

Schaefer, Kurt M., Fuller, D. W., & Aldana, G. (2014). Movements, behavior, and habitat utilization of yellowfin tuna (Thunnus albacares) in waters surrounding the Revillagigedo Islands Archipelago Biosphere Reserve, Mexico. *Fisheries Oceanography*, *23*(1), 65–82. https://doi.org/10.1111/fog.12047

Schmidtko, S., Stramma, L., & Visbeck, M. (2017). Decline in global oceanic oxygen content during the past five decades. *Nature*, *542*(7641), 335–339. https://doi.org/10.1038/nature21399

Seibel, B. A. (2011). Critical oxygen levels and metabolic suppression in oceanic oxygen minimum zones. *Journal of Experimental Biology*, *214*(2), 326–336. https://doi.org/10.1242/jeb.049171

Seibel, B. A. (2013). The jumbo squid, Dosidicus gigas (Ommastrephidae), living in oxygen minimum zones II: Blood–oxygen binding. *Deep Sea Research Part II: Topical Studies in Oceanography*, *95*, 139–144. https://doi.org/10.1016/j.dsr2.2012.10.003

Sepulveda, C. A., Knight, A., Nasby‐Lucas, N., & Domeier, M. L. (2010). Fine‐scale movements of the swordfish Xiphias gladius in the Southern California Bight. *Fisheries Oceanography*, *19*(4), 279–289. https://doi.org/10.1111/j.1365-2419.2010.00543.x

Sharp, G. D. (1975). A comparison of the O2 dissociation properties of some scombrid hemoglobins. *Comparative Biochemistry and Physiology Part A: Physiology*, *51*(3), 683–691. https://doi.org/10.1016/0300-9629(75)90357-6

Sharp, G. D. (1978). Behavioral and physiological ecology of tunas and their effects on vulnerability to fishing gear. *Physiological Ecology of Tunas*, 397–449.

Sharp, G. D. (1983). Trends in respiratory work and ecological position in the marine ecosystem. *Comparative Biochemistry and Physiology Part A: Physiology*, *76*(3), 405–411. https://doi.org/10.1016/0300-9629(83)90440-1

Sharp, G. D. (1995). It's about time: new beginnings and old good ideas in fisheries science. *Fisheries Oceanography*, *4*(4), 324–341. https://doi.org/10.1111/j.1365-2419.1995.tb00077.x

Sharp, G. D. (2001). Tuna oceanography—an applied science. In *Fish Physiology* (Vol. 19, pp. 345–389). Academic Press. https://doi.org/10.1016/S1546-5098(01)19010-2

Shiels, H. A., Freund, E. V., Farrell, A. P., & Block, B. A. (1999). The sarcoplasmic reticulum plays a major role in isometric contraction in atrial muscle of yellowfin tuna. *Journal of Experimental Biology*, *202*(7), 881–890.

Shiels, H. A., Galli, G. L. J., & Block, B. A. (2015). Cardiac function in an endothermic fish: cellular mechanisms for overcoming acute thermal challenges during diving. *Proceedings of the Royal Society B: Biological Sciences*, *282*(1800), 20141989. https://doi.org/10.1098/rspb.2014.1989

Sibert, J., Hampton, J., Kleiber, P., & Maunder, M. (2006). Biomass, Size, and Trophic Status of Top Predators in the Pacific Ocean. *Science*, *314*(5806), 1773–1776. https://doi.org/10.1126/science.1135347

Stevens, E. D. (1972). Some Aspects of Gas Exchange in Tuna. *Journal of Experimental Biology*, *56*(3), 809–823.

Stevens, E. D., & Carey, F. G. (1981). One why of the warmth of warm-bodied fish. *American Journal of Physiology-Regulatory, Integrative and Comparative Physiology*, *240*(3), R151–R155. https://doi.org/10.1152/ajpregu.1981.240.3.R151

Stevens, E. Don. (1982). The effect of temperature on facilitated oxygen diffusion and its relation to warm tuna muscle. *Canadian Journal of Zoology*, *60*(5), 1148–1152. https://doi.org/10.1139/z82-160

Stevens, E. Don, & Fry, F. E. J. (1972). The effect of changes in ambient temperature on spontaneous activity in skipjack tuna. *Comparative Biochemistry and Physiology Part A: Physiology*, *42*(3), 803–805. https://doi.org/10.1016/0300-9629(72)90457-4

Stock, C. A., Alexander, M. A., Bond, N. A., Brander, K. M., Cheung, W. W. L., Curchitser, E. N., et al. (2011). On the use of IPCC-class models to assess the impact of climate on Living Marine Resources. *Progress in Oceanography*, *88*(1), 1–27. https://doi.org/10.1016/j.pocean.2010.09.001

Stoffels, R. J. (2015). Physiological Trade-Offs Along a Fast-Slow Lifestyle Continuum in Fishes: What Do They Tell Us about Resistance and Resilience to Hypoxia? *PLOS ONE*, *10*(6), e0130303. https://doi.org/10.1371/journal.pone.0130303

Stramma, L., Johnson, G. C., Sprintall, J., & Mohrholz, V. (2008). Expanding Oxygen-Minimum Zones in the Tropical Oceans. *Science*, *320*(5876), 655–658. https://doi.org/10.1126/science.1153847

Stramma, L., Johnson, G. C., Firing, E., & Schmidtko, S. (2010). Eastern Pacific oxygen minimum zones: Supply paths and multidecadal changes. *Journal of Geophysical Research: Oceans*, *115*(C9). https://doi.org/10.1029/2009JC005976

Stramma, L., Schmidtko, S., Levin, L. A., & Johnson, G. C. (2010). Ocean oxygen minima expansions and their biological impacts. *Deep Sea Research Part I: Oceanographic Research Papers*, *57*(4), 587–595. https://doi.org/10.1016/j.dsr.2010.01.005

Stramma, L., Prince, E. D., Schmidtko, S., Luo, J., Hoolihan, J. P., Visbeck, M., et al. (2012). Expansion of oxygen minimum zones may reduce available habitat for tropical pelagic fishes. *Nature Climate Change*, *2*(1), 33–37. https://doi.org/10.1038/nclimate1304

Sumaila, U. R., Zeller, D., Watson, R., Alder, J., & Pauly, D. (2007). Potential costs and benefits of marine reserves in the high seas. *Marine Ecology Progress Series*, *345*, 305–310. https://doi.org/10.3354/meps07065

Sund, P., Blackburn, M., & Williams, F. (1981). Tunas and their environments in the Pacific Ocean: A review. *Oceanography and Marine Biology Annual Review*, *19*, 443–512.

Takahashi, M., Okamura, H., Yokawa, K., & Okazaki, M. (2003). Swimming behaviour and migration of a swordfish recorded by an archival tag. *Marine and Freshwater Research*, *54*(4), 527–534. https://doi.org/10.1071/mf01245

Taylor, K. E., Stouffer, R. J., & Meehl, G. A. (2011). An Overview of CMIP5 and the Experiment Design. *Bulletin of the American Meteorological Society*, *93*(4), 485–498. https://doi.org/10.1175/BAMS-D-11-00094.1

Teo, S. L. H., & Boustany, A. M. (2016). Movements and habitat use of Atlantic bluefin tuna. In *Biology and Ecology of Bluefin Tuna* (pp. 137–188). Boca Raton, FL: CRC Press. Retrieved from https://doi.org/10.1201/b18714-11

Teo, Steven L. H., Boustany, A., Dewar, H., Stokesbury, M. J. W., Weng, K. C., Beemer, S., et al. (2007). Annual migrations, diving behavior, and thermal biology of Atlantic bluefin tuna, Thunnus thynnus, on their Gulf of Mexico breeding grounds. *Marine Biology*, *151*(1), 1–18. https://doi.org/10.1007/s00227-006-0447-5

Ward, P., & Hindmarsh, S. (2007). An overview of historical changes in the fishing gear and practices of pelagic longliners, with particular reference to Japan's Pacific fleet. *Reviews in Fish Biology and Fisheries*, *17*(4), 501–516. https://doi.org/10.1007/s11160-007-9051-0

Ward, P., & Myers, R. A. (2005). Inferring the depth distribution of catchability for pelagic fishes and correcting for variations in the depth of longline fishing gear. *Canadian Journal of Fisheries and Aquatic Sciences*, *62*(5), 1130–1142. https://doi.org/10.1139/f05-021

Watters, G. M., Olson, R. J., Francis, R. C., Fiedler, P. C., Polovina, J. J., Reilly, S. B., et al. (2003). Physical forcing and the dynamics of the pelagic ecosystem in the eastern tropical Pacific: simulations with ENSO-scale and global-warming climate drivers. *Canadian Journal of Fisheries and Aquatic Sciences*, *60*(9), 1161–1175. https://doi.org/10.1139/f03-100

Wegner, N. C., Sepulveda, C. A., Aalbers, S. A., & Graham, J. B. (2013). Structural adaptations for ram ventilation: Gill fusions in scombrids and billfishes. *Journal of Morphology*, *274*(1), 108–120. https://doi.org/10.1002/jmor.20082

Wells, R. M. G. (2009). Chapter 6 Blood−Gas Transport and Hemoglobin Function: Adaptations for Functional and Environmental Hypoxia. In J. G. Richards, A. P. Farrell, & C. J. Brauner (Eds.), *Fish Physiology* (Vol. 27, pp. 255–299). Academic Press. https://doi.org/10.1016/S1546-5098(08)00006-X

Westberry, T., Behrenfeld, M. J., Siegel, D. A., & Boss, E. (2008). Carbon-based primary productivity modeling with vertically resolved photoacclimation. *Global Biogeochemical Cycles*, *22*(2). https://doi.org/10.1029/2007GB003078

Wilberg, M. J., Thorson, J. T., Linton, B. C., & Berkson, J. (2009). Incorporating Time-Varying Catchability into Population Dynamic Stock Assessment Models. *Reviews in Fisheries Science*, *18*(1), 7–24. https://doi.org/10.1080/10641260903294647

Wild, A. (1986). Growth of yellowfin tuna, Thunnus albacares, in the Eastern Pacific Ocean based on otolith increments. *Inter-American Tropical Tuna Commission Bulletin*, *18*(6), 421–482.

Williams, A. J., Allain, V., Nicol, S. J., Evans, K. J., Hoyle, S. D., Dupoux, C., et al. (2015). Vertical behavior and diet of albacore tuna (Thunnus alalunga) vary with latitude in the South Pacific Ocean. *Deep Sea Research Part II: Topical Studies in Oceanography*, *113*, 154–169. https://doi.org/10.1016/j.dsr2.2014.03.010

Williams, P., & Terawasi, P. (2011). *Overview of tuna fisheries in the western and central Pacific Ocean, including economic conditions–2010* (No. WCPFC–SC7–2011/GN WP–1). Western & Central Pacific Fisheries Commission. Retrieved from https://www.wcpfc.int/node/2810

Wilson, S. G., Lutcavage, M. E., Brill, R. W., Genovese, M. P., Cooper, A. B., & Everly, A. W. (2005). Movements of bluefin tuna (Thunnus thynnus) in the northwestern Atlantic Ocean recorded by pop-up satellite archival tags. *Marine Biology*, *146*(2), 409–423. https://doi.org/10.1007/s00227-004-1445-0

Wilson, Steven G., Jonsen, I. D., Schallert, R. J., Ganong, J. E., Castleton, M. R., Spares, A. D., et al. (2015). Tracking the fidelity of Atlantic bluefin tuna released in Canadian waters to the Gulf of Mexico spawning grounds. *Canadian Journal of Fisheries and Aquatic Sciences*, *72*(11), 1700–1717. https://doi.org/10.1139/cjfas-2015-0110

Xu, Y., Nieto, K., Teo, S. L. H., McClatchie, S., & Holmes, J. (2017). Influence of fronts on the spatial distribution of albacore tuna (Thunnus alalunga) in the Northeast Pacific over the past 30 years (1982–2011). *Progress in Oceanography*, *150*, 72–78. https://doi.org/10.1016/j.pocean.2015.04.013

Yang, T. H., Lai, N. C., Graham, J. B., & Somero, G. N. (1992). Respiratory, Blood, and Heart Enzymatic Adaptations of Sebastolobus alascanus (Scorpaenidae; Teleostei) to the Oxygen Minimum Zone: A Comparative Study. *The Biological Bulletin*, *183*(3), 490–499. https://doi.org/10.2307/1542026

Yatsu, A., Yamanaka, K., & Yamashiro, C. (1999). Tracking experiments of the jumbo flying squid, Dosidicus gigas, with an ultrasonic telemetry system in the Eastern Pacific Ocean. *Bulletin of National Research Institute of Far Seas Fisheries*, *36*, 55–60.

Chapter 5: ENSO drives lateral separation of FAD-associated skipjack and bigeye tuna in the Western Tropical Pacific

This chapter is an edited version of the submitted publication: Leung, S., Mislan, K. A. S., & Thompson, L. ENSO drives lateral separation of FAD-associated skipjack and bigeye tuna in the Western Tropical Pacific. *Submitted to PLOS ONE and published as a preprint on BioRxiv at* https://doi.org/10.1101/2020.06.25.170613.

5.1 Summary

Incidental capture of juvenile bigeye tuna in fish aggregating device (FAD)-associated purse seine fisheries targeting skipjack tuna have contributed significantly to the degradation of bigeye stocks in the Western Tropical Pacific (WTP) Ocean. One way to reduce this incidental catch is to simply limit purse seine fishing effort; however, skipjack tuna stocks are healthy and economically important to many small island nations in the region. Here we assess whether there is sufficient lateral separation of skipjack and bigeye within FAD-associated purse seine fisheries in the WTP to allow limiting bigeye catch while maintaining a robust skipjack fishery. Based on monthly 5°-longitude-by-5°-latitude catch and effort data, FAD-associated bigeye and skipjack catch per unit effort (CPUE) covary tightly throughout the WTP, such that lateral separation between the two species is generally small. There are, however, significant variations in the amount of separation over both space and time. Waters within the Party to the Nauru Agreement exclusive economic zones (EEZs) belonging to Palau, Solomon Islands, and Tuvalu regularly exhibit some of the smallest bigeye-to-skipjack catch ratios, especially during El Niño. In contrast, waters within Kiribati's Phoenix Islands EEZ regularly exhibit some of the largest

bigeye-to-skipjack catch ratios, which are particularly high during La Niña. In general, El Niño lowers bigeye-to-skipjack catch ratios east of 170°E, while La Niña lowers bigeye-to-skipjack catch ratios west of 170°E. These ENSO-driven variations in separability are larger and more widespread than those driven by seasonality, due to larger associated variations in environmental conditions. Sea surface height anomalies may be particularly useful for demarcating the different environments preferred by skipjack and bigeye throughout the WTP. Sea surface temperatures, temperatures at 100 m, and thermocline depths may also help distinguish between the two species' preferred habitats in many areas. These analyses can help better inform the complex decisions made by both fishers during operations and fisheries managers during creation of effective, dynamic policies to preserve bigeye stocks in the WTP. They also show that climate variability can have substantial effects on the spatial distributions of top pelagic predators and their interactions with one another.

5.2 Introduction

The Western and Central Pacific Ocean (WCPO) accounts for more than 60% of total global tuna catch (Williams & Terawasi, 2015). Tuna and other highly migratory species in this region are managed by the Western and Central Pacific Fisheries Commission (WCPFC), which is one of five tuna Regional Fishing Management Organizations in operation around the world. The most commonly fished tuna species in the WCPO are skipjack (*Katsuwonus pelamis*), yellowfin (*Thunnus albacares*), bigeye (*Thunnus obesus*), and albacore tuna (*Thunnus alalunga*) (SPC, 2019). Though these sought-after tuna species often inhabit the same waters within the WCPO, they historically have had very different stock statuses. For example, skipjack stocks

have always been considered healthy (SPC-OFP, 2019; Vincent et al., 2019), while bigeye stocks were considered overfished and undergoing overfishing until the most recent stock assessment in 2017 (Harley et al., 2014; McKechnie et al., 2017; Vincent et al., 2018). Differences between the 2017 stock assessment and those that came before were due to use of an updated growth model calibrated to new otolith age data (Farley et al., 2017, 2018; McKechnie et al., 2017; Vincent et al., 2018). Based on the 2017 stock assessment, the WCPFC adopted a tropical tuna bridging measure that increased bigeye catch limits for WCPO longline fisheries by 11% (WCPFC, 2017). A follow-up analysis, however, indicated that there is a >20% risk of bigeye populations falling below the limit reference point (adult biomass relative to unfished levels = $SB/SB_{F=0} = 0.2$) over the next 30 years with this bridging measure in place (SPC-OFP, 2018a, 2018b), leading some scientists and conservationists to oppose the measure ("14th Regular Session of the Scientific Committee Summary Report," 2018; Bittenbender, 2017). In response to these concerns, the WCPFC encouraged more "research to identify ways for purse seine vessels to minimize the mortality of juvenile bigeye tuna" (WCPFC, 2017).

Incidental take of juvenile bigeye tuna in fish aggregating device (FAD)-associated purse seine fisheries has indeed contributed significantly to bigeye stock depletion in the WCPO (Griffiths et al., 2019; Leroy et al., 2013; Sibert et al., 2012). The simplest way to reduce the number of juvenile bigeye caught in purse seine sets is to limit effort, but skipjack tuna caught by purse seine are not at risk of being overfished and have tremendous economic value for small island nations in the region (SPC-OFP, 2019; Vincent et al., 2019; Williams & Terawasi, 2015). The research efforts encouraged by the WCPFC should thus focus on reducing incidental juvenile bigeye catch while maintaining current levels of purse seine skipjack catch. Past work

within the Tropical Pacific has indeed taken this constraint into account (Harley & Suter, 2007; Hu et al., 2018; Lennert-Cody et al., 2008; Leroy et al., 2009; Phillips et al., 2017; Schaefer & Fuller, 2013). For instance, Harley & Suter (2007) investigated whether time-area closures in the Eastern Pacific Ocean could reduce purse seine bigeye catch without also significantly reducing that of skipjack. They found that in the best case scenario, a 3-month closure in the Eastern Equatorial Pacific during the third quarter of the year could reduce bigeye catch by 11.5%, while reducing skipjack catch by 4.3%. This led them to conclude that because of the strong tendency for bigeye and skipjack to be caught together, reducing bigeye catches further would not be possible via time-area closures without unacceptably large reductions in skipjack catch. Using ultrasonic telemetry, Schaefer & Fuller (2013) documented the simultaneous behaviors of skipjack, bigeye, and yellowfin tuna within large, FAD-associated aggregations in the Eastern Equatorial Pacific; they found that differences in the behavior and vertical distributions of the three tuna species were not big enough that practical modifications to purse seine fishing practices could effectively avoid capturing small yellowfin and bigeye tunas while still optimizing skipjack capture. Leroy et al. (2009) also concluded that the potential for targeting specific species through fishing depth selection is limited, based on an analysis of the vertical behaviors of the same three species associated with anchored FADs within Papua New Guinea's exclusive economic zone (EEZ). Given the difficulties associated with separating bigeye and skipjack vertically and/or via time-area closures, Hu et al. (2018) sought to separate the two species laterally by investigating differences in their habitat preferences using 1°-latitude by 1°-longitude monthly purse seine catch and effort data in the Eastern Tropical Pacific (ETP). They found that within the ETP, purse seine-caught bigeye occupy waters further from the coast

where the hypoxic layer is deeper, while purse seine-caught skipjack occupy more productive waters associated with equatorial and coastal upwelling. Thus, to reduce incidental bigeye catch rates, Hu et al. (2018) suggested targeting skipjack where hypoxic layers are shallowest (i.e., where there is coastal upwelling).

Here we expand upon this previous work by analyzing lateral FAD-associated, purse seine skipjack-bigeye catch separability in the Western Tropical Pacific (WTP), where the majority of skipjack tuna are caught (SPC, 2019). Oceanographic conditions are quite different in the WTP compared to the ETP regions examined by Harley & Suter (2007), Hu et al. (2018), Lennert-Cody et al. (2008), and Schaefer & Fuller (2013) (e.g., Lehodey, 2001; Leung et al., 2019). Furthermore, new growth rate measurements suggest that Tropical Pacific bigeye potentially consist of two separate stocks (though with mixing in between), divided between the WTP and ETP at approximately 150°W ("14th Regular Session of the Scientific Committee Summary Report," 2018; Farley et al., 2018). Incidental catches of juvenile bigeye may therefore have quite different patterns and causes in the WTP compared to neighboring regions, necessitating WTP-specific analyses of lateral skipjack-bigeye separability. Previous studies have also overlooked the potentially important effects of El Niño Southern Oscillation (ENSO) on skipjack-bigeye purse seine catch separability. Rather, they have focused primarily on seasonal effects (i.e., Harley & Suter, 2007) or on ENSO-related variations in purse seine skipjack catch alone (e.g., Lehodey et al., 1997; Wang et al., 2016). Studies quantifying ENSO-driven variations in bigeye catch have focused solely on adult longline fisheries (Abascal et al., 2018; Howell & Kobayashi, 2006), and have not examined incidental juvenile purse seine capture.

Here we quantify the effects of both seasonality and ENSO on lateral skipjack-bigeye catch separability within FAD-associated purse seine fisheries in the Western Tropical Pacific. We also examine the environmental conditions that drive lateral separation of skipjack and bigeye catches in this region. Based on these analyses, we offer suggestions on how to maximize skipjack catch while simultaneously minimizing incidental juvenile bigeye catch within FAD-associated purse seine fisheries in the WTP.

5.3 Materials and methods

5.3.1 Data sources

5.3.1.1 Purse seine catch and set data

Public domain purse seine fisheries catch and effort data was obtained at https://www.wcpfc.int/folder/public-domain-data on May 1, 2019 (date of issue: July 18, 2018). This data was aggregated by the WCPFC from information gathered in fishing vessel logbooks and by observers. The temporal resolution is monthly and the spatial resolution is 5°-latitude by 5°-longitude. Any monthly 5°-by-5° grid cell with data from less than three vessels was excluded to protect operational privacy (WCPFC, 2007). This dataset runs from January 1967 to December 2017, though not all variables are available throughout this entire period. Catch (in metric tons) is broken up by species (skipjack, yellowfin, bigeye, and other), while sets are broken up by type (unassociated schools, natural log/debris, drifting FAD, anchored FAD, and other). Supp. Fig. 5.1 shows the total number of sets of each type. In this study, we examine only FAD-associated skipjack and bigeye catches (i.e., from sets made on natural log/debris, drifting

FADs, and anchored FADs only). For a given month and grid cell, we compute skipjack and bigeye catch per unit effort (SKJ and BET CPUE, respectively) by dividing skipjack and bigeye catch by the total number of FAD-associated sets. We assume that CPUEs are a reasonable proxy for abundance. We also compute bigeye-to-skipjack (BET:SKJ) catch ratios by dividing SKJ CPUE by BET CPUE.

5.3.1.2 Oceanographic data from in situ observations

In situ profiles of temperature, salinity, and dissolved oxygen concentrations (O_2) were downloaded from the World Ocean Database (WOD) at https://www.nodc.noaa.gov/OC5/SELECT/dbsearch/dbsearch.html on December 9, 2018. WOD gathers and stores quality-controlled data from buoys, ships, gliders, and floats (Boyer et al., 2013). Flagged profiles were excluded and XBT/MBT temperatures were corrected using Levitus et al. (2009). The profiles of temperature, salinity, and O_2 down to 700 m depth were binned onto the same 5°-by-5° grid as the WCPFC data and then averaged over each month within the WCPFC data's timeframe (Jan 1967 - Dec 2017). These monthly mean maps were then used to calculate corresponding maps of thermocline depth, oxygen partial pressure (pO_2), and tuna hypoxic depth. Thermocline depths were computed using the variable representative isotherm method, as recommended for tropical waters by Fiedler (2010). To describe oxygen availability, we report water column oxygen content in terms of both partial pressures (pO_2) as well as dissolved concentrations (O_2). Though dissolved concentrations are more commonly used, pO_2 is more biologically relevant as it provides the force which drives oxygen transfer into animal tissue (Hofmann et al., 2011; Seibel, 2011). To compute pO_2 from input variables of

temperature, salinity, and O_2, we convert O_2 to percent oxygen saturation (Garcia & Gordon, 1992), divide percent oxygen saturation by the fractional atmospheric concentration of oxygen (21%), and then correct for hydrostatic pressure at depth (Enns et al., 1965). To describe oxygenated vertical habitat availability, we use tuna hypoxic depth, defined as the shallowest depth at which pO_2 first falls below 15 kPa (Leung et al., 2019). This 15 kPa pO_2 threshold is approximately equivalent to the 3.5 ml l^{-1} dissolved concentration threshold below which conditions are considered hypoxic for skipjack tuna (Arrizabalaga et al., 2015; Barkley et al., 1978; Bushnell et al., 1990; Evans et al., 1981; Gooding et al., 1981; Ingham et al., 1977; Prince & Goodyear, 2006).

5.3.1.3 Oceanographic data from satellite and reanalysis

Monthly mean mixed layer depths interpolated to a 0.5°-by-0.5° grid were obtained from ECCO Version 4, Release 4 (Forget et al., 2015; Fukumori et al., 2020) global ocean state estimate (also known as ECCO reanalysis) at https://ecco.jpl.nasa.gov/drive/files/Version4/Release4/interp_monthly/MXLDEPTH on March 12, 2020. Data coverage is from January 1992 – December 2017.

Monthly mean chlorophyll-a concentrations interpolated to a 4-by-4 km grid were obtained from the European Space Agency Ocean Colour Climate Change Initiative version 4.2 (Sathyendranath et al., 2019) at ftp://oc-cci-data:ELaiWai8ae@ftp.rsg.pml.ac.uk/occci-v4.2/geographic/netcdf/monthly/chlor_a/ on March 12, 2020. Data coverage is from September 1997 to December 2017.

Monthly mean sea surface height anomalies interpolated to a 0.25°-by-0.25° grid were obtained from AVISO+ at https://www.aviso.altimetry.fr/en/data/products/sea-surface-height-products/global/gridded-sea-level-anomalies-mean-and-climatology.html on October 18, 2019. Data coverage is from January 1993 to December 2017.

After downloading, all monthly mean satellite maps were re-interpolated onto the same 5°-by-5° grid as the WCPFC data. Supp. Fig. 5.2 shows the total number of months of data available for each variable discussed in Section 5.3.1, while Table 5.1 summarizes pertinent information about each variable.

Variable	Time period used	Product grid	Data type	Source
BET, SKJ purse seine catch and sets	Monthly, Jan 1967 – Dec 2017	WCPO, 5° x 5°	Aggregated catch and effort	Western & Central Pacific Fisheries Commission (WCPFC)
ONI	Monthly, Jan 1967 – Dec 2017	No grid, a time series	Constructed from ERSSTv5 SSTs	NOAA Climate Prediction Center
SST, SSS, O_2	Jan 1967 – Dec 2017	Global, raw profiles	In situ measurements	World Ocean Database (WOD)
TCD, $O_{2,100m}$, $pO_{2,100m}$, THD	Monthly means, Jan 1967 – Dec 2017	Global, 5° x 5°	Derived from in situ measurements	Calculated from WOD binned monthly mean measurements
CHL	Monthly means, Sep 1997 – Dec 2017	Global, 4km x 4km	Satellite	ESA Ocean Colour Climate Change Initiative version 4.2 dataset
MLD	Monthly means, Jan 1992 – Dec 2017	Global, 0.5° x 0.5°	Reanalysis	ECCO version 4, release 4
SSHA	Monthly means, Jan 1993 – Dec 2017	Global, 0.25° x 0.25°	Satellite	AVISO gridded sea level anomalies

Table 5.1 | Summary of datasets utilized.

5.3.1.4 ENSO index

The ENSO index used here, called the Oceanic Niño Index or ONI, is calculated as the three-month running mean of sea surface temperature anomalies in the Niño 3.4 region (5°N-5°S, 120°-170°W) (Huang et al., 2016). Periods when ONI is greater than 0.5°C or less than -0.5°C for at least five consecutive three-month running-mean periods are classified as El Niño and La Niña phases, respectively. Time series of ONI were downloaded from http://origin.cpc.ncep.noaa.gov/products/analysis_monitoring/ensostuff/ONI_v5.php on June 4th, 2018.

5.3.2 Spatiotemporal computations

5.3.2.1 Fieldwise statistical significance

To avoid incorrect and/or overstated interpretations, we control the fieldwise false discovery rate (FDR) for each set of multiple hypothesis tests conducted here (Fig. 5.1, 5.4c-d, 5.5-5.6, 5.8, c-d in Supp. Fig. 5.3-5.4, column 2 in Supp. Fig. 5.5-5.7, and Supp. Fig. 5.10-5.12). The FDR is the statistically expected fraction of local null hypothesis rejections for which the null hypotheses are actually true. In this context, local is defined as being at a single grid point in the case of mapped analyses (Fig. 5.1, 5.4c-d, 5.8, c-d in Supp. Fig. 5.3-5.4, column 2 in Supp. Fig. 5.5-5.7, Supp. Fig. 5.10-5.12) or within a single EEZ in the case of comparisons across EEZs (Fig. 5.5-5.6). Controlling the FDR in the context of multiple-hypothesis tests requires smaller *p*-values to reject local null hypotheses compared to a single-hypothesis test. The procedure for determining significance under a specified FDR is as follows (Wilks, 2016): 1.)

Sort the collection of p-values from N (i.e., the total number of grid cells or total number of EEZs) local hypothesis tests p_i, with $i = 1, \ldots, N$, in ascending order. 2.) Reject local null hypotheses only if their respective p-values are smaller than or equal to a threshold level p_{FDR}, where p_{FDR} is equal to the largest p_i that is smaller than or equal to the fraction of α_{FDR} specified by i/N. p_{FDR} is thus calculated as follows:

$p_{FDR} = \max[p_i : p_i \leq (i/N)\alpha_{FDR}]$, where α_{FDR} is the chosen FDR (expressed as a fraction). (Eqn. 5.1)

This method assumes that the multiple local tests are statistically independent, but is also valid when the results of the multiple tests are strongly correlated, as is the case with the spatially and temporally autocorrelated fisheries and oceanographic data used here. Indeed, for data of this nature, the achieved FDR will be smaller than the specified FDR by about two times; the specified FDR should thus be approximately double the desired level (Ventura et al., 2004; Wilks, 2006, 2016). In this study, we specify an FDR of 0.1 for all analyses, resulting in an achieved FDR of ~0.05.

5.3.2.2 Temporal correlation maps

Temporal correlation maps (Fig. 5.1, 5.8; Supp. Fig. 5.10-5.12) were created by calculating the correlation coefficient between monthly times series of two variables at each individual grid point. For all correlation coefficient maps, we also calculated the two-tailed probability, or p-value, that each grid point's correlation coefficient is at least as extreme as the calculated value assuming no correlation. We deemed grid points with p-values below p_{FDR}

(defined in Section 5.3.2.1 above) significantly correlated. These significantly correlated grid cells are demarcated with open circles.

5.3.2.3 Distinguishing timescales of variability (standard deviation maps)

To separate out different sources of temporal variability in BET:SKJ catch ratios, we computed total (raw monthly) (Fig. 5.3a), climatological (Fig. 5.3b), anomaly-driven (Fig. 5.3c), and ENSO anomaly-driven (Fig. 5.3d) standard deviations in BET:SKJ catch ratios at every grid point. Total standard deviations at each grid point were computed over the entire monthly BET:SKJ time series at that grid point (Fig. 5.3a). To compute climatological standard deviations, the climatological cycle of BET:SKJ at each grid point was first computed by averaging BET:SKJ values over each of the 12 months of the year. No lower threshold was placed on the number of years required to compute a climatological value. For example, if a given grid cell had only one valid January BET:SKJ value over the entire time series, then that data point became January's climatological value at that grid cell. Climatological standard deviations at each grid point were then calculated over the 12-month long climatological BET:SKJ times series at that grid point (Fig. 5.3b). These climatological standard deviations represent the amount of variability in BET:SKJ that is due to seasonality. Next, monthly anomalies of BET:SKJ were computed by subtracting the climatological cycle from the raw monthly values at each grid point. The resulting monthly anomalies were then used to compute anomaly-driven standard deviations at each grid point (Fig. 5.3c). These monthly anomalous standard deviations represent the amount of variability in BET:SKJ due to all sources except for seasonality. Finally, ENSO anomaly-driven standard deviations were calculated over ENSO-only

phases (that is, either El Niño or La Niña months) of the monthly anomalies (Fig. 5.3d). These ENSO anomalous standard deviations represent the amount of variability in BET:SKJ due to ENSO alone (i.e., with the effects of seasonality subtracted out). The same procedures were used to create Supp. Fig. 5.13, which illustrates sources of temporal variability in the listed environmental variables rather than BET:SKJ catch ratios.

5.3.3 Quotient analysis

Quantification of habitat preferences was done using quotient analysis, which determines whether a given environmental condition is preferred, tolerated, or avoided by a certain species based on how frequently that species appears within that condition (e.g., Arrizabalaga et al., 2015; Bernal et al., 2007; Hu et al., 2018). The steps involved in the quotient analysis performed here are as follows:

1.) Divide monthly measurements of the environmental variable under investigation into a user-specified number of equally-spaced bins (30 here). Create a histogram of the given environmental variable's values, using all measurements available at the same time and place as BET or SKJ catch data (gray bars in Supp. Fig. 5.8-5.9).

2.) For each bin, compute the cumulative total SKJ or BET CPUE that corresponds with those environmental conditions (light blue bars in Supp. Fig. 5.8-5.9). For example, if sea surface temperature (SST) was the environmental variable of interest and there were a total of three 5°-by-5° monthly grid cells containing SSTs between 24.0-24.3°C over the entire CPUE-overlapped SST dataset, then we would add up all three corresponding monthly SKJ or BET CPUE values to obtain the cumulative total

SKJ or BET CPUE associated with the 24.0-24.3°C SST bin. We would then repeat this procedure for all 29 other SST bins.

3.) Compute the quotient, Q, for each bin, as follows (blue dots in Supp. Fig. 5.8-5.9):

$$Q_i = \frac{\frac{A_i}{\Sigma A_i}}{\frac{N_i}{\Sigma N_i}}, \text{ (Eqn. 5.2)}$$

where A_i is total CPUE associated with bin i (calculated in step 2) and N_i is the total number of environmental measurements in bin i (calculated in step 1).

The numerator in Eqn. 5.2 represents the fraction of total BET or SKJ CPUE over the entire WCPFC dataset that corresponds with environmental conditions in bin i, while the denominator represents the fraction of all observations of the given environmental variable that fall within bin i. Bins with Q_i significantly greater than 1 contain environmental conditions that are *preferred* by a given species, while bins with Q_i significantly less than 1 contain conditions that are *avoided* by that species. Bins with Q_i that are statistically indistinguishable from 1 contain conditions that the given species merely tolerates, rather than actively prefers or avoids.

4.) To determine whether Q_i is significantly different from 1, we compute 95% confidence intervals for the null hypothesis that the observed value of Q_i is drawn from a random distribution, using a resampling procedure (repeated 399 times) developed by Bernal et al. (2007). The resulting 2.5 and 97.5 percentile confidence

intervals are plotted as blue dashed lines in Supp. Fig. 5.8-5.9. Q_i that lie outside of these confidence intervals are considered significantly different from 1.

5.) Finally, to directly compare preferred skipjack and bigeye habitats, we plot their preferences (Supp. Fig. 5.8-5.9) together in one figure (Fig. 5.7), with different colors denoting environmental conditions that are preferred, avoided, and tolerated by each species (see Fig. 5.7 caption).

5.3.4 Code availability

The Python code and Dockerfile required to reproduce all of the figures and tables generated here can be found at https://doi.org/10.5281/zenodo.3904134.

5.3.5 Data availability

Data in the form of NetCDF files required to reproduce all of the figures and tables generated here can be found at https://doi.org/10.5281/zenodo.3904157.

5.4 Results and discussion

5.4.1 Assessment of potential bigeye-skipjack lateral separability

Monthly FAD-associated purse seine catches of skipjack and bigeye are highly positively correlated throughout the WTP (Fig. 5.1a). Thus, in most places, BET CPUE increases whenever SKJ CPUE increases and decreases whenever SKJ CPUE decreases. This initial result suggests that the potential for lateral separation of FAD-associated skipjack and bigeye on the

spatiotemporal scales investigated here may be quite limited. Correlations between monthly SKJ CPUE and BET:SKJ catch ratios tell a different story, however. As monthly SKJ CPUEs increase, fractional bigeye catches decrease throughout the WTP (Fig. 5.1b). Thus, when skipjack are more easily captured, juvenile bigeye are caught proportionally less frequently, suggesting that the two species may be laterally separable on these spatiotemporal scales after all. (This separability is a result of the two species preferring somewhat different environmental conditions, such that they become more strongly separated when conditions are just right for skipjack, but not bigeye - see Sections 5.4.5 and 5.4.6 for details.) Having shown that lateral separation of bigeye and skipjack in the WTP is possible, we move onto quantification of where and when separation is most evident (Sections 5.4.2-5.4.5) and examine how variations in environmental conditions can alter separability (Section 5.4.6).

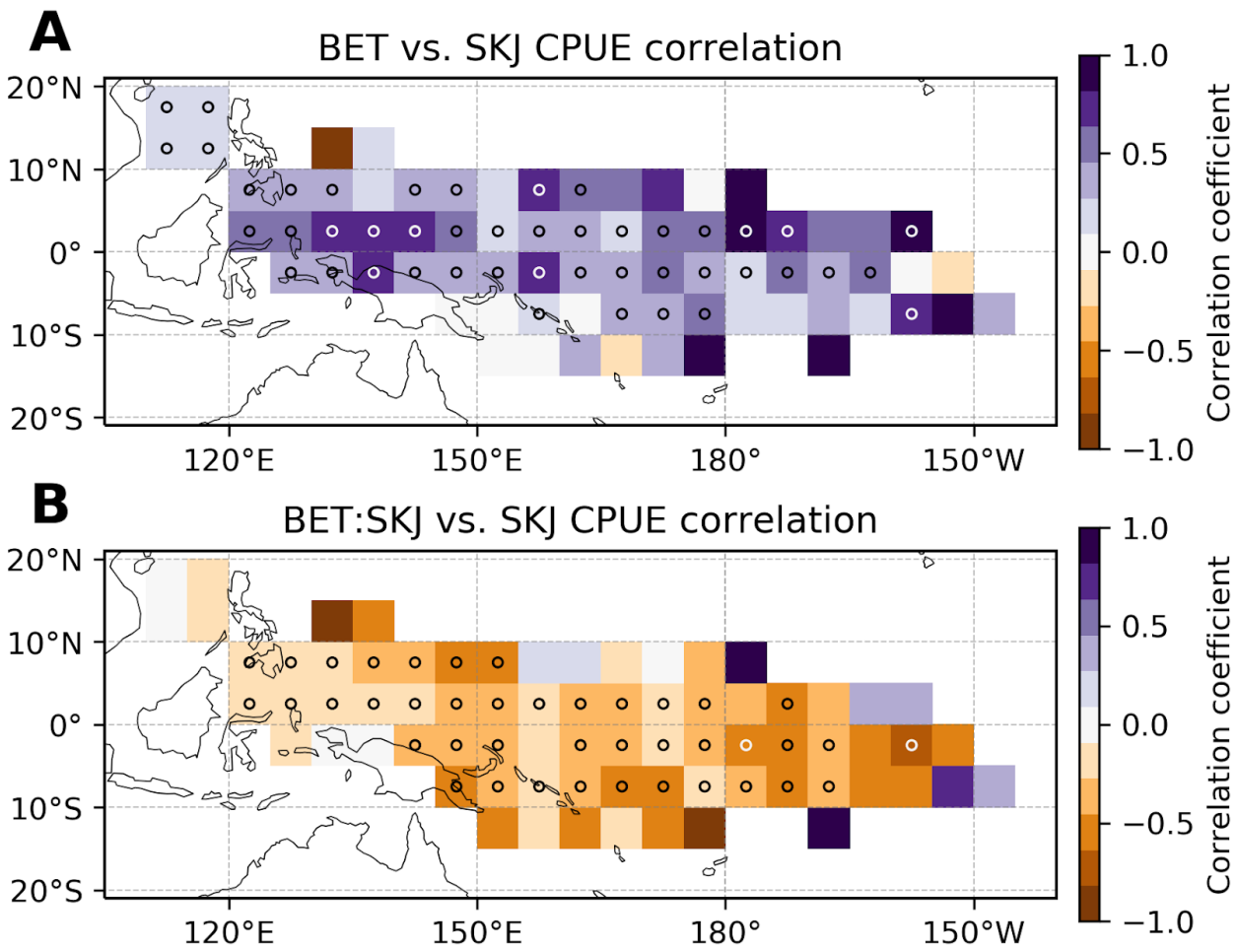

Figure 5.1 | Potential lateral separability of FAD-associated skipjack and bigeye tuna. Temporal correlation coefficients between (a) monthly bigeye and skipjack catch per unit effort (CPUE), and (b) monthly bigeye-to-skipjack catch ratios and skipjack CPUE. Stippling (circles) indicates grid points where the correlation coefficient is significantly different from zero using a multiple-hypothesis-test false discovery rate of 0.1. Correlations are computed over all available data in the WCPFC purse seine catch dataset (Jan 1967 - Dec 2017). See Section 5.3.2.2 for further computational details.

5.4.2 Mean lateral bigeye-skipjack catch separation

Side-by-side comparison of annual mean BET and SKJ CPUE maps support the notion that there is subtle but discernible lateral separation between the two species (Fig. 5.2a-b). For instance, although both SKJ and BET CPUEs are greatest in the northeast, BET CPUE drops off dramatically east of ~180° (Fig. 5.2b), while SKJ CPUE remains relatively elevated within the central-eastern WTP (Fig. 5.2a). Annual mean BET:SKJ catch ratios further demonstrate that the

average degree of lateral separability between the two species is largely dependent on the exact location within the WTP (Fig. 5.2c). Annual mean BET:SKJ catch ratios range from near zero along the southern edge of the WTP, for example, to upwards of 0.3 in the northeast corner (Fig. 5.2c). Thus, based on catch ratios alone, the southern boundary of the WTP would be a highly desirable fishing ground for those seeking to minimize fractional bigeye bycatch, while the northeast corner may be a less desirable region.

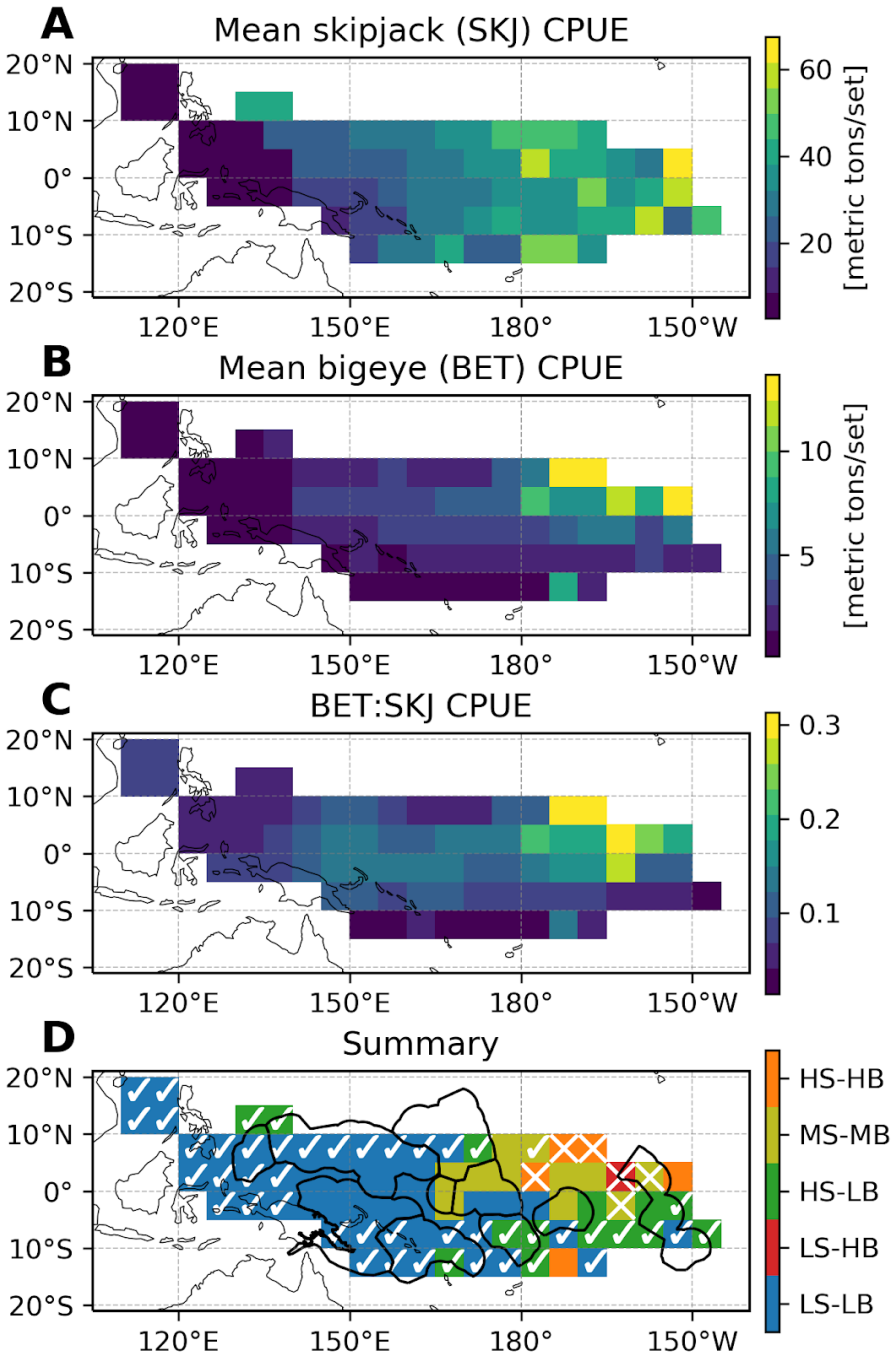

Figure 5.2 | Mean FAD-associated skipjack-bigeye lateral separability. (a) Mean skipjack CPUE. (b) Mean bigeye CPUE. (c) Mean bigeye-to-skipjack catch ratio. Means are computed over all available data in the monthly WCPFC purse seine catch dataset (Jan 1967 - Dec 2017). (d) Region types based on mean skipjack (shown in a) and bigeye CPUE (shown in b) (described in detail in Section 5.4.2). Underlying colors correspond to region type, where S stands for skipjack, B for bigeye, H for high CPUE values, M for medium CPUE values, and L for low CPUE values. HS-LB regions, for example, exhibit high mean skipjack and low mean bigeye CPUE values. Overlain checkmarks and X's correspond to mean bigeye-to-skipjack catch ratios (shown in c), where a checkmark denotes low (favorable) bigeye-to-skipjack catch ratios and an X denotes high (unfavorable) catch ratios. (The absence of any overlain symbol denotes moderate bigeye-to-skipjack catch ratios.) See Table 5.2 for CPUE and catch ratio ranges corresponding to the different region types.

However, because absolute BET and SKJ CPUE values also matter greatly in decisions of where to fish, it is most useful to examine SKJ/BET CPUE *and* BET:SKJ catch ratios at the same time to determine overall fishing desirability. We therefore combine the SKJ/BET CPUE maps in Fig. 5.2a-b with the BET:SKJ catch ratio map in Fig. 5.2c to produce one summary map with simultaneous information on all three factors (Fig. 5.2d). On this summary map in Fig. 5.2d, checkmarks denote regions with low BET:SKJ catch ratios, while X's denote regions with high BET:SKJ catch ratios. (Regions with medium catch ratios are denoted with a lack of symbols to prevent visual clutter.) To classify catch ratios into appropriate high, medium, and low groups, we first computed minimum and maximum annual mean BET:SKJ ratios (i.e., the smallest and largest ratios in Fig. 5.2c). We then divided the range from the minimum to maximum ratios into three equal intervals. BET:SKJ ratios within the first interval were considered low, while BET:SKJ ratios within the last (third) interval were considered high. Table 5.2 lists the exact cutoff values that define these intervals. To denote absolute SKJ and BET CPUE values, we also classified each grid cell on the summary map in Fig. 5.2d into one of five region types as follows (Table 5.2):

1.) Regions with high SKJ and BET CPUE values (high SKJ, high BET = HS-HB type; denoted in orange in Table 5.2 and Fig. 5.2d)

2.) Regions with medium SKJ and BET CPUE values (medium SKJ, medium BET = MS-MB type; denoted in yellow in Table 5.2 and Fig. 5.2d)

3.) Regions with high SKJ and low BET CPUE values (high SKJ, low BET = HS-LB type; denoted in green in Table 5.2 and Fig. 5.2d)

4.) Regions with low SKJ and high BET CPUE values (low SKJ, high BET = LS-HB type; denoted in red in Table 5.2 and Fig. 5.2d)

5.) Regions with low SKJ and BET CPUE values (low SKJ, low BET = LS-LB type; denoted in blue in Table 5.2 and Fig. 5.2d)

Low, medium, and high SKJ and BET CPUE values were classified in the same way as BET:SKJ catch ratios, using four (instead of three) equally-spaced intervals. SKJ/BET CPUE values within the first two intervals were considered low, while SKJ/BET CPUE values within the last two intervals were considered high. Table 5.2 again lists the exact cutoff values that define these intervals. Because there can be some overlap in CPUE values between MS-MB and other region types, MS-MB regions were classified last by selecting grid cells with SKJ and BET CPUE values within their respective middle two intervals (intervals 2-3 out of 4). HS-LB regions contain the most desirable fishing grounds, where fishers can productively target skipjack while avoiding bigeye. LS-HB regions contain the least desirable fishing grounds, where fishers will catch relatively large amounts of bigeye and small amounts of skipjack. HS-HB, MS-MB, and LS-LB regions contain fishing grounds with moderate desirabilities depending on their exact BET:SKJ catch ratios. For fishers that highly value bigeye catch reduction and do not mind finding fewer skipjack, LS-LB waters may ultimately be more desirable. For fishers that must prioritize skipjack fishing efficiency and production, fishing within HS-HB waters with the lowest possible BET:SKJ catch ratios may be the right compromise.

Region type	SKJ CPUE ranges [metric tons/set]	BET CPUE ranges [metric tons/set]	Mean (Fig 2d): # of grid cells			El Niño (Fig 4c): # of grid cells			La Niña (Fig 4f): # of grid cells		
BET:SKJ catch ratio →			Low (✓)	Med	High (X)	Low (✓)	Med	High (X)	Low (✓)	Med	High (X)
HS-HB	≥ 35.1	≥ 6.9	0	2	3	0	2	0	0	0	4
MS-MB	19.0 < x < 51.3	3.5 < x < 10.3	1	8	2	0	11	1	0	10	1
HS-LB	> 35.1	< 6.9	12	2	0	8	2	0	6	0	0
LS-HB	< 35.1	> 6.9	0	0	1	0	0	1	0	0	0
LS-LB	≤ 35.1	≤ 6.9	34	14	0	27	18	1	32	8	0
BET:SKJ catch ratio ranges →			Low (✓): ≤ 0.11			Med: 0.11 < x < 0.21			High (X): ≥ 0.21		

Table 5.2 | Region type classifications and occurrences. Skipjack and bigeye CPUE ranges corresponding to 5 different region types: HS-HB (high skipjack and bigeye CPUE), MS-MB (medium skipjack and bigeye CPUE), HS-LB (high skipjack and low bigeye CPUE), LS-HB (low skipjack and high bigeye CPUE), and LS-LB (low skipjack and bigeye CPUE). Bigeye-to-skipjack (BET:SKJ) catch ratio ranges corresponding to high, medium, and low groupings. See Section 5.4.2 for details on how these ranges were computed. The number of 5°-by-5° grid cells classified as each region type, divided up by BET:SKJ catch ratios, is also listed for annual mean (Fig. 5.2d), El Niño (Fig. 5.4c), and La Niña (Fig. 5.4f) conditions.

The annual mean summary map shows the existence of all five SKJ/BET CPUE-based region types in the WTP (Fig. 5.2d). One relatively contiguous HS-LB region occurs south of 5°S between ~175°E-145°W (Fig. 5.2d), where mean BET CPUE and BET:SKJ catch ratios are somewhat low (Fig. 5.2b,c) and SKJ CPUE (Fig. 5.2a) is relatively high. This area is thus one of the best and most desirable HS-LB regions within the WTP. In contrast, just north of this region, between ~10°N-~5°S and the same longitudes (~180°-~150°W), BET:SKJ catch ratios as well as SKJ/BET CPUE values increase substantially (Fig. 5.2a-c), making this a less desirable MS-MB/HS-HB region (Fig. 5.2d). LS-LB region types are primarily located west of ~175°E, with low BET:SKJ catch ratios in the far west/north and medium BET:SKJ catch ratios in the more central WTP (Fig. 5.2c,d). Indeed, LS-LB regions cover all grid cells west of 165°E apart

from two HS-LB cells between 10°-15°N and 130°-140°E. Fishing in these LS-LB areas will likely yield small catches of skipjack as well as bigeye. The swath of ocean classified as MS-MB in the central-eastern WTP exhibits moderate SKJ and BET CPUE values, and a wide range of BET:SKJ catch ratios (Fig. 5.2a-d). The MS-MB subregion exhibiting small to medium BET:SKJ catch ratios (165°E-165°W, 5°S-10°N) would be a reasonable area to target for those seeking to catch moderate amounts of skipjack while reducing fractional bigeye catch, compared to fishing in the high BET:SKJ catch ratio regions to the north and east (Fig. 5.2d). Fractional bigeye catch would be higher here than in the aforementioned HS-LB regions, however. In sum, there are obvious spatial variations in the typical degree of skipjack-bigeye separation and fishing ground desirability within the WTP, with some regions exhibiting much higher (i.e., the southeast) and others exhibiting much lower (i.e., the northeast) lateral separabilities and fishing ground desirabilities.

Though these annual mean maps (Fig. 5.2) are highly useful for understanding where lateral separation and fishing desirability is greatest on average, in reality, increased temporal resolution may be needed to make more actionable and timely decisions about where to fish. In particular, these mean maps do not provide any information on the temporal variability in the relationships between BET and SKJ CPUE caused by seasonal or ENSO-driven phenomena, both of which can greatly affect spatial distributions of tuna (e.g., Howell & Kobayashi, 2006; Lehodey et al., 1997).

5.4.3 Sources of lateral separation variability

To better understand distinct sources of temporal variability in BET-SKJ separation patterns, we computed overall, climatological, anomalous, and ENSO-related standard deviations (σ) in BET:SKJ catch ratios throughout the WTP (Fig. 5.3) (see Section 5.3.2.3 for more details on how these computations were done). Seasonality does not greatly affect the spatial structure of BET:SKJ catch ratios, as can be seen from the small values and distinct patterns of seasonally-driven σ's in Fig. 5.3b, compared to total σ's in Fig. 5.3a. ENSO, on the other hand, accounts for much of the temporal variability in BET:SKJ throughout the WTP, as can be seen from the large values and similar patterns of ENSO-driven σ's in Fig. 5.3d, compared to both monthly anomalous (Fig. 5.3c) and total σ's (Fig. 5.3a). This implies that ENSO state, rather than season, is a more important determinant of where one should fish to capture skipjack but avoid bigeye. In other words, different phases of ENSO alter spatial patterns of BET:SKJ catch ratios more strongly than different seasons. In the following two sections, we analyze ENSO (Section 5.4.4) and seasonally-driven (Section 5.4.5) variations in lateral BET-SKJ separability in more detail. In Sections 5.4.5 and 5.4.6, we explain why ENSO is the more important driver of bigeye-skipjack lateral separation variability.

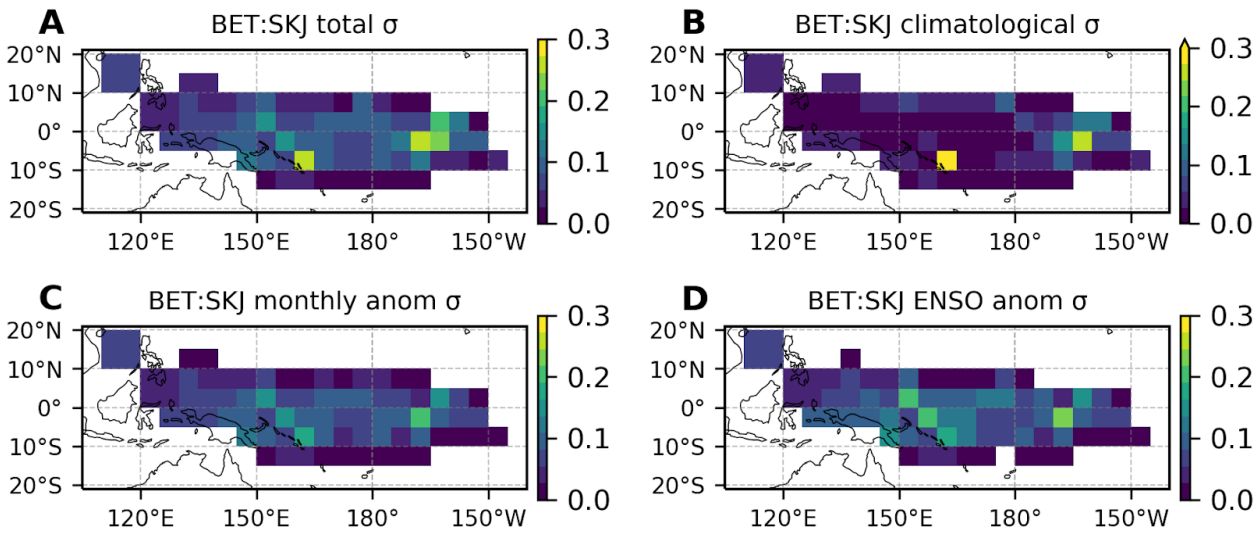

Figure 5.3 | Sources of skipjack-bigeye lateral separation variability. Standard deviations (σ) of FAD-associated bigeye-to-skipjack catch ratios computed from (a) raw monthly values, (b) monthly climatologies, (c) monthly anomalies, and (d) monthly anomalies occurring during El Niño and La Niña phases. See Section 5.3.2.3 for further computational details.

5.4.4 ENSO-driven lateral separation variability

Spatial patterns of FAD-associated skipjack-bigeye separability vary substantially between different phases of ENSO throughout the WTP (Fig. 5.4; Supp. Fig. 5.3-5.4) and across Party to the Nauru Agreement EEZs (PNA EEZs) (Fig. 5.5). El Niño decreases BET:SKJ catch ratios east of ~170°E and increases ratios west of ~170°E, while La Niña acts in the opposite direction (Fig. 5.4c-d; Fig. 5.5c). The effects of El Niño and La Niña on BET:SKJ catch ratios thus oppose one another in the WTP, as is also the case for temperature, dissolved oxygen content, primary productivity, and other environmental variables (e.g., Leung et al., 2019; Radenac et al., 2012; Sharma et al., 2019).

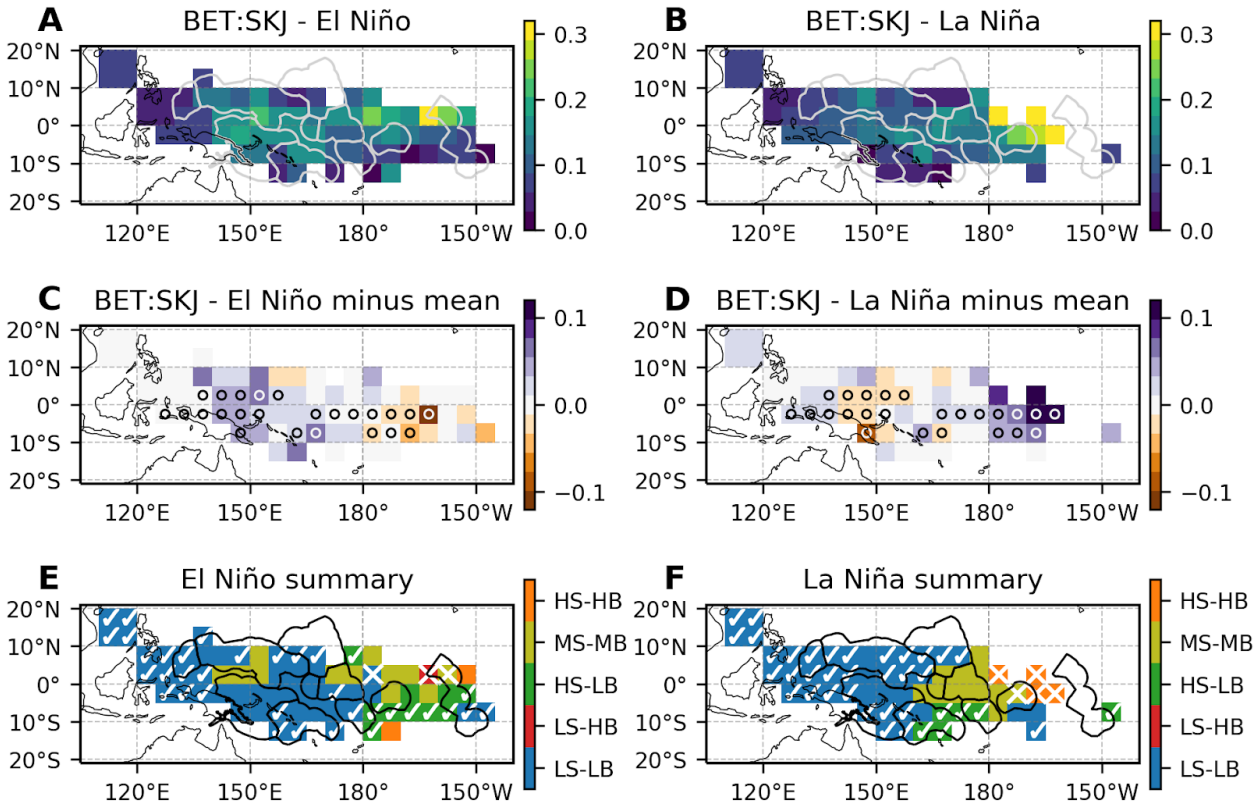

Figure 5.4 | ENSO-driven skipjack-bigeye lateral separation variability. Bigeye-to-skipjack FAD-associated catch ratios averaged over (a) El Niño months and (b) La Niña months. (c, d) Same as (a, b), but with mean bigeye-to-skipjack catch ratios subtracted. Stippling (circles) indicate grid points where El Niño and La Niña composite BET:SKJ are significantly different from one another using a two-sided Wilcoxon rank-sum test and a multiple-hypothesis-test false discovery rate of 0.1 (see Section 5.3.2.1 for details). (e) Region types based on El Niño composite skipjack (shown in Supp. Fig. 5.3a) and bigeye CPUE (shown in Supp. Fig. 5.4a). Underlying colors correspond to region type, where S stands for skipjack, B for bigeye, H for high CPUE values, M for medium CPUE values, and L for low CPUE values. HS-LB regions, for example, exhibit high skipjack and low bigeye CPUE values during El Niño. Overlain checkmarks and X's correspond to El Niño composite bigeye-to-skipjack catch ratios (shown in a), where a checkmark denotes low (favorable) bigeye-to-skipjack catch ratios and an X denotes high (unfavorable) catch ratios. (The absence of any overlain symbol denotes moderate bigeye-to-skipjack catch ratios.) See Table 5.2 for CPUE and catch ratio ranges corresponding to the different region types. (f) Same as (e), but based on La Niña composite maps. The light gray lines in (a,b) and black lines in (e,f) denote the exclusive economic zones (EEZs) of the eight Parties to the Nauru Agreement (PNA).

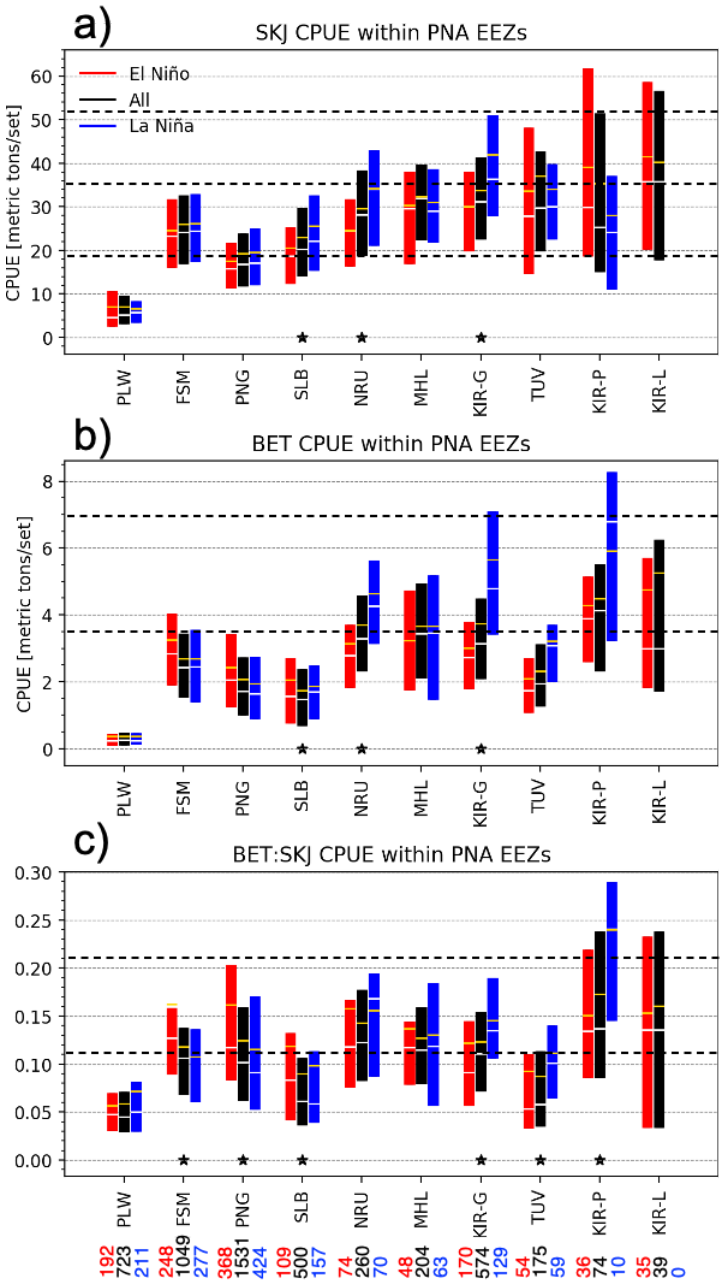

Figure 5.5 | ENSO-driven lateral separation variability within Parties to the Nauru Agreement (PNA) exclusive economic zones (EEZs). Boxplot (without the whiskers; showing interquartile ranges, medians in white, and means in yellow) of FAD-associated (a) skipjack CPUE, (b) bigeye CPUE, and (c) bigeye-to-skipjack catch ratios within each PNA EEZ, composited temporally over all data (black bars), El Niño months alone (red bars), and La Niña months alone (blue bars). From left to right, the PNA countries are roughly arranged from east to west. Asterisks indicate when El Niño and La Niña composite values are significantly different from one another within a given country's EEZ, using a two-sided Wilcoxon rank-sum test and a multiple-hypothesis-test false discovery rate of 0.1 (see Section 5.3.2.1 for details). Horizontal dashed lines denote the cut-off values for low, medium, and high values (see Table 5.2). In (c), the total number of months of BET:SKJ data available in each EEZ is listed in black below the abbreviated country names, while the number of months available during El Niño and La Niña are listed in red and blue, respectively.

These ENSO-driven variations in skipjack-bigeye separability make the WTP region east of ~180° longitude, where the highest annual mean BET:SKJ catch ratios occur, slightly more desirable during El Niño (i.e., BET:SKJ catch ratios are still quite high, but lower than the annual mean) and even less desirable during La Niña (i.e., BET:SKJ catch ratios are considerably higher than the annual mean) (Fig. 5.4c-f). Kiribati's Phoenix Island (KIR-P) EEZ is located in this region and exhibits some of the highest BET CPUE values of all PNA EEZs no matter the ENSO phase. La Niña further exacerbates the maximum bigeye CPUEs and BET:SKJ catch ratios within this EEZ (Fig. 5.5b-c). Thus, although SKJ CPUE values are generally high here, if one's goal is to minimize fractional BET catch, then Kiribati's Phoenix Island EEZ should be avoided most of the time, but especially during La Niña.

Moving slightly west, between 170°E-180° and 0°-5°S, BET:SKJ catch ratios are also significantly higher during La Niña compared to El Niño (Fig. 5.4c-d).This small 10°-longitude-by-5°-latitude region within Kiribati's Gilbert Islands (KIR-G) EEZ thus contains desirable waters for fishers seeking to minimize fractional BET catch while simultaneously maintaining reasonably high SKJ catches during El Niño (Fig. 5.4a,e; Fig. 5.5a,c; Supp Fig. 5.3a). During La Niña, however, BET CPUEs increase substantially (Fig. 5.5b; Supp. Fig. 5.4d) and turn this EEZ from an LS-LB/MS-MB region with low to moderate BET:SKJ catch ratios (Fig. 5.2d) into a fully MS-MB region with moderate BET:SKJ catch ratios (Fig. 5.4f; Fig. 5.5c). Fishers looking to decrease fractional BET catch may therefore try to avoid Kiribati's Gilbert Islands EEZ during La Niña, but shift to targeting these same waters during El Niño.

Within Tuvalu's (TUV) EEZ just south of Kiribati's Gilbert Islands', even though BET:SKJ catch ratios differ significantly between ENSO phases, they remain relatively low

while SKJ CPUEs remain relatively high, no matter the ENSO phase (Fig. 5.4a-b,e-f; Fig. 5.5a,c). Tuvalu's annual mean EEZ waters were already classified as HS-LB with low BET:SKJ catch ratios, but conditions improve even further during El Niño when BET CPUEs and BET:SKJ catch ratios are especially low (Fig. 5.5b-c) and SKJ CPUEs do not change much (Fig. 5.5a). Tuvalu's EEZ waters thus regularly exhibit ideal conditions for fishers seeking productive skipjack fishing grounds containing low BET:SKJ catch rates, with conditions being especially ideal during El Niño.

Moving west across 170°E, which marks the approximate longitude where ENSO effects on BET:SKJ catch ratios switch direction, and into the region between 140-155°E and ~5°N-10°S (largely contained within the EEZs of Micronesia and Papua New Guinea), BET:SKJ catch ratios are significantly higher during El Niño (due to increases in BET CPUE and decreases in SKJ CPUE, Supp. Fig. 5.3-5.4) and lower during La Niña (due to decreases in BET CPUE and increases in SKJ CPUE, Supp. Fig. 5.3-5.4). Papua New Guinea's (PNG) EEZ waters exhibit especially large (though highly variable) BET:SKJ catch ratios during El Niño (Fig. 5.5c), again driven by decreases in SKJ CPUE (Fig. 5.5a) and increases in BET CPUE (Fig. 5.5b). Although absolute BET CPUEs here are low all the time compared to other EEZs (including during El Niño), so are absolute SKJ CPUEs (Fig. 5.5a-b). Papua New Guinea's EEZ waters can thus be considered LS-LB almost all of the time, with moderate BET:SKJ catch ratios that increase during El Niño (Fig. 5.2d; Fig. 5.4e-f). Compared to Papua New Guinea, Micronesia's (FSM) EEZ waters produce slightly higher (though still relatively small) absolute BET and SKJ CPUE values (Fig. 5.5a-b), but comparable moderate BET:SKJ catch ratios (Fig. 5.5c). BET:SKJ catch ratios also increase here during El Niño, but are slightly less variable and

do not typically go as high as ratios in Papua New Guinea's EEZ during El Niño (Fig. 5.5c). Though relatively unproductive for skipjack, during La Niña, waters within the EEZs of Micronesia and Papua New Guinea are moderately desirable if minimization of fractional bigeye catch is the goal; this desirability is reduced by quite a bit during El Niño, however, particularly in Papua New Guinea's EEZ, as BET:SKJ catch ratios increase significantly during this phase of ENSO.

Within Solomon Islands' (SLB) EEZ just southeast of Papua New Guinea's, BET:SKJ catch ratios are relatively low all the time, but are especially reduced during La Niña (Fig. 5.5c). Absolute SKJ CPUEs tend to be higher here than in Papua New Guinea's EEZ, but are on par with Micronesia's EEZ to the north, particularly during La Niña (Fig. 5.5a). Waters in and surrounding Solomon Islands' EEZ thus exhibit some of the lowest absolute BET CPUE and BET:SKJ values of any PNA nation (Fig. 5.5b-c), while producing low to moderate SKJ CPUEs (Fig. 5.5a), with particularly favorable higher SKJ and lower BET CPUE values during La Niña (Fig. 5.4f).

In sum, waters within EEZs belonging to Palau, Solomon Islands, and Tuvalu regularly exhibit the smallest BET:SKJ catch ratios of all PNA countries. SKJ CPUE is, however, quite low within Palau's EEZ and low-to-moderate within Solomon Islands' EEZ. In contrast, Tuvalu EEZ waters contain higher SKJ CPUE values and is therefore one of the most effective PNA EEZs to target for maximizing skipjack catch while simultaneously minimizing bigeye catch, especially during El Niño. Waters within Kiribati's Phoenix Islands EEZ regularly exhibit the largest BET:SKJ catch ratios of the PNA countries, with especially large ratios during La Niña. Fishers looking to greatly minimize fractional bigeye catch may therefore try to avoid this

region, even though SKJ CPUE is quite high here. Generally speaking, El Niño creates more favorable conditions (lower BET:SKJ catch ratios) east of ~170°E, while La Niña creates more favorable conditions west of ~170°E. Thus, during periods of El Niño or La Niña, the best regions to target or avoid to effectively reduce fractional bigeye catch may be quite different from those suggested by annual mean maps alone (Fig. 5.2; Section 5.4.2).

5.4.5 Seasonal lateral separation variability

Seasonally-driven variations in lateral bigeye-skipjack separability are not nearly as pronounced or widespread as ENSO-driven variations (Fig. 5.6; Supp. Fig. 5.5). Of the PNA EEZs, only Papua New Guinea's exhibits significantly different BET:SKJ catch ratios between seasons (Fig. 5.6c). Here BET:SKJ catch ratios are highest in summer and lowest in winter, though absolute differences in ratios are quite small between all seasons. In contrast, 6 of the PNA EEZs exhibited significantly different BET:SKJ catch ratios between El Niño and La Niña (Fig. 5.5c; Section 5.4.4).

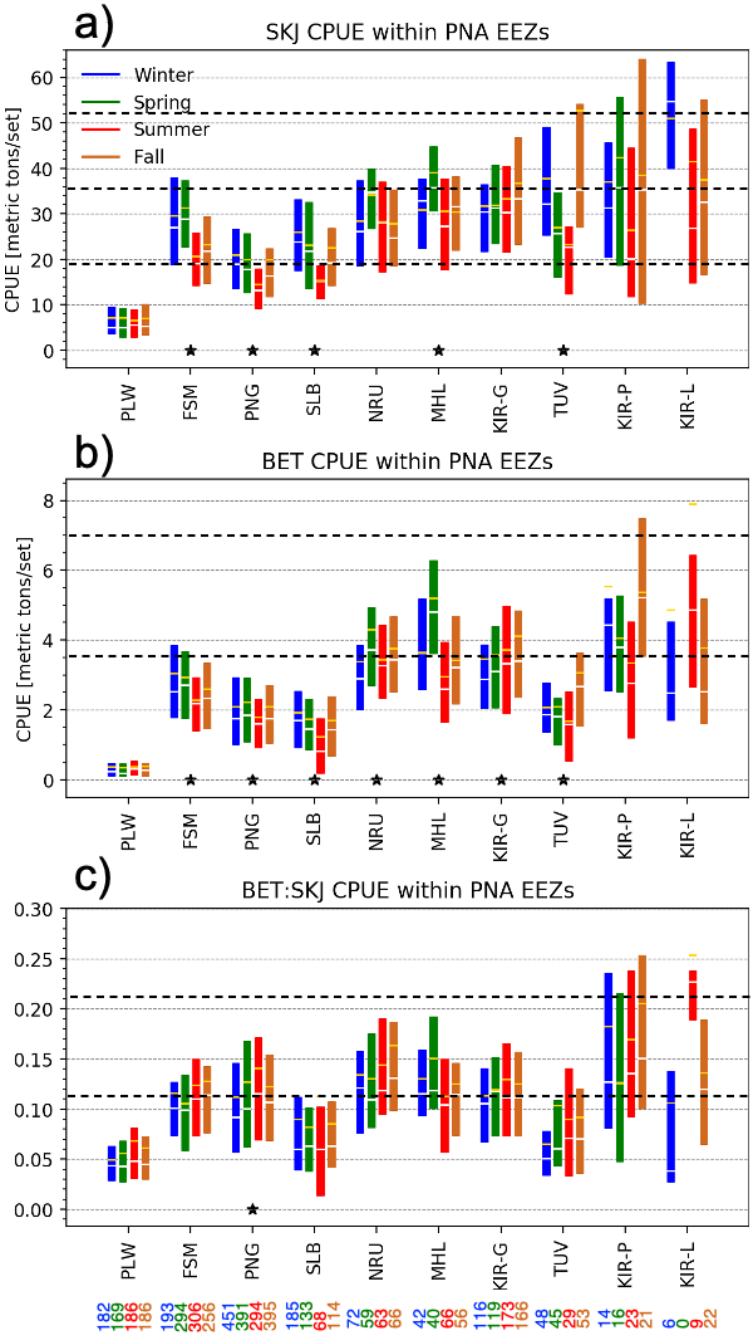

Figure 5.6 | Seasonal lateral separation variability within Parties to the Nauru Agreement (PNA) exclusive economic zones (EEZs). Boxplot (without the whiskers; showing interquartile ranges, medians in white, and means in yellow) of FAD-associated (a) skipjack CPUE, (b) bigeye CPUE, and (c) bigeye-to-skipjack catch ratios within each PNA EEZ, composited temporally over the winter (December-February; blue bars), spring (March-May; green bars), summer (June-August; red bars), and autumn (September-November; brown bars) months alone. From left to right, the PNA countries are roughly arranged from east to west. Asterisks indicate when seasonal composite values are significantly different from one another within a given country's EEZ, using a Kruskal-Wallis H-test and a multiple-hypothesis-test false discovery rate of 0.1 (see Section 5.3.2.1 for details). Horizontal dashed lines denote the cut-off values for low, medium, and high values (see Table 5.2). In (c), the number of months of BET:SKJ data available during each season in each EEZ are listed below the country names.

While significant differences in BET:SKJ catch ratios between the seasons are relatively rare and concentrated in only a couple of small regions (Fig. 5.6c; Supp. Fig. 5.5), SKJ and BET CPUE values do differ significantly between the seasons in many areas throughout the WTP (Fig. 5.6a-b; Supp. Fig. 5.6-5.7). This seemingly counterintuitive result is possible because different seasons alter spatial patterns of BET and SKJ CPUE in nearly the same way. Different phases of ENSO, on the other hand, alter spatial patterns of BET CPUE quite differently from those of SKJ CPUE (Fig. 5.5a-b; Supp. Fig. 5.3-5.4); ENSO thus causes CPUEs for the two species to vary in different proportions or directions at any given location, ultimately leading to variable BET:SKJ catch ratios between El Niño and La Niña. The underlying physical reasons for this are discussed in Section 5.4.6.

In sum, the effects of ENSO on bigeye-skipjack lateral separability are more important than the effects of seasonality, though seasonality also significantly alters BET:SKJ catch ratios in some small regions within the western WTP. In these small regions, including within Papua New Guinea's EEZ, BET:SKJ catch ratios tend to be lowest in the winter and highest in the summer, creating marginally better conditions for fractional bigeye catch minimization between December and February in this area.

5.4.6 Environmental drivers of lateral separation

Lateral separation of FAD-associated, purse seine-caught bigeye and skipjack tuna via environmental conditions alone is difficult (though not impossible) because FAD-attracted bigeye and skipjack tend to prefer and avoid very similar habitats (Fig. 5.7; Supp. Fig. 5.8-5.9). Of the environmental variables tested here (listed in x-axes of Fig. 5.7 subplots), only sea surface

height anomalies (SSHA) can usefully distinguish between the two species' preferred habitats over most of the WTP (Fig. 5.8). In general, both FAD-associated skipjack and bigeye appear to prefer waters with small positive SSHA values ranging from >1 to ~8 cm (Fig. 5.7). However, skipjack tend to avoid negative SSHA values just below this range, while bigeye tolerate and then avoid positive SSHA values just above this range. This suggests that waters with SSHA values >~11 cm could be effectively targeted by those seeking to minimize fractional bigeye catch. Targeting waters with positive sea surface height anomalies between ~8 and ~15 cm in particular would potentially minimize fractional bigeye catch while also maintaining relatively high skipjack catches. Sea surface temperatures (SST), 100-m temperatures (T_{100m}), and thermocline depths (TCD) may also aid in identifying distinct skipjack and bigeye habitats, but the areas over which these environmental variables are potentially useful for this purpose are smaller than that of SSHA (Supp. Fig. 5.10-5.12). Nevertheless, SSTs around 30°C and TCDs greater than 190 m appear to be preferred by skipjack but only tolerated by bigeye, thus signifying potentially desirable temperature conditions to fish in (Fig. 5.7; Supp. Fig. 5.8-5.9). Where T_{100m} can potentially separate the two species, skipjack prefer warmer 100-m water temperatures, while bigeye prefer cooler ones, as evidenced by the respective significant positive and negative correlation coefficients between T_{100m} and SKJ/BET CPUE (Supp. Fig. 5.11-5.12b, boxed grid cells).

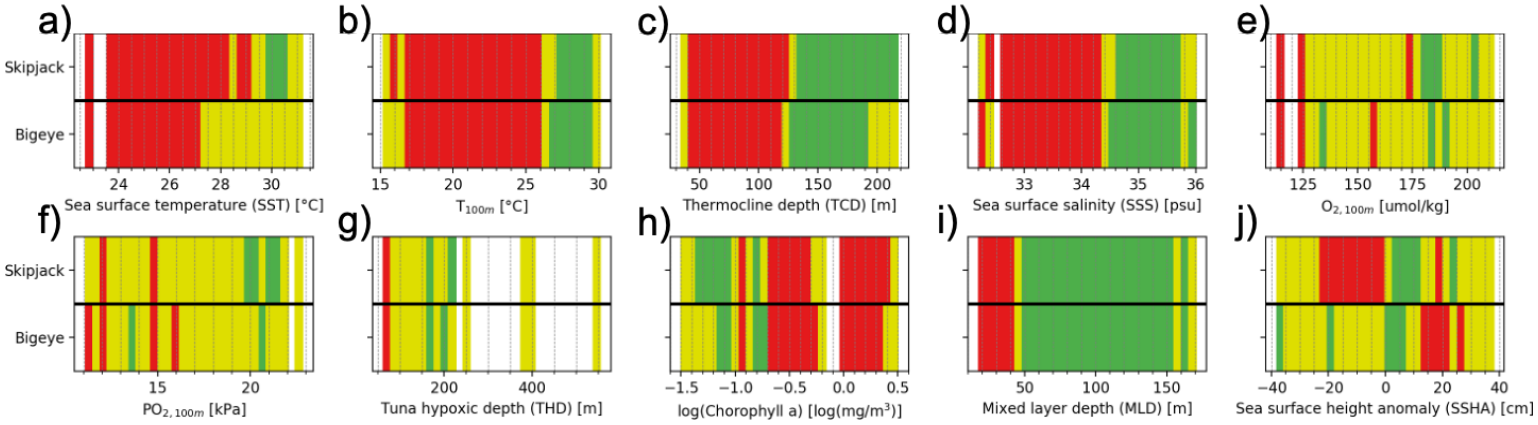

Figure 5.7 | Environmental drivers of lateral FAD-associated bigeye-skipjack separability in the WTP. The color red denotes environmental conditions that the given species tends to avoid, while yellow denotes conditions that the given species tolerates and green denotes conditions that the given species prefer. The color white signifies a lack of environmental conditions in this range within the associated dataset. The top and bottom row of each subplot correspond to habitat preferences of skipjack and bigeye, respectively. See Section 5.3.3 for further details on how these preferences were computed.

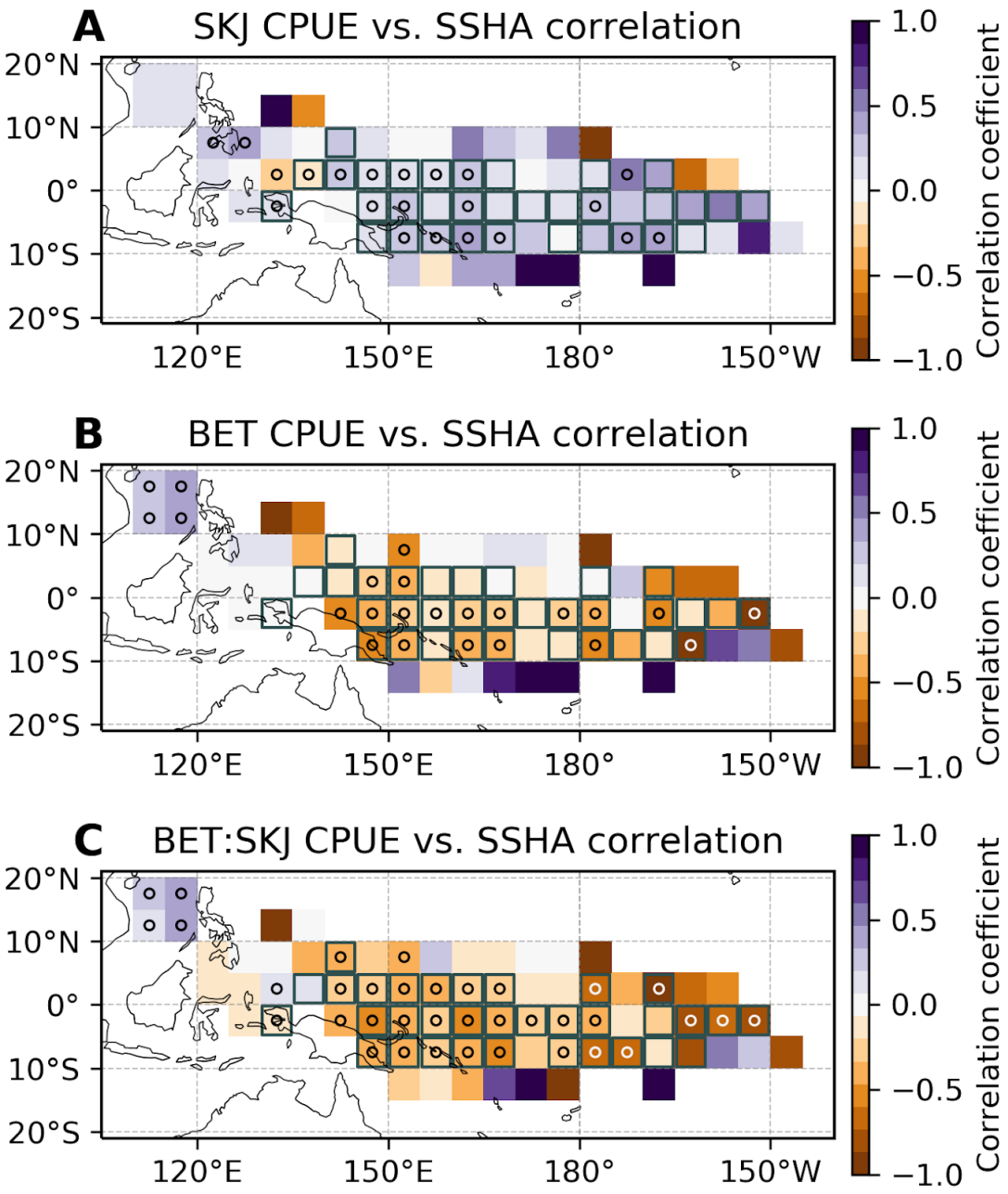

Figure 5.8 | WTP regions over which sea surface height anomalies (SSHA) may be effective at laterally separating FAD-associated bigeye and skipjack. Temporal correlation coefficients between monthly SSHA and (a) skipjack CPUE, (b) bigeye CPUE, and (c) bigeye-to-skipjack catch ratios. Stippling (circles) indicates grid points where the correlation coefficient is significantly different from zero using a multiple-hypothesis-test false discovery rate of 0.1 (see Section 5.3.2.1 for details). Square boxes denote grid points where the following 3 criteria are met: 1.) At least one of the above maps (a-c) contains a statistically-significantly different from zero correlation coefficient; 2.) SSHA is correlated with SKJ and BET CPUEs in opposite directions (that is, the sign of the correlation coefficient is different in maps a and b above); 3.) SSHA is correlated with SKJ CPUE and BET:SKJ catch ratios in opposite directions (that is, the sign of the correlation coefficient is different in maps a and c above). Boxed grid cells thus indicate areas where a given change in SSHA conditions lead to opposite responses in skipjack and bigeye due to differential habitat preferences. Correlations are computed over all available data between Jan 1967 - Dec 2017.

These findings are in contrast to those of Hu et al. (2018), who found that hypoxic layer depths, rather than temperature-related conditions and SSHAs, were most useful for laterally demarcating preferred skipjack and bigeye habitats in the ETP. There are several potential reasons for these differences. First of all, subsurface oxygen content and gradients differ greatly between the Eastern and Western Tropical Pacific (Leung et al., 2019). In the west, oxygen is less likely to be limiting due to the presence of better oxygenated waters and much deeper hypoxic layers. Oxygen content would therefore be less likely to play an appreciable role in laterally separating bigeye and skipjack since conditions would be perfectly acceptable to both. Second of all, as in many other habitat studies, Hu et al. (2018) use climatological oxygen concentrations, which may not be representative of real-time oxygen conditions, particularly during the strongest phases of El Niño or La Niña (Leung et al., 2019). Third of all, we analyzed monthly purse seine skipjack and bigeye catches in FAD-associated sets on a 5°-by-5° horizontal grid, while Hu et al. (2018) analyzed monthly purse seine catches in all set types on a 1°-by-1° horizontal grid. Because of these differences in set type and/or spatial resolution, results from our two studies may not be directly comparable. Lastly, because observations of oxygen in the WTP are relatively sparse compared to those of temperature and sea surface height anomalies, it is possible that there was simply not enough data to differentiate between the oxygen conditions preferred by skipjack and bigeye. With more complete observations, we may find that subsurface oxygen conditions can also serve to effectively separate FAD-associated bigeye and skipjack in the WTP.

In Sections 5.4.3 and 5.4.5, we noted that different ENSO phases alter spatial patterns in BET:SKJ catch ratios more strongly than different seasons in the WTP. This is because

ENSO-driven changes in environmental conditions that separate FAD-associated bigeye and skipjack (SSHA, T_{100m}, TCD, and SST) are more extreme than those driven by changing seasons here (Supp. Fig. 5.13). These larger ENSO-driven habitat variations are more likely to create conditions that reach the limit of one species' preferences or avoidances, while entering another species' preferred or avoided range. In contrast, the much smaller seasonal changes in SSHA, T_{100m}, TCD, and SST tend to drive bigeye and skipjack abundances in the same direction, leading to variations in both species' CPUEs, but not in resultant BET:SKJ catch ratios.

In sum, skipjack and bigeye are not easily laterally separated by differences in habitat preferences alone, but SSHA conditions may be most useful in demarcating their preferred environments. SST, T_{100m}, and TCD may also play secondary roles in distinguishing habitats preferred/avoided by FAD-associated skipjack and bigeye within the WTP. Temperature-related environmental conditions thus appear to be more important drivers of lateral skipjack-bigeye separability in the WTP, while oxygen appears to be more important in the ETP (Hu et al., 2018). Larger ENSO-driven changes in environmental conditions are able to better separate skipjack and bigeye compared to seasonally-driven changes, given the two species' somewhat distinct habitat preferences.

5.5 Conclusions

Incidental capture of juvenile bigeye tuna in FAD-associated purse seine fisheries targeting skipjack has contributed significantly to the degradation of bigeye stocks in the Western Tropical Pacific (WTP). However, efforts to reduce bigeye catch should also prioritize maintenance of skipjack catch at current levels. Here we examined spatial patterns in

FAD-associated purse seine bigeye and skipjack CPUE, as well as bigeye-to-skipjack catch ratios, and quantified how these spatial patterns vary between different seasons and phases of ENSO. We also examined the environmental conditions that are most efficient at laterally separating bigeye and skipjack. We find that FAD-associated bigeye and skipjack CPUE covary tightly throughout the WTP on the spatiotemporal scales examined here (5°-by-5°, monthly). There are, however, significant variations in this separability both spatially and temporally. Temporally, El Niño phases create more desirable conditions (lower bigeye-to-skipjack catch ratios) east of ~170°E longitude, while La Niña phases create more desirable conditions west of ~170°E. The effects of these ENSO cycles on bigeye-skipjack separability were found to be more important than the effects of seasonality throughout the WTP. Spatially, waters within the EEZs belonging to Palau, Solomon Islands, and Tuvalu regularly exhibit some of the smallest bigeye-to-skipjack catch ratios in the WTP. Tuvalu's EEZ waters also exhibit relatively high skipjack CPUEs and is therefore one of the most desirable EEZs to target when seeking to simultaneously minimize bigeye while maximizing skipjack catch, particularly during El Niño. In contrast, waters within Kiribati's Phoenix Islands EEZ regularly exhibit some of the largest bigeye-to-skipjack catch ratios, with especially large ratios during La Niña. Fishers looking to minimize fractional bigeye catch may therefore want to avoid this region, even though skipjack CPUE is quite high here. Skipjack and bigeye are not easily laterally separated by differences in habitat preferences alone, but real-time maps of sea surface height anomalies (available from https://marine.copernicus.eu/ and others) may be useful in demarcating their different environments. Sea surface temperatures, temperatures at 100 m, and thermocline depths may also be helpful in distinguishing between habitats preferred by skipjack and bigeye.

Two caveats of this study to keep in mind are that the FAD-associated purse seine catches relied upon here may sometimes be misreported or misidentified (Hampton & Williams, 2017), and CPUE values are not always a representative proxy for abundance (Tremblay-Boyer et al., 2017). Nevertheless, we show that there are significant spatiotemporal variations in FAD-associated bigeye-skipjack purse seine catch separability that should be taken into account when determining where to fish or to implement FAD set restrictions.

5.6 Supporting information

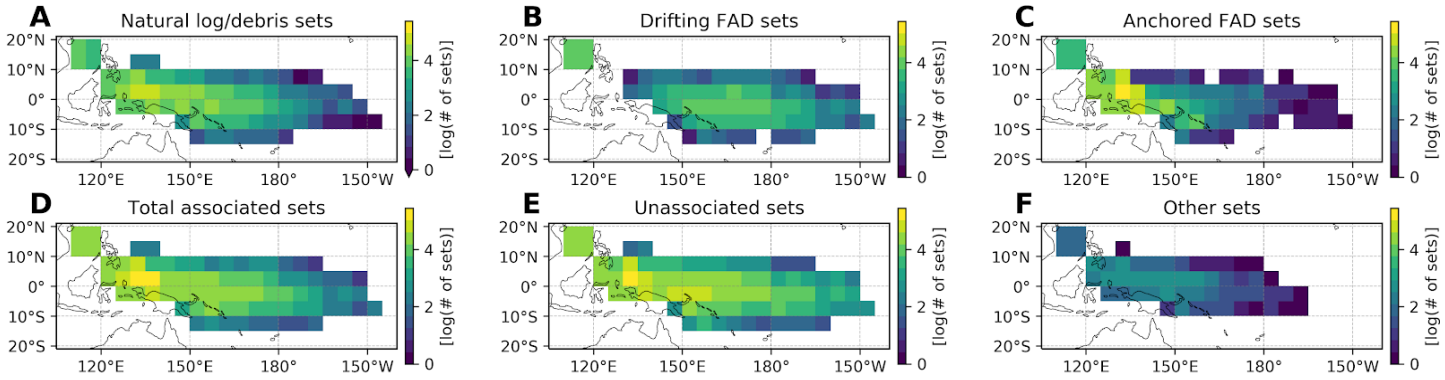

Supporting Figure 5.1 | Number of purse seine sets of different types in the WCPFC catch and effort dataset. Total number of (a) natural log/debris associated sets, (b) drifting fish-aggregating device (FAD) associated sets, (c) anchored FAD associated sets, (d) all associated sets (natural log/debris, drifting FAD, and anchored FAD combined), (e) unassociated sets, and (f) other types of sets in the WCPFC purse seine catch and effort dataset.

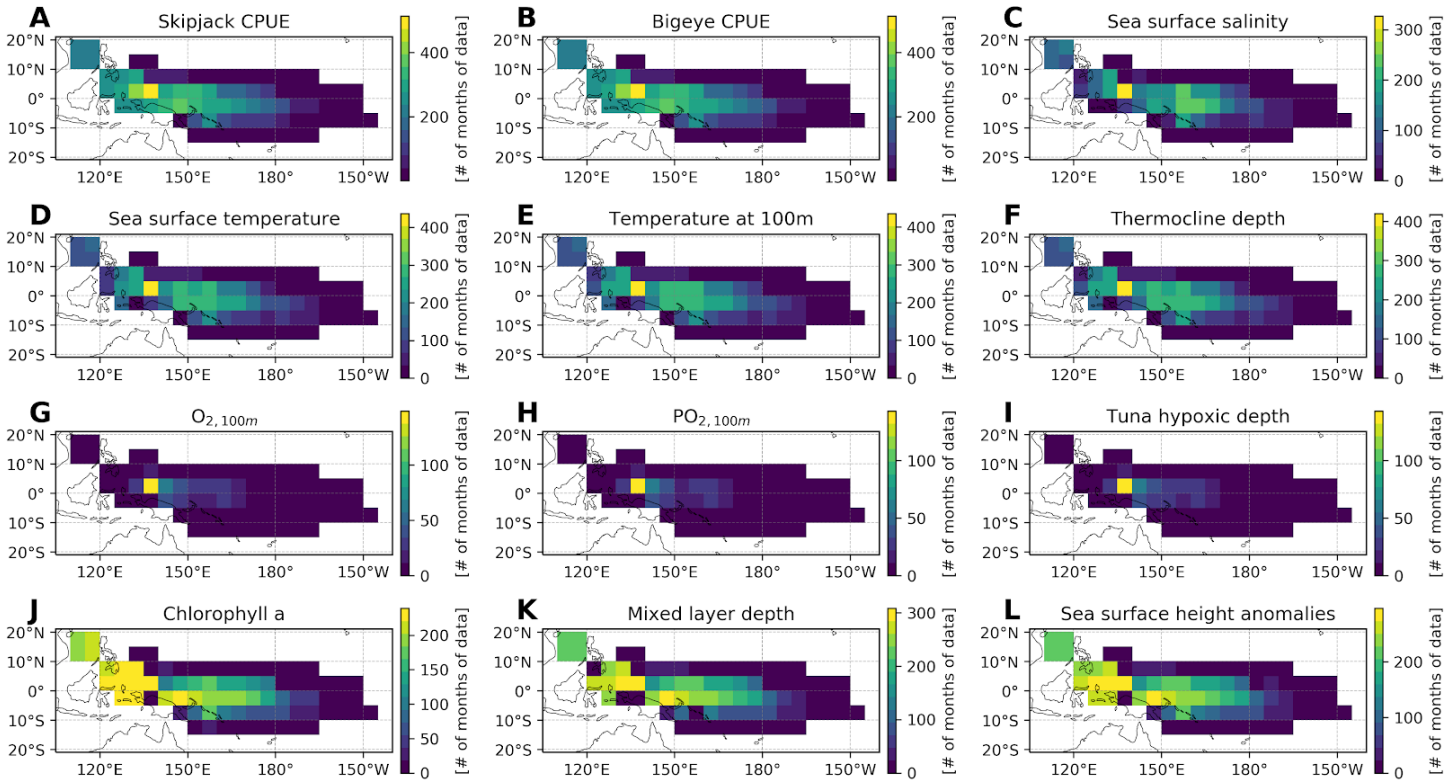

Supporting Figure 5.2 | Number of monthly data points available for skipjack/bigeye CPUEs and corresponding environmental conditions. (a, b) Total number of months of data on skipjack and bigeye CPUE available in the WCPFC purse seine catch dataset. (c-l) Total number of months of available environmental data overlapping with available months of both skipjack and bigeye CPUE. See Table 5.1 for further information on each environmental variable's dataset.

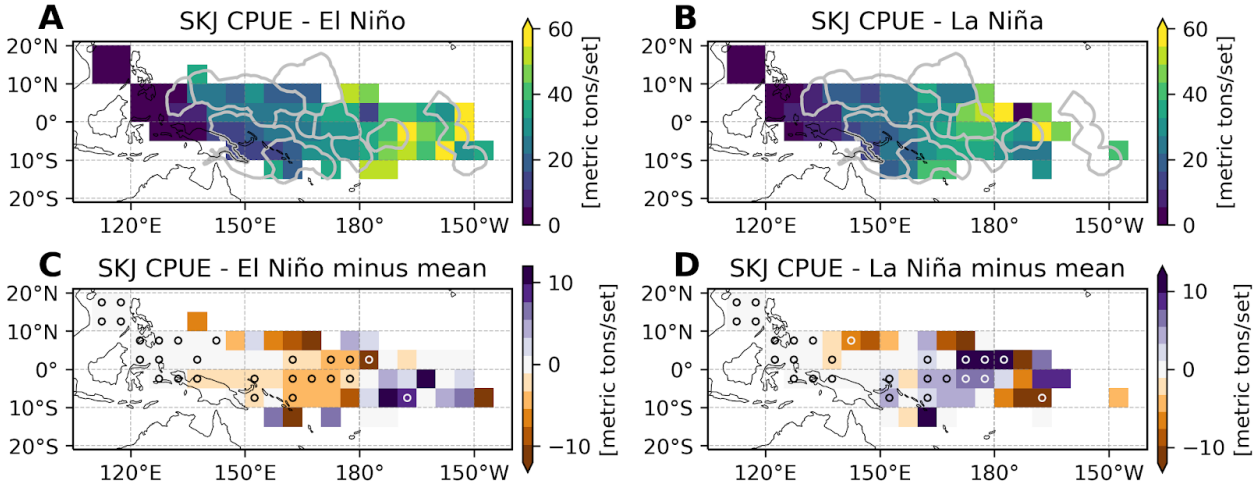

Supporting Figure 5.3 | ENSO-driven skipjack CPUE variability. Skipjack CPUE averaged over (a) El Niño months and (b) La Niña months. (c, d) Same as (a, b), but with mean SKJ CPUE subtracted. Stippling (circles) indicate grid points where El Niño and La Niña composite SKJ CPUE are significantly different from one another using a two-sided Wilcoxon rank-sum test and a multiple-hypothesis-test false discovery rate of 0.1 (see Section 5.3.2.1 for details). The light gray lines in (a,b) denote the exclusive economic zones (EEZs) of the eight Parties to the Nauru Agreement (PNA).

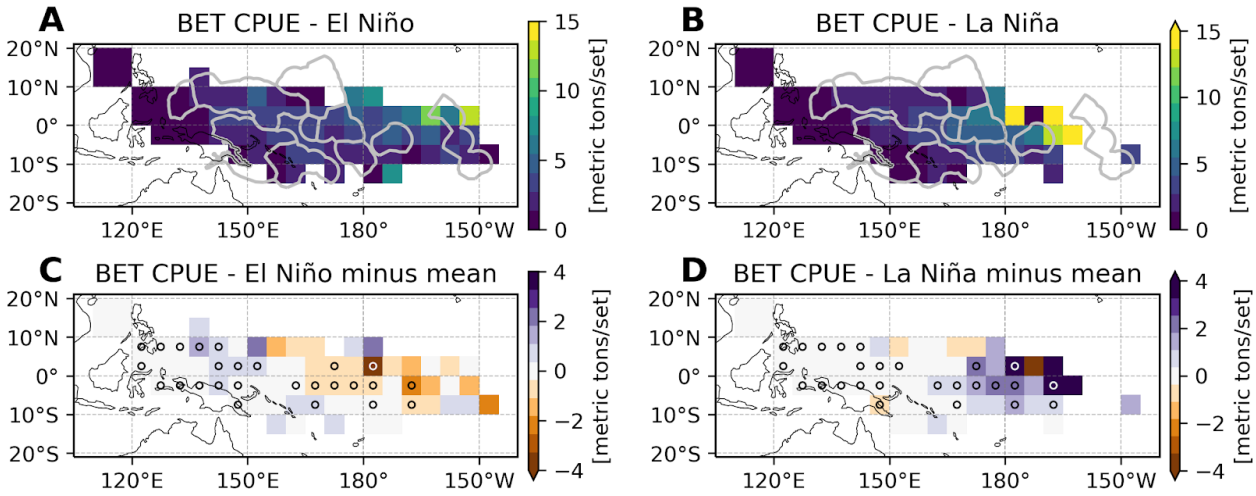

Supporting Figure 5.4 | ENSO-driven bigeye CPUE variability. Bigeye CPUE averaged over (a) El Niño months and (b) La Niña months. (c, d) Same as (a, b), but with mean BET CPUE subtracted. Stippling (circles) indicate grid points where El Niño and La Niña composite BET CPUE are significantly different from one another using a two-sided Wilcoxon rank-sum test and a multiple-hypothesis-test false discovery rate of 0.1 (see Section 5.3.2.1 for details). The light gray lines in (a,b) denote the exclusive economic zones (EEZs) of the eight Parties to the Nauru Agreement (PNA).

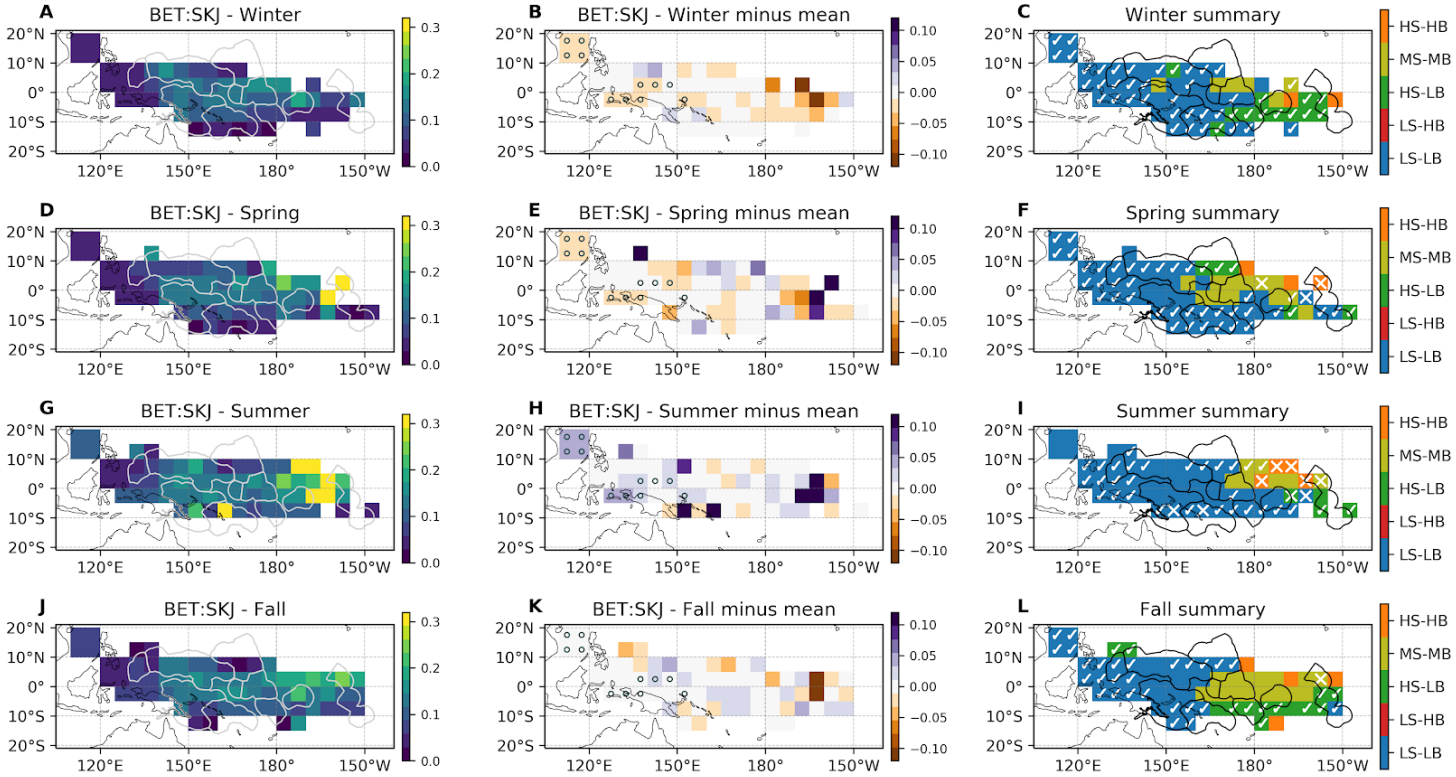

Supporting Figure 5.5 | Seasonally-driven skipjack and bigeye lateral separation variability. (Column 1) Bigeye-to-skipjack catch ratios averaged over winter, spring, summer, and autumn months. (Column 2) Same as (Column 1), but with mean bigeye-to-skipjack catch ratios subtracted. Stippling (circles) in (Column 2) indicate grid points where seasonal composite BET:SKJ values are significantly different from one another using a Kruskal-Wallis H-test and a multiple-hypothesis-test false discovery rate of 0.1 (see Section 5.3.2.1 for details).

(Column 3) Region types based on seasonal mean skipjack (shown in Supp. Fig. 5.3a) and bigeye CPUE (shown in Supp. Fig. 5.4a). Underlying colors correspond to region type, where S stands for skipjack, B for bigeye, H for high CPUE values, M for medium CPUE values, and L for low CPUE values. HS-LB regions, for example, exhibit high seasonal mean skipjack and low seasonal mean bigeye CPUE values. Overlain checkmarks and X's correspond to seasonal mean bigeye-to-skipjack catch ratios (shown in Column 1), where a checkmark denotes low (favorable) bigeye-to-skipjack catch ratios and an X denotes high (unfavorable) catch ratios. (The absence of any overlain symbol denotes moderate bigeye-to-skipjack catch ratios.) See Table 5.2 for CPUE and catch ratio ranges corresponding to the different region types. The light gray lines in Column 1 and black lines in Column 3 denote the exclusive economic zones (EEZs) of the eight Parties to the Nauru Agreement (PNA).

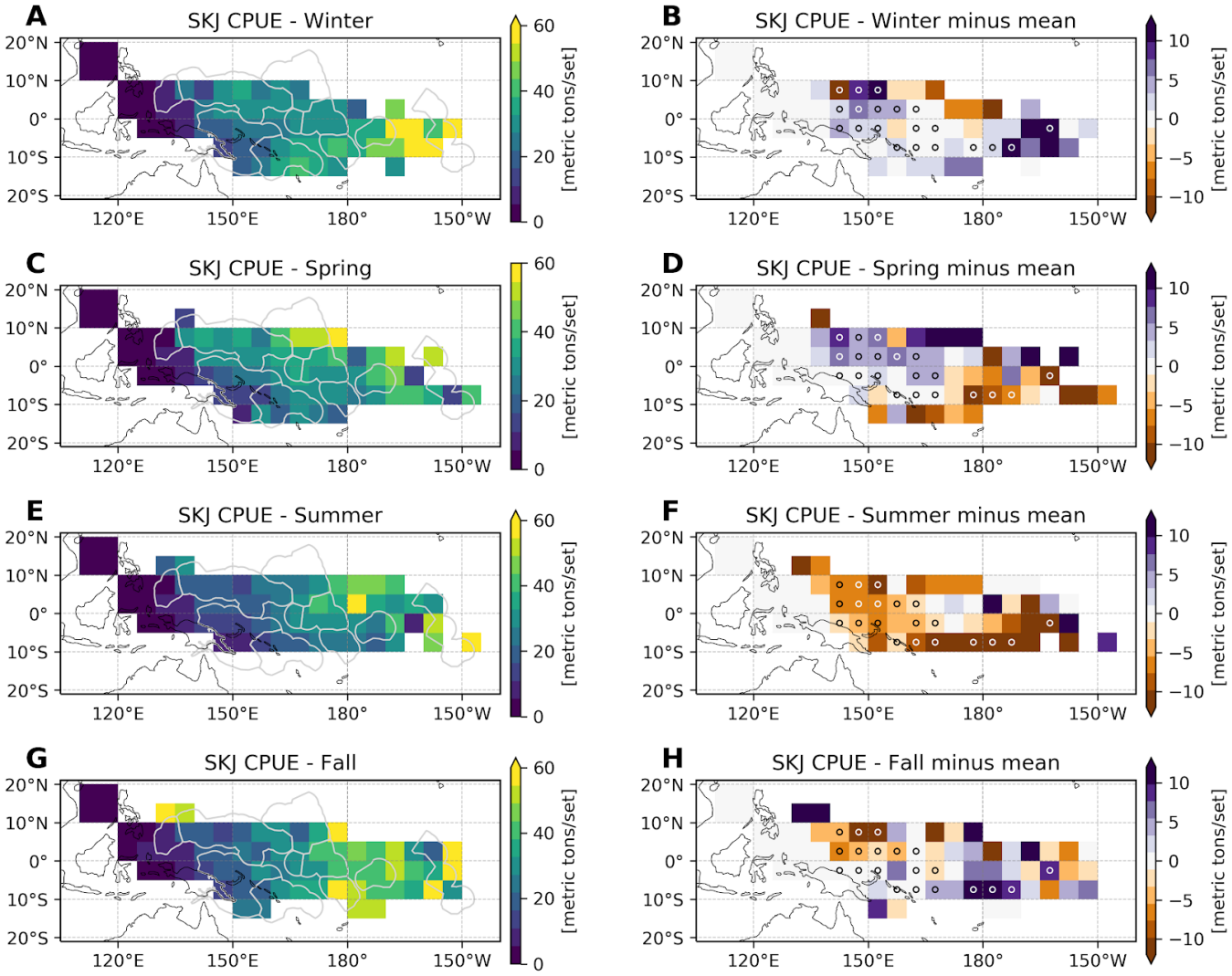

Supporting Figure 5.6 | Seasonally-driven skipjack CPUE variability. (Column 1) Skipjack CPUE averaged over winter, spring, summer, and autumn months. (Column 2) Same as (Column 1), but with mean skipjack CPUE subtracted. Stippling (circles) in (Column 2) indicate grid points where seasonal composite SKJ CPUE values are significantly different from one another using a Kruskal-Wallis H-test and a multiple-hypothesis-test false discovery rate of 0.1 (see Section 5.3.2.1 for details). The light gray lines in Column 1 denote the exclusive economic zones (EEZs) of the eight Parties to the Nauru Agreement (PNA).

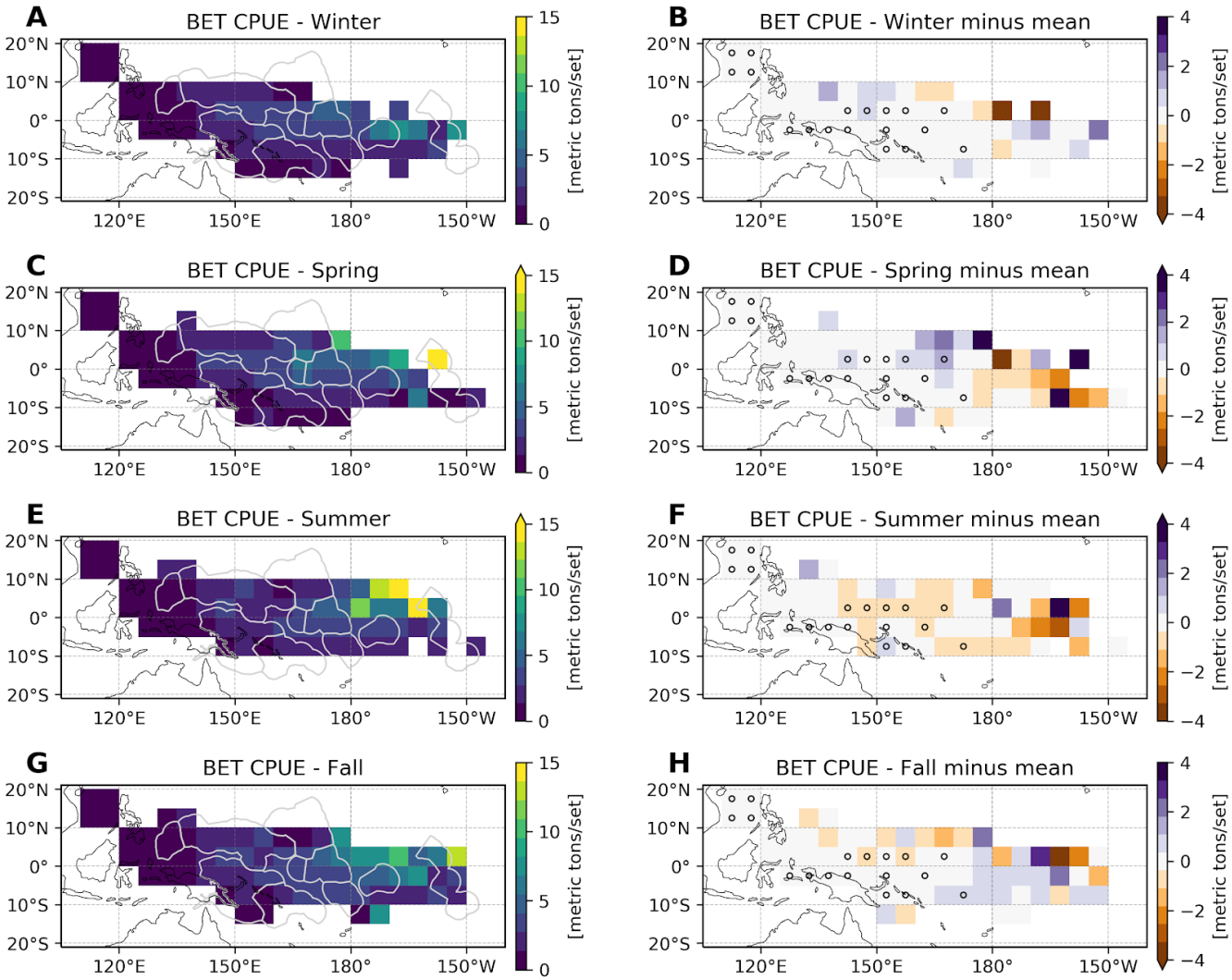

Supporting Figure 5.7 | Seasonally-driven bigeye CPUE variability. (Column 1) Bigeye CPUE averaged over winter, spring, summer, and autumn months. (Column 2) Same as (Column 1), but with mean bigeye CPUE subtracted. Stippling (circles) in (Column 2) indicate grid points where seasonal composite BET CPUE values are significantly different from one another using a Kruskal-Wallis H-test and a multiple-hypothesis-test false discovery rate of 0.1 (see Section 5.3.2.1 for details). The light gray lines in Column 1 denote the exclusive economic zones (EEZs) of the eight Parties to the Nauru Agreement (PNA).

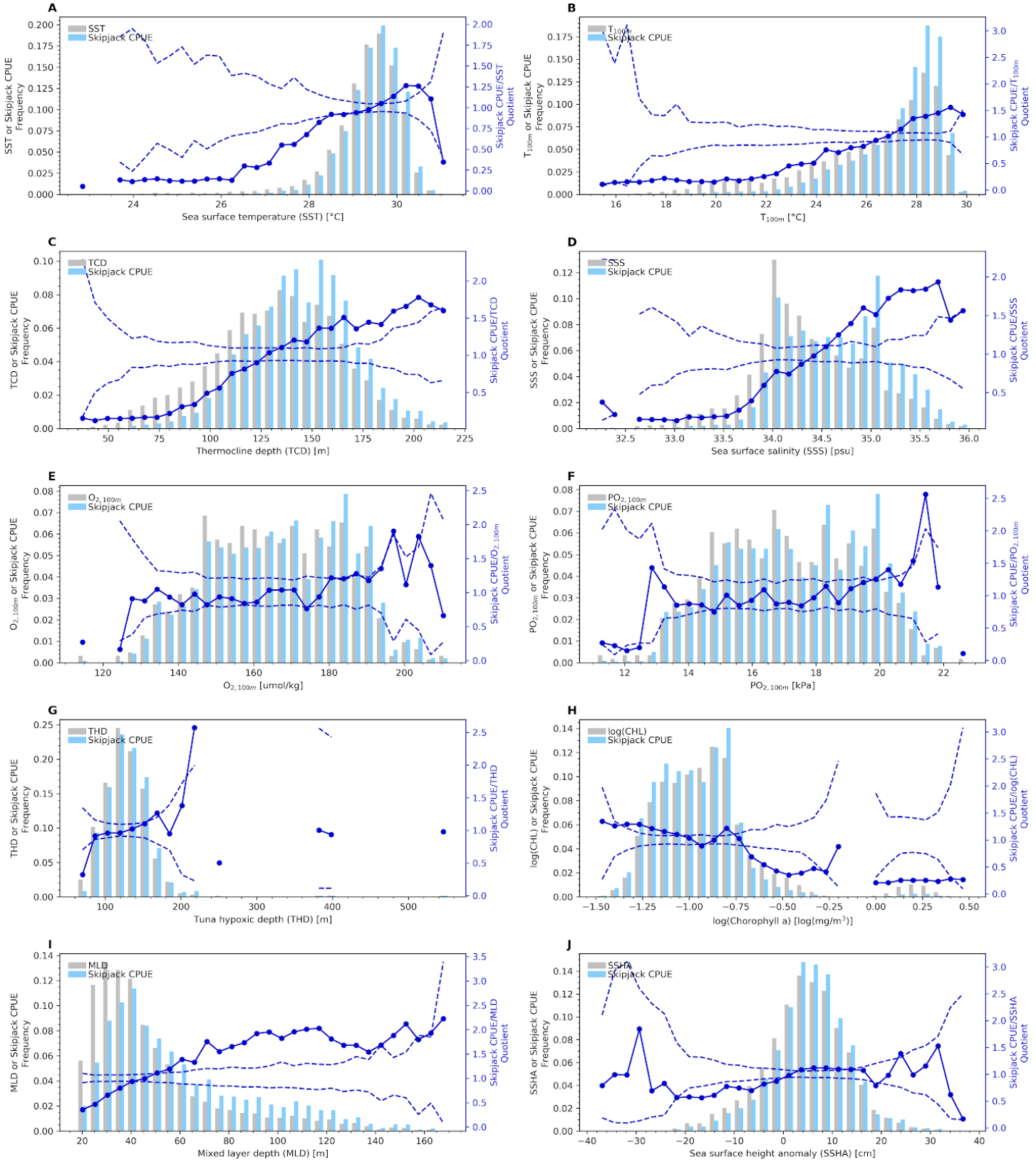

Supporting Figure 5.8 | Quotient analysis for associated purse seine-caught skipjack habitat preferences. See Section 5.3.3 for details.

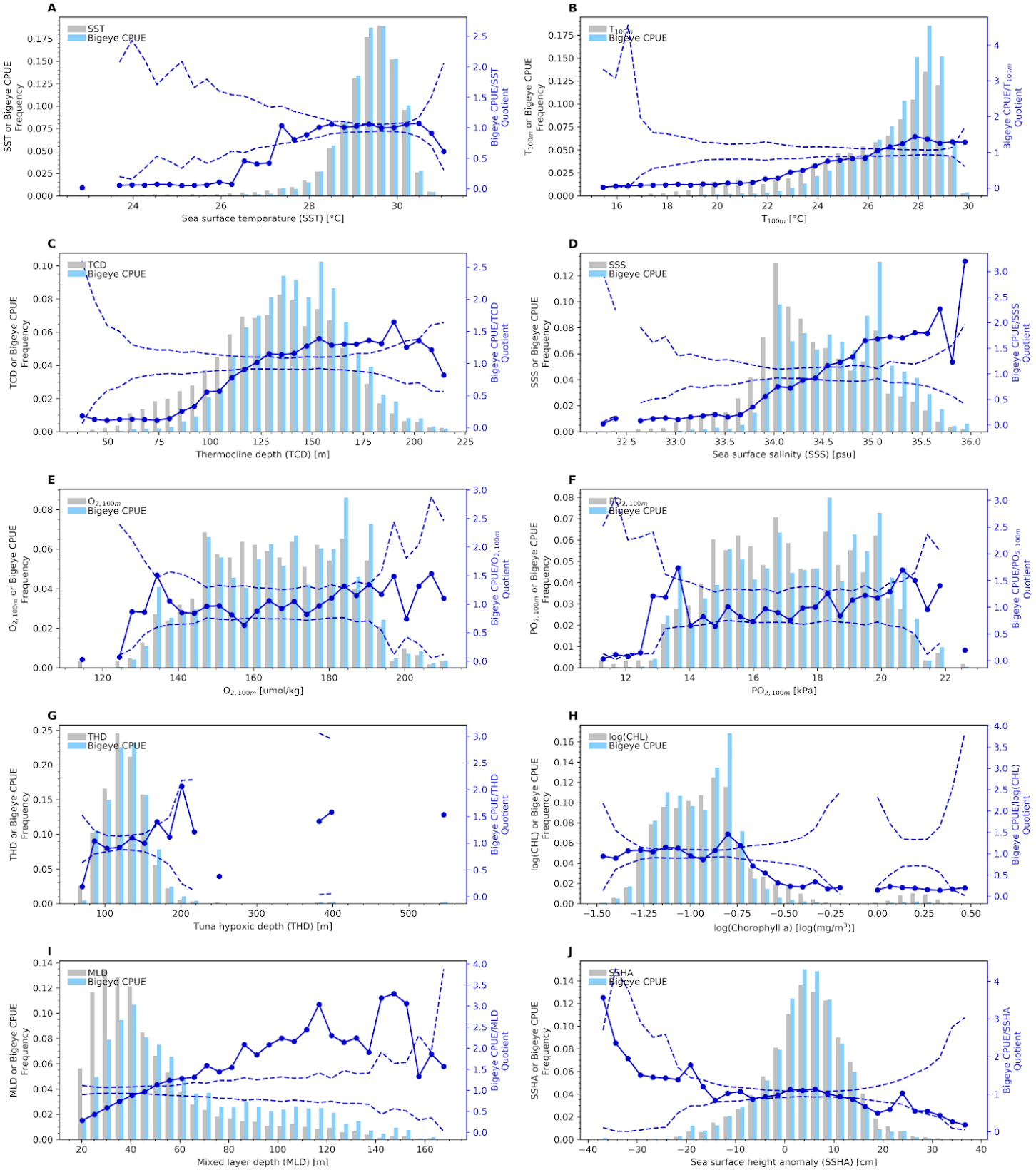

Supporting Figure 5.9 | Quotient analysis for associated purse seine-caught bigeye habitat preferences. See Section 5.3.3 for details.

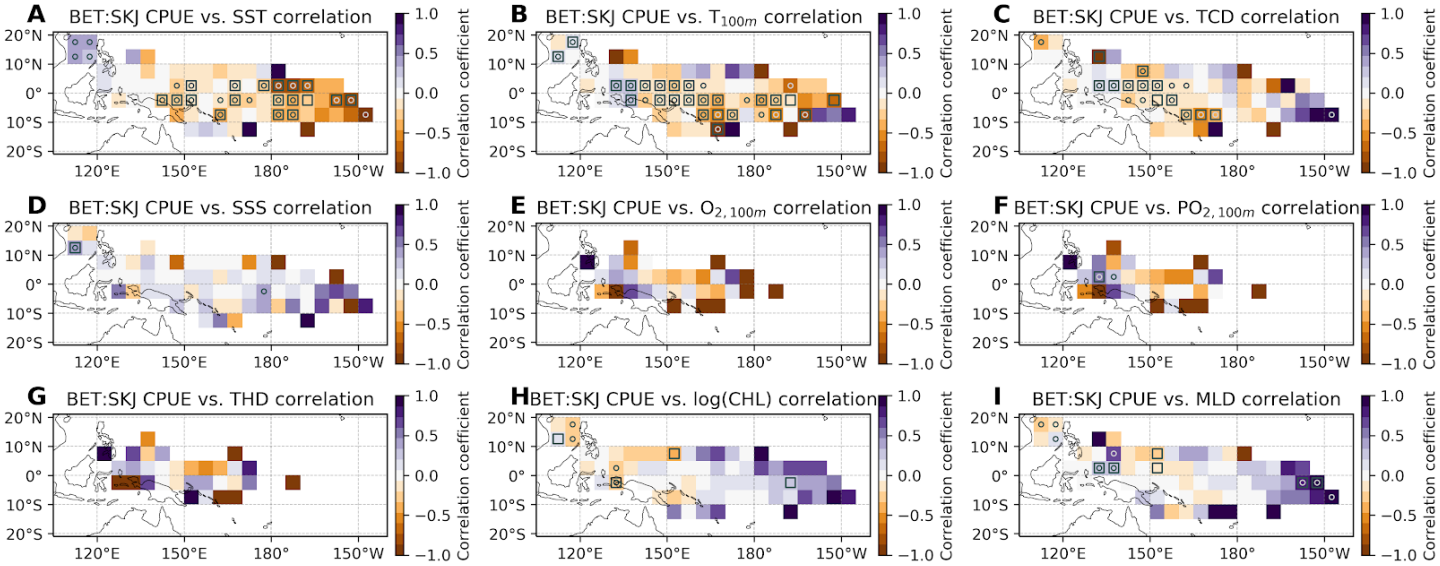

Supporting Figure 5.10 | WTP regions over which different environmental variables may be effective at laterally separating bigeye and skipjack. Temporal correlation coefficients between monthly BET:SKJ catch ratios and the environmental variables shown. Stippling (circles) indicates grid points where the correlation coefficient is significantly different from zero using a multiple-hypothesis-test false discovery rate of 0.1 (see Section 5.3.2.1 for details). Square boxes denote grid points where the following 3 criteria are met: 1.) At least one of the corresponding maps in Supp. Fig. 5.10-5.12 contains a statistically-significantly different from zero correlation coefficient; 2.) The given environmental variable is correlated with SKJ and BET CPUEs in opposite directions (that is, the sign of the correlation coefficient is different on corresponding maps in Supp. Fig. 5.11-5.12); 3.) The given environmental variable is correlated with SKJ CPUE and BET:SKJ catch ratios in opposite directions (that is, the sign of the correlation coefficient is different on corresponding maps in Supp. Fig. 5.10-5.11). Boxed grid cells thus indicate areas where a given change in the environmental variable at hand leads to opposite responses in skipjack and bigeye due to differential habitat preferences. Correlations are computed over all available data between Jan 1967 - Dec 2017.

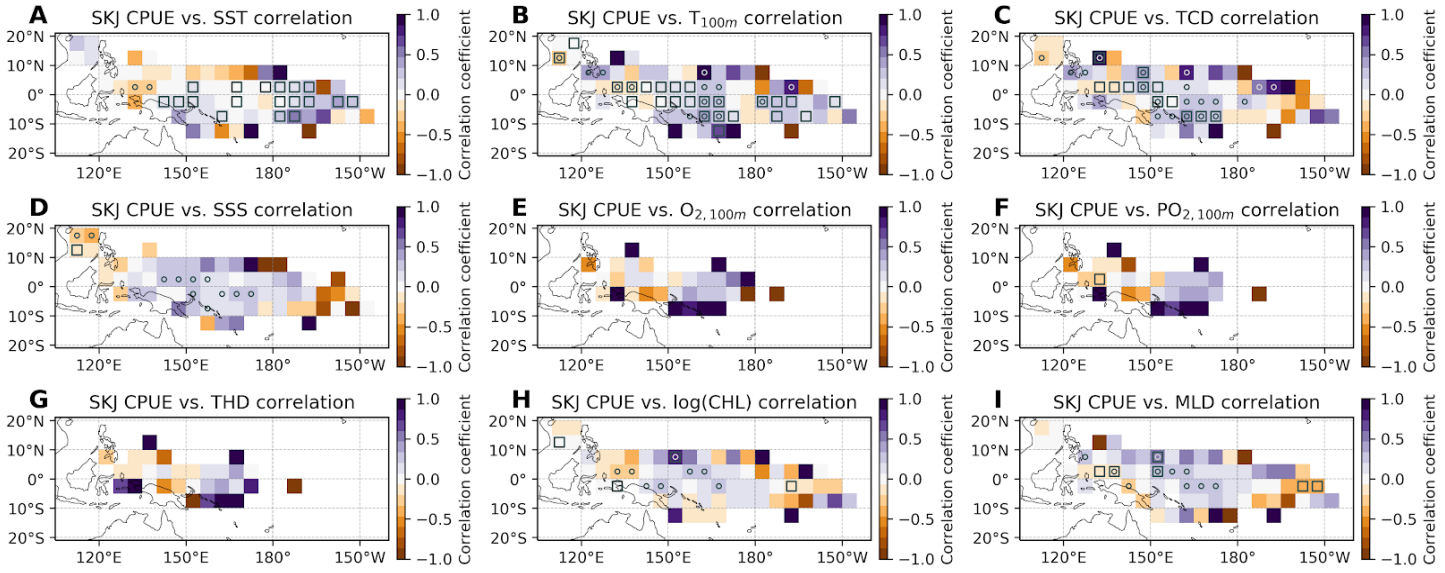

Supporting Figure 5.11 | Correlations between environmental conditions and skipjack CPUE. Temporal correlation coefficients between monthly SKJ CPUE values and the environmental variables shown. Supp. Fig. 5.10's legend applies here as well.

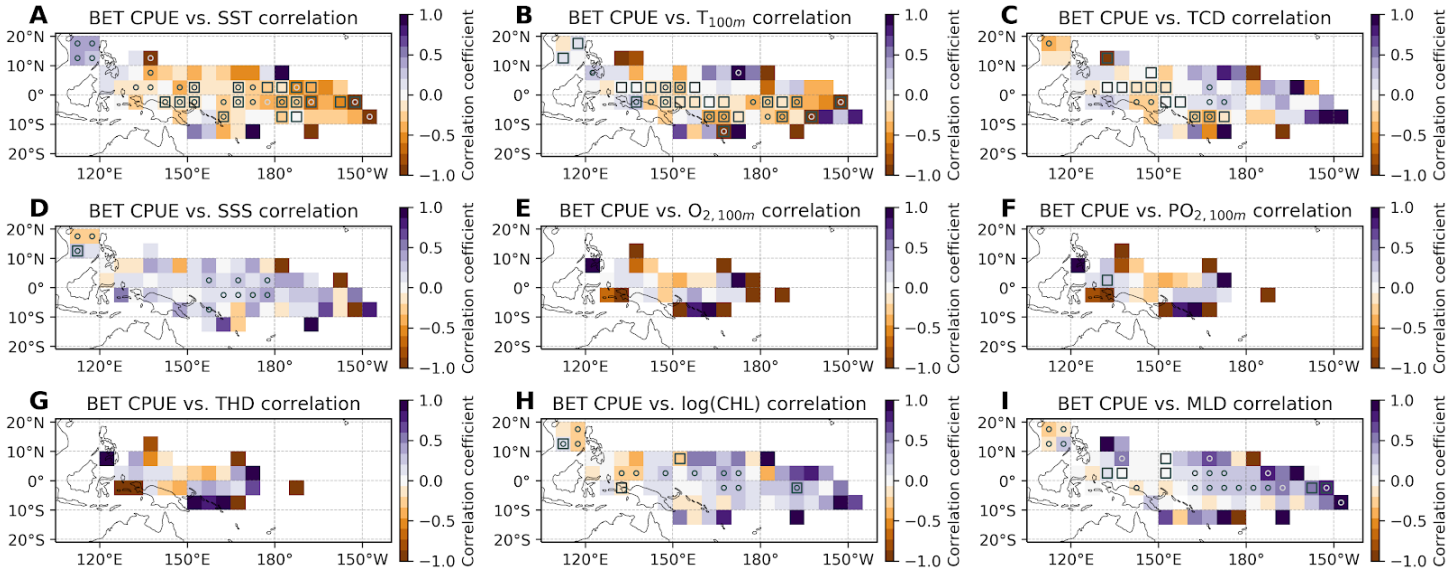

Supporting Figure 5.12 | Correlations between environmental conditions and bigeye CPUE. Temporal correlation coefficients between monthly BET CPUE values and the environmental variables shown. Supp. Fig. 5.10's legend applies here as well.

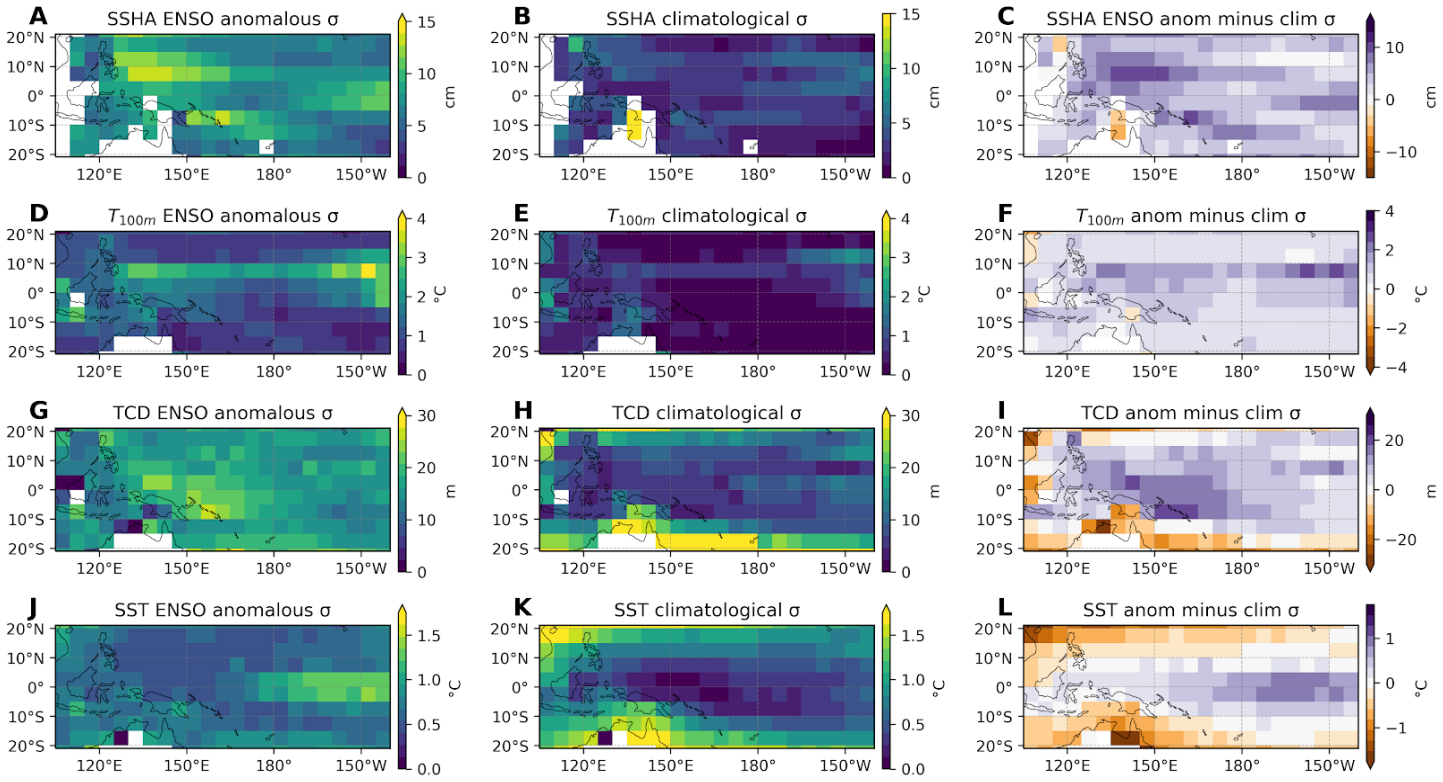

Supporting Figure 5.13 | Sources of environmental variability. Standard deviations of sea surface height anomalies (SSHA) computed from (a) monthly anomalies occurring during El Niño/La Niña phases and (b) from monthly climatologies. (c) Difference between standard deviations computed from ENSO-driven monthly anomalies and monthly climatologies (that is, a minus b). See Section 5.3.2.3 for further computational details. (d-f) Same as (a-c), but for 100-m temperatures (T_{100m}). (g-i) Same as (a-c), but for thermocline depths (TCD). (j-l) Same as (a-c), but for sea surface temperatures (SST).

5.7 References

14th Regular Session of the Scientific Committee Summary Report. (2018, August). The Commission for the Conservation and Management of Highly Migratory Fish Stocks in the Western and Central Pacific Ocean. Retrieved from https://www.wcpfc.int/meetings/14th-regular-session-scientific-committee

Abascal, F. J., Peatman, T., Leroy, B., Nicol, S., Schaefer, K., Fuller, D. W., & Hampton, J. (2018). Spatiotemporal variability in bigeye vertical distribution in the Pacific Ocean. *Fisheries Research*, *204*, 371–379. https://doi.org/10.1016/j.fishres.2018.03.013

Arrizabalaga, H., Dufour, F., Kell, L., Merino, G., Ibaibarriaga, L., Chust, G., et al. (2015). Global habitat preferences of commercially valuable tuna. *Deep Sea Research Part II: Topical Studies in Oceanography*, *113*, 102–112. https://doi.org/10.1016/j.dsr2.2014.07.001

Barkley, R. A., Neill, W. H., & Gooding, R. M. (1978). Skipjack tuna, Katsuwonus pelamis,

habitat based on temperature and oxygen requirements. *Fishery Bulletin*, *76*(3). Retrieved from https://swfsc.noaa.gov/publications/CR/1978/7804.PDF

Bernal, M., Stratoudakis, Y., Coombs, S., Angelico, M. M., de Lanzós, A. L., Porteiro, C., et al. (2007). Sardine spawning off the European Atlantic coast: Characterization of and spatio-temporal variability in spawning habitat. *Progress in Oceanography*, *74*(2), 210–227. https://doi.org/10.1016/j.pocean.2007.04.018

Bittenbender, S. (2017, December 8). WCPFC members agree to increase bigeye limits. Retrieved April 17, 2020, from https://www.seafoodsource.com/news/supply-trade/wcpfc-members-agree-to-increase-bigeye-limits

Boyer, T. P., Antonov, J. I., Baranova, O. K., Coleman, C., Garcia, H. E., Grodsky, A., et al. (2013). World Ocean Database 2013. National Environmental Satellite and Data Information Service (NESDIS). Retrieved from http://doi.org/10.7289/V5NZ85MT

Bushnell, Peter. G., Brill, R. W., & Bourke, R. E. (1990). Cardiorespiratory responses of skipjack tuna (Katsuwonus pelamis), yellowfin tuna (Thunnus albacares), and bigeye tuna (Thunnus obesus) to acute reductions of ambient oxygen. *Canadian Journal of Zoology*, *68*(9), 1857–1865. https://doi.org/10.1139/z90-265

Enns, T., Scholander, P. F., & Bradstreet, E. D. (1965). Effect of Hydrostatic Pressure on Gases Dissolved in Water. *The Journal of Physical Chemistry*, *69*(2), 389–391. https://doi.org/10.1021/j100886a005

Evans, R. H., McLain, D. R., & Bauer, R. A. (1981). Atlantic skipjack tuna: influences of mean environmental conditions on their vulnerability to surface fishing gear. *Marine Fisheries Review*, *43*(6). Retrieved from https://spo.nmfs.noaa.gov/sites/default/files/pdf-content/MFR/mfr436/mfr4361.pdf

Farley, J., Eveson, P., Krusic-Golub, K., Sanchez, C., Roupsard, F., McKechnie, S., et al. (2017, August 9). Project 35: Age, growth and maturity of bigeye tuna in the western and central Pacific Ocean. Retrieved from https://www.wcpfc.int/system/files/SC13-SA-WP-01%20BET%20age%20growth%20maturity.pdf

Farley, J., Eveson, P., Krusic-Golub, K., Clear, N., Sanchez, C., Roupsard, F., et al. (2018, August 8). Project 81: Update on age and growth of bigeye tuna in the western and central pacific ocean. Retrieved from https://www.wcpfc.int/file/217846/

Fiedler, P. C. (2010). Comparison of objective descriptions of the thermocline. *Limnology and Oceanography: Methods*, *8*(6), 313–325. https://doi.org/10.4319/lom.2010.8.313

Forget, G., Campin, J.-M., Heimbach, P., Hill, C. N., Ponte, R. M., & Wunsch, C. (2015). ECCO version 4: an integrated framework for non-linear inverse modeling and global ocean state estimation. Geoscientific Model Development, 8(10), 3071–3104.

https://doi.org/10.5194/gmd-8-3071-2015

Fukumori, I., Wang, O., Fenty, I., Forget, G., Heimbach, P., & Ponte, R. M. (2020, March 19). ECCO Version 4 Release 4 Notes. Retrieved from https://ecco.jpl.nasa.gov/drive/files/Version4/Release4/doc/v4r4_synopsis.pdf

Garcia, H. E., & Gordon, L. I. (1992). Oxygen solubility in seawater: Better fitting equations. *Limnology and Oceanography*, *37*(6), 1307–1312. https://doi.org/10.4319/lo.1992.37.6.1307

Gooding, R. M., Neill, W. H., & Dizon, A. E. (1981). Respiration rates and low-oxygen tolerance limits in skipjack tuna, Katsuwonus pelamis. *Fishery Bulletin*, *79*(1). Retrieved from https://spo.nmfs.noaa.gov/sites/default/files/pdf-content/1981/791/gooding.pdf

Griffiths, S. P., Allain, V., Hoyle, S. D., Lawson, T. A., & Nicol, S. J. (2019). Just a FAD? Ecosystem impacts of tuna purse-seine fishing associated with fish aggregating devices in the western Pacific Warm Pool Province. *Fisheries Oceanography*, *28*(1), 94–112. https://doi.org/10.1111/fog.12389

Hampton, J., & Williams, P. G. (2017, August 9). Annual estimates of purse seine catches by species based on alternative data sources. Retrieved from https://www.wcpfc.int/node/29507

Harley, S. J., Davies, N., Hampton, J., & McKechnie, S. (2014, August 6). Stock assessment of bigeye tuna in the Western and Central Pacific Ocean. Retrieved from https://www.wcpfc.int/system/files/SC10-SA-WP-01%20%5BBET%20Assessment%5D_rev1_25July.pdf

Harley, Shelton J., & Suter, J. M. (2007). The potential use of time-area closures to reduce catches of bigeye tuna (Thunnus obesus) in the purse-seine fishery of the eastern Pacific Ocean. *Fishery Bulletin*, *105*(1), 49–62.

Hofmann, A. F., Peltzer, E. T., Walz, P. M., & Brewer, P. G. (2011). Hypoxia by degrees: Establishing definitions for a changing ocean. *Deep Sea Research Part I: Oceanographic Research Papers*, *58*(12), 1212–1226. https://doi.org/10.1016/j.dsr.2011.09.004

Howell, E. A., & Kobayashi, D. R. (2006). El Niño effects in the Palmyra Atoll region: oceanographic changes and bigeye tuna (Thunnus obesus) catch rate variability. *Fisheries Oceanography*, *15*(6), 477–489. https://doi.org/10.1111/j.1365-2419.2005.00397.x

Hu, C., Harrison, D. P., Hinton, M. G., Siegrist, Z. C., & Kiefer, D. A. (2018). Habitat analysis of the commercial tuna of the Eastern Tropical Pacific Ocean. *Fisheries Oceanography*, *27*(5), 417–434. https://doi.org/10.1111/fog.12263

Huang, B., L'Heureux, M., Hu, Z.-Z., & Zhang, H.-M. (2016). Ranking the strongest ENSO events while incorporating SST uncertainty. *Geophysical Research Letters*, *43*(17), 9165–9172. https://doi.org/10.1002/2016GL070888

Ingham, M. C., Cook, S. K., & Hausknecht, K. A. (1977). Oxycline characteristics and skipjack tuna distribution in the southeastern tropical Atlantic. *Fishery Bulletin*, *75*(4). Retrieved from https://spo.nmfs.noaa.gov/sites/default/files/pdf-content/1977/754/ingham.pdf

Lehodey, P., Bertignac, M., Hampton, J., Lewis, A., & Picaut, J. (1997). El Niño Southern Oscillation and tuna in the western Pacific. *Nature*, *389*(6652), 715–718. https://doi.org/10.1038/39575

Lehodey, Patrick. (2001). The pelagic ecosystem of the tropical Pacific Ocean: dynamic spatial modelling and biological consequences of ENSO. *Progress in Oceanography*, *49*(1), 439–468. https://doi.org/10.1016/S0079-6611(01)00035-0

Lennert-Cody, C. E., Roberts, J. J., & Stephenson, R. J. (2008). Effects of gear characteristics on the presence of bigeye tuna (Thunnus obesus) in the catches of the purse-seine fishery of the eastern Pacific Ocean. *ICES Journal of Marine Science*, *65*(6), 970–978. https://doi.org/10.1093/icesjms/fsn075

Leroy, B., Itano, D. G., Usu, T., Nicol, S. J., Holland, K. N., & Hampton, J. (2009). Vertical Behavior and the Observation of FAD Effects on Tropical Tuna in the Warm-Pool of the Western Pacific Ocean. In J. L. Nielsen, H. Arrizabalaga, N. Fragoso, A. Hobday, M. Lutcavage, & J. Sibert (Eds.), *Tagging and Tracking of Marine Animals with Electronic Devices* (pp. 161–179). Dordrecht: Springer Netherlands. https://doi.org/10.1007/978-1-4020-9640-2_10

Leroy, B., Phillips, J. S., Nicol, S., Pilling, G. M., Harley, S., Bromhead, D., et al. (2013). A critique of the ecosystem impacts of drifting and anchored FADs use by purse-seine tuna fisheries in the Western and Central Pacific Ocean. *Aquatic Living Resources*, *26*(1), 49–61. https://doi.org/10.1051/alr/2012033

Leung, S., Thompson, L., McPhaden, M. J., & Mislan, K. A. S. (2019). ENSO drives near-surface oxygen and vertical habitat variability in the tropical Pacific. *Environmental Research Letters*, *14*(6), 064020. https://doi.org/10.1088/1748-9326/ab1c13

McKechnie, S., Pilling, G., & Hampton, J. (2017, August 9). Stock assessment of bigeye tuna in the western and central Pacific Ocean. Retrieved from https://www.wcpfc.int/system/files/SC13-SA-WP-05%20%5Bbet-assessment%5D%20REV1.pdf

Phillips, J. S., Pilling, G. M., Leroy, B., Evans, K., Usu, T., Lam, C. H., et al. (2017). Revisiting the vulnerability of juvenile bigeye (Thunnus obesus) and yellowfin (T. albacares) tuna caught by purse-seine fisheries while associating with surface waters and floating objects. *PLOS ONE*, *12*(6), e0179045. https://doi.org/10.1371/journal.pone.0179045

Prince, E. D., & Goodyear, C. P. (2006). Hypoxia-based habitat compression of tropical pelagic fishes. *Fisheries Oceanography*, *15*(6), 451–464. https://doi.org/10.1111/j.1365-2419.2005.00393.x

Radenac, M.-H., Léger, F., Singh, A., & Delcroix, T. (2012). Sea surface chlorophyll signature in

the tropical Pacific during eastern and central Pacific ENSO events. *Journal of Geophysical Research: Oceans*, *117*(C4). https://doi.org/10.1029/2011JC007841

Sathyendranath, S., Brewin, R. J. W., Brockmann, C., Brotas, V., Calton, B., Chuprin, A., et al. (2019). An Ocean-Colour Time Series for Use in Climate Studies: The Experience of the Ocean-Colour Climate Change Initiative (OC-CCI). *Sensors*, *19*(19), 4285. https://doi.org/10.3390/s19194285

Schaefer, K. M., & Fuller, D. W. (2013). Simultaneous behavior of skipjack (Katsuwonus pelamis), bigeye (Thunnus obsesus), and yellowfin (T. albacares) tunas, within large multi-species aggregations associated with drifting fish aggregating devices (FADs) in the equatorial eastern Pacific Ocean. *Marine Biology*, *160*(11), 3005–3014. https://doi.org/10.1007/s00227-013-2290-9

Seibel, B. A. (2011). Critical oxygen levels and metabolic suppression in oceanic oxygen minimum zones. *Journal of Experimental Biology*, *214*(2), 326–336. https://doi.org/10.1242/jeb.049171

Sharma, P., Singh, A., Marinov, I., & Kostadinov, T. (2019). Contrasting ENSO Types With Satellite-Derived Ocean Phytoplankton Biomass in the Tropical Pacific. *Geophysical Research Letters*, *46*(11), 5987–5996. https://doi.org/10.1029/2018GL080689

Sibert, J., Senina, I., Lehodey, P., & Hampton, J. (2012). Shifting from marine reserves to maritime zoning for conservation of Pacific bigeye tuna (Thunnus obesus). *Proceedings of the National Academy of Sciences*, *109*(44), 18221–18225. https://doi.org/10.1073/pnas.1209468109

SPC. (2019, November 3). WCPFC tuna fisheries yearbook 2018. WCPFC. Retrieved from https://www.wcpfc.int/file/355404/

SPC-OFP. (2018a, August 8). SPC updated evaluation of WCP draft bridging CMM 2017-01 on tropical tunas (Chair's draft). Retrieved from https://www.wcpfc.int/file/187767/

SPC-OFP. (2018b, December 10). Evaluation of CMM 2017-01 for bigeye tuna with additional evaluations for skipjack and yellowfin tuna. Retrieved from https://www.wcpfc.int/file/224476/

SPC-OFP. (2019, December). Current and projected stock status of WCPO skipjack tuna to inform consideration of an updated target reference point. WCPFC. Retrieved from https://www.wcpfc.int/file/355281/

Tremblay-Boyer, L., McKechnie, S., Pilling, G. M., & Hampton, J. (2017, August 9). Exploratory geostatistical analyses of Pacific-wide operational longline CPUE data for WCPO tuna assessments. Retrieved from https://www.wcpfc.int/system/files/SC13-SA-WP-03%20CPUE%20geostats%20approach%20LL.pdf

Ventura, V., Paciorek, C. J., & Risbey, J. S. (2004). Controlling the Proportion of Falsely

Rejected Hypotheses when Conducting Multiple Tests with Climatological Data. *Journal of Climate*, *17*(22), 4343–4356. https://doi.org/10.1175/3199.1

Vincent, M. T., Pilling, G. M., & Hampton, J. (2018, August 8). Incorporation of updated growth information within the 2017 WCPO bigeye stock assessment grid, and examination of the sensitivity of estimates to alternative model spatial structures. Retrieved from https://www.wcpfc.int/file/217052/

Vincent, M. T., Pilling, G. M., & Hampton, J. (2019, August). Stock assessment of skipjack tuna in the western and central Pacific Ocean. WCPFC. Retrieved from https://www.wcpfc.int/file/309836/

Wang, J., Chen, X., & Chen, Y. (2016). Spatio-temporal distribution of skipjack in relation to oceanographic conditions in the west-central Pacific Ocean. *International Journal of Remote Sensing*, *37*(24), 6149–6164. https://doi.org/10.1080/01431161.2016.1256509

WCPFC. (2007, December). Rules and Procedures for the Protection, Access to, and Dissemination of Data Compiled by the Commission. Retrieved from https://www.wcpfc.int/file/300/

WCPFC. (2017, December). Draft bridging CMM 2017-01 on Tropical Tunas (Revision 1). Retrieved from https://www.wcpfc.int/system/files/WCPFC14-2017-30_rev1%20draft%20bridging%20measure%20on%20tropical%20tunas%20rev1.pdf

Wilks, D. S. (2006). On “Field Significance” and the False Discovery Rate. *Journal of Applied Meteorology and Climatology*, *45*(9), 1181–1189. https://doi.org/10.1175/JAM2404.1

Wilks, D. S. (2016). “The Stippling Shows Statistically Significant Grid Points”: How Research Results are Routinely Overstated and Overinterpreted, and What to Do about It. *Bulletin of the American Meteorological Society*, *97*(12), 2263–2273. https://doi.org/10.1175/BAMS-D-15-00267.1

Williams, P., & Terawasi, P. (2015, July 28). Overview of tuna fisheries in the western and central Pacific Ocean, including economic conditions. Western and Central Pacific Fisheries Commission. Retrieved from https://www.wcpfc.int/system/files/GN-WP-01%20Overview%20of%20WCPFC%20Fisheries%20Rev%201.pdf

Chapter 6: Conclusion

This dissertation has examined the far-reaching impacts of climate variability and change on marine ecosystem processes and organisms of many shapes and sizes, important for various ecological, cultural, and economic reasons.

In Chapter 2, I show that more detailed modeling of sinking particles in the ocean can have a considerable effect on the accuracy of future climate change-driven projections of particulate carbon export, which can in turn affect projections of mesopelagic biomass availability and subsurface oxygen concentrations. Indeed, accounting for the effects of variable phytoplankton and particle sizes on nutrient remineralization depths reduces the magnitude of predicted 100-year changes in global export production by ~14% in a mechanistic biogeochemical model constrained with satellite observations. Projections of export production within state-of-the-art Earth System Models could thus be improved by better resolving phytoplankton and particle size-dependent remineralization depths.

In Chapter 3, I show that ENSO is the primary driver of substantial upper-ocean oxygen variability on interannual time scales in the Tropical Pacific. Oxygen, in addition to temperature, thus likely plays an important role in altering available tuna vertical habitat space between different phases of ENSO. Because of this, ENSO-driven variations in water column oxygen content should be considered in models of habitat quality and catchability used to assess tuna species stock statuses.

In Chapter 4, I show that climate warming-driven changes in ocean oxygen content over the next century will most greatly affect species residing in the temperate North Pacific, where projected decreases in oxygen concentrations between 200-700 m depth are greatest and most

certain. These species include swordfish and yellowfin, bigeye, Pacific bluefin, and albacore tunas. The least certain projections of subsurface oxygen concentration changes and effects occur within the Tropical Pacific. Given these high levels of uncertainty and the extreme economic importance of tuna and billfish fisheries in this region, more attention should be focused on improving model projections here. Vertically, the depth at which oxygen concentrations drop below 3.5 ml l^{-1} (a threshold hypoxic concentration for several tuna and billfish species) is projected to become shallower throughout the global oceans, which may lead to widespread vertical habitat compression and changes in vertical movement patterns. Where populations of targeted tuna and billfish species decrease in abundance or move away from traditional fishing grounds due to either vertical or lateral changes in their habitats, fishers will have to spend more resources to locate and catch these species, or reconfigure their gear to target new ones. Economic, political, and regulatory constraints can, however, hinder the ability of fishers, particularly those who operate on a small-scale, to effectively adapt.

In Chapter 5, I show that FAD-associated bigeye and skipjack catch covary tightly in purse seine fisheries throughout the WCPO, such that lateral separation between the two species is generally small. There are, however, significant variations in this separability over both time and space, with especially large variations driven by ENSO. El Niño lowers (raises) fractional incidental bigeye catch east (west) of ~170°E, while La Niña has the opposite effect. Spatial patterns in sea surface height anomalies, which also vary greatly with ENSO, may be especially useful in separating different habitats preferred by skipjack and bigeye throughout the Western Central Pacific Ocean. This information on skipjack-bigeye lateral separability and their

environmental drivers can be used by fisheries managers to create more effective, spatially and temporally dynamic policies regarding FAD-associated purse seine catches in the WCPO.

In Appendix A, I show that ENSO also drives sizable variations in micronektonic prey availability and diel vertical migration depths within the Tropical Pacific. As was the case with subsurface oxygen concentrations, these variations in prey availability should also be considered in models of tuna habitat quality and catchability used in stock assessments.

In sum, I have shown that climate variability and change can have profound effects on marine ecosystem processes on all scales, from the size and sinking speed of particles to the spatial distributions of top pelagic predators and their relationships with other species, including humans. These ecosystem process effects are typically mediated by physical and biogeochemical factors in the environment including changes in circulation rates, oxygen availability, temperatures, and distributions of micronektonic prey. I have also shown that there are many ways to improve the accuracy of models, including better resolving small-scale processes with large effects, better constraining parameterized relationships with observational data, and better establishing more detailed information on biologically relevant background conditions. Lastly, I have shown that much can be answered and understood using only already-existing public domain data, in combination with computational savvy and a keen eye for creative new uses of old information. Armed with this new knowledge of what the future might hold for the marine organisms and ecosystem processes studied here, we can begin adapting to these coming changes in a way that will most effectively reduce harm to those most dependent on these marine resources.

Appendix A: Repurposing ADCP data: A case study on Tropical Pacific mid-trophic level prey

This appendix is preliminary work and should be used/cited with care. To properly employ the open-source code associated with this appendix (uploaded here: https://doi.org/10.5281/zenodo.3907368 and here: https://github.com/shirleyswirley/acoustic-variability), each individual user should begin by verifying that the code is working how they expect. Each individual user is also responsible for calculating the errors caused by any assumptions made in the associated code for their individual dataset and purpose. A version of this appendix was presented in poster form at the 2020 Ocean Sciences Meeting: https://doi.org/10.1002/essoar.10502383.1.

A.1 Summary

Mid-trophic level macrozooplankton (2–20 mm) and micronekton (2–20 cm) are important sources of food for tuna and other large pelagic predators across the global ocean. These organisms also contribute significantly to the biological carbon pump through excretion of fecal pellets and diel vertical migrations (DVMs) between the surface and mesopelagic ocean. In spite of their importance, distributions of these mid-trophic level species and their variations in space and time are not well-known, due to a lack of comprehensive *in situ* observations. Acoustic doppler current profiler (ADCP) data is routinely gathered by research cruises and moorings and can help fill this observational gap. Here I present the novel use of an existing publicly-available, global ADCP dataset (JASADCP, or the Joint Archive for Shipboard ADCP) to better characterize *in situ* distributions of mid-trophic level organisms, as well as their spatiotemporal variabilities throughout the Tropical Pacific. I find that ENSO drives variability in mid-trophic level prey distributions, abundance, and potentially composition throughout the Tropical Pacific. To promote awareness and utilization of JASADCP and other

publicly-available ADCP datasets, I also publish easy-to-use, open-source code that readily computes total backscatter and detects DVMs from ADCP data. Because this work is still preliminary, however, it is the responsibility of each individual user to compute the errors and uncertainties associated with the various assumptions made in the code; these assumptions are detailed explicitly and meticulously both in the code itself and the text below.

A.2 Introduction

Tuna catches in the Tropical Pacific Ocean are an important food source and economic driver, but are highly variable in both space and time (e.g., Lehodey et al., 1997). This variability remains quite poorly explained even though much work has tried to quantify its underlying drivers (e.g., Lehodey et al., 1997; Leung et al., 2019). The relationships between spatiotemporal distributions of tuna and their forage are particularly poorly understood and have been mostly derived from model estimates (Menkes et al., 2015). Because most stock assessments upon which fisheries management decisions are made use fisheries-based abundance indices (such as catch per unit effort, or CPUE) normalized by climatological habitat favorability to estimate population sizes (Brill and Lutcavage, 2001; Bigelow et al., 2002; Goodyear, 2003; Prince and Goodyear, 2006; Maunder et al., 2006; Maunder and Piner, 2015), more accurate stock assessments also require better information on prey availability.

Mid-trophic level macrozooplankton (2–20 mm) and micronekton (2–20 cm) are especially important sources of food for tuna and other large pelagic fish species both in the Tropical Pacific and across the global ocean (LeBorgne et al., 2011; Duffy et al., 2017). Macrozooplankton include jellyfish and copepods among others, while micronekton include

euphausiids, squid, shrimp, and small fish among others. In addition to feeding culturally and economically important top pelagic predators, these organisms can also play important roles in the biological pump through the excretion of fecal pellets and via diel vertical migrations (DVMs) between the surface and mesopelagic ocean (Bianchi et al., 2013a; Archibald et al., 2019). Thus, spatiotemporal variations in macrozooplanktonic/micronektonic biomass and distributions can have significant effects on carbon storage, biogeochemical cycling, pelagic habitat quality, and rates of energy transfer to higher trophic levels.

In spite of their importance, large-scale distributions of these mid-trophic level species and their variations in space and time are not well-known, due to the lack of comprehensive *in situ* observations of these organisms. This observational gap exists in part because traditional methods used to measure these species (such as trawling and net tows) are difficult, time-consuming, and expensive. It would therefore be more efficient and time-saving to quantify prey abundance from information that is relatively cheap and already readily available, such as acoustic data from acoustic doppler current profilers (ADCPs).

ADCP data is routinely gathered by all research cruises and moorings, but its vast potential has not yet been fully realized by fisheries scientists or biological oceanographers. To date, ADCP data has been used primarily to quantify the speed and direction of currents in the ocean, with biological backscattering from prey species of interest essentially considered noise to be subtracted out. Part of the reason why this rich acoustic dataset has been underutilized is because of the lack of established methods to identify and quantify the biological signal in the data, which was not originally calibrated for this task.

Here I present the novel use of an existing publicly-available, global acoustic doppler current profiler (ADCP) dataset to better characterize *in situ* distributions of mid-trophic level organisms, as well as their spatiotemporal variabilities throughout the tuna-rich Tropical Pacific. In combination with the work already done by Radenac et al. (2010) using moored TAO array ADCP data along the Equatorial Pacific, this analysis will help better resolve prey-based measures of tuna habitat quality and causes of catch variability, as well as variations in biogeochemical cycling and carbon export rates in the region. Alongside our scientific results, I also publish open-source code to promote awareness and utilization of this public ADCP dataset. I thus demonstrate how ADCP data can be analyzed to automatically quantify total backscatter and detect sound scattering layers/diel vertical migrations in any ocean region.

A.3 Methods

A.3.1 Use of publicly-available ADCP dataset

From the Joint Archive for Shipboard ADCP (JASADCP), I downloaded acoustic data taken by ADCPs mounted on ships cruising between 1985 and 2018. In general, one acoustic profile (40 points in depth) is taken every 5 minutes over the duration of each cruise. At the time of download (October 16, 2019), the archive contained data from 2277 cruises crisscrossing the global oceans. ADCP data for each cruise is contained in its own netcdf file, with the entire dataset totalling about 15 GB in size over all cruises. JASADCP (located here: https://uhslc.soest.hawaii.edu/sadcp/) is established and maintained by the National Centers for Environmental in collaboration with Eric Firing's ADCP Laboratory at the University of Hawaii.

Cruise tracks that traverse the Tropical Pacific (defined as 20°N-20°S, 120°E-75°W) at some point are shown in Fig. A.1a. The number of Tropical Pacific cruises within JASADCP is greatest between about 2004 and 2012, but there are also a number of cruises going back to 1985 (Fig. A.1b). The cruises in this region are relatively evenly spread out over the different months of the years, though the months of March/April and October/November were most frequently sampled (Fig. A.1c). The most commonly operated ADCP frequency in the Tropical Pacific was 150 kHz, followed by 75, 38, and 300 kHz in order (Fig. A.1d). Scatterers most likely to be detected at 150 kHz range in size from a few millimeters to a few centimeters (Sutor et al., 2005), with a minimum equivalent spherical diameter of ~1 mm (Luo et al., 2000). These 150 kHz scatterers thus include many mid-trophic level organisms of interest. At 38 and 75 kHz, larger scatterers such as euphausiids, squids, and fish swim bladders are well-detected. Meanwhile at 300 kHz, detection of the smallest mid-trophic level organisms, such as ~2 mm copepods and other macrozooplankton, is strengthened (Benoit-Bird and Lawson, 2016). Though these different ADCP frequencies penetrate the water column down to different depths and detect different organisms with different strengths, here I combine data from all frequencies in order to quantify total prey availabilities to top pelagic predators.

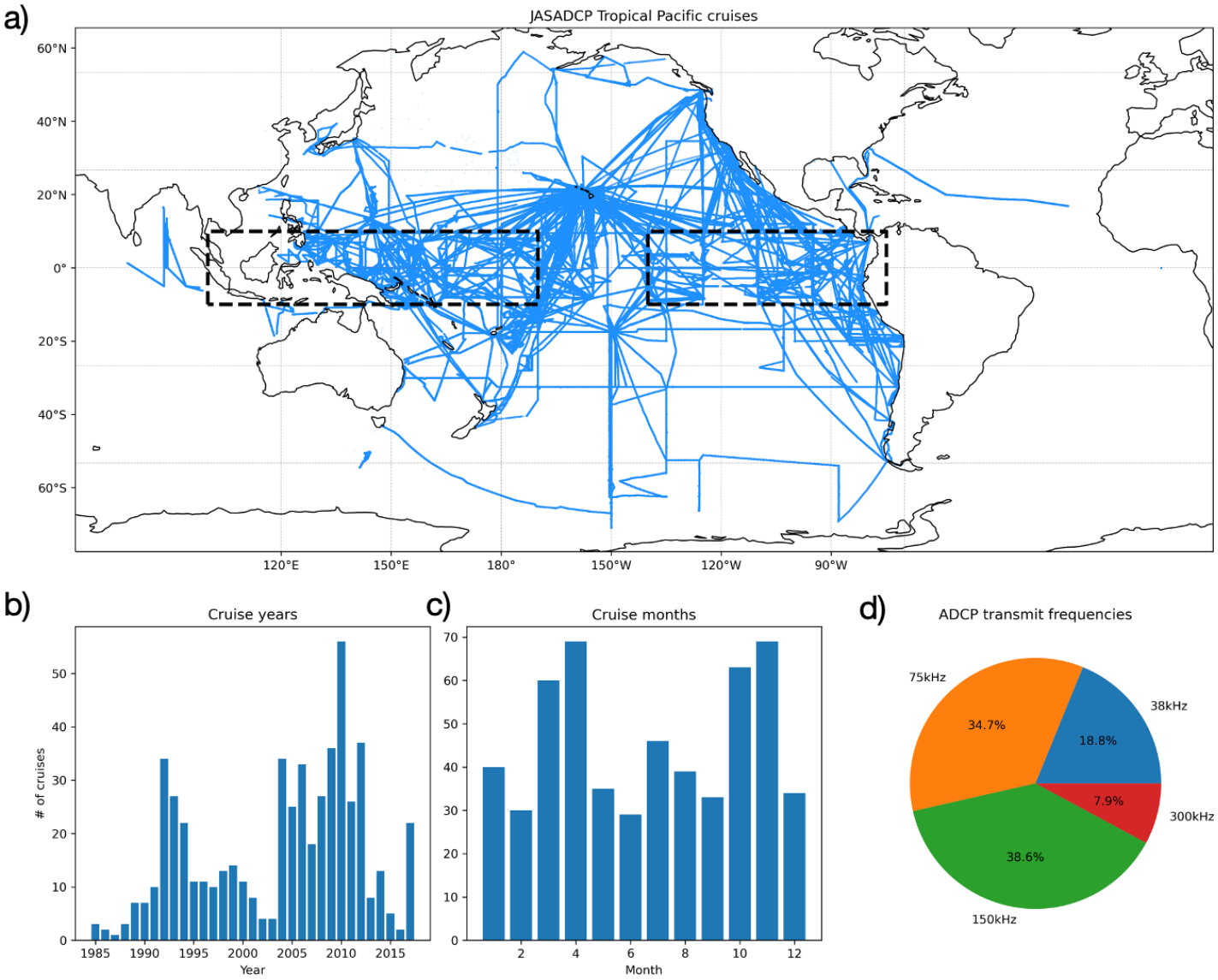

Figure A.1 | a.) Map of all cruise tracks that pass through the Tropical Pacific (120°E-75°W, 20°N-20°S) at some point. b.) Histogram of the years corresponding to the first day of each cruise shown in (a). c.) Histogram of the months corresponding to the first day of each cruise shown in (a). d.) Pie chart of ADCP transmit frequencies for all cruises shown in (a).

A.3.2 Computation of total volumetric backscatter (S_v)

To compute total volumetric backscatter (S_v) from raw ADCP received signal strength (named "amp" in the JASADCP netcdf files; also known as echo intensity or Received Signal Strength Indicator, RSSI), the following equation was used:

$$S_v = C + 10log((T_x + 273.16)R^2) - L_{DBM} - P_{DBW} + 2\alpha R + 10log(10^{k_c(E-E_r)/10} - 1)\text{ , (Eqn. 1)}$$

where:

- C = constant combining several parameters specific to each ADCP instrument [dB]
- T_x = temperature measured at the transducer [°C]
- R = along-beam range to the measurement [m]
- L_{DBM} = 10log(transmit pulse length [m])
- P_{DBW} = 10log(transmit power [Watts])
- α = absorption coefficient of the water [dB m^{-1}]
- k_c = RSSI slope [dB $count^{-1}$]
- E = RSSI [counts]
- E_r = noise floor [counts]
- Units of S_v are dB, referenced to [meters × 4π]$^{-1}$

T_x, R (computed as depth to scatterer divided by *cosine*(transducer beam angle)), transmit pulse length (needed to compute L_{DBM}), and E were all included in the metadata or data within the JASADCP archive, so these values did not require further processing. However, as can be seen from Eqn. 1, many constants from the ADCP instrument manufacturer (Teledyne RD Instruments), in addition to instrument output data that are not necessary for the ADCP's primary purpose (measuring current speeds and directions), are required to compute S_v. Because ADCP data have traditionally been used for measuring currents, many of these additional parameters/output data, including instrument serial numbers, are missing from the JASADCP archive. In cases where this information was not available, well-informed assumptions and approximations were used, as detailed in the sections and linked code below. The errors and uncertainties caused by these assumptions and approximations should be carefully computed by each individual researcher for each future analysis.

A.3.2.1 Narrowband instrument-specific values and calculations for S_v

For Narrowband ADCP (NBADCP) instruments, C was computed as:

$$C\ [dB] = 10log(\frac{4.47\times10^{-20}K_2K_S}{c})\text{ , (Eqn. 2)}$$

where c = speed of sound at the scattering layer being measured (details on how this is computed will be discussed in Section 2.2.2), according to Teledyne RD Instruments (1998), hereafter referred to as TRDI-1998. Values for K_2 (dimensionless system noise factor) and K_s (system constant depending on NBADCP frequency) were obtained from TRDI-1998. Transmit power (needed to compute P_{DBW}) was computed as:

$$Transmit\ power\ [Watts] = \frac{(V_s\times a)-b}{c}^2 \times K_{1c}\text{ , (Eqn. 3)}$$

where V_s is the real-time supply voltage to the NBADCP transmitter in Volts, assumed to be a constant 220 V. Varying V_s between 110 and 220 V only alters S_v by 0.0006 dB, which is a negligible error in total backscatter. K_{1c} is the power into the water during factory calibration in Watts, while a, b, and c are constants, all from TRDI-1998. k_c is computed as:

$$k_c\ [dB\ count^{-1}] = \frac{127.3}{T_e+271}\text{ , (Eqn. 4)}$$

where T_e [°C] is the temperature of system electronics. Because information on T_e is not available for any JASADCP cruise, T_e is replaced with T_x in Eqn. 4 whenever T_x is available. Eqn. 4 was only applied when $E < 200$ counts, as specified by TRDI-1998. (TRDI-1998 also states that if E is between 200 and 230 counts, calibration of k_c must be done by TRDI and if $E >$ 230 counts, k_c cannot be calibrated at all.) Whenever E was above 200 counts, that datapoint was thrown out.

A.3.2.2 Ocean Surveyor instrument-specific values and calculations for S_v

Values for C and P_{DBW} associated with all Ocean Surveyor (OS) instruments were taken from Mullison (2017). It was assumed that values of C corresponding to OS instruments

operating in 25% bandwidth (broadband) mode also applied to OS instruments operating in 6% bandwidth (narrowband) mode. k_c and E_r values were obtained for OS instruments via email correspondence with Jerry Mullison, Senior Scientist at Teledyne RD Instruments, in January 2020. It was also assumed that all parameters could be used for both generations of OS instruments (OS-I and OS-II).

A.3.2.3 Workhorse instrument-specific values and calculations for S_v

As for the OS instruments discussed in Section A.3.2.2 above, values for C and P_{DBW} associated with all Workhorse (WH) instruments were taken from Mullison (2017). A nominal k_c value for WH instruments was obtained via email correspondence with Scott Idle, Field Service Engineer at Teledyne RD Instruments, in January 2020. It was assumed that this nominal k_c value applied equally well to all frequencies.

A.3.2.4 BroadBand instrument-specific values and calculations for S_v

There was a general lack of information on parameters associated with BroadBand (BB) ADCP instruments. C for 150 kHz BroadBand (BB) instruments was therefore computed as the average of OS's C value at 150 kHz and WH's C value at 300 kHz. P_{DBW} was assumed to be equal to that of OS's at 150 kHz. A nominal k_c value for BB instruments was obtained via email correspondence with Scott Idle, Field Service Engineer at Teledyne RD Instruments, in January 2020.

A.3.2.5 Values and calculations for S_v applicable to all instruments

There are two parameters needed to calculate S_v which are computed in the same way across all instrument types: α and E_r. E_r is taken to be the lowest recorded RSSI within each cruise, as in Lee et al. (2004) and Gostiaux and van Haren (2010). α is computed as:

$$\alpha\ [dB\ km^{-1}] = \frac{A_1 P_1 f_1 f^2}{f^2 + f_1^2} + \frac{A_2 P_2 f_2 f^2}{f^2 + f_2^2} + A_3 P_3 f^2 \text{ , (Eqn. 5)}$$

where:

- $A_1 = (8.86/c)10^{0.78pH-5}$
- $f_1 = 2.8(S/35)^{0.5} 10^{[4-1245/(T+273)]}$
- $P_1 = 1$
- $A_2 = 21.44(S/c)(1 + 0.025T)$
- $P_2 = 1 - 1.37 \times 10^{-4} z + 6.2 \times 10^{-9} z^2$
- $f_2 = 8.17 \times 10^{[8-1990/(T+273)]}/[1 + 0.0018(S - 35)]$
- $P_3 = 1 - 3.83 \times 10^{-5} z + 4.9 \times 10^{-10} z^2$
- $T \le 20°C : A_3 = 4.937 \times 10^{-4} - 2.59 \times 10^{-5} T + 9.11 \times 10^{-7} T^2 - 1.5 \times 10^{-8} T^3$
- $T > 20°C : A_3 = 3.964 \times 10^{-4} - 1.146 \times 10^{-5} T + 1.45 \times 10^{-7} T^2 - 6.5 \times 10^{-10} T^3$
- f = frequency in kHz
- T = water temperature [°C]
- S = salinity [PSU, parts per thousand]
- z = depth [meters]
- pH = pH [unitless]
- c = sound speed [m s^{-1}]
- Predicts α to an accuracy of 5% for temperatures from -1.8 to 30°C, salinities from 30 to 35 ppt, and frequencies from 400 Hz to 1 MHz
- From Francois and Garrison (1982) via Simmonds and MacLennan (2008)

The speed of sound, c, is computed as:

$$c = 1448.96 + 4.591T - 0.05304T^2 + 2.374 \times 10^{-4} T^3 + 1.34(S - 35) + 0.0163z + 1.675 \times 10^{-7} z^2 - 0.01025T(S - 35) - 7.139 \times 10^{-13} T z^3 \text{ , (Eqn. 6)}$$

where:

- T = water temperature [°C]
- S = salinity [PSU, parts per thousand]
- z = depth [meters]
- Valid for temperatures from -2 to 30 °C, salinities from 25 to 40 ppt, and depths from 0 to 8000 m
- Standard error of the computed c is 0.07 m s^{-1}

- From Mackenzie (1981) via Simmonds and MacLennan (2008)

Finally, the total absorption term, $2\alpha R$, is computed as:

$$2\alpha R\,[dB] = \frac{2\alpha_p B}{cos(\theta)} + \sum_{n=1}^{b} \alpha_n \text{ , (Eqn. 7)}$$

where:

- α_p = absorption coefficient at the transducer [db m^{-1}]
- B = blank length [m]
- θ = transducer beam angle from vertical [degrees or radians]
- b = total number of depth cells
- $\alpha_n = \frac{2\alpha D}{cos(\theta)}$,
    - D = given depth cell length [m]
    - α = absorption coefficient in the given depth cell [db m^{-1}]
- From Deines (1999)

For the figures shown in Section A.4, a constant temperature of 25°C, a constant salinity of 35 psu, and a constant pH of 8.1 was assumed. Future work should evaluate the errors associated with this assumption by using contemporaneously measured temperatures, salinities, and pH values to compute α and c.

A.3.3 Detection of diel vertical migrations (DVMs) and sound scattering layers (SSLs) from S_v cross sections

There are many ways of automatically identifying SSLs and DVMs in acoustic data (Bianchi et al., 2013b; Cade and Benoit-Bird, 2014; Proud et al., 2015). I first attempted the two simple methods used in Bianchi et al. (2013b) (computing the depth of maximum day-to-night S_v change and the depth of maximum daytime subsurface S_v, though they use RSSI rather than S_v), but these methods were not able to identify the desired features (verified by eye) in the Tropical Pacific ADCP data analyzed here, due to the noisy nature of the data. Before attempting the

complex, multi-step, computationally-expensive methods used by others (Cade and Benoit-Bird, 2014; Proud et al., 2015), I consulted with data scientist Valentina Staneva in the eScience Institute at the University of Washington to explore whether there were any simpler algorithms that are readily usable by those with less computational power and experience, but which are still robust to noise. With minimal effort and data cleaning, both principal component analysis (PCA) and canny edge detection worked very well at reproducing DVMs and SSLs identified by eye. Canny edge detection operates by first Gaussian smoothing an image (or time-depth cross section in this case) to reduce the effect of noise and then finding the sharpest gradients in the smoothed image ("Canny edge detector — skimage v0.17.2 docs"). This method was ultimately chosen for analysis of Tropical Pacific prey variability here due to its ease of use and the high degree of interpretability of its results (see Fig. A.4).

A.4 Results and Discussion

A.4.1 Open source Python code

A.4.1.1 Code for JASADCP cruise metadata processing

The code linked here (create_JASADCP_metadata_df.ipynb at https://doi.org/10.5281/zenodo.3907368) processes the metadata from all of the netcdf files in JASADCP and enters it into a Pandas dataframe (or simply, a table or csv file). Assuming that one has already procured the JASADCP files (or a subset of them), one should be able to use this code right out-of-the-box after changing appropriate file paths. As the JASADCP archive grows, one can rerun this notebook as needed to generate a new dataframe containing all old and newly

added cruises. One can also use the output dataframe to select the netcdf files corresponding to user-defined frequencies, instruments, and regions, among many other subsettable attributes. Some netcdf files were missing metadata that could not be filled in. However, oftentimes when metadata was missing, it could be filled in based on some simple rules or via further investigation. For example, when transmit frequency was missing, it could often be inferred from the instrument's name. When the instrument name was missing, it could sometimes be inferred from the cruise's date, since only Narrowband ADCPs existed before 1991 (Teledyne RD Instruments, 2011); at other times, instrument name could be inferred by looking up spec sheets for the given cruise's vessel. When bandwidth was missing, it could sometimes be inferred from the cruise name or the instrument type. All occurrences of inferred metadata are coded and commented in detail in create_JASADCP_metadata_df.ipynb (https://doi.org/10.5281/zenodo.3907368). This code will work for the same above described situations associated with future entries into the JASADCP archive; however, as new issues arise with new entries, new ways to deal with these issues will have to be added into the existing code. For example, in the code version currently linked here, if a cruise's bandwidth is missing, but "os38bb", "os75bb", or "os150bb" are part of the cruise's name, then that cruise's bandwidth is filled in as broadband; if in the future, cruise name formats are changed, then new code will need to be added that properly reads the new cruise names and fills in missing bandwidths appropriately.

A.4.1.2 Code for computing and analyzing S_v

The notebooks/scripts here (fxns_Sv_compute.ipynb, setup_Sv_compute.ipynb, calc_Sv.py at https://doi.org/10.5281/zenodo.3907368) calculate S_v from RSSI, as described in Section 2.2. Assumptions needed to calculate S_v, first meticulously discussed in Section 2.2, are also detailed in each relevant section of code, which can be subsequently updated and improved as assumptions are disproved or solidified. The notebook here (adcp_main.ipynb at https://doi.org/10.5281/zenodo.3907368) calls the abovementioned S_v calculation notebooks/scripts and shows how JASADCP-derived S_v values can be used to analyze spatiotemporal variability in total backscatter and prey availability within the Tropical pacific between 1985 and 2018. This code can be easily adapted for any other ocean region, timeframe, etc. and demonstrates the use of canny edge detection to identify SSLs and DVM paths. It is also usable right out-of-the-box as long as one already has all JASADCP netcdf files downloaded and is able to install all Python packages listed in the associated Dockerfile (Dockerfile at https://doi.org/10.5281/zenodo.3907368).

A.4.2 Spatiotemporal variability in prey distributions in the Tropical Pacific

On average, the vertical distributions and availability of mid-trophic level scatterers differ substantially between the Eastern and Western Tropical Pacific, with shallower DVMs/SSLs and greater overall backscatter in the east (Fig. A.2). However, depths exhibiting greatest overall daytime backscatter, between 400 and 500 m, are similar between the east and west. Both

regions also contain some scatterers that stay at these depths all day. In the Eastern Tropical Pacific (Fig. A.2b), there also appears to be a community of scatterers that stay at around 600 m depth all day, which does not exist in the west (Fig. A.2a).

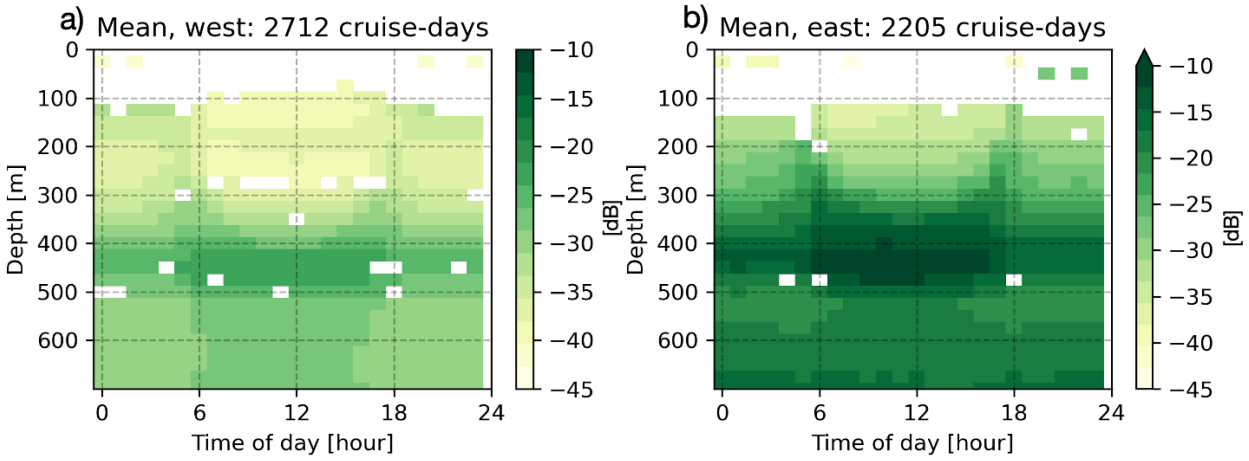

Figure A.2 | Total volumetric backscatter (S_v) temporally averaged over all available cruise-days and spatially averaged over the a.) Western Tropical Pacific (100°E-150°W, 10°N-10°S; western box denoted with dashed lines in Fig. A.1a) and b.) Eastern Tropical Pacific (140°W-75°W, 10°N-10°S; eastern box denoted with dashed lines in Fig. A.1a).

As with many other biogeochemical variables, ENSO drives substantial variability in the vertical distributions of zooplanktonic and micronektonic scatterers throughout the Tropical Pacific (Fig. A.3-A.4). During El Niño, greater backscattering values (Fig. A.3a,c), along with more pronounced and deeper DVMs (Fig. A.4a,c), occur in the west compared to during La Niña. An increase in total backscatter is in line with increased productivity in the west during El Niño (Chavez et al., 1999; Behrenfeld, et al., 2001; Lehodey, 2001; Turk et al., 2001). However, relatively oxygen-poor, colder waters are also brought closer to the surface in the west during El Niño (Leung et al., 2019); assuming that maximum DVM depths are limited by oxygen or temperature, one would thus expect DVMs to shoal in the west during El Niño. Because DVM depths instead deepen, it is likely that changes in light availability, rather than temperature and oxygen conditions, are driving the variations in DVM depth seen here. Though increases in

productivity promote light attenuation (thus decreasing light availability in the subsurface), decreases in cloud cover over the Western Equatorial Pacific during El Niño (Deser and Wallace, 1990; Deser et al., 1993) enhance the amount of sunlight reaching into the water column. The exact balance between these two factors needs to be further investigated, but because zooplankton/micronekton go deeper here during El Niño (opposite of what would be expected from temperature and oxygen changes), it is likely that the effect of decreased cloud cover wins out, causing migrating animals to descend to darker depths in order to avoid their visual predators.

During La Niña, smaller backscattering values (Fig. A.3b,d), along with more pronounced but similarly deep DVMs (Fig. A.4b,d), occur in the east compared to during El Niño. These more pronounced DVMs may also be due to decreases in cloud cover during La Niña by the same mechanisms discussed above for the Western Equatorial Pacific during El Niño. Further investigation is needed, however, to better understand the decreases in total backscatter here, as productivity typically increases during La Niña phases in the Eastern Equatorial Pacific (Chavez et al., 1999; Behrenfeld, et al., 2001; Lehodey, 2001; Turk et al., 2001). Changes in species composition from stronger (gas bladder-containing) to weaker (fluid-filled animals) scatterers could be confounding the result; future work should thus ground truth these ENSO-related variations using data from species-discriminating image analyses or net tows (Picheral et al., 2017; Lombard et al., 2019). Future work should also quantify the underlying drivers of these backscatter/DVM changes more precisely, as well as better characterize the significance of all ENSO-driven changes.

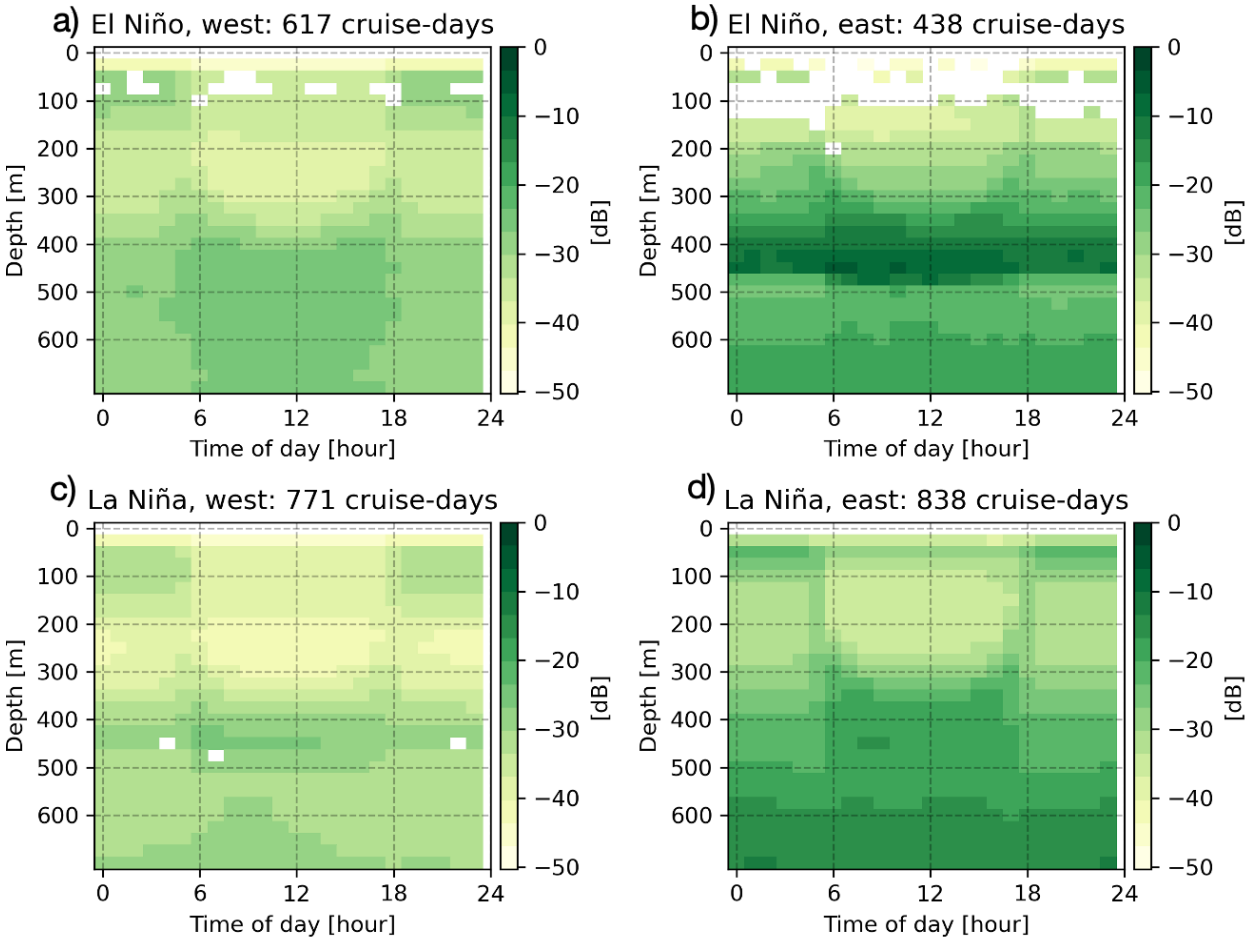

Figure A.3 | Total volumetric backscatter (S_v) temporally averaged over all available cruise-days and spatially averaged over a.) the Western Tropical Pacific (100°E-150°W, 10°N-10°S; western box denoted with dashed lines in Fig. A.1a) during El Niño, b.) the Eastern Tropical Pacific (140°W-75°W, 10°N-10°S; eastern box denoted with dashed lines in Fig. A.1a) during El Niño, c.) the Western Tropical Pacific during La Niña, and d.) the Eastern Tropical Pacific during La Niña.

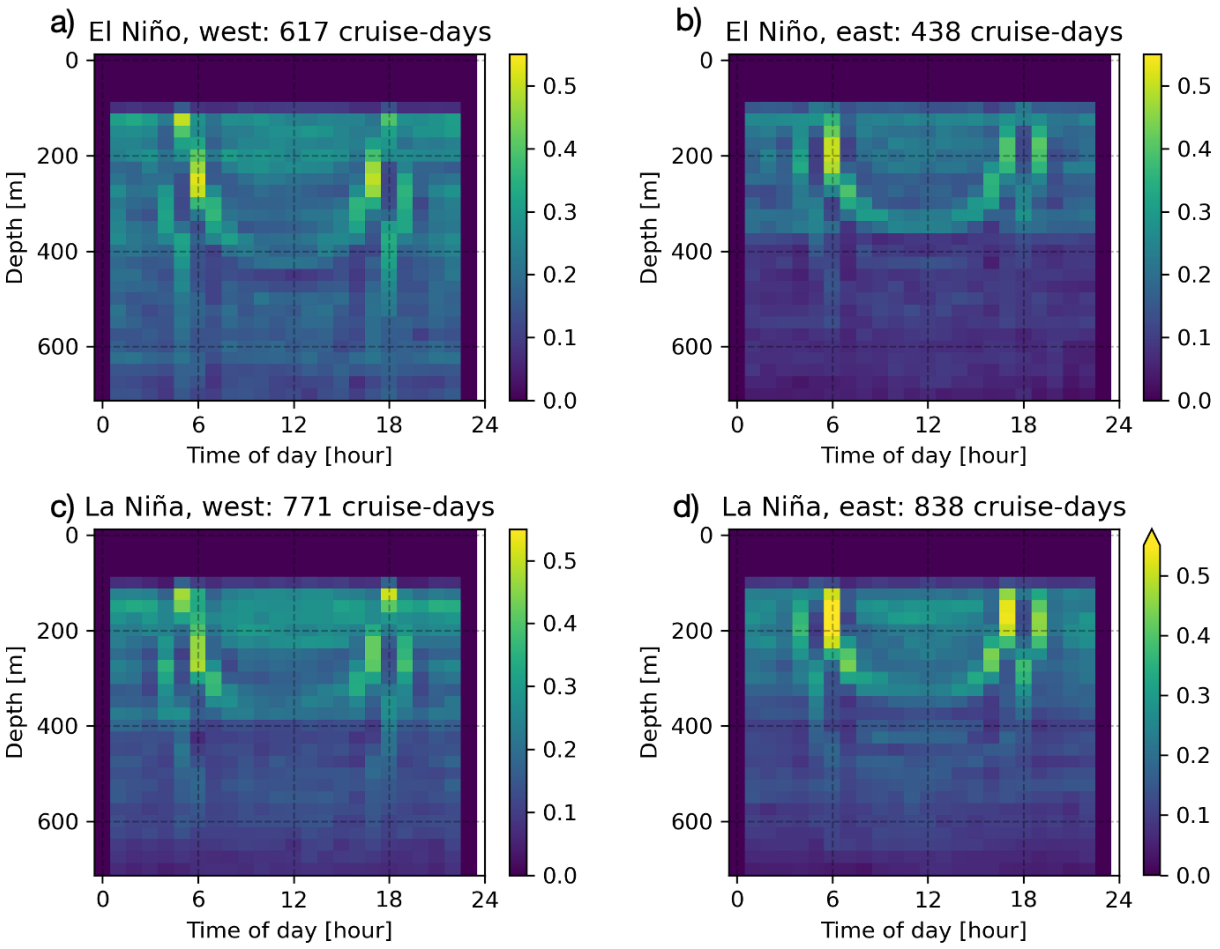

Figure A.4 | Normalized detected edge strength temporally averaged over all available cruise-days and spatially averaged over a.) the Western Tropical Pacific (100°E-150°W, 10°N-10°S; western box denoted with dashed lines in Fig. A.1a) during El Niño, b.) the Eastern Tropical Pacific (140°W-75°W, 10°N-10°S; eastern box denoted with dashed lines in Fig. A.1a) during El Niño, c.) the Western Tropical Pacific during La Niña, and d.) the Eastern Tropical Pacific during La Niña. Canny edge detection is performed on raw S_v for each cruise-day, where the value 1 is assigned to edges and 0 is assigned to non-edges. This output is then averaged over the given spatial regions and time periods to generate the subplots here.

A.5 Conclusions

The first goal of this chapter was to illuminate how and why spatial distributions and abundances of prey for top pelagic predators in the Tropical Pacific, particularly culturally and economically important tuna species, vary over time and space. I found that prey availability is higher and DVMs are shallower in the Eastern Tropical Pacific. Unsurprisingly, ENSO drives

variability in mid-trophic level prey distributions, abundance, and potentially composition throughout the Tropical Pacific. ENSO-induced changes in cloud cover and light availability may be the dominant cause of observed vertical variations in prey distributions here; these variations in cloud cover counteract the effects of ENSO-induced changes in other variables such as temperature and oxygen. Climate change effects on ENSO, cloud cover, and prey availability are uncertain. Thus, continued monitoring of prey availability and collection of ADCP data are needed given the socioeconomic importance of tuna and other top pelagic predators. Knowledge of spatiotemporal variability in prey availability and their physical drivers will help inform better management of the tuna stocks in this region.

Though this study focuses on tuna in the Tropical Pacific, the methods and datasets used here can be applied to virtually all other commercially and ecologically valuable top predators throughout the world's open oceans as well. The second goal of this chapter was therefore to demonstrate how to use already-existing ADCP data to quantify distributions of mid-trophic level organisms. The work here thus creates globally-applicable, highly-automated code for quantifying total backscatter and detecting aggregated layers of mid-trophic level prey species (often called sound scattering layers, or SSLs) in this type of acoustic data.

A.6 Future work

The most immediate next steps would be to quantify uncertainty and error due to the assumptions described throughout the above text in both output S_v values and resultant computed DVM/SSL depths. It would be particularly important to examine the effects of using contemporaneously measured temperatures and salinities on S_v calculations. The beginnings of

this work can be found here: https://github.com/shirleyswirley/acoustic-variability/blob/develop/python/adcp_main.ipynb on June 24, 2020. After quantification of these various uncertainties, the significance of differences between locations and ENSO phases can be better computed for the composite cross sections shown here. ADCP data from different frequencies could also be split out to see how this alters resulting S_v values and DVM depths.

After this, better techniques to filter and clean the ADCP data need to be developed. The beginnings of this work can be found here: https://github.com/shirleyswirley/acoustic-variability/blob/develop/python/helper_notebooks/filter_and_calc_DVM_SSL_depth_JASADCP.ipynb on June 24, 2020.

Next, someone (or multiple people) should click through and label SSLs/DVMs in the entire JASADCP dataset so that future users can validate their algorithms using more than just a handful of cruises examined by eye. Many methods of identifying DVM depths and SSLs were attempted here, but there are still many more to try. Machine learning techniques, particularly a convolutional neural network, would likely do a good job of identifying DVMs and SSLs in future datasets once the current ones are labeled and validated against. Again, the first step toward beginning this work would be labeling of DVMs/SSLs in the currently available data. These machine learning and other techniques should be attempted and compared with the ones in this study as well as with labeled cross sections in future work.

Future work should also release temporally-resolved, gridded global maps of DVM/SSL depths and water column-integrated total backscatter. Fisheries scientists can then use these maps to force/parameterize prey availability in their habitat, spatial distribution, and stock assessment

models. Code used to create these gridded global maps should of course also be released. Higher-resolution mapping and spatial averaging over more targeted areas of user interest would also be possible upon release of this open-source code that can readily process the ADCP data.

Here I did not compute biomasses of the scatterers detected, but future work should calculate approximate biomasses of the scatterers present by integrating the ADCP dataset with net tows, imaging analyses, or other measurement methods that can identify species making up scattering layers. When these complementary datasets are not available, ranges of biomass can be computed by assuming animals of various sizes/shapes and compositions (fluid-filled, hard elastic shelled, or containing gas-bladders) (Bertrand, 2003; Jech et al., 2015; Proud et al., 2019). Continued validation and ground truthing of ADCP data against these other methods should also be performed.

Besides describing the spatiotemporal variability in prey species abundances as was done here, it is also important to carefully quantify what drives this variability and determine whether these drivers can be measured from space and subsequently used to estimate prey availability remotely. Future work should establish globally-applicable relationships between easily-observed oceanographic characteristics and prey abundances to enable a more accurate understanding of prey availability in real-time and as drivers of prey availability change with future warming. In particular, the roles of temperature, oxygen, and light in driving this variability should be better quantified. If prey availability is readily predicted by drivers with globally-available observations, one can also create a global map of derived average prey availabilities, as well as a global map of potential changes in prey availabilities with climate change.

Future work and analyses should also combine JASADCP with other acoustic datasets, including data from the TAO moored array (as was analyzed by Radenac et al., 2010), the NOAA Water Column Sonar Data Collection, IMOS, and BODC. The combined spatiotemporal coverage from all of these datasets gathered together would be tremendous.

Finally, and perhaps most importantly of all, future work should seek to generate an updated set of requirements in JASADCP cruise reporting so that valuable ADCP data from all future cruises can be readily used for biological as well as physical measurement purposes. Adherence to this updated set of requirements would increase the value of all ADCP measurements and provide marine biologists, biological oceanographers, and fisheries scientists/managers with much-needed spatially and temporally resolved information on micronektonic organism distributions. To begin, instrument names should be made uniform and serial numbers, bandwidth modes, transmit powers, and instrument-specific k_c and E_r values should always be reported.

A.6 Acknowledgments

Thank you to Jerry Mullison and Scott Idle at Teledyne RD Instruments for their assistance in getting needed information on the ADCP instruments. Thank you to Ali Della Penna for guidance on calculating S_v values. Thank you to Valentina Staneva for assistance with detecting DVMs/SSLs. And thank you especially to all the scientists who gathered and curated this amazing ADCP data, especially Eric Firing!

A.7 References

Archibald, K. M., Siegel, D. A., & Doney, S. C. (2019). Modeling the Impact of Zooplankton Diel Vertical Migration on the Carbon Export Flux of the Biological Pump. *Global Biogeochemical Cycles*, *33*(2), 181–199. https://doi.org/10.1029/2018GB005983

Behrenfeld, M. J., Randerson, J. T., McClain, C. R., Feldman, G. C., Los, S. O., Tucker, C. J., et al. (2001). Biospheric Primary Production During an ENSO Transition. *Science*, *291*(5513), 2594–2597. https://doi.org/10.1126/science.1055071

Benoit-Bird, K. J., & Lawson, G. L. (2016). Ecological Insights from Pelagic Habitats Acquired Using Active Acoustic Techniques. *Annual Review of Marine Science*, *8*, 463–490. https://doi.org/10.1146/annurev-marine-122414-034001

Bertrand, A., Bard, F.-X., & Josse, E. (2002). Tuna food habits related to the micronekton distribution in French Polynesia. *Marine Biology*, *140*(5), 1023–1037. https://doi.org/10.1007/s00227-001-0776-3

Bianchi, D., Stock, C., Galbraith, E. D., & Sarmiento, J. L. (2013a). Diel vertical migration: Ecological controls and impacts on the biological pump in a one-dimensional ocean model. *Global Biogeochemical Cycles*, *27*(2), 478–491. https://doi.org/10.1002/gbc.20031

Bianchi, D., Galbraith, E. D., Carozza, D. A., Mislan, K. a. S., & Stock, C. A. (2013b). Intensification of open-ocean oxygen depletion by vertically migrating animals. *Nature Geoscience*, *6*(7), 545–548. https://doi.org/10.1038/ngeo1837

Bigelow, K. A., Hampton, J., & Miyabe, N. (2002). Application of a habitat-based model to estimate effective longline fishing effort and relative abundance of Pacific bigeye tuna (Thunnus obesus). *Fisheries Oceanography*, *11*(3), 143–155. https://doi.org/10.1046/j.1365-2419.2002.00196.x

Brill, R. W., & Lutcavage, M. E. (2001). Understanding Environmental Influences on Movements and Depth Distributions of Tunas and Billfishes Can Significantly Improve Population Assessments. *American Fisheries Society Symposium*, *25*, 179–198.

Cade, D. E., & Benoit−Bird, K. J. (2014). An automatic and quantitative approach to the detection and tracking of acoustic scattering layers. *Limnology and Oceanography: Methods*, *12*(11), 742–756. https://doi.org/10.4319/lom.2014.12.742

Chavez, F. P., Strutton, P. G., Friederich, G. E., Feely, R. A., Feldman, G. C., Foley, D. G., & McPhaden, M. J. (1999). Biological and Chemical Response of the Equatorial Pacific Ocean to the 1997-98 El Niño. *Science*, *286*(5447), 2126–2131. https://doi.org/10.1126/science.286.5447.2126

Deines, K. L. (1999). Backscatter estimation using Broadband acoustic Doppler current profilers. In *Proceedings of the IEEE Sixth Working Conference on Current Measurement (Cat. No.99CH36331)* (pp. 249–253). https://doi.org/10.1109/CCM.1999.755249

Deser, C., & Wallace, J. M. (1990). Large-Scale Atmospheric Circulation Features of Warm and Cold Episodes in the Tropical Pacific. *Journal of Climate*, *3*(11), 1254–1281. https://doi.org/10.1175/1520-0442(1990)003<1254:LSACFO>2.0.CO;2

Deser, C., Wahl, S., & Bates, J. J. (1993). The Influence of Sea Surface Temperature Gradients on Stratiform Cloudiness along the Equatorial Front in the Pacific Ocean. *Journal of Climate*, *6*(6), 1172–1180. https://doi.org/10.1175/1520-0442(1993)006<1172:TIOSST>2.0.CO;2

Duffy, L. M., Kuhnert, P. M., Pethybridge, H. R., Young, J. W., Olson, R. J., Logan, J. M., et al. (2017). Global trophic ecology of yellowfin, bigeye, and albacore tunas: Understanding predation on micronekton communities at ocean-basin scales. *Deep Sea Research Part II: Topical Studies in Oceanography*, *140*, 55–73. https://doi.org/10.1016/j.dsr2.2017.03.003

Dwinovantyo, A., Manik, H. M., Prartono, T., Susilohadi, S., & Mukai, T. (2019). Variation of Zooplankton Mean Volume Backscattering Strength from Moored and Mobile ADCP Instruments for Diel Vertical Migration Observation. *Applied Sciences*, *9*(9), 1851. https://doi.org/10.3390/app9091851

Francois, R. E., & Garrison, G. R. (1982). Sound absorption based on ocean measurements. Part II: Boric acid contribution and equation for total absorption. *The Journal of the Acoustical Society of America*, *72*(6), 1879–1890. https://doi.org/10.1121/1.388673

Goodyear, C. P. (2003). Tests of the robustness of habitat-standardized abundance indices using simulated blue marlin catch–effort data. *Marine and Freshwater Research*, *54*(4), 369–381. https://doi.org/10.1071/mf01253

Gostiaux, L., & van Haren, H. (2009). Extracting Meaningful Information from Uncalibrated Backscattered Echo Intensity Data. *Journal of Atmospheric and Oceanic Technology*, *27*(5), 943–949. https://doi.org/10.1175/2009JTECHO704.1

Jech, J. M., Horne, J. K., Chu, D., Demer, D. A., Francis, D. T. I., Gorska, N., et al. (2015). Comparisons among ten models of acoustic backscattering used in aquatic ecosystem research. *The Journal of the Acoustical Society of America*, *138*(6), 3742–3764. https://doi.org/10.1121/1.4937607

Le Borgne, R., Allain, V., Griffiths, S. P., Matear, R. J., McKinnon, D. A., & Richardson, A. J. (2011). Vulnerability of open ocean food webs in the tropical Pacific to climate change. In *Vulnerability of Tropical Pacific Fisheries and Aquaculture to Climate Change* (pp. 189–250). New Caledonia: Secretariat of the Pacific community.

Lee, K., Mukai, T., Kang, D., & Iida, K. (2004). Application of acoustic Doppler current profiler combined with a scientific echo sounder for krill Euphausia pacifica density estimation. *Fisheries Science*, *70*(6), 1051–1060. https://doi.org/10.1111/j.1444-2906.2004.00905.x

Lehodey, P., Bertignac, M., Hampton, J., Lewis, A., & Picaut, J. (1997). El Niño Southern Oscillation and tuna in the western Pacific. *Nature*, *389*(6652), 715–718. https://doi.org/10.1038/39575

Lehodey, Patrick. (2001). The pelagic ecosystem of the tropical Pacific Ocean: dynamic spatial modelling and biological consequences of ENSO. *Progress in Oceanography*, *49*(1), 439–468. https://doi.org/10.1016/S0079-6611(01)00035-0

Leroy, C. C. (1969). Development of Simple Equations for Accurate and More Realistic Calculation of the Speed of Sound in Seawater. *The Journal of the Acoustical Society of America*, *46*(1B), 216–226. https://doi.org/10.1121/1.1911673

Leung, S., Thompson, L., McPhaden, M. J., & Mislan, K. A. S. (2019). ENSO drives near-surface oxygen and vertical habitat variability in the tropical Pacific. *Environmental Research Letters*, *14*(6), 064020. https://doi.org/10.1088/1748-9326/ab1c13

Lombard, F., Boss, E., Waite, A. M., Vogt, M., Uitz, J., Stemmann, L., et al. (2019). Globally Consistent Quantitative Observations of Planktonic Ecosystems. Frontiers in Marine Science, 6. https://doi.org/10.3389/fmars.2019.00196

Luo, J., Ortner, P. B., Forcucci, D., & Cummings, S. R. (2000). Diel vertical migration of zooplankton and mesopelagic fish in the Arabian Sea. *Deep Sea Research Part II: Topical Studies in Oceanography*, *47*(7), 1451–1473. https://doi.org/10.1016/S0967-0645(99)00150-2

Mackenzie, K. V. (1981). Nine−term equation for sound speed in the oceans. *The Journal of the Acoustical Society of America*, *70*(3), 807–812. https://doi.org/10.1121/1.386920

Maunder, M. N., & Piner, K. R. (2015). Contemporary fisheries stock assessment: many issues still remain. *ICES Journal of Marine Science*, *72*(1), 7–18. https://doi.org/10.1093/icesjms/fsu015

Maunder, M. N., Sibert, J. R., Fonteneau, A., Hampton, J., Kleiber, P., & Harley, S. J. (2006). Interpreting catch per unit effort data to assess the status of individual stocks and communities. *ICES Journal of Marine Science*, *63*(8), 1373–1385. https://doi.org/10.1016/j.icesjms.2006.05.008

Menkes, C. E., Allain, V., Rodier, M., Gallois, F., Lebourges-Dhaussy, A., Hunt, B. P. V., et al. (2015). Seasonal oceanography from physics to micronekton in the south-west Pacific. *Deep Sea Research Part II: Topical Studies in Oceanography*, *113*, 125–144. https://doi.org/10.1016/j.dsr2.2014.10.026

Mullison, J. (2017). *Backscatter Estimation Using Broadband Acoustic Doppler Current Profilers - Updated* (FSA No. 031). Poway, CA: Teledyne RD Instruments. Retrieved

from http://www.teledynemarine.com/Documents/Brand%20Support/RD%20INSTRUMENTS/Technical%20Resources/Technical%20Notes/WorkHorse%20-%20ADCP%20Special%20Applications%20and%20Modes/FSA031.pdf

Picheral M, Colin S, Irisson J-O (2017). EcoTaxa, a tool for the taxonomic classification of images. http://ecotaxa.obs-vlfr.fr

Prince, E. D., & Goodyear, C. P. (2006). Hypoxia-based habitat compression of tropical pelagic fishes. *Fisheries Oceanography*, *15*(6), 451–464. https://doi.org/10.1111/j.1365-2419.2005.00393.x

Proud, R., Cox, M. J., Wotherspoon, S., & Brierley, A. S. (2015). A method for identifying Sound Scattering Layers and extracting key characteristics. *Methods in Ecology and Evolution*, *6*(10), 1190–1198. https://doi.org/10.1111/2041-210X.12396

Proud, R., Handegard, N. O., Kloser, R. J., Cox, M. J., & Brierley, A. S. (2019). From siphonophores to deep scattering layers: uncertainty ranges for the estimation of global mesopelagic fish biomass. *ICES Journal of Marine Science*, *76*(3), 718–733. https://doi.org/10.1093/icesjms/fsy037

Radenac, M.-H., Plimpton, P. E., Lebourges-Dhaussy, A., Commien, L., & McPhaden, M. J. (2010). Impact of environmental forcing on the acoustic backscattering strength in the equatorial Pacific: Diurnal, lunar, intraseasonal, and interannual variability. Deep Sea Research Part I: Oceanographic Research Papers, 57(10), 1314–1328. https://doi.org/10.1016/j.dsr.2010.06.004

Renard, B. (2003). *Inversion of acoustic zooplankton measurement for adaptive physical-biological ocean forecast* (Thesis). Massachusetts Institute of Technology. Retrieved from https://dspace.mit.edu/handle/1721.1/91801

Canny edge detector — skimage v0.17.2 docs. (n.d.). Retrieved June 23, 2020, from https://scikit-image.org/docs/stable/auto_examples/edges/plot_canny.html

Simmonds, J., & MacLennan, D. N. (2008). *Fisheries Acoustics: Theory and Practice*. John Wiley & Sons.

Smeti, H., Pagano, M., Menkes, C., Lebourges−Dhaussy, A., Hunt, B. P. V., Allain, V., et al. (2015). Spatial and temporal variability of zooplankton off New Caledonia (Southwestern Pacific) from acoustics and net measurements. *Journal of Geophysical Research: Oceans*, *120*(4), 2676–2700. https://doi.org/10.1002/2014JC010441

Sutor, M. M., Cowles, T. J., Peterson, W. T., & Pierce, S. D. (2005). Acoustic observations of finescale zooplankton distributions in the Oregon upwelling region. *Deep Sea Research Part II: Topical Studies in Oceanography*, *52*(1), 109–121. https://doi.org/10.1016/j.dsr2.2004.09.029

Teledyne RD Instruments. (1998). *FST-003 - Calculating absolute backscatter in narrowband ADCPs* (Field Service Technical Paper No. FST-003). Retrieved from http://www.teledynemarine.com/Documents/Brand%20Support/RD%20INSTRUMENTS/Technical%20Resources/Technical%20Notes/Narrowband/FST003.PDF

Teledyne RD Instruments. (2011). *Acoustic Doppler Current Profiler Principles of Operation: A Practical Primer* (No. P/N 951-6069-00). Retrieved from https://www.comm-tec.com/Docs/Manuali/RDI/BBPRIME.pdf

Urick, R. (1983). *Principles of Underwater Sound, Third edition (Soft and Hard Covers)*. Peninsula Pub